A genetic algorithm approach to characterising post-AGB circumstellar environments

Daniel Macdonald

A thesis presented to Macquarie University
for the degree of
Doctor of Philosophy
Department of Physics & Astronomy
May 2017

MACQUARIE
University
SYDNEY·AUSTRALIA

I certify that the work in this thesis has not previously been submitted for a degree nor has it been submitted as part of the requirements for a degree to any other university or institution other than Macquarie University and Université Nice Sophia Antipolis. I certify that the thesis is an original piece of research, other than where indicated, and it has been written by me. In addition, I certify that all information sources and literature used are indicated in the thesis.

. . . . . .

Daniel Macdonald

Abstract

The topic of this thesis is the characterisation of the circumstellar environments about AGB and post-AGB stars via high resolution optical (mid-infrared) interferometry. Interferometric observations provide the required high angular resolution to study of these objects, and the parametric constraints of such regions provide insight into the evolutionary pathways that have given rise to these astrophysical objects. This will helps us to reach the goal of understanding the stellar pathways that turn AGB stars into white dwarfs.

In this thesis we focus on the development and application of a systematic method of fitting optical interferometric data products, in a quantitative, fully reproducible and non-subjective fashion. Such methods improve upon previous attempts to solve the inverse optimisation problem that exists between the interferometric data outputs and the radiative transfer models that are needed to give quantitative environmental descriptions. By running a number of search heuristics (genetic algorithms) we generate probability density functions associated with each parameter, and reveal parametric correlations, degeneracies, confidence intervals, as well as final best fit solutions.

By applying the algorithm to 4 nebulae for which interferometric data had been obtained previously, we confirm the existence of dusty tori. The parameters we derive point to the existence of post-AGB stars at their core. These data, together with other observations from the literature lead us to conclude that the collimated nebulae observed must be the product of a strong binary interaction, where jets have shaped the nebulae or where the collimated nebulae derive from a common envelope ejection of the entire envelope.

Acknowledgements

I would like to gratefully thank and acknowledge all those whose assistance and guidance has made this research possible.

I would like to send particular thanks to Orsola DeMarco for her support and guidance over the course of this thesis, and to Olivier Chesneau, Eric Lagadec and Thierry Lanz and Mark Wardle for their direction and assistance.

I would like to also acknowledge and thank those that have helped improve upon, and contribute to, various aspects of this research, in particular: Jun Ma, Stacey Bright, Alain Spang, Claudia Paladini, Gilles Niccolini, Geoff Clayton, Jan Staff, Florentin Millour and Andrea Chiavassa.

I would like to less formally thank those who have helped in less formal ways, you know who you are. And to my parents and family for being as good as they are.

Contents

List of Figures

List of Tables

Chapter 1

Introduction

"To know the laws that govern the winds,
and to know that you know them. . . "
J. Slocum – 1900

In early studies of stellar evolution the relatively hot planetary nebula (PN) phase, or *'planetaries'*, were considered young objects representative of an early phase in the stellar evolutionary path. The evolutionary interpretation at the time was a trajectory in which stars were suggested to evolve from hot to cool temperature objects (e.g., Russell, 1914). Though stellar evolution understanding has matured greatly since this time (it is after all known that these early ideas could hardly be further removed from the current depiction), the PN and pre-PN phase still remains a relatively poorly understood period of stellar evolution.

The PN phase is in a fact a short-lived period found late in the stellar lifetime. The phase follows substantial mass loss from a star on its evolutionary trajectory from red giant to white dwarf (e.g., Lutz, 1993). Despite progress made in PN understanding, present day models are still considered incomplete, and we are yet to establish a fully consistent narrative that describes the evolutionary transition. Currently it is accepted that late in the red giant phase, the object undergoes a period of high mass loss, resulting in the formation of a circumstellar gas structure. In the objects we recognise as PNe, the structure is later ionised by the radiation from the remaining (hot) stellar core. There are, however two major problems with the current understanding: (i) the nature of the mass loss and (ii) why the PNe observed are predominantly aspherical in nature.

Importantly, knowledge of the predominant mechanism(s) that drive mass at this late phase of evolution, is critical to understanding galaxy evolution. It is the mass loss phase of the red giants that allows the processed elements of the stellar interior to migrate out into the interstellar medium (ISM) for example. It is also known that a great fraction of the carbon and nitrogen found in the ISM, is introduced via this phase. To understand the chemical make-up of the ISM and the impact it has on future generations of stars and galactic evolution more generally, one needs to first gain a deeper understanding of these final, complex stages of stellar evolution.

The second problem: why PNe are generally not spherical in nature as theory predicts, remains a contested topic. The conversation generally takes place between two camps of thought, the first in which the AGB star is proposed to evolve in an

isolated state (i.e. without companion interaction), and the second that advocates for the interaction of a nearby companion(s). These topics will be discussed later in the chapter, but let us first begin by providing an overview of stellar evolution from the main sequence (MS) to the PN phase.

1.1 Planetary nebulae progenitors

1.1.1 Evolution from the main sequence

Intermediate mass MS stars ($\sim$1.0 to 8.0 $M_{\odot}$) are the progenitors of PN central stars. Following $\sim 10^8 - 10^{10}$ years of hydrogen burning on the MS, the stellar core is eventually converted to helium (Iben, 1991, 1995). As the helium core contracts it fuels an increased nuclear shell burning. This extra burning forces the radial expansion of the photosphere, and the Stefan-Boltzmann law sees the stellar photosphere cool dramatically (to temperatures near $\sim$3500K). With this, the luminosity also increases (to a value of the order of hundreds of $L_{\odot}$). At this point the star has well and truly left the MS.

The evolutionary changes that take place post MS, are perhaps best characterised in the context of the Hertzsprung-Russell (HR) diagram, a plot of luminosity vs effective temperature. The phase following the exhaustion of the hydrogen core, is the first of two giant phases of the star, known as the first-ascent red giant or red-giant branch (RGB) phase. On the HR diagram, the evolutionary step is seen as a movement to the right and then upwards (refer to Figure 1.1). Once on the RGB, the newly formed helium in the core continues to increase in temperature and will ignite when the temperature grows to $\sim 3 \times 10^8$ K. When the helium core is exhausted, the star begins its second-ascent red giant phase. At this point the star's evolution follows very similarly the processes of the first ascent, and is aptly named the asymptotic giant branch (AGB) phase, coming from the fact that during the expansion, the $T_\star - L_\star$ relation is asymptotic to the $T_\star - L_\star$ relation of the RGB expansion phase (e.g., Kwok, 2007).

The AGB phase is perhaps the most dynamic and unstable stage in single star stellar evolution, and is typically examined in two parts. The first, known as the early AGB (E-AGB) phase, follows directly the quenching of the hydrogen shell (caused by the abrupt stellar expansion). While the second stage is the much shorter ($\sim 10^5 - 10^6$ years Iben, 1995), and more dynamic phase that follows, known as the thermally-pulsating AGB (TP-AGB) phase.

During the E-AGB the main source of energy is provided by helium burning in a shell just above the degenerate core, a phase ordinarily lasting $\sim 10^7$ years (Iben & Renzini, 1983). During the E-AGB, the core of the AGB star is an electron degenerate mixture of predominantly carbon and oxygen. Of those stars considered more massive than intermediate, the core is made up of a non-degenerate mixture of carbon and oxygen, in which further nuclear core burning is able to continue. The inactive core of our lower mass star, however, expands with the accumulation of helium-byproducts from the hydrogen burning shell above, and expansion continues until a point in which a thin shell of hydrogen beyond the helium shell is re-ignited. At this stage the TP-AGB phase has commenced. For upwards of ninety percent of the TP-AGB lifetime hydrogen burns in this outer

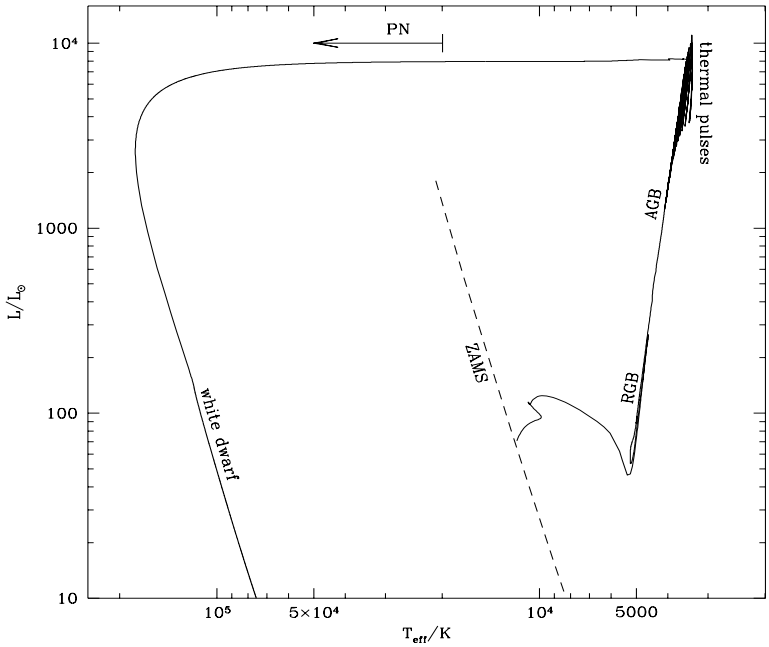

Figure 1.1: The evolutionary track of a 3-$M_\odot$ zero age main sequence star on the H-R diagram. The PN phase is indicated at the top of the evolutionary track. Figure from Kwok (2007).

shell, it is during this time that the shell burning becomes the dominant form of energy. However, as its byproducts accumulate in the helium shell below, the He-shell eventually becomes massive enough that a triple-α reaction starts under degenerate conditions and leads to a thermonuclear runaway, a violent and explosive event known as a He-shell flash (Schwarzschild & Härm, 1965).

He-shell flashes are found to self-quench as a result of eventual cooling due to expansion. The He-flash phases are perhaps the most important phases in regards to the contribution to the chemical makeup of the ISM, as the convective envelope is known to reach down beyond the inter-shell region (the region between the H and He shell) and drag up helium, and heavier He burning by-products, in particular ^{12}C, in a process known as third dredge-up (Iben & Renzini, 1983).

The He-flash events are followed by periods of quiescent hydrogen burning, and the pulse cycle is found to repeat semi-periodically every $\sim 10^4 - 10^5$ years (Olofsson, 1999) as the hydrogen shell re-deposits its by-products. The number of He-flashes endured is known to be mass dependent. For those stars that become PNe, the AGB phase ends following the complete removal of the hydrogen envelope due to mass loss.

The evolutionary phases from MS to PN are presented for the case of a 3-$M_\odot$ zero age MS (ZAMS) star on the HR diagram in Figure 1.1. For more in depth accounts RGB and AGB stellar evolution the reader is referred to the following sources Iben (1967), Iben & Renzini (1983), Vassiliadis & Wood (1994), Bloecker (1995), Herwig (2005), Kwok (2007) and Miller Bertolami (2016).

1.1.2 Interacting Stellar Wind (ISW) model

In comparing mid-infrared measurements of the AGB phase to images taken at optical wavelengths, an excess of infrared flux can be found. Opaque dusty shells were initially proposed as the cause of this infrared-excess, and were soon confirmed observationally. The distinct 10μm silicate emission features was the first indication to confirm dusty circumstellar material (e.g., Woolf & Ney, 1969), while additional evidence for dusty material was observed a few years later with the $11.3\mu m$ SiC feature (e.g., Treffers & Cohen, 1974), common to carbon dust. These findings were supported by the earlier molecular equilibrium calculations of Gilman (1969), in which the atmosphere of O-rich stars were proposed to condense into silicate grains, while carbon and silicon carbide grains were proposed to form in carbon stars.

Early models of PNe formation (e.g., Swamy & Stecher, 1969; Paczyński, 1971) considered the effects of stellar radiation pressure on such circumstellar dust grains, and supposed it to be the sole driving force in the creation of a PNe shell. However, these models were in time found to exhibit significant shortcomings, including: (i) why the PN expansion velocities observed were much higher than AGB stellar wind velocities, (ii) why the PN shell densities were significantly higher than those observed and (iii) why there existed well-defined, and concentrated PN structures as opposed to the diffuse and unbroken density structures as observed of the AGB circumstellar envelopes.

The interacting stellar wind (ISW) model (Kwok et al., 1978) brought more nuanced ideas to PNe formation theory. It proposed that with ongoing mass loss the AGB's core would be revealed, and a fast tenuous wind would arise from the core with speeds of $\sim$1000 km s^{-1}. The insight came in quantifying the resulting shocks that would form, which in turn would increase the gas temperature, and concomitant pressure to levels that would provide significant, supplementary acceleration to the PN shell. It was this shocked region, known as the hot bubble, that was proposed to provide the adequate driving force to plough up the slower (10 km s^{-1}) moving winds of the previous phase, and expand the PN (e.g., Balick & Frank, 2002; Soker & Livio, 1989). A schematic of the models' shock-fronts and wind interactions is presented in Figure 1.2.

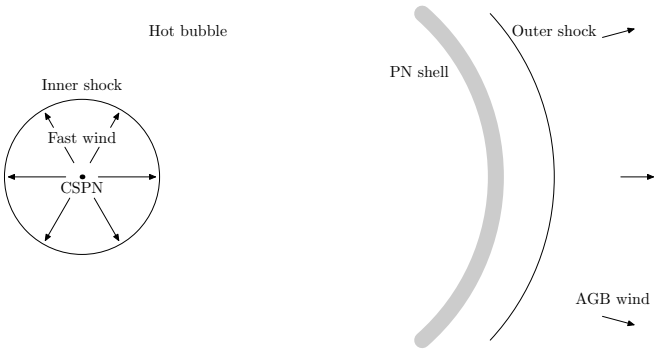

Figure 1.2: Interacting stellar winds model schematic. Figure adapted from Kwok (2007).

The ISW model has existed as the predominant PN formation theory almost since its inception, as not only did the ISW fit within the observational constraints

of the time, but also due to the later observational confirmations of predicted phenomena, including: (i) the prediction of a faint halo existing beyond the PN shell, (ii) prevalent high speed CSPN winds (Heap et al., 1978) and (iii) thermal x-ray emission in the hot bubble (e.g., Ruiz et al., 2011).

However, over the last few decades, with improved observational methods (particularly the Hubble Space Telescope), the PN population has grown to include a menagerie of PN morphologies. This is evident in the number of geometrical classifications that have been introduced into the literature over the relatively short period, for example such classifications include: bipolar, elliptical, point-symmetric, irregular, butterfly, peculiar, anomalous, spherical, ring, round, interlocking and quadropolar (see for example; García-Segura et al., 1999; Parker et al., 2006; Kwok, 2007). The ISW model is now understood to provide a reasonable description of the underlying physics that leads to the visible PN, but it does not provide the theoretical means to explain large percentages of the PN detailed morphologies.

1.2 AGB Mass Loss

It has been known for some time that during the giant phases, significant mass loss events take place (e.g, Deutsch, 1956), in which some $\sim 1 - 7 M_{\odot}$ can be lost.[1] As noted however the physical mechanism(s) and their exact physical nature are not well understood (e.g., Bloecker, 1995; Ohnaka et al., 2005; Herwig, 2005). At present AGB mass loss can be classified into the following categories: (i) thermally driven, (ii) wave driven, (iii) radiation pressure driven and (iv) companion interaction driven.

It is understood that for much of the giant phase, the stars will endure some form of mass-loss. It is however, the dynamics of the mass-loss rate over this evolutionary period that has proven difficult to explain. Originally it was thought that the mass-loss rate would gradually increase over the lifetime of the AGB phase (e.g., Volk & Kwok, 1988; Bryan et al., 1990; Bloecker, 1995). More recent proposals however, suggest that the mass-loss rate will remain reasonably low for much of the giant's lifetime until a point at the tip of the TP-AGB, in which mass loss will exponentially increase (e.g., Willson, 2000; Rosenfield et al., 2014). Using empirical and theoretical evidence Rosenfield et al. (2014) provides an up to date summary in regard to mass-loss rate over the giant phase, physical descriptions do however, still remain vague. It is proposed that there exist three phases of mass loss, (i) an initial low mass-loss rate taking place in the pre-dust phases (ii) an exponential increase in this mass loss caused by dust-driven/pulsation assisted wind and (iii) a final high mass loss rate, sometimes referred to as the *superwind*, a phase that is perhaps the least understood of the three.

Mass-loss at the stage before significant dust formation, is found to be relatively low and is proposed to be driven by radiation pressure or wave mechanisms such as Alfvén waves (e.g., Hartmann & MacGregor, 1980). This early mass loss phase is sometimes known as Reimers type (Reimers, 1975) mass loss, from the empirically-derived mass loss formula that has been synonymous with this phase over many

[1] With an AGB mass range of $\sim 1 - 8 M_{\odot}$, and a resulting WD core of $\sim 0.5 - 1.4 M_{\odot}$, $7 M_{\odot}$ of material can potentially be ejected. Though we more commonly expect $\sim 1 - 2 M_{\odot}$.

decades, though, as many point out, it again provides no insight into the underlying physics involved.

Once the dust forms, mass-loss is seen to increase dramatically, and dominate overall mass-loss. This dust-driven mass-loss phase, is proposed to result as the momentum of the radiation pressure being more efficiently absorbed by the opaque dust grains. There is also evidence that the dust may also drag gas in partnership beyond the photosphere and contribute further to the overall mass-loss (e.g., Volk & Kwok, 1988), but a full description of this phase requires the inclusion of stellar pulsation.

As the luminosity and radius of the star increase over the AGB phase, large amplitude radial pulsations of the extended envelope are observed. Such pulsations are found to be mono-periodic (Zijlstra et al., 2002) with periods of 200-2000 days (e.g., Kwok, 2007; Chen et al., 2001); the objects are classified as long-period variables. It is believed that the radial changes are driven by hydrogen ionisation effects (Kwok, 2007). These objects, known as Mira OH/IR variables, are found to exist with well defined period-luminosity relationships, with the more luminous objects having longer periods. It is also found that the rate of mass loss from the objects increase with increasing period (Iben, 1995).

Whether Mira variables and their OH/IR equivalents are the result of distinct evolutionary paths is not clear. It has been suggested for example that the Mira phase may be the earlier stage of the OH/IR star; they do for example exhibit shorter periods, which does make sense when considering the mass loss-period relationship. The OH/IR stars also exhibit OH maser emission, which is thought to develop as result of the high mass-loss rates, and with some $\sim$30% of Mira variables displaying OH emission, the argument of a shared history is certainly strengthened (Kwok, 2007). It is thought that the pulsations of the TP-AGB, and the long-period variables, could levitate matter beyond the photosphere allowing additional dust to condensate from the cool gas, further strengthening mass loss (Holzer & MacGregor, 1985).

Pulsation is then quite important when considering mass-loss on the AGB, not only via the mass-loss it provides directly, but through the increased mass loss it provides via dust creation. However, additional mechanisms may be required as the mass-loss rates witnessed at the end of this phase ($\sim 10^{-5}$–10^{-4} $M_{\odot}$ yr^{-1}) may be beyond the abilities of pulsation enhanced dust-driven mass-loss alone (Morris, 1987). An additional problem also exists: it has been known for quite some time that bipolar geometries occur very often in these mass-losing systems (e.g., Zuckerman & Aller, 1986). Non-radial envelope pulsations, as with progenitor rotation and magnetic fields, have been considered, but ultimately ruled out (see Morris, 1981; Pascoli, 1987; Nordhaus et al., 2007; García-Segura et al., 2014). The bipolar nature will be considered shortly. First let us continue with red giant evolution to PN. The transitory phase is understandably dependent on the mass loss phase prior.

1.2.1 Aspherical mass loss

The range of PN morphologies is indeed numerous, For example it is estimated that of the objects recognised as PNe, approximately 80% are aspherical (with the remaining $\sim$20% classified as round). Of those objects considered aspherical,

approximately 13% are categorised as bipolar, $\sim 28\%$ extremely elliptical. The remaining $\sim$40% are found to be split equally between mildly elliptical PN with jets and mildly elliptical PN without jets (see for example Soker, 1997; Parker et al., 2006).

It has also been suggested that the morphologies may represent a series of evolutionary steps. Balick (1987) for example, proposed that the ISW mechanisms with the aid of a mid-plane density contrast, such as a disc or torus (as suggested by Calvet & Peimbert, 1983), could cause pole-ward favouring outflows. Such a density contrast is hypothesised to increase with ongoing evolution, such that an otherwise spherical PN would become, first elliptical and eventually bipolar. Such ideas (e.g., Kahn & West, 1985; Balick, 1987), however, did not provide explanations regarding the formation of the disc density contrast. They have however inspired numerous refinements and extensions to the ISW model. For example numerous numerical and empirical modelling focusing on the interaction between stellar winds and mid-plane density structures have resulted (see Icke, 1988; Icke et al., 1989; Frank et al., 1993; Mellema & Frank, 1995). Such studies have become the basis to what is now known as the generalised ISW or GISW.

The GISW model formed predominantly out of the ideas of Kahn & West (1985). Anisotropic winds were believed to result in aspherical PNe. A density contrast existing between the equator and the poles is believed to cause asymmetrical outflows. The origin of the contrast being either a protostellar disc remnant, a result of stellar rotation, equatorially compressed outflows, binary interactions or magnetic field influences. The ISW were found to amplify the proposed contrast density, and simulations were shown to account for mildly elliptical shapes, and even the more complex figure of eight type structures (Icke, 1988; Soker & Livio, 1989; García-Segura et al., 1999, 2005) and additionally PN with jets (Bond & Livio, 1990; Schwarz et al., 1992).

However, limits to GISW models soon become apparent when trying to account for point-symmetries, and a variety of other non-axisymmetric complex structures such as jets, quadrouple axis lobes and small scale low-ionisation structures (e.g., Gonçalves et al., 2001) in context of a large-scale collimating torus (Livio, 1999; Blackman et al., 2001b; Dwarkadas, 2004). An early example was CRL 2688 (The Egg Nebula), in which the GISW models could not describe the proper dynamics of the collimated jets (Balick & Frank, 2002). As De Marco (2009) explains, the GISW interpretation *assumes* the equatorial density contrast, but does not explain its origin, nor reproduce many of the PNe details seen more broadly. It is perhaps best said by Balick & Frank (2002) who states *"GISW models are, by themselves, inadequate"*. The acknowledged limitations of the GISW has seen other classes of single star PN shaping models emerge, but as will become apparent, they too exist with their own shortcomings.

1.2.2 The protoplanetary nebula

Protoplanetary nebulae or preplanetary nebulae (PPNe) is the short-lived phase preceding the PN phase and following the AGB phase. It is during the PPN phase that the steadily expanding spherical circumstellar envelopes of AGB stars transitions to the rapidly expanding ($\gtrsim 100$ km s^{-1}) non-spherical outflows (e.g., Neri et al., 1998; Balick & Frank, 2002; Sahai et al., 2007). It is thought that the circumstellar environment of PPNe, specifically the presence (or absence) of

discs, is fundamental to apprehending AGB mass-loss symmetry, and the mass loss mechanisms more generally.

Upon observing CO spectra, Bujarrabal et al. (2001) analysed the immediate environment of PPN and their outflows, and provided limits to linear momentum and nebula mass. It was found that outflow masses can surpass ~ 1 $M_{\odot}$, with the moss loss rates exceeding 10^{-4} $M_{\odot}$ yr^{-1}. They also showed for approximately 90% (21) of the 23 PPNe sample, that despite the relatively luminous central star (with $L \sim 10^4$ $L_{\odot}$), the radiation pressure was often many orders of magnitude too low to drive ejection alone (see also Sahai et al., 2006). It was concluded that the mechanism powering the bipolar outflows was unknown. As Sahai et al. (2007) suggests, kinematical data of these objects at high angular resolution are *"sorely"* needed for the formulation and verification of theoretical models.

Short of such data, Blackman & Lucchini (2014) show that if jet collimation can be preserved, accretion, resulting from binary interactions within a common envelope, may act as an engine with the required kinematics to drive the outflows. Blackman & Lucchini (2014) showed that such accretion could explain all objects in their 19 PPN sample. Accretion within the common envelope, (see also Ricker & Taam, 2008, 2012) occurs following the rapid in-spiral of a companion into the AGB CE, with the outflow energy sustained by the orbital energy. Ricker & Taam (2012), upon running hydrodynamical simulations of a 1.05-$M_{\odot}$red giant and a 0.6-$M_{\odot}$ companion, found transformation from orbital energy to mass-loss to be 25% efficient (Ricker & Taam, 2012). It was also found that following the first pass of the companion into the CE, 25% of the red giant's mass was ejected, and mass would continue to be ejected at a rate of of ~ 2 $M_{\odot}$ yr^{-1}.

Observational proof of binaries in PPN is however lacking (e.g., Hrivnak et al., 2011). Radial velocity measurements for example showed that perhaps only 1 in the sample of 7 PPNs considered, contained a binary companion. Though it was suggested that the lower mass (0.25 $M_{\odot}$) brown dwarf or super-Jupiter planets, or binaries in longer period (25 yr) orbits would elude detection. Direct comparison of the PPNe binaries, with the binary fraction of stars (50% e.g., Duquennoy & Mayor, 1991) may support this. Observations of binaries in PPN are however difficult, not only as the objects require high-resolution techniques, but that the nebular are typically cool and dim, and can hence be easily overlooked (Sahai et al., 2007).

In an attempt to understand the physical mechanisms at play. Sahai et al. (2011) set about classifying PPN and the young PN morphologies. The geometries of the resulting PN, in additional to kinematic analysis via long-list spectroscopy, was found to suggest underlying physical causes in some instances. Most notably, pinched waists were considered a likely derivative of CE ejection and thus a potential route for bipolar nebulae, and in general, collimated fast winds, whether jets, featured prominently. Point symmetries for example, are thought to result from jet or wind precession. While episodic, collimated fast winds, whether caused by precession or driven directionally by an accretion disc, would break assymmetry (see also Sahai & Trauger, 1998). How this ultimately pieces together with observations that indicate all PPN to be non-spherical (with the young PN being almost never spherical), yet of the PN, some $\sim$20% are found to be spherical, is yet to be determined.

Insight into the evolutionary transition from AGB to PN can come from the

understanding of the discs within the post-AGB PPN objects. Understanding the relation between the old, Keplerian discs of the post-AGB objects, and the lower mass non-Keplerian discs of the young PN, is just one such route that may allow better understanding of the AGB-PN transition. In this section, we have seen that despite an observational shortage of binaries in PPNe, their presence is in many cases necessary to accommodate the processes considered. Without knowledge of the true binary fraction, we cannot determine evolutionary paths, however, we are able to present mass loss mechanisms as developed for the single star scenario. As we will find, the mass-loss engines, in many cases do not provide the necessary energy requirements, nor explain aspherical mass loss more generally.

1.2.3 Shortcomings of the single-star scenario for aspherical mass loss on the AGB

In recent years, it has become evident that the single-star scenario for aspherical mass loss exists with shortcomings and the problems, as we will see in this section, go beyond just the absence of physical explanations, and need for assumptions, as was seen in the GISW. Observational and theoretical evidence over the last decade has slowly began to question the notion that single-stars can form asymmetric PNe.

Magnetic fields are found in a number of the central stars, circumstellar envelopes and outflows of PNe and post-AGB objects (e.g., Bains et al., 2004; Leal-Ferreira et al., 2013; Sabin et al., 2015). Yet, the exact role they play in the shaping of PNe is not known. Dynamos, driven by fast rotation of the AGB cores of CSPNe, have long been proposed as the source of such fields (e.g., Pascoli, 1997; Blackman et al., 2001a). Early studies suggested that magnetic fields at the stellar surface may drive high velocity winds ($\sim$10 km s^{-1}), and a stellar magnetic field may be the predominant cause of mass ejection, and PNe formation (e.g., Pascoli, 1997).

Asymmetry was later accounted for, when Matt et al. (2000) considered a dipole stellar magnetic field at the surface of the star. Matt et al. (2000) showed that such a field could result in an equatorial disc, and provide the necessary density contrast required by the GISW, to produce aspherical PNe. Blackman et al. (2001a) too proposed that magnetic fields could produce asymmetric outflows, but driven via magnetically collimated outflows. Additional asymmetries were also speculated to be provided by eruptions on the stellar surface (comparable to coronal mass ejections) as a result of the dynamos below the surface. García-Segura et al. (2005), in simulating magnetic pressure driven winds, reproduced the high mass loss rates required, and replicated the quick transition from late-AGB to PN phase. Highly collimated bipolar outflows were also reproduced. Such magnetic field models however, do not consider the interaction of radiation pressure on dust.

Alternative magnetic models, considered the interaction of the magnetic field, beyond the stellar surface. Chevalier & Luo (1994) considered the interaction of the toroidal field with the stellar winds, and suggested they would carry the magnetic field. Upon reaching the shocked gas of the hot bubble the toroidal component of the field would increase, and a magnetic tension would restrict magnetic pressure along the equatorial plane, resulting in a pressure contrast

that could drive elliptical or bipolar outflows.[2] García-Segura et al. (1999) also considered the toroidal magnetic field, and carried out simulations that showed that even modest stellar rotation ($\sim$2 km s^{-1}) and weak magnetic fields, would be sufficient enough to impart some equatorial enhancement to the AGB mass loss, and again, in terms of the GISW approach, provide a density contrast adequate to deflect the fast wind of the AGB and inflate an axisymmetric PN.

However, since the discovery of the magnetic fields in PPNe (Bains et al., 2004), the magnetic fields influence on isolated CSPNe stellar winds has been more rigorously tested. Perhaps the most notable problems regarding magnetically formed aspherical PNe, were exposed by Soker (2006) and Nordhaus et al. (2007). When considering angular momentum and energy requirements of the proposed large-scale magnetic fields alone, both Soker (2006) and Nordhaus et al. (2007) showed that the magnitudes involved would exceed the capacity of a single isolated AGB. A toroidal field, supported by a single AGB, would act to drain the angular momentum from the system on time scales too short ($\sim$100 yr) to affect outflows that could encourage aspherical morphologies.

García-Segura et al. (1999) also indicated that shaping of PNe could be obtained without magnetic fields, and suggest that a superwind, if induced via AGB instabilities, would only require stellar rotation of the order of only a few km s^{-1}. De Marco (2009) however, questions whether the premise is at all physical: could a rotating and convecting giant even exist without a magnetic field? If not, then we find ourselves re-visiting the arguments of Soker (2006) and Nordhaus et al. (2007), in which stellar rotation would cease, and with it, a path to aspherical PN as an isolated AGB. Others (e.g., Ignace et al., 1996), question whether such low rotation rates could even produce the required asphericity.

It cannot be denied that magnetic fields may play a role in the formation of aspherical PNe, but to what degree is still up for debate. The attentive reader will note however, that we have yet to consider the mass-loss mechanism provided by binary interactions. As early studies have shown (e.g., Livio et al., 1979; Morris, 1981), angular momentum considerations in a binary context provides an innate and clear-cut distinction of the equatorial plane and the polar axis, i.e. a situation that naturally provides the required density contrast at the mid-plane.

Magnetic fields, binarity and stellar rotation have long been attributed to the formation of aspherical PNe, but as Soker (1997) and De Marco (2009) make clear, there should be a distinction made between the *original* and *derived* cause of PNe shaping. If, for example, a magnetic field could not be supported by a single AGB star (as indicated Soker, 2006 and Nordhaus et al., 2007), and instead was the result of a binary interaction to provide the additional source of angular momentum, the binary is in fact the original cause of shaping, while the magnetic field is instead a derived cause.

1.2.4 The binary scenario

Planetary nebulae with binary nuclei are observed (e.g., Bond & Livio, 1990; Ciardullo et al., 1999; Miszalski et al., 2009b; Douchin et al., 2015), and it has been estimated that approximately half of the solar mass stars that ascend the AGB

[2] The model is known as the magnetised wind blown bubble (MWBB).

exist within a binary system (Duquennoy & Mayor, 1991; Raghavan et al., 2010). The possibility of binary systems being fundamentally connected to the aspherical morphologies of PN is not new, being proposed at about the same time as the ISW (e.g., Bond et al., 1978; Meyer & Meyer-Hofmeister, 1979; Livio, 1982). Mounting evidence however suggests that isolated AGB stars cannot support magnetic fields, rotation and/or mass loss rates required to create the non-spherical morphologies. Fortunately, at minimum, half of all AGB stars exist with a companion, of which approximately half are at close enough proximity to influence PNe shaping (e.g., Iben, 1995). As many agree (e.g., Soker, 1997; Zijlstra, 2006; De Marco, 2009; De Marco & Soker, 2011) the companions have the ability to influence shaping in many ways.

The number of evolutionary routes available to a PN progenitor, in a binary context, is indeed numerous. For example Soker (2002) hypothesises there to be approximately one-hundred qualitatively different evolutionary paths to the bipolar PNe alone, and additional numerous quantitative permutations. However, the unravelling of a progenitor's complex history can indeed be difficult. For example, Yungelson et al. (1993) on studying the orbital properties of binary systems considered common-envelope evolution, and found that single star CSPNe could in fact be the product of mergers.

In this section we will present current understanding of binary interactions, and their influence on PNe shaping. Mass transfer and interaction in a binary system cannot however be understood without an account of the gravitational equipotential surface that exists between two bodies, as was studied by Édouard Roche in the mid-19th century.

The Roche lobe is the largest volume about a star that can be hydrostatically occupied in the presences of an external body (e.g., Warner, 2003). For example, when in the vicinity of another mass, a star that occupies the regions beyond its Roche lobe, would begin to transfer material to the second body via a point known as the inner Lagrangian point, L_1. The size and shape of the Roche lobe is dependent on the separation and the mass ratio of the two bodies, such that an increase in the orbital separation between the two bodies decreases the Roche lobe volume. The Roche lobes are as such important when considering mass transfer for binary systems. Additional boundaries, beyond the Roche lobe exist with their own Lagrangian points. These surfaces are known as gravitational equipotential surfaces, as in a perfect system, mass at these points would be in equilibrium; balanced by the gravitational potential and the centripetal acceleration imparted by the rotating frame. A cross-section of the equipotential surfaces is provided in Figure 1.3.

Paczynski (1976), in trying to understand why cataclysmic variables existed with such short periods, demonstrated what would happen to material as it crossed these equipotential surfaces. Upon filling the Roche lobe, mass is transferred to the companion via the inner Lagrangian point. At low enough transfer rates, angular momentum prevents the matter falling directly onto the companion surface, and is instead put on a trajectory around the companion and back on to itself, creating an accretion disc. Matter can be transferred to the stellar surface via this accretion disc, but as the transfer rate increases, the angular momentum involved forestalls the ability of the companion to receive the matter, the gas stream spreads as an annulus about the star until eventually the Roche lobe is filled. Upon overflowing the outer Lagrangian point (L_2, see Figure 1.3), the system becomes enveloped

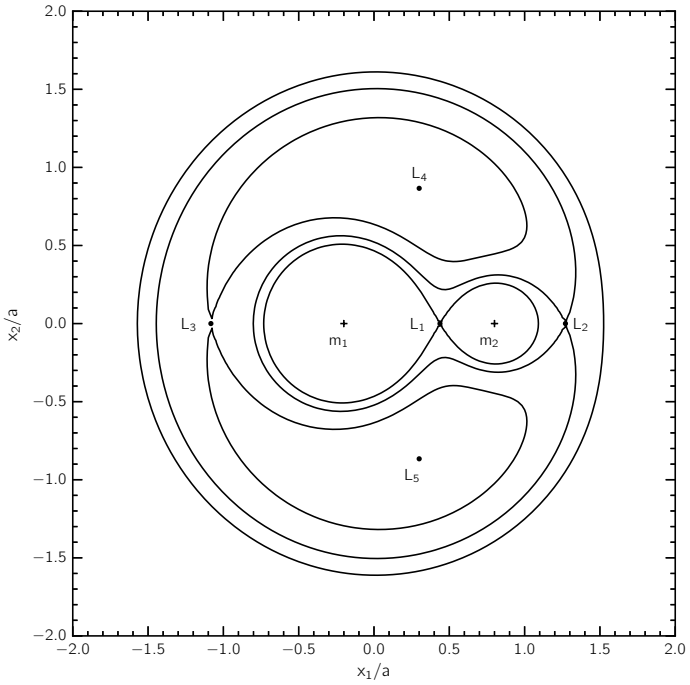

Figure 1.3: The cross-section of the gravitational equipotential surfaces at the orbital plane. The two masses considered have a mass ratio of 0.2, with their positions represented as plus signs separated by a. The Inner Lagrangian point joins the figure of eight type structure which is the Roche lobe. The centre of mass is located at axis origin.

by a gaseous envelope, known a common envelope. This envelope typically does not rotate with the system and the rotating binary will undergo a drag force, it was this drag force that explained the Cataclysmic variable's short period that Paczynski (1976) was considering. As the associated force would drain orbital energy from the system, ultimately causing the orbital distance to shrink.

As has been made apparent, binary progenitors lead naturally to the shaping of bipolar PNe because of the influence the companion has on the mass-loss process of a transitioning AGB primary. As Soker (2002) points out, it may in fact be possible to describe all non-spherical PNe by considering only binary interactions. We present the prominent binary models considered regarding PNe formation and shaping as presented in the literature (e.g., Soker, 1997, 2002; Zijlstra, 2006; De Marco, 2009; De Marco & Soker, 2011). As Soker (1997) points out, a binary explanation to the PNe shaping problem relies heavily on the angular momentum that can be provided by the companion (whether that is stellar or sub-stellar). In an attempt to categorise the interaction type, it is thus worth considering the binary orbits themselves. Which are generally examined in the following four categories.

1. The distant companion.

   This category of PN is given to those systems where the PN formation period ($\tau_F \sim 10^5$ yr) is approximately equivalent to the orbital period ($P_{\rm orb}$), which equates to separations of 100 AU $\lesssim a \lesssim$ 1000 AU. At these separations mass transfer does not occur, but mass-loss from the primary may be assisted by

the companion, and the matter lost from the primary may amass on the orbital plane. A disc has the potential to result via wind accretion onto the companion (e.g., Morris, 1987; Mastrodemos & Morris, 1998; Reyes-Ruiz & López, 1999), and jets may also form. We also consider in this category the extremely wide binaries. These are the systems where $\tau_F \ll P_{\rm orb}$, ($a \gtrsim 5000$ AU). At these distances the interaction is minimal, and at best contribute only small features to the PN, such as bubbles (see for example Soker, 1996, 1997).

2. The close companion that avoids the common envelope phase.

   This is the category in which a stellar or sub-stellar companion's influence is non-negligible, orbiting at distances of 20 AU $\lesssim a \lesssim$ 100 AU. This category of binary interaction may well result in a number of PN shapes, depending on the mass ratio, separation and evolutionary timing for example. The definition of the category is quite broad, and the *avoidance* of the common envelope, is taken to be an avoidance for a significant fraction of the interaction time, i.e. requiring substantial mass to be lost prior to, or following the common envelope interaction. Mass loss rates are found to increase due to tidal forces from the companion. In this regime, elliptical orbits can cause periodic mass loss events which occur at apastron (e.g., Staff et al., 2016). Such orbits may explain off-centre CSPN (as found in MyCn 18). Discs can form via wind accretion onto the companion, and multiple pairs of lobes can be inflated by precessing jets, explaining the quadropolar PNe. Elliptical PNe can also emerge from this class.

3. The companions survives the common envelope phase.

   In this category we consider the interaction of a companion that has survived the common envelope. It is perhaps the most complex phase considered so far. A companion has the ability to transfer energy and angular momentum to the primary and unbind the envelope. In those systems that do survive the common envelopes, periods can be on the order of a few days (Paczynski, 1976; Nordhaus & Blackman, 2006), and such periods are observed in PNe (e.g., Burleigh et al., 2006; Miszalski et al., 2009a), such systems have been observed within circumbinary structures (see van Winckel, 2003), indicating that they have survived through a common envelope phase. The outflows are thought to preferentially favour equatorial regions (see for example the simulations of Passy et al., 2012) and result in circumbinary discs, accretion discs and jets (Staff et al., 2016) and elliptical or bipolar PNe are thought to result (e.g., De Marco, 2009). Sub-stellar companions are also found to survive the common envelope, though they provide significantly less energy than stellar counterparts, and they may only enter the phase late in the AGB lifetime (Soker, 1995), and are believed to more often result in a merger.

4. Common envelope phase results in a merger.

   In this situation we may expect a disc (and with it, the potential for jet formation) to form as the companion is tidally destroyed upon merging (see Nordhaus & Blackman, 2006). From this category we can expect elliptical morphologies, as the angular momentum of the companion will be imparted to the envelope.

Some have also differentiated between stellar and sub-stellar companions. Where

the sub-stellar interaction is thought to be overall more mild. As simulations show (e.g., Sandquist et al., 1998; De Marco et al., 2003; Staff et al., 2016), the resulting density contrast is seen to decrease with companion mass. For example it has been suggested (e.g., De Marco & Soker, 2011) that planets may be entirely responsible for the elliptical PN with no jets.

Other interactions not considered, include the triple systems (e.g., Exter et al., 2010; Soker, 2016), a regime in which the interactions can become very complex. Soker (2016) hypothesises that $\sim$12% of the systems that are thought to undergo a binary interaction, are in fact triple systems, and be the origin of the irregular *messy* PNe. The energy contributions of a triple system, as Soker (2016) explains, can be provided to a primary's envelope via the merging process of the companion, or from the orbital energy of the companion binary which is proposed to be extracted when the system approaches the AGB. Soker (2016) also argues for, in rare cases, the contribution of a fourth star.

The plethora of evolutionary paths available to an evolving AGB with one or more companions has hopefully been conveyed. Yet it is also clear most seem to depend on a density contrast focused equatorially, a situation that has been difficult to accommodate theoretically in the single star scenario. It is for this reason that the binary origin for PNe has become favoured in some circles (for a review, see De Marco, 2009), and that they may be preferentially responsible for the formation and shaping of PN, an idea known as the binary hypothesis (e.g., De Marco, 2009; Soker, 1997).

The binary hypothesis states that a substantial fraction of single, isolated AGB stars do not form luminous PNe. As such, upon comparing the binary fraction in the progenitor PN population with the equivalent PN binary fraction, an over representation of binaries should be witnessed of the latter category. Observations of binary systems however, in general prove difficult (Zijlstra, 2006), with detection either through spectroscopic techniques, photometric brightness fluctuations, radial velocity measurements or direct imaging. The problem is detecting such systems. For example, current constraints on the binary fraction have only been provided via photometric flux variability of the very close central star binaries (with periods of up to $\sim$1 day). Approximately 15% of CSPNe have binary central stars in this category. These are binaries that have survive the CE phase with a companion. Photometric techniques however are believed to detect companions of periods of up to $\sim$ 2 weeks De Marco et al. (2008). As such, it is suspected that there may be few systems with periods between and few days and 2 weeks De Marco et al. (2008). How many binary central stars exist with periods longer than $\sim$2 weeks is completely unconstrained.

Additionally, the current binary ratio observed at the shorter periods may in fact increase with improved observations. For example, the irradiance effect that we observe photometrically, may be too low for smaller companions, or for the systems with unfavourable orientations for detection De Marco et al. (2015). Observations are, in their present state, yet to provide sufficient evidence to the binary hypothesis.

1.3 Observing post-AGB objects

As has hopefully been conveyed, it is not only the binary nature of the PN central star that is difficult to establish, but also the nature of the mass loss processes, and the path to aspherical PNe. It is through high angular resolution observations of the immediate circumstellar environment that the binary hypothesis can be tested, and the nature of disc formation tested. Ultimately however, understanding of the transitional phase between AGB and PN, requires multi-wavelength, multi-aperture observations. Such measurements will provide a self consistent understanding of the post-AGB composition, morphology, temperature, mass, and kinematics of such objects. In this section we very briefly outline common post-AGB, particularly the transitional PPN objects, observational methods.

1.3.1 Infrared

The study of post-AGB objects in this thesis rely most heavily on this bandwidth. The relatively cool dusty environments of these objects (150-330 K) are for example most luminous at this wavelength, the spectral energy distributions (SEDs), for example display IR excess features, caused by stellar reddening (e.g., de Ruyter et al., 2006). As has been mentioned, it is in the infrared that many clues to the chemical composition of dust exist, such as the 10-μm and 18-μm silicate emission of O-rich objects (e.g., Volk & Kwok, 1989), or the 11.3-μm and 21-μm SiC feature of C-rich objects.

In this thesis we almost exclusively deal with infrared interferometric observations. We take advantage of the high angular resolution capabilities (1-10 mas) of near-IR Very Large Telescope Interferometer (VLTI). The facility consists of 8 independent telescopes, 4 large 8.2m apertures and 4 smaller mobile 1.8m telescopes. This combination provides the sensitivity necessary to measure these relatively dim objects (provided by the 8.2m telescopes), as well as versatility in baseline assignment, and resolutional capabilities from numerous potential baselines of the mobile instruments. The VLTI is thus an excellent tool in the probing the immediate environments of infrared-bright AGBs (A more in depth of VLTI capabilities will be provided in Section 2.3). With respect to post-AGB objects, Chesneau et al. (2007a) labels the VLTI a powerful disc-hunter.

Infrared interferometric techniques however require modelling to pair the observational data products to a spatial description of the object. In this thesis this pairing is achieved by way of radiative transfer modelling. Radiative transfer modelling was chosen as it affords us the ability to recreate spatial representations of given astronomical distributions, and additionally investigate the objects physical properties. For example disc structures, dust properties and appropriate stellar parameters. We analyse data from two separate VLTI instruments, the MID-infrared Interferometric instrument (MIDI) which is capable of combining beams with bandwidth $8-14\mu$m from two of the 8 VLTI telescopes. The second instrument is the near-IR Astronomical Multi-Beam combineR (AMBER), which combines three telescopes at the $1-2.5\mu$m wavelength range. In two of the objects studied in this thesis data from both instruments exists, and is naturally taken advantage of to provide more effective constraint. At this bandwidth we also rely on photometry, for example large surveys such as the Deep Near Infrared

Survey of the Southern Sky (DENIS) and the 2-μm All sky Survey (2MASS). For a more in depth consideration of PPN observation in the infrared consult Kwok (2007).

1.3.2 Optical

In the optical, post-AGB surveys have provided important insight in the morphological classification and characterisation of the PPNe and young PNe (see for example Hrivnak, 1995; Sahai & Trauger, 1998; Ueta et al., 2000; Sahai, 2004; Sahai et al., 2007, 2011). As opposed to the PN in which optical light is primarily a result of the surrounding nebula, in PPN, it is largely originates from the CSPN. Of the PPN bright enough, insight into the chemical makeup, spectral types, and physical structure have successfully been discerned via spectroscopic techniques (e.g., Hrivnak, 1995; Klochkova et al., 1999; Sánchez Contreras et al., 2002). The flux in the optical bandwidth can vary greatly in the PPN, this is predominantly dependent on orientation of the surrounding dust. For example the extinction properties of the dust cause significant reddening in equatorially dense structures when viewed edge on. Imaging at optical wavelengths has been very successful. The high dynamic range of the Hubble Space Telescope (HST), allows for the detection of the dim circumstellar structures that exist in close vicinity to the bright stellar objects. Hubble has successfully detected circumstellar axisymmetries, collimated outflows and bipolarity, results which indicate the presence of discs and jet like features.

1.3.3 Radio

Molecular emission, detected as OH, H_2O and SiO masers for example have provided kinematical information. One of the best early examples of this was the OH 1667 MHz emission from IRAS 11385-5517, in which te Lintel Hekkert et al. (1992) discovered a bipolar outflow, with a strong velocity gradient in which the outer edges of the lobes were found to be expanding at ~ 40km s^{-1}, with the inner inner edges at $\sim$9km s^{-1}, indicative of a stellar wind and circumstellar envelope interaction. Other emission such as the CO lines have provided constraint of molecular discs and tori in PPN (e.g., Bujarrabal et al., 1998; Zweigle et al., 1997; Bujarrabal et al., 2003, 2005; Murakawa et al., 2010). Such observations have provided fundamental constraint of PPN discs in particular, for example disc size, rotation, expansion velocities, mass, temperature and density have been successfully constrained (e.g., Bujarrabal et al., 2003, 2005). These observations require relatively high angular resolution, sub-1$''$, though to detect disc formation through more subtle binary interactions, we need to investigate the immediate stellar environment. It is only with sub-100mas measurements that we can begin to piece together disc formation as it exists during the PPN phase.

The Atacama Large Millimetre/submillimetre Array (ALMA), with first light in September 2011, has the potential to revolutionise PPN study. With its sub-100mas spatial resolution (10mas at the shortest wavelengths), it will not only be able to probe the immediate circumstellar environment at near-VLTI levels, but provide kinematic details of disc rotation, axial outflows and provide the ability for systematic magnetic field analysis, all of which are essential to understanding the shaping mechanisms that form the bipolar PN. Initial studies have begun, (e.g.,

Bujarrabal et al., 2013; Sahai et al., 2013; Bujarrabal et al., 2016; Santander-García et al., 2016), with promising results. Insight into the disc and outflow properties of the Red Rectangle have been constrained (e.g., Bujarrabal et al., 2013), in which a rotating equatorial disc was accompanied by low-velocity outflows. Further analysis revealed the outflow to be gas that originated in the disc (e.g., Bujarrabal et al., 2016). There is no doubt that ALMA shows great promise in revealing details in the post-AGB objects previously hidden to us. Ultimately, a multi-wavelength, high spatial resolution study of these objects is necessary to fully constrain the complex post-AGB environments.

1.4 Motivation and outline

The topic of this thesis is the characterisation of the circumstellar environments about post-AGB stars via high resolution optical interferometry. The work focuses on developing and applying a systematic approach to determine the limits of a number of physical parameters that describe the immediate post-AGB environments. In particular we aim to develop a systematic way to fit interferometric data, that is quantitative, fully reproducible and non-subjective.

Such methods allow us more thoroughly analyse the data products of the high angular resolution infrared interferometer of the VLTI. We do so by improving previous methods of approaching the inverse optimisation problem, in which radiative transfer models of typical post-AGB environments need be compared to the interferometric outputs. We apply a search heuristic in the form of numerous evolutionary based algorithms, to recover potential parametric distributions. The resulting probability density functions of such a method, reveals parametric correlations, degeneracies, confidence intervals as well as final best-fit solutions.

In Chapter 2 we provide an introduction to the fundamental theories that underpin this work. We begin with interferometric theory, and build an understanding of optical interferometry in the context of Young's famous experiment. We explore the relation between the interference contrast (the interferometric output), and the physical nature of the observed object, culminating in a derivation of the Van Cittert-Zernike theorem. We provide an overview of current optical interferometric techniques and a background on the interferometric instruments used for this thesis. Finally we present interferometric modelling approaches.

In Chapter 3 we present the genetic algorithm (a global optimisation algorithm) as a viable candidate for determining *fit* radiative transfer solutions to the observational data products, culminating in the development of `GADRAD`. In testing `GADRAD` we apply a genetic algorithm on a standardised global optimisation function, a step necessary in gaining confidence and understanding of algorithm efficiency. We present the parameters that describe the circumstellar environments in a radiative transfer context, and consider potential parametric correlations. We then further develop the algorithm, optimising algorithm performance for the circumstellar environments of interest. Finally we apply `GADRAD` to a synthetic astrophysical test object, and further test algorithm performance and efficiency in the recovery of the test object's initial input parameters. Degeneracy and parametric correlations are also discussed.

In Chapters 4 and 5 we apply `GADRAD` to the bipolar nebulae Menzel 3 and

Minkowski 2-9 respectively. With reference to the MIDI interferometric data products, we construct probability density functions of the parameters that describe a prescribed stratified disc structure. Menzel 3 is a good candidate for initial application of GADRAD as simple and good fitting radiative transfer models have been presented Chesneau et al. (2007b), these models provide context in which we can compare directly the performance of GADRAD. Minkowski 2-9 was chosen as it shares many characteristics with Menzel 3, and again radiative transfer models exist in which we can compare (e.g., Lykou et al., 2011).

In Chapters 6 and 7 we apply GADRAD to the two IRAS objects: IRAS 08005-2356 and IRAS 16279-4757. These objects show complex outflows, and though radiative transfer modelling attempts at the inner regions of both objects have been made (e.g., Bright, 2013), the environment is ultimately less well accounted for than the more simple environments determined in the case of Menzel 3 and Minkowski 2-9. In Chapter 8 we present our conclusions and discuss future work.

Chapter 2

Optical interferometry, modelling techniques and methods

In this chapter we provide an introduction to the fundamental principles that constitute stellar interferometry (Section 2.1). Applying these principles to optical and infrared (IR) wavelengths, we show how such techniques can then be adopted in the context of astronomical study (and discuss the relevant difficulties; Section 2.2). In Section 2.3 we introduce the Very Large Telescope Interferometer (VLTI), and provide an overview of the relevant combiner instruments. In Section 2.4 we summarise modelling techniques as necessitated in the interpretation of the interferometric data products.

For the reader who seeks more detailed descriptions of much of the introductory material presented in this chapter we direct them to the following sources in which portions of this chapter is based, i.e: Monnier (2003), Labeyrie et al. (2006), Glindemann (2011) and Millour (2014).

2.1 Interferometric principles

As theories and ideas of the cosmos develop, so does, not only the desire, but the scientific need to advance and improve observational instrumentation and methods. Only as these improvements resolve ever deeper layers of the universe, does our understanding progress. Over the centuries, since Galileo Galilei first pointed his telescope at the moons of Jupiter, attempts to increase the telescopes angular resolution have relied on the basic principle of increasing the aperture's diameter. A shift to this thinking came with the development of stellar interferometric techniques by H. Fizeau in the mid-19th century.

As light enters a telescope it is diffracted by the aperture's edges. The response in the case of a point source (the so-called point spread function) for a typical circular aperture is a diffraction pattern at the focal plane known as an Airy disc (see for example Figure 2.1). In the case of a pair of point sources the resulting Airy discs are superimposed and when the angular separation between the central peaks of the Airy discs is closer than the Airy disc radius (the function's first minimum), we reach the Rayleigh criterion, which is the limiting resolution of the telescope, defined as follows:

$$R \;=\; 1.22\,\frac{\lambda}{D}, \tag{2.1}$$

where λ is the wavelength of the light observed, and D is the aperture's diameter.[1] In interferometry a similar resolution limitation applies, however this is instead found to be limited by the distance between apertures, B (the baseline length), as:

$$R \;=\; \frac{\lambda}{B}, \tag{2.2}$$

This realisation proved to be a practical alternative for high angular resolution studies. For example, the same resolution can be obtained with a single large (expensive) aperture of diameter D, as with two smaller (much cheaper) apertures separated by a distance $B = D$ (and potentially even a much higher resolution i.e., $B \gg D$). There are however, shortcomings and difficulties in practise (of which will become apparent in Chapter 2.2). First however, we develop an understanding of the physical processes that underpin interferometric theory, as is done typically (i.e., Labeyrie et al., 2006) by considering the experiment of Thomas Young.

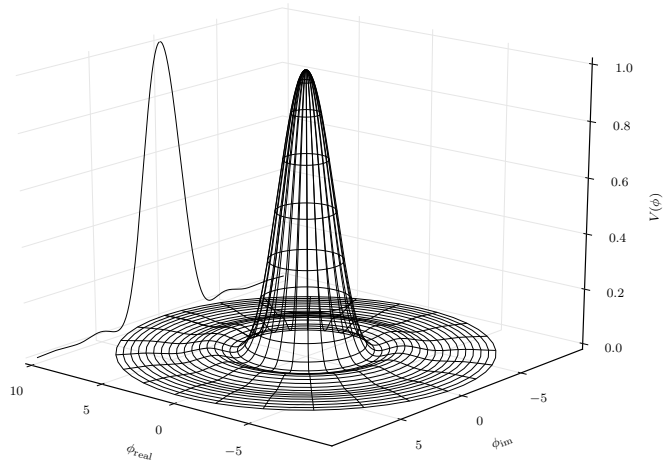

Figure 2.1: A plot of the Airy disc intensity. The angular resolution, R, is the width of the first maximum and defined (in the Rayleigh case) as the angular resolution of a single aperture instrument.

2.1.1 Young's experiment

Thomas Young, in his now famous experiment (Young, 1802), demonstrated the wave nature of light by passing a source of monochromatic light through two small

[1] The Rayleigh criteria is often considered a conservative estimate of the limiting angular resolution, additionally the full width at half maximum (FWHM) of the Airy disc can be taken as a limiting criteria, such that $R = \lambda/D$.

apertures. The resulting interferogram could only be described by the wave like nature of light. A schematic of Young's experiment is presented in Figure 2.2.

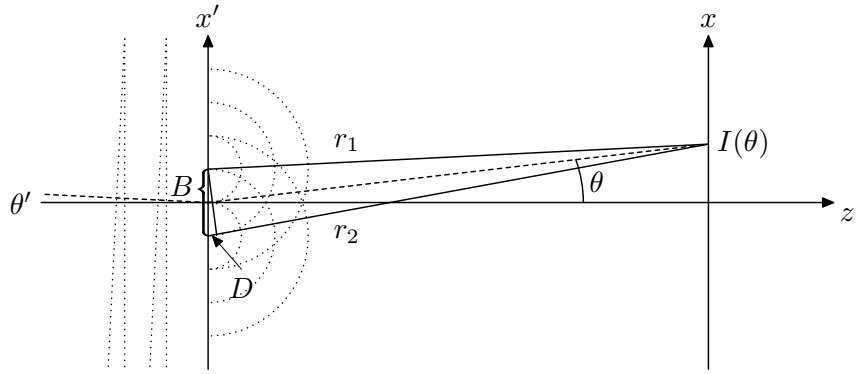

Figure 2.2: A schematic of Young's double slit experiment. The plane of observation is located at the x axis and the aperture plane is the represented by the x' axis. B is this the distance between apertures, and D is the optical path difference (the difference between r_2 and r_1). $I(\theta)$ is the resulting intensity distribution at the aperture plane, and θ' is the source distribution function.

Young's experiment provides a unique, geometrical insight into the theory of stellar interferometry. Consider for example a distant monochromatic point source situated on the z axis (i.e. positioned at equal distance from each pinhole). The amplitude of the interference patterns observed at the plane of observation, x, as a function of angle θ, can be described as the sum of the spherical waves emitted from each pinhole, i.e:

$$A(\theta) \;=\; \frac{A_0}{r_1} e^{ikr_1} \;+\; \frac{A_0}{r_2} e^{ikr_2}, \tag{2.3}$$

where $r_1 \; - r_2$ is the optical path difference. The intensity at the plane of observation is equal to the squared modulus of the amplitude, such that the intensity distribution, or fringe pattern at the observation plane becomes:

$$I(\theta) \;=\; |A(\theta)|^2 \;\approx\; I_0 \left(1 \;+\; \cos(k\theta B)\right). \tag{2.4}$$

In beginning to replicate an extended light source, we need only introduce a second point source, situated above the z axis at some angle θ' (as depicted in Figure 2.2), the extra distance travelled is simply $\theta' B$, and the intensity becomes:

$$I(\theta) \;=\; I_0 \left(1 \;+\; \cos(k(\theta \;+\; \theta')B)\right), \tag{2.5}$$

or, in its complex form

$$I(\theta) \;=\; I_0 + \mathrm{Re}\left(I_0 \; e^{-ik(\theta+\theta')B}\right). \tag{2.6}$$

For two monochromatic point sources, we then observe a phase difference in the waves observed at x, and hence a reduction in the overall contrast between peaks and troughs of the fringe pattern observed at the image plane. An extended source

can then be described as an array of such sources, with the resulting interferogram being the superposition of the fringes from the array (such a situation is seen in Figure 2.3b). Over a large enough angle θ', this superposition will result in a blurring of the distributions, a phenomenon known as coherence.

We have so far considered an approximate, and non-physical case; having only re-created what is known as partial spatial coherence. In building a true picture of an astronomical source we must consider another form of partial coherence, known as temporal coherence, by considering the intensity fringes of a non-monochromatic point source. For example, the intensity of a point source emitting over some bandwidth is the result of the superposition of all the wavelengths that make up that bandwidth (the situation is considered in Figure 2.3c). In Figure 2.3, the resulting intensity distributions for four cases are provided, a monochromatic point source, a monochromatic extended source, and the chromatic equivalents (see also Chesneau & Rivinius, 2005).

Coherence theory naturally considers both the spatial and temporal coherence together (a simple case is represented in Figure 2.3d) and it leads to a remarkable finding: a dependence between the intensity distribution at the observation plane (more specifically the contrast of this intensity) and the angular structure of some distant astronomical source. The relationship is known as the van Cittert-Zernike theorem, it is this theorem that has become the basis of stellar interferometric theory.

2.1.2 Van Cittert-Zernike theorem

We will not derive the van Cittert-Zernike theorem in a purely mathematical sense here, but will try to develop an intuition for it by continuing to consider Young's experiment in the context of the previous section.

First, consider what is known as the contrast of the fringe pattern at the observation plane, also known as the visibility amplitude, defined as:

$$|\mu| \;=\; \frac{I_{max} - I_{min}}{I_{max} + I_{min}}. \tag{2.7}$$

Perfect coherence will occur when the visibility amplitude equates to one. This is the case when perfect constructive and destructive interference occurs, a state caused by an unresolved coherent light source, such as a monochromatic point source (see for example Figure 2.3a). In contrast, $|\mu| = 0$ depicts an interferometrically non-coherent light source created by what is classified as an over-resolved target (an object too extended for the interferometric instrument). An extended source ($0 < |\mu| < 1$), can be represented by a series of independent, incoherent point sources of position θ'. In terms of the source intensity distribution $I(\theta')$, an extended source takes the form:

$$I_0 = \int I(\theta') d\theta'. \tag{2.8}$$

Similarly, the two-dimensional intensity distribution can be quantified. From Equation 2.5 we find:

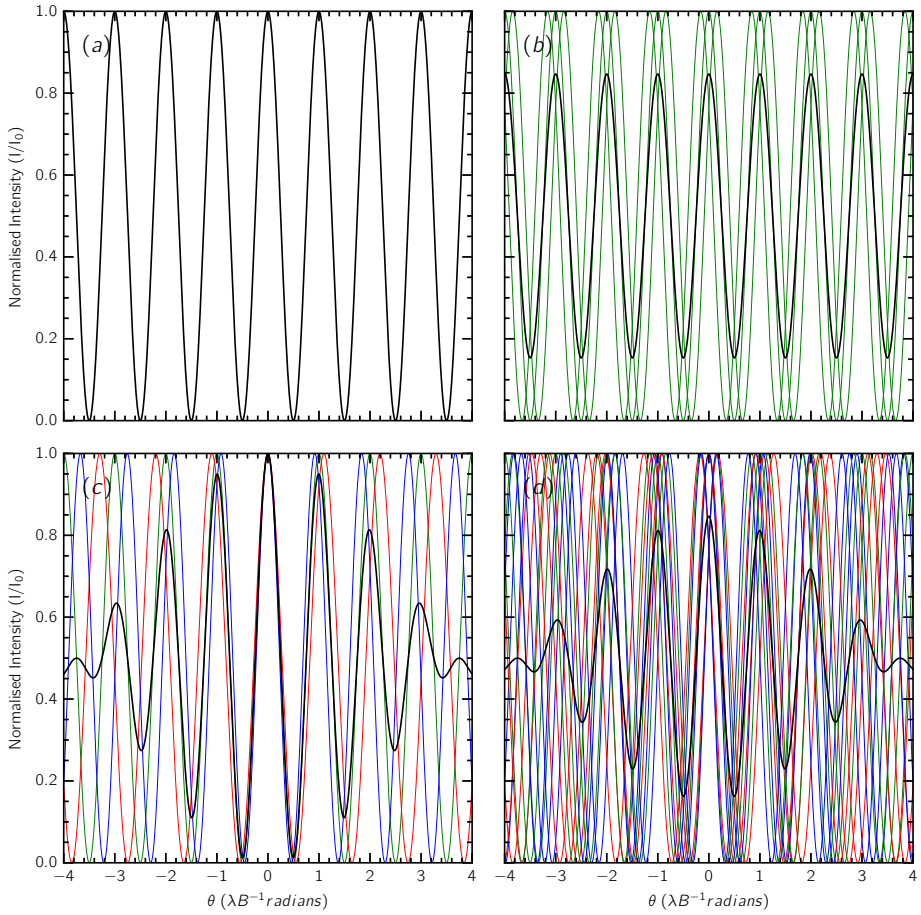

Figure 2.3: Dependence of fringe patterns on extended and chromatic sources. In all plots the black solid line is the observed fringe pattern. The resulting intensity distribution of a monochromatic point source is depicted in (a), while in (b) we show a monochromatic extended source. In (c) and (d) we depict chromatic points sources (in this example for only three wavelengths, represented by the three colours). In (c) we represent a chromatic point source and in (d) a chromatic extended source. Plots are based on those found in Chesneau & Rivinius (2005) and Glindemann (2011), see also Grellmann (2012).

$$I(\vec{\theta}) = \int I(\vec{\theta'})d\theta' + \int I(\vec{\theta'}) \cos\left(k(\vec{\theta} + \vec{\theta'})\vec{B}\right) d\vec{\theta'}. \tag{2.9}$$

With the substitution:

$$\mu(\vec{B}) = \int \hat{I}(\theta')e^{-ik\vec{\theta'}\cdot\vec{B}}\ d\vec{\theta'}, \tag{2.10}$$

where $\hat{I} = I(\theta')/I_0$, we can rewrite Equation 2.9 in its complex form (from Equation 2.6) as:

$$I(\vec{\theta}) = I_0\left(1 + \mathrm{Re}\left(\mu(\vec{B})e^{-ik\vec{\theta}\cdot\vec{B}}\right)\right) \tag{2.11}$$

$$= I_0\left(1 + |\mu(\vec{B})|\cos(\phi(\vec{B}) - k\vec{\theta}\cdot\vec{B})\right), \tag{2.12}$$

which is the full complex visibility function. Comparing with Equation 2.6, we see that $\mu(\vec{B})$ is the complex visibility function, with amplitude $|\mu(\vec{B})|$, and phase $\phi(\vec{B})$. Rearranging for $\mu(\vec{B})$ we obtain the van Cittert-Zernike theorem (van Cittert, 1934; Zernike, 1938):

$$\mu(\vec{B}) = \frac{\int I(\theta')e^{-ik\vec{\theta'}\cdot\vec{B}}\ d\vec{\theta'}}{\int I(\vec{\theta'})\ d\vec{\theta'}} = |\mu|\exp(i\phi). \tag{2.13}$$

A result that shows the consequent visibility function at the observation plane can be related to the source intensity at the aperture plane via its Fourier transform. The relation allows for the reconstruction of the source intensity from its *unique* intensity distribution at the plane of observation. We now need only apply this knowledge to the practical observation of astronomical sources. In the following section we will however show that the task can be a technically difficult one.

2.2 Interferometry in practise

Significant technical advances have been made over the last few decades in the transition from interferometric theory to its practical application in high resolution astronomical studies (see for example, Labeyrie et al., 2006). Concepts are for example easily transferred, e.g., to obtain the complex visibility function of an astronomical source, one needs simply replace the slit opening of Young's experiment (Figure 2.2) with telescopes separated by distance B. The transition however, imposes many technical difficulties. Betelgeuse, for example, one of the largest stellar objects in the sky, with an angular diameter of the order of $\sim 0.05''$ requires a baseline length B, of the order of $\lambda/(2.5 \times 10^{-7}) \sim 2$m to resolve interferometrically. Optical interferometric study is thus required to overcome huge dynamic ranges, with the requirement of interfering light (that necessitates precision to fractions of a wavelength) over baseline lengths of tens of meters (and in smaller angular diameter sources, potentially hundreds of meters).

In Section 2.2.2 we provide a brief overview of interferometric instrumentation and telescope design.

The passage from theory to practise is however not complete without considering an effect that plagues almost all terrestrially bound observational study: the atmospheric influence, this problem will be considered in Section 2.2.3, and shown to be particularly harmful at optical and near-infrared wavelengths. We will also introduce interferometric data products, specifically devised in attempt to overcome these atmospheric effects in Section 2.2.4.

2.2.1 Delay lines

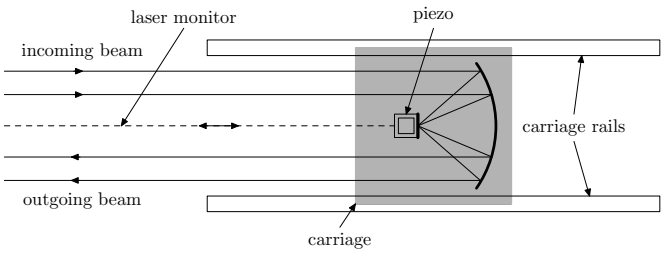

Figure 2.4: Schematic of a typical delay line design. Figure adapted from Labeyrie et al. (2006).

As mentioned, modern optical interferometry is made technically challenging by the requirement of interfering light to fractions of a wavelength over scales of hundreds of metres. The task of the delay lines, sometimes known as path equalisers or *optical trombones*, is to maintain a zero optical path difference between two or more incoming aperture beams. Optical path differences (OPD) of up to the baseline length commonly need accounting for, and it is the job of the delay lines to make the adjustment, and do so at an accuracy of the order of the light coherence length. The task is commonly approached in two stages. First, coarse adjustment is made by motor drives that position the delay line carriage, the carriage supports a mirror that redirects the incoming beam back along the path equaliser's length, the stroke length (i.e. the length of the carriage rails) needs only be approximately half the OPD. The proper motion of the the carriage is accurately monitored by a laser and reflector. A schematic of a typical delay line system is presented in Figure 2.4. For more information regarding the VLTI delay lines in particular, see for example Derie (2000) or Hogenhuis et al. (2003).

2.2.2 Interferometric receivers

Radio interferometry, in contrast to the vast majority of optical interferometers, relies on heterodyne detection, meaning the incoming radiation is combined with a reference source, a frequency close to that of the incoming radiation. The difference between the two frequencies will produce a lower frequency beat that is dependent on the original source frequency and reference frequency. The resulting beat frequency is however much more easily amplified, referenced, and because of its lower frequency, recorded. The ability to record the signal makes the heterodyne process in radio interferometry incredibly versatile, as one ultimately foregoes the need for a physical connection between apertures, allowing for the

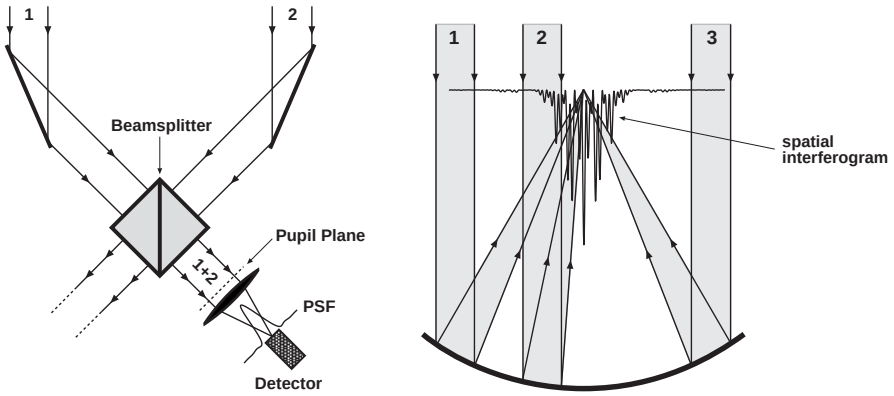

(a) Coaxial, pupil-plane beam combination. (b) Multiaxial, image-plane combination.

Figure 2.5: The geometries of typical pupil-plane, coaxial beam and multiaxial, image-plane combination schemes. Figures from Schöller et al. (2000).

interferometric study over multiple arrays and over very long baseline distances, even with telescopes on opposite sides of the world.

The frequency of the visible and far-infrared spectrum is, however much higher, and currently heterodyne techniques applied to the visible spectrum has only been successful for highly collimated, lab-based, light sources. Typical optical interferometers instead must rely on homodyne techniques, in which the beam from one telescope is combined directly with the beam from a second. In other words, the measurements must be combined concurrently, forfeiting benefits of amplification and storage of the heterodyne technique. At present the resolution of the optical interferometers is limited by the technical practicalities of homodyne combination. The task of interfering light over large baseline lengths, in which optical path differences need to quickly accommodate variations, and do so with precise movements to tenths of a wavelength is a difficult task indeed, and limits current baselines to a few hundred meters. Currently optical resolution is limited by the technical requirements of the large dynamic range.

In an attempt to meet these technical requirements, two main interferometry configurations have emerged: classified as (i) the image-plane interferometer and (ii) the pupil-plane interferometer. The image-plane interferometer, otherwise known as the Fizeau configuration, is, as the name suggests, interferometry in which the beams are combined at the image plane. The benefit of the method is that it does not require a beam combining instrument, instead focusing the beams directly onto the imaging camera. The Fizeau arrangement is most suited to common-mount telescope(s), such as a single aperture masking telescope, pair-mounted telescopes, such as the two telescope Large Binocular Telescope Interferometer (LBTI), or the proposed, spherically arranged hyper-telescopes (e.g., Labeyrie et al., 2003). The optical path difference in Fizeau arrangements is however highly susceptible to atmospheric effects, and requires high speed cameras or adaptive optics to prevent the blurring of fringes. Large fields of view are also typical, but necessitate large, high resolution, and expensive imaging devices.

Pupil-plane configurations are more commonly seen in long-baseline interferometers. The pupil-plane interferometer, also known as the Michelson configuration

(made famous in the Michelson-Morley experiment, in which the speed of light was accurately measured, e.g., Michelson & Morley, 1887). The configuration relies on a beamsplitter to combine apertures interferometrically, thus allowing beam interference between independent telescopes. For multiple aperture systems the Michelson interferometer, as opposed to the Fizeau configuration, does not require precise co-phasing for each combined beam. Allowing for the formation of the interferogram without knowledge of the baseline lengths and optical path differences to the required few tenths of a wavelength necessary of the image-plane interferometer. The pupil-plane interferometer does however have a reduced field of view in comparison to their image-plane counterparts, but requires less sensitive, lower resolution detectors. In this thesis, astronomical measurements were obtained with pupil-plane instruments.

Beam combination schemes are however further classified into coaxial and multiaxial geometries. A coaxial combination relies on beam splitters to record the separate beams, as opposed the multi-axial beam combiner that relies on a lens for example. The coaxial scheme relies on temporal modulations of the optical path difference between apertures to detect fringes, otherwise known as a temporal encoding of the fringes. The coaxial geometry is shared with the Michelson-Morley interferometer. The multiaxial beam combiner configuration resembles that of Young's experiment, in which the beams from the separate apertures are collimated and focused, and then interfered at the observation plane to reveal the fringes. The multiaxial combiner hence obtains spatially encoded fringes. The two geometries can be distinguished perhaps most easily by considering the resulting beam directions following combination. A coaxial instrument will produce parallel beams, while a multiaxial scheme will result in differing beam directions. For comparison a pupil-plane coaxial beam geometry is presented along side a multiaxial image-plane combiner geometry in Figure 2.5.

2.2.3 The atmosphere

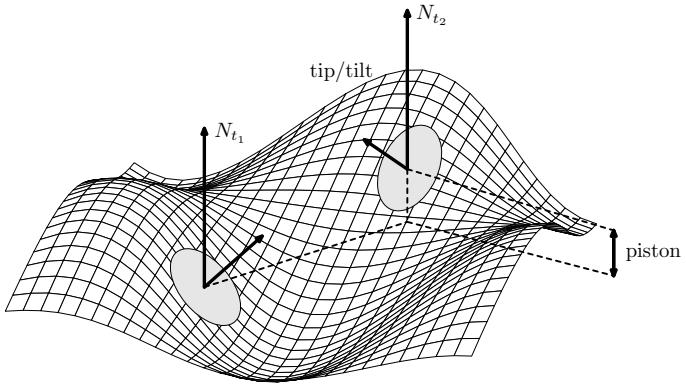

Figure 2.6: The influence of the atmospheric perturbation on incoming wavefronts is presented here in terms of the atmospheric piston. An incoming wavefront, normal to the non-projected telescopic apertures N_{t_1} and N_{t_2}, is considered. As the atmospheric function changes, so does the atmospheric piston length, resulting in a fluctuation optical path difference at the interferometer. The tip/tilt effect can be seen as the change in angle between the projected aperture normal, and the non-projected aperture normal. Illustration based on that found in Hillen (2013).

As is explained by Labeyrie et al. (2006), the atmosphere can be considered "a

very thick bad piece of glass in front of your telescope". In ground based optical interferometry its influence will actively destruct the visibility phase via an effect known as the *atmospheric piston*. The refractive index of the gases that make up the atmosphere are density dependent, which makes them in turn vulnerable to fluctions in pressure, temperature and humidity. Thus the light scattering properties of the atmospheric medium will, with the atmospheric changes to the optical path length, destroy source phase information. This effect is illustrated in Figure 2.6, where we see how the initial wavefront is ultimately perturbed by these atmospheric effects. To first order, the atmospheric piston contributes an additional phase term, $\phi^{\mathrm{atm}}(t)$. Its temporal dependence sees it fluctuate as $2\pi\delta(t)/\lambda$, where $\delta(t)$ is the change to the optical path difference. An example of the atmospheric piston's temporal changes can be seen in Figure 2.7, where we also see the resulting effect on the phase information.

Second and higher order atmospheric influences will not only result in changes to overall phase. The visibility amplitude will also be affected by tip/tilt effects (see again Figure 2.6) and other instrument phase byproducts. However, its consequence is not as damaging; present day instrumentation can overcome the influence almost entirely, but we will not discuss this effect further. We instead focus our attention to the interferometric data products that have been developed to partly overcome atmospheric influences.

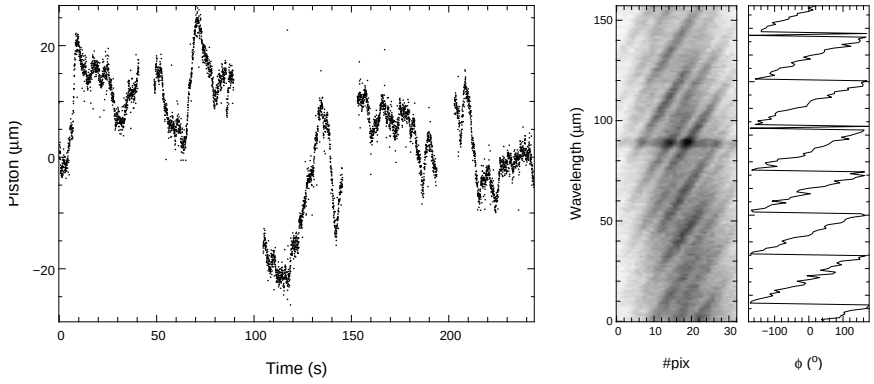

Figure 2.7: The left figure represents a typical change in the optical path difference caused by the atmospheric piston (from Tatulli et al., 2007). While the two figures on the right show the piston effect on the phase shape as is seen in the AMBER fringes and phase measurements respectively, reproduced with permission of F. Millour (see also Millour (2014)).

2.2.4 Interferometric data products

2.2.4.1 Visibility amplitude

The visibility amplitude is sensitive to the geometric characteristics, equivalent size and orientation of the object. For this reason (for the post-AGB and PPN objects at least) the visibility amplitude is perhaps the most valued of interferometric observable. Perhaps the most important quality of the observable is however its fidelity. Its resilience to atmospheric turbulence, in which temporal averaging of

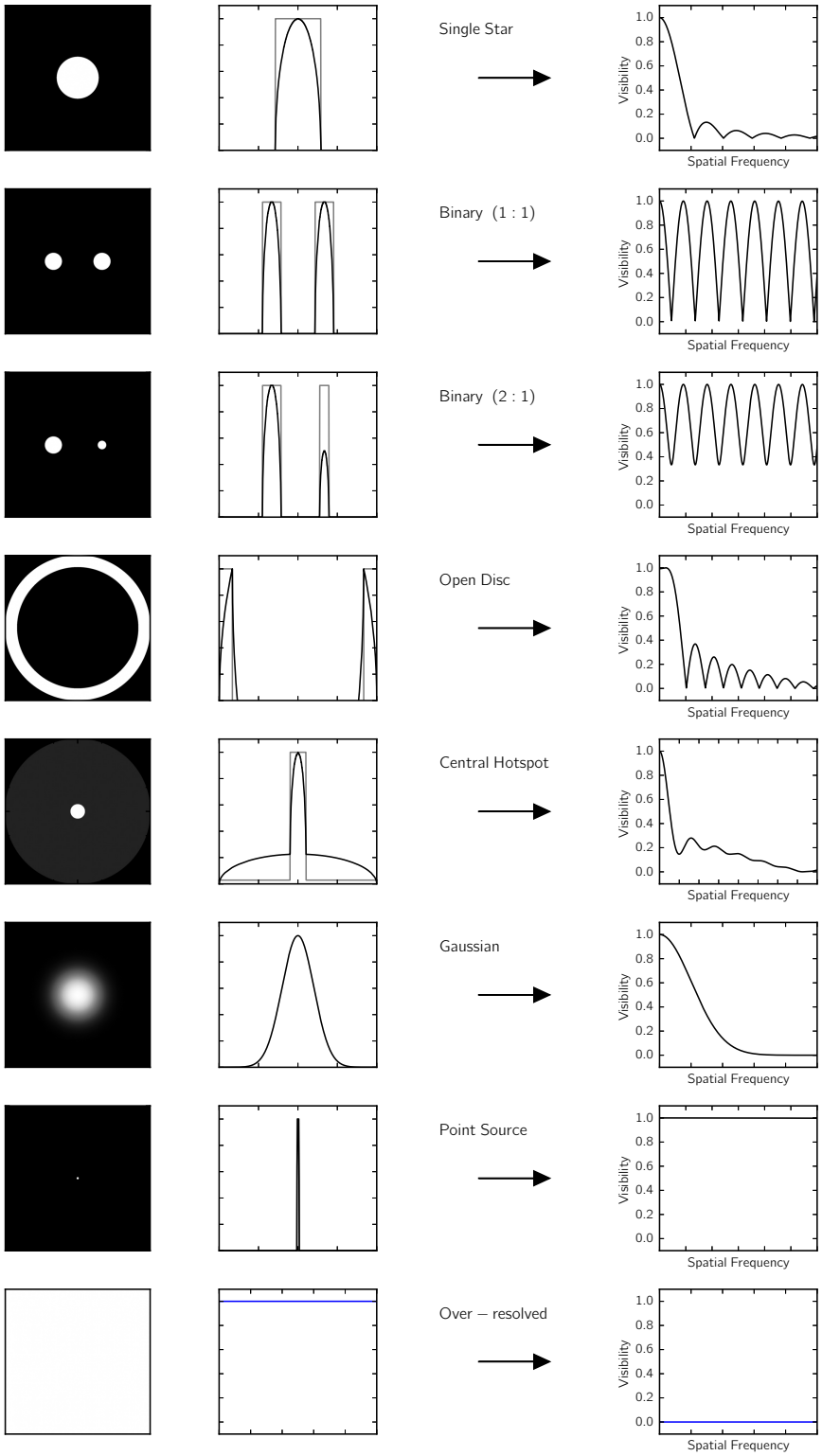

Figure 2.8: An illustration of the resulting visibility curves for a selection of simple astronomical morphologies. The astronomical shapes appear in the left most column, In the centre image the grey lines representing the flux magnitude for the astronomical image with respect to a centred horizontal line. The black solid line is the normalised sum of the pixels fluxes in columns perpendicular to this centred horizontal line, the Fourier transform of this distribution gives the the resulting image visibility which is presented in the right most column image as a function of spatial frequency. Inspired by that presented in Chesneau & Rivinius (2005).

the data products (through speckle interferometry for example) allows for the removal of first-order atmospheric perturbations, which is a rare quality among the optical interferometric observables. In fact when taking the squared modulus of the complex visibility (the visibility amplitude squared), atmospheric effects can almost entirely be removed.

The visibility amplitude is however susceptible to higher order terms, caused both by instrumental and atmospheric effects, as such terms tend to accumulate, and even in the best calibrated instruments non-zero, systematic biases may result. This accumulation thus makes calibration in interferometry imperative to achieve accurate scientific study. In fact, much of scientific observing time is dedicated solely to calibration. Observation of calibrator targets must be taken with the same instrumental setup, and preferably within a few degrees of the science object. To serve its purpose, calibrator objects have well-established targets fluxes and spatial dimensions. In the case of spectral calibration, a calibrator source is preferably of similar type to the science object. The final calibration spectrum is derived from a template spectrum based on the calibration target (e.g., Cohen et al., 1999). Visibility calibration is more straight-forward with the final science target's visibility being the quotient of the visibility of the science object and the calibrator's visibility. Unfortunately however, calibration cannot be performed in parallel with the target observations, significantly reducing observation efficiency. An example of common astronomical geometries, and their resulting visibility amplitudes are provided in Figure 2.8 (we additionally provide mathematical derivations of the visibility amplitude of some common astrophysical geometries are presented in Section 2.4.2.1).

It can be seen in Figure 2.8, that the resulting visibility of a point source has high visibility ($\mu = 1$), and conversely an over-resolved point source has a visibility of 0. Some geometries can be unintuitive for example, the open disc and central hot-spot, while others more so, a Gaussian intensity distribution becomes a Gaussian for example. The general rule is that a lower visibility is representative of a larger structure, and a higher visibility indicative of a smaller structure. The importance however is the one-to-one mapping of the visibility to the source morphology.

2.2.5 Phase

An object's complex visibility does not just contain information pertaining to the contrast amplitude. In fact, phase information, which quantifies the relative fringe positioning, carries more information with regard to signal structure than does the visibility amplitude (Skarbnik & Yehoshua Y, 2009). The importance of phase information can be visualised when considering Figure 2.9. We take the Fourier transform of the two images (the Lena standard test image and the image of NGC 6720, Figure 2.9a and Figure 2.9b respectively), and swap the resulting Fourier components, that is we take the magnitude component of the Lena image (i.e. $|\hat{f}(\xi_{\text{lena}})|$), and combine it with the phase information of the ring nebula image ($\angle\hat{f}(\xi_{\text{ring}})$), the inverse Fourier transform of this result is then calculated (i.e. $f\{|\hat{f}(\xi_{\text{lena}})| \angle\hat{f}(\xi_{\text{ring}})\}$) and depicted in Figure 2.9e. Similarly we take the magnitude component of NGC 6720 and combine with the phase information of the Lena test image to determine the inverse Fourier transform (i.e. $f\{|\hat{f}(\xi_{\text{ring}})| \angle\hat{f}(\xi_{\text{lena}})\}$) in Figure 2.9f. The phase information of both images (i.e.,

(a) Lena, standard test image.

(b) NGC 6720, The Ring Nebula.

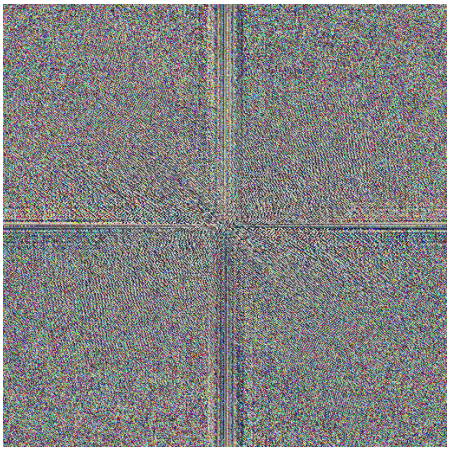

(c) $\angle\hat{f}(\omega_{\text{lena}})$

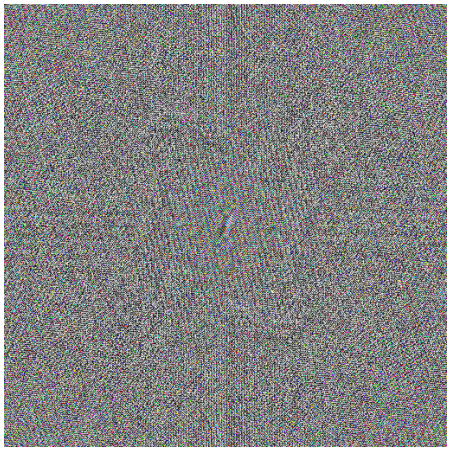

(d) $\angle\hat{f}(\omega_{\text{ring}})$

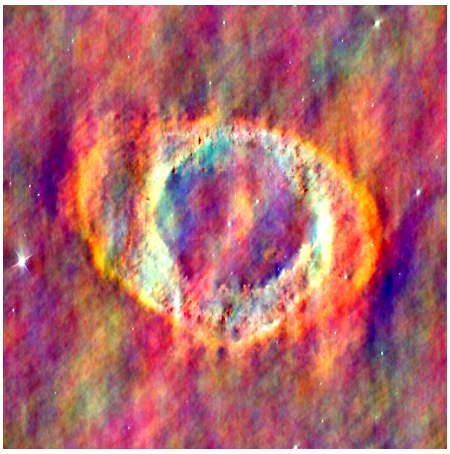

(e) $\mathcal{f}\{|\hat{f}(\xi_{\text{lena}})|\angle\hat{f}(\xi_{\text{ring}})\}$

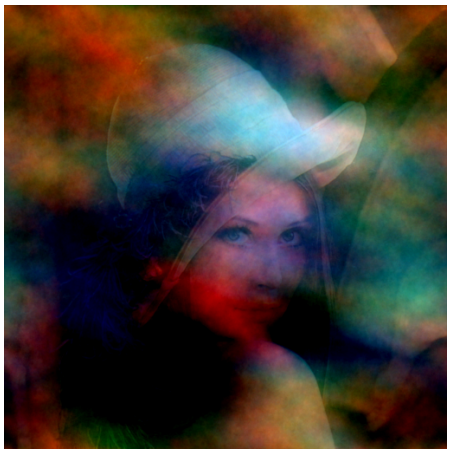

(f) $\mathcal{f}\{|\hat{f}(\xi_{\text{ring}})|\angle\hat{f}(\xi_{\text{lena}})\}$

Figure 2.9: The phase component of the Fourier transform of the Lena image in a) is given in c), and similarly the ring nebula (NGC 6720) in b) provided in d). These phase components are then switched, and recombined with the amplitude of the Fourier transform of the opposite image, and the resultant inverse Fourier transform is given in e) and f). It is evident that following the set transformations, it is the resulting image that contains the phase component of the original image that shares more visual similarities to that of the original image. See also Grellmann (2012).

$\angle\hat{f}(\xi_{\text{lena}})$ and $\angle\hat{f}(\xi_{\text{ring}})$) are plotted as a function of frequency in in Figure 2.9c and 2.9d respectively.[2] By comparing the final images Figure 2.9e and Figure 2.9f directly with Figure 2.9a and Figure 2.9b, it becomes evident that the images that contain the phase information of the input images better resemble the initial images visually. Which indicates the information that spatially distinguishes the images is encoded in the phase, as opposed to the magnitudal information (as first demonstrated by Oppenheim & Lim, 1981).

In an astronomical context this dictates that it is the phase information that better constrains spatial information, i.e. the location of features. For example, it is the phase information that allows the component position of a binary source to be determined, or provide information pertaining to object asymmetries. In practise however, despite the visibility amplitude being insensitive to non-centrosymetric brightness distributions, it is more commonly the favoured observable. After all, current interferometric combiners are limited to six interferometric apertures, as such, the broad uv-coverage needed for full image reconstruction is not yet feasible (uv-coverage is addressed in Section 2.2.6). In this case simple non-centrosymetric brightness distribution approximations suffice. As mentioned, the phase component of the visibility is difficult to acquire reliably, and the extraction of the outright complete phase is not currently achievable (see for example Labeyrie et al., 2003; Millour, 2014). Atmospheric effects cause differences in the pathlengths above individual apertures of an interferometer (refer to Figure 2.6), which results in a shift in the observed interferogram. With the atmospheric effect on phase unaccounted for, the phase is contaminated, and the van Cittert-Zernike theorem no longer applies (Monnier, 2003). On the other hand, the visibility amplitude is not so strongly coupled to atmospheric effects, for example the shift in the resulting fringes is independent to their amplitude and, for short exposure times at least, the visibility remains a reliable data product.

We may lose the capacity to analyse directly the positional information provided by the interferometric phase information because of the atmospheric influence. However, it is possible to analyse higher order phase information, for example the relative phase between two or more wavelengths, known as differential phase, remains unaffected. Differential phase though not as robust as visibility amplitudes, nor as descriptive as the full phase information has been used to constrain astronomical environments (for example Tristram et al., 2014). For a more thorough study of phase information in optical interferometry and the challenge of extracting phase information see Monnier (2003, 2007), Chelli et al. (2009a) and Millour (2014). In the following Sections we now consider phase derivatives (differential phase and closure phase), as useful and applicable optical interferometric data products.

2.2.5.1 Differential phase

The observed phase of the complex visibility is made up of three main components: (i) the true source phase, (ii) the phase introduced by the optical path difference created by the atmospheric influence (i.e. the atmospheric piston) and, to a lesser extent (iii) an instrumental phase term. To reproduce the objects visibility source

[2] Images of magnitude are not illustrated here as the dynamic range of the Fourier intensity values for natural images are much too large, resulting in a black image (logarithmic scaling is required, but is not provided here for reasons of typesetting).

phase we require the ability to separate the phase terms from the atmospheric and instrumental phase. In optical interferometry however, this requires nanometer accurate metrology. Adaptive optics and phase tracking have improved optical techniques significantly over the last few decades, but we are yet to decouple the unwanted noisy phase terms from the source phase. It is possible to rely instead on second order phase information, and measure for example the relative visibility phase between wavelengths, an observable known as the differential phase. For example:

$$\phi^{\text{diff}}(\lambda_1, \lambda_2) = \phi(\lambda_1) - \phi(\lambda_2), \tag{2.14}$$

where $\phi(\lambda_1)$ is the phase at the reference wavelength, and $\phi(\lambda_2)$ the phase of the working, or current wavelength. To first order, the assumption that a shift in the measured phase caused by the atmospheric and instrumental phase is common over all wavelengths can be made. We can thus extract the differential source phase independent of noisy phase terms that can commonly exceed 0.2 radians.

Analysis of the differential phase can however be unintuitive, but in general, a non-zero differential phase will result if there exists an asymmetric, or complex, brightness distribution. As the differential phase is a measurement of relative phase, it is chromatically sensitive, and cannot only detect spatially asymmetric sources, but also identify chromatically asymmetric sources. Some non-chromatic, yet, symmetric geometries, such as rings or discs, can also be detected. In general, a near zero differential phase indicates a chromatic image shift, while a higher differential phase offset ($\sim 0.7 - 0.9$ radians) suggests a spatially asymmetric target. However, as (Tristram et al., 2014) point out, the reality is not near as clear cut as this, for example a binary (a spatially asymmetric object) would commonly exist as two separate spectral types, of which it is hard to distinguish between the two resulting phase effects.

It should be noted, however, that higher order phase terms, introduced both atmospherically and via wavelength dependencies of the instrumentation, will introduce noise to the final differential phase. Fortunately there exists a more robust phase derivative, immune to such additions, though it requires the addition of a third telescope. A telescopic triangle allows the measurement of what is known as the closure phase.

2.2.5.2 Closure phase

The sum of the fringe phases for three telescopes is known as the closure phase. Such a measurement is a good observable as, unlike the differential phase, it is independent from the atmospheric phase terms. With the introduction of a phase delay above telescope b (see Figure 2.10), the observed phase for the baseline connecting telescope a and b (Φ_{ab}), comprises of the object phase ϕ_{ab}^{obj} and the atmospheric delay between the two telescope (i.e. $\phi_b^{\text{atm}} - \phi_a^{\text{atm}}$), the observed phase can thus be written:

$$\Phi_{ab} = \phi_{ab}^{\text{obj}} + (\phi_b^{\text{atm}} - \phi_a^{\text{atm}}). \tag{2.15}$$

For three apertures, we can account for the other two baselines in a similar fashion, such that:

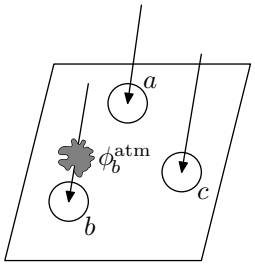

Figure 2.10: Atmospheric phase error introduced in one of three apertures, these phases however are seen to cancel out when considering the closure phase. After Monnier (2003).

$$\Phi_{bc} = \phi_{bc}^{\rm obj} + (\phi_c^{\rm atm} - \phi_b^{\rm atm}) \tag{2.16}$$
$$\Phi_{ca} = \phi_{ca}^{\rm obj} + (\phi_a^{\rm atm} - \phi_c^{\rm atm}). \tag{2.17}$$

Upon summation, we obtain the closure phase in which the atmospheric terms are seen to cancel out, leaving us the respective object phases, i.e:

$$\Psi_{abc} = \phi_{ab}^{\rm obj} + \phi_{bc}^{\rm obj} + \phi_{ca}^{\rm obj}. \tag{2.18}$$

The closure phase, similar to the differential phase, is sensitive to object asymmetries, where a result of zero (or π), indicate a symmetric object, while a non-zero (modulo π), demonstrates an asymmetric brightness distribution. However, closure phase is not sensitive to the object's asymmetric position. The three-telescope instrument combiner AMBER (see Section 2.3.1) provides closure phase with an accuracy of ~ 0.01 rad (Petrov et al., 2007), and the instrument has been used to diagnose asymmetric properties in many post-AGB objects (e.g., Deroo et al., 2007b; Le Bouquin et al., 2009; Wittkowski et al., 2011). Good work has additionally been done with closure phase measurements on the VLTI PIONIER instrument (Le Bouquin et al., 2011).

2.2.6 UV coverage

Full image reconstruction requires full *uv*-coverage, which is the case in a single aperture telescope in which spatial information of an object is available on all spatial scales and orientations within the aperture's diameter. However, the benefits that come with interferometric techniques (i.e., the potential high angular resolution), come at the cost of obtaining information along only the baseline in which which the object was observed. By increasing coverage of the *uv*-plane (by taking additional baseline observations of the source) we gain source information at different spatial scales and orientations, theoretically with enough *uv*-coverage we can recreate that seen with a single dish. Fortunately however, we need not go that far. Though increasing the *uv*-coverage is almost always desired in optical interferometric study, we can make do with limited access, and construct models which *fill in the gaps* (these techniques are addressed in Section 2.4.1). In this section we introduce common methods adopted in optical interferometry in the attempt to overcome the commonly limited *uv*-plane access.

The most obvious approach in increasing *uv*-coverage, is through the addition of observing apertures, $N_{\rm tel}$. This comes from the fact that the number of *uv*-points is proportional to the square of the number of observing apertures, i.e. $N_{\rm bases} = \frac{N_{\rm tel}(N_{\rm tel}-1)}{2}$. Currently however this route is limited by the combiner instruments, which is generally restricted to less than a dozen apertures. Hence, more commonly one relies on the super-synthesis technique. Super-synthesis arises due to the rotation of the earth, as the earth rotates, the projected baseline of the interferometer moves in an arc-like path across the source plane, thus simulating a scanning of the frequency plane. Super-synthesis however requires the object morphology to remain constant over the sampling time. However, in concert with only a few additional apertures, super-synthesis can dramatically increase *uv*-coverage. A third, though somewhat less practical method to increasing *uv*-coverage can

Table 2.1: Comparison between *uv*-coverage techniques.

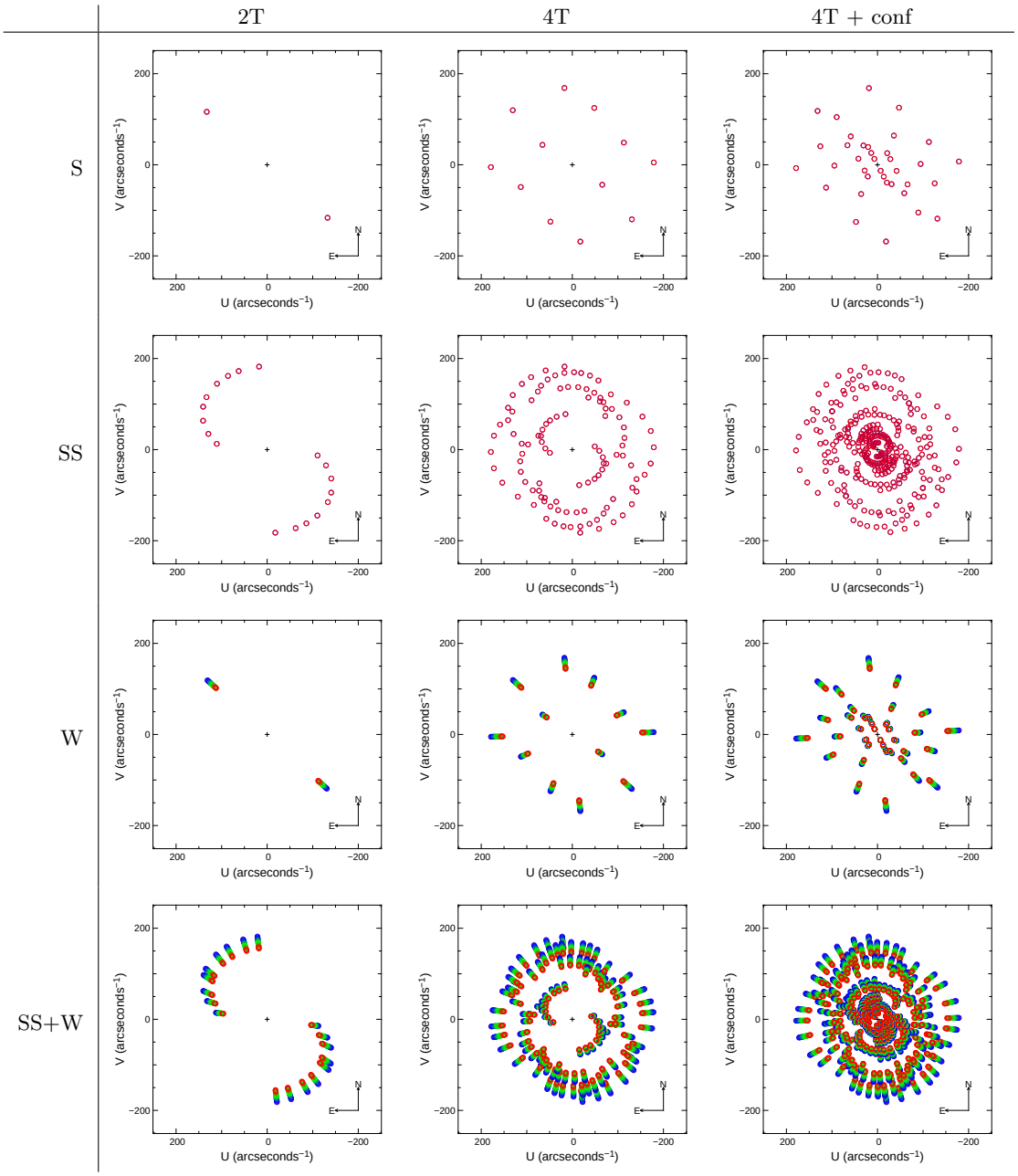

A diagram representing the techniques in which to fill the *uv*-plane. S is the *uv*-coverage provided by a single measurement, SS represents telescope super-synthesis. The coverage as provided for a wavelength band is given by W, and supersynthesis, in combination with wavelength coverage is given in SS+W row. We provide coverage as appears for the Matisse instrument on the VLTI for 2 telescopes (2T), 4 telescopes (4T) and 4 telescopes with a change in configuration (4T+conf). Reproduced with the permission of F. Millour (see also Millour 2014).

also be exploited. uv-plane access along radial lines arise with changes in the observational wavelength. For example, each wavelength corresponds to a point on the uv-plane, as such, an area of the plane can be covered by considering the wavelength dependence. However, the dependency is difficult to separate from the underlying wavelength dependency that generally arises with source geometry, the method is thus limited to objects that don't exhibit morphological changes with wavelength. An illustration of the uv-coverage as a function of the above techniques is presented in Figure 2.1.

2.3 The VLTI

The European Southern Observatory Very Large Telescope Interferometer (VLTI) is the largest aperture infrared interferometer observatory in operation today, and the largest yet built (with first light in 2001; Glindemann et al., 2001). The facility is located on Cerro Paranal in Chile, and it is currently the most scientifically productive interferometer in the world (Millour, 2014). The VLTI consists of four independent optical/IR 8.2m Unit Telescopes (UTs), in addition to four, mobile, 1.8m auxiliary telescopes (ATs). The 4 UTs, when used in interferometric mode provide ultimate sensitivity. Versatility however is provided through the ability of the smaller, interferometrically dedicated ATs to provide numerous baselines (of up to 202m), when positioned at one of 30 possible locations. Currently four telescopes can be combined with the PIONIER instrument. However, the telescopes have (or have had) the ability to be combined in groups of two with the VINCI and MIDI instruments or three with AMBER. The next generation of instruments MATISSE and GRAVITY (First light January 2016 Eisenhauer et al., 2011) will offer for the first time, real imaging capabilities, with high resolution combination of four telescopes (Millour, 2014). A schematic of the observatory is provided in Figure 2.11.

2.3.1 The VLTI instruments

In this thesis two combiner instruments were used, the now decommissioned MID-infrared Interferometric instrument (MIDI) (Leinert et al., 2003), and the three-telescope near-infrared Astronomical Multi-BEam CombinerR (AMBER) (Petrov et al., 2007).

MIDI is a mid-infrared N-band ($\lambda \simeq 8\mu$m - 13μm) two-telescope combiner of coaxial design (see Section 2.2.2). MIDI is capable of producing five data products: (i) photometric images; (ii) an N-band spectrum and (iii) visibility; (iv) correlated fluxes and (v) the differential phase. The instrument is operated in one of two primary modes: the more commonly used high-sensitivity (`HIGH_SENS`) mode in which fringes and photometric fluxes are obtained separately; and the second science-photometry `SCI_PHOT` mode, in which beam splitters are inserted, directing $\sim$30% of the incoming light to photometric channels (see Figure 2.12), allowing the simultaneous obtainment of photometric and interferometry measurements.

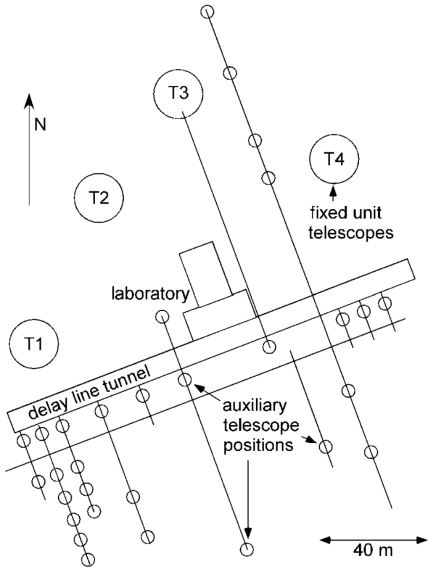

Figure 2.11: The VLTI arrangement, the fixed unit telescopes UTs: T1, T2, T3 and T4, are given in addition to as the auxiliary telescope positions, delay line position and laboratory. Figure from Labeyrie et al. (2006).

Photometry exposures are required to determine the visibility (V), as the fringe amplitude is related to the raw visibility, or correlated flux ($F_{\rm corr}$), and the total spectrum flux ($F_{\rm tot}$) as $V = F_{\rm corr}/F_{\rm tot}$. Two spectral modes are also available: a lower resolution ($R = \lambda/\Delta\lambda = 30$), NaCl prism or the higher resolution KRS5 grism ($R = 230$). The lower resolution prism is more commonly used as ultimately the light is spilt into fewer channels, allowing the measurement of dimmer targets, brighter targets on the other hand can benefit from the higher spectral resolution of the grism in which more subtle spectral features can be distinguished. Both the science-photometry mode and high-sensitivity mode can be used with the prism or grism. The limiting N-band correlated flux is thus dependent on the telescope mode chosen, on whether the prism or grism is selected, and on which telescopes are used. The limiting magnitudes for each case is presented in Table 2.2. A schematic of the MIDI instrument is presented in Figure 2.12.

The MIDI instrument has successfully been used as a so called 'disc hunter' with respect to the analysis of many post-AGB objects. The high resolution capabilities of the VLTI lead to resulting MIDI visibilities of the young nebulae objects Mz3 and M2-9 (Chesneau et al., 2007a; Lykou et al., 2011), that allowed for both the determination and constraint of an inner circumstellar disc. Similar constraints were made possible with the MIDI instrument in the case of Sakuarai object (Chesneau et al., 2009), and the many objects analysed by (Bright, 2013).

AMBER The AMBER instrument is a three-telescope J-,H-, and K-band ($\lambda \simeq 1.0\mu$m - 2.5μm) single-mode, multi-axial beam combiner. AMBER can provide up to five observables including: spectrum, visibility, differential or relative visibility[3], differential phase and closure phase. Similarly to MIDI, AMBER pro-

[3] i.e. $V(f,\lambda)/V(f,\lambda_0)$, see (Petrov et al., 2007).

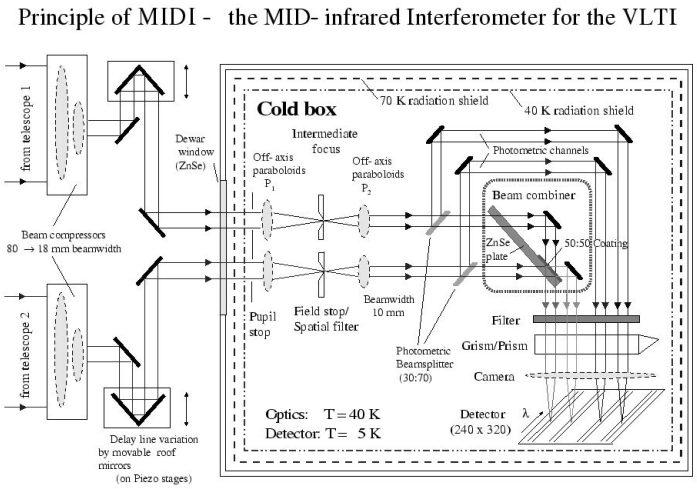

Figure 2.12: MIDI instrument schematic. Image: ESO.

Table 2.2: MIDI limiting correlated magnitudes

Telescope	Mode	Spectrograph	Limit N_{corr} (mag)	(Jy @ 12 μm)
UTs	HIGH_SENS	PRISM	4	1
UTs	HIGH_SENS	GRISM	2.8	3
UTs	SCI_PHOT	PRISM	3.2	2
UTs	SCI_PHOT	GRISM	2	6
ATs	HIGH_SENS	PRISM	0.74	20
ATs	HIGH_SENS	GRISM	0.31	30
ATs	SCI_PHOT	PRISM	0.0	40
ATs	SCI_PHOT	GRISM	-0.44	60

The limiting correlated magnitudes for MIDI. N_{corr} is the is the limiting flux of the object, it is here presented in terms of magnitude and Jy at 12μm, for the respective telescopes, modes and spectrograph configurations.

vides varying levels of spectral resolution, with a low-resolution (LR) prism mode (R=30) available for the J,H and K band (a mode that does not provide differential phase information); a medium-resolution (MR) mode (R=1500) available for the H and K filters and a high-resolution (HR) mode (R=12000) available for the K band (for AMBER configurations and limiting magnitudes see Table 2.3).

Importantly AMBER can provide angular resolution at the 1mas level, currently the best of any ESO instrument. The capabilities of the AMBER instrument has seen feature prominently in the constraint of many post-AGB environments (e.g., Chesneau et al., 2007a; Ruiz-Velasco et al., 2011; Acke et al., 2013; Hillen et al., 2013). Circumstellar disc constraints of post-AGB objects have also been determined, for example IRAS 16279-4757 (e.g., Bright, 2013). A description of the instrument is provided in Figure 2.13. For a comprehensive overview of the capabilities of AMBER and its data outputs see for example Petrov et al. (2007), Robbe-Dubois et al. (2007) or Millour et al. (2008).

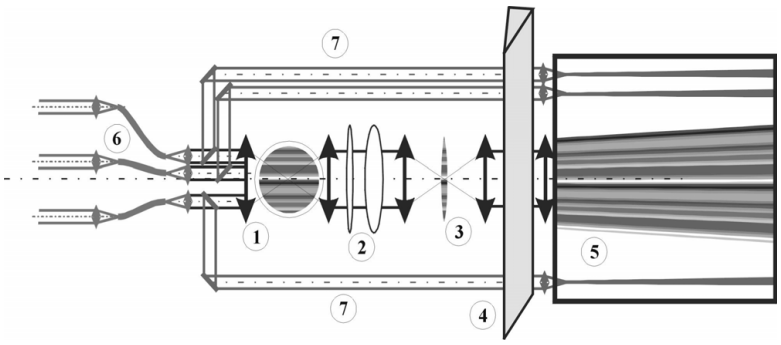

Figure 2.13: The AMBER instrument configuration as appears in Robbe-Dubois et al. (2007). (1) multiaxial beam combiner, (2) cylindrical optics, (3) anamorphosed focal image with fringes, (4) 'long slit spectrograph', (5) dispersed fringes on 2-D detector, (6) spatial filter with single mode optical fibres, (7) photometric beams.

Table 2.3: AMBER limiting magnitudes.

Telescope	Mode	Limit K_{corr} (mag)	Limit H_{corr} (mag)
UTs	LR-HK	9.0	9.0
UTs	LR-HK, MR-K	8.5	8.0
UTs	MR-H	-	6.5
UTs	HR-K	7.5	7.0
ATs	LR-HK	6.5	6.5
ATs	MR-H	-	4.5
ATs	LR-HK, MR-K, HR-K	6.0	5.0

The limiting correlated magnitudes for AMBER. H_{corr} and K_{corr} is the is the limiting magnitude and is here presented as a function of instrumental mode and spectral resolution (for example LR-HK is the low resolution mode in the H and K bands) These limits assume seeing $< 0.6''$, for a more comprehensive table that includes environmental constraints and tracking methods see the ESO manual.

2.4 Modelling

With knowledge of the spatial interferometry data products, we dedicate a small section to the application of them in an astrophysical sense. There exists two general approaches in gaining information regarding the source structure from the data products. The first is image reconstruction, in which images are constructed to fit the complex visibilities of the telescopic outputs. The second approach, which is the method used throughout this thesis, is known as model reconstruction, or model fitting, in which a physical model is simulated and the Fourier transform taken of its resulting intensity distribution. We discuss both techniques below.

2.4.1 Image reconstruction

Theoretically, given the van Cittert-Zernike theorem, one can simply calculate the source brightness function by taking the inverse Fourier transform. As mentioned however, optical interferometry at present is faced with what is known as the *uv* problem. In contrast to classical imaging techniques, the van Cittert-Zernike theorem is sampling just one point of the *uv*-plane. As such, only a finite number of frequency domain points can be sampled. Fortunately however astrophysical sources are typically composed of smooth intensity distributions, in which the voids in the Fourier space can be approximated *across*. For this reason imaging of typical astronomical objects does not necessarily require exhaustive sampling of the *uv*-plane.

Without knowledge of the Fourier frequencies in the *uv*-plane, image reconstruction becomes what is known as an ill-posed general inverse problem. As such, a single, unique image cannot simply be extracted from the sparse Fourier data. In fact an infinite number of solution images will exist within the imposed errors. The general approach in overcoming this is to impose *a priori* restrictions to the data until a single, unique, result is considered the 'correct' solution. *A priori* constraints can be relatively simple, for example, the image brightness distribution must be positive. Other constraints will however be more problem specific. Image reconstruction does have advantages over model reconstruction, for example by building an image pixel by pixel. Complex geometries, which are typically difficult to model can result, but perhaps more importantly image reconstruction can result in unbiased solutions. In tackling ill-posed problems such as this, information theory ideas have been applied. For example maximum entropy methods (MEM, e.g., Jaynes, 1957). Typically, as Ables (1974) indicates, it is the least informative image that abides by the *a priori* constraints that becomes the solution image. The idea is not far removed from Occam's razor, in which the least complicated model congruous to the data becomes the *best* candidate solution.

Image reconstruction, as applied to optical interferometric data products has improved greatly over the last few years, with many competing reconstruction algorithms appearing (e.g., Baron & Young, 2008; Baron et al., 2010; Thiébaut, 2008; Meimon et al., 2005). Model fitting however remains the more common approach of reconstruction, thanks in part to the *uv*-limitations. With improvements in interferometric instrumentation, image reconstruction will likely become more commonplace. For a more comprehensive overview of image reconstruction

see for example Thiébaut (2013) or Young & Thiébaut (2014).

2.4.2 Model reconstruction

As opposed to randomly filling pixels to suit the respective complex visibilities, model fitting recreates the interferometric data products by building an image from either geometric or physical constraints, and often both. Model reconstruction can be broke into two main methods, the first is geometrical modelling, in which one relies on analytic solutions to common, elementary astrophysical geometries. Depending on the objects complexity, these solutions can be combined to build more complex morphologies. Geometrical modelling is however limited in model complexity, and generally limited to modest, axi-symmetric structures. For more elaborate structures we rely on numerical modelling. This form of model reconstruction comes with additional benefits, it relies not only on geometrical constraints but on physical constraints as well. Numerical modelling can thus consider an object's complex visibility in addition to accurately reproducing spectral energy distributions for example.

2.4.2.1 Analytic geometric modelling

The van Cittert-Zernike theorem allows us to directly relate the intensity function at the image plane to the source intensity at the observation plane via the Fourier transform. With analytical solutions known, and some powerful Fourier transform relationships quite complicated geometrical models can be constrained efficiently and reliably, it is here worth quantifying the resulting visibilities for some typical geometries one is likely to encounter of astrophysical sources. Let us first consider a uniformly bright circular disc, indicative of a star.

We can rewrite the projected baseline vector $\vec{B}$, in terms of source coordinates (α, β) and observation coordinates (u, v). The intensity distribution of a disc of angular diameter Θ becomes:

$$I(\alpha,\beta) = \begin{cases} I_0, & \text{if } \sqrt{\alpha^2+\beta^2} \leq \Theta/2 \\ 0, & \text{otherwise} \end{cases} \tag{2.19}$$

Such that the visibility, through the van Cittert-Zernike theorem, becomes:

$$V(r) = \left| \frac{2J_1(\pi\Theta r)}{\pi\Theta r} \right|. \tag{2.20}$$

Where $r = \sqrt{u^2+v^2}$. Further analytical solutions to common astrophysical geometries are provided in Table 2.4. With use of the Fourier transform properties, such as addition, rotation, shift, convolution etc, geometries can be combined to create relatively complex structures. The difficulty comes in determining what final geometry we require, as we again find ourselves solving an ill-posed general inverse type problem. Geometric fitting engines exist, such as `LITpro` (Tallon-Bosc et al., 2008), which uses the Levenberg-Marquardt method (Levenberg, 1944; Marquardt, 1963) to find appropriate object morphologies. `LITpro` is however limited to objects that display very little variation in visibility with wavelength.

Table 2.4: Analytical visibility solutions for a selection geometric brightness distributions. The following parameters are used: $\varnothing$ is the the diameter, whether that a disc, ring or FWHM. r and $\vec{x}$ are the image plane angles and $\rho = B/\lambda$, $\vec{\rho}$ are the spatial frequencies. See Millour (2014) for a more complete list.

Shape	Distribution	Visibility
Point source	$\delta(\vec{x})$	1
Pixel	$\begin{cases}(lL)^{-1}, & \text{if } x < l \text{ and } y < L \\ 0, & \text{otherwise.}\end{cases}$	$\frac{\sin(\pi x l)\sin(\pi y L)}{\pi^2 x y l L}$
Circular object	$I(r)$	$2\pi \int_0^\infty I(r) J_0(2\pi r\rho) r dr$
Gaussian	$I_0 \sqrt{\frac{4\ln(2\varnothing)}{\pi}} \exp\left(\frac{-4r^2 \ln 2}{\varnothing^2}\right)$	$\exp\left(\frac{-(\pi \varnothing \rho)^2}{4\ln 2}\right)$
Limb-darkened	$\begin{cases} I_0\left(1 - u_\lambda(1-\mu)\right), \text{ if } r < \frac{\varnothing}{2} \\ \text{where } \mu = \cos(2r/\varnothing)\end{cases}$	$\begin{cases} \frac{\left(\alpha \frac{J_1(x)}{x} + \beta\sqrt{\pi/2}\frac{J_{3/2}(x)}{x^{3/2}}\right)^2}{\left(\frac{\alpha}{2}+\frac{\beta}{3}\right)^2} \\ \alpha = 1 - u_\lambda \\ \beta = u_l \lambda \\ x = \pi B \theta_{LD}/\lambda \end{cases}$
Ring	$\frac{1}{\pi\varnothing}\delta\left(r - \frac{\varnothing}{2}\right)$	$J_0(\pi \varnothing \rho)$
Binary star	$I_0\left(\delta(\vec{x}) + R\delta(\vec{x} - \vec{x}_0)\right)$	$\sqrt{\frac{1+R^2+2R\cos\left(\frac{\vec{\rho}\cdot\vec{x}_0}{\lambda}\right)}{1+R^2}}$

Analytic geometric modelling's main advantages is that simple astronomical geometries can be determined quickly. This form of modelling however does not give us insight into the physicality of the structures, such as temperature or luminosity. For more complicated polychromatic variant structures, or objects in which physical constraint is important, one instead turns to numerical modelling techniques.

2.4.2.2 Numerical modelling

To fit the complex visibility data product, numerical modelling relies on producing a simulated object, and comparing the visibility with the Fourier transform of the resulting image. To simulate an object however, *a priori* knowledge of its physical nature is again required, and temperatures, chemical composition, and masses etc, are commonly necessary. Providing such inputs allows resulting energy densities to be determined, which can be compared with the telescopic input, and provide flux limitations for example. Numerical modelling additionally allows for the fitting of wavelength dependent structures, i.e., polychromatic objects. Numerical modelling however is commonly more computationally expensive than other forms of modelling. For example, 1D radiative transfer codes such as `DUSTY` (Nenkova et al., 2000), analytically solves the radiative transfer equations to obtain the spectral energy distributions. These calculations can be completed quickly, but the number of input parameters quickly makes a grid type search of parameter space unfeasible. To compound the problem in more complicated, non-symmetric three-dimensional environments analytical solutions are not possible, and computationally expensive simulations are necessary, the result being

that grid based searches are similarly impractical. In fitting the data products of this thesis, we adopt the numerical modelling method, in the form of ray-tracing Monte Carlo radiative transfer. In the following section we introduce the theory of radiative transfer, in which problems regarding computational expense become evident.

2.4.3 Radiative transfer

The theory of radiative transfer is a description of the interaction of photons with matter. The ideas of which are indeed simple, however computationally it can be difficult. For example, in most astrophysical instances we can be dealing with an enormously large number of photons, a typical star for instance can emit 10^{45} photons per second. A short development of radiation transfer will here be given, and the difficulties of application attempted to be made clear.

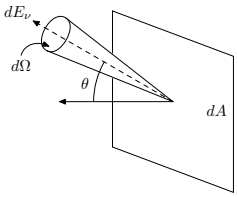

Figure 2.14: Specific intensity.

Begin by considering specific intensity I_ν of a radiation field, defined as the radiant energy dE_ν exiting at an angle θ normal to a surface dA within a solid angle $d\Omega$, in time dt and frequency range $d\nu$ (see Fig 2.14). From Chandrasekhar (1960) we have:

$$I_\nu = \frac{dE_\nu}{dA\cos\theta dt d\nu d\Omega} \tag{2.21}$$

Which can be related to the total flux passing through area dA (units [ergs cm^{-1} s^{-1} Hz^{-1}]) by:

$$F_\nu = \int I_\nu \cos\theta d\Omega \tag{2.22}$$

Let us now consider the change in spectral intensity, I_ν, along the line of travel, l. In a vacuum this value would remain constant, i.e:

$$\frac{dI_\nu}{dl} = 0. \tag{2.23}$$

Radiative transfer is however a description of the interaction of radiation with matter, and this material can alter the intensity along the line of travel dramatically. Matter can extinguish and emit radiation, phenomena that is taken care of by radiation transfer theory by the extinction coefficient, κ (units [cm^{-1}]), and emission coefficient, j ([ergs cm^{-3} s^{-1} Hz^{-1} ster^{-1}]), respectively.

Following a ray of radiation through a medium, and realising that an extinction will simply result in an overall subtraction to the spectral intensity, and similarly an emission resulting in an addition, taking account of the frequency dependencies, we formulate the formal radiative transfer equation.

$$\frac{dI_\nu}{dl} = -I_\nu\kappa_\nu + j_\nu \tag{2.24}$$

Equation 2.24 gives us a relatively simple description of the transport of radiation through a medium. The reason radiative transfer is considered such a difficult

subject computationally is that for anything other than the simplest example, the radiative transfer equation needs to be solved for all beams of radiation and for all wavelengths simultaneously. For example, to compute the spectral intensity at a point, one needs knowledge of the extinction emmisivity at that point, which is dependant on the spectral intensity introduced by other radiation beams. Along the line of sight for example, a second beam can influence the first, and this coupling can extend over the entire volume of simulation, and a regions radiation properties can become depend on other distant and remote areas.

2.4.3.1 The Monte Carlo approach

The application of the Monte Carlo method to radiative transfer problem has become common practise, and the technique has been applied to many areas of astronomy, for example galaxies, molecular clouds, the interstellar medium, circumstellar discs and planetary nebulae.

The Monte Carlo approach is a stochastic approach, that allows many simplifications to be made. Consider a photon emitted into a medium, the distance travelled before interaction, and the path it is to take following interaction. Such quantities can be calculated by sampling a probability distribution function. By repeating the process until the photon is exhausted or ejected from the medium, and repeating for all photons, the result is a simulation of radiative transfer. Let us introduce the fundamentals of Monte Carlo radiative transfer, and apply the method to a simply example.

To sample a quantity, x_0, from a probability distribution function is relatively straightforward. Consider the cumulative probability distribution $\phi(x_0)$ in which $\phi(x_0)$ (ranging from 0 to 1) uniformly samples x from a to b.

$$\phi(x_0) = \frac{\int_a^{x_0} P(x)dx}{\int_a^b P(x)dx}. \tag{2.25}$$

By replacing $\phi(x_0)$ with a random number (ξ) of range 0 to 1, we can sample the probability distribution. Let us determine the probability of a photon travelling length L.

The number of photons scattered or absorbed per unit length is related to the number density, n, and cross Section, σ, by the volume absorption coefficient, $n\sigma$. The probability that a photon interacts within length dl thus becomes $n\sigma dl$. The probability of travelling length L (made up of N equal parts) without interacting then becomes:

$$P(L) = (1 - nL\sigma/N)^N = e^{-nL\sigma} \tag{2.26}$$

where $nL\sigma$ is known as the optical depth (τ), which is the number of mean free paths that make up distance L. Sampling Equation 2.26 by applying Equation 2.25, we obtain:

$$\phi(\tau) = \frac{\int_0^{\tau_0} e^{-\tau} d\tau}{\int_0^{\infty} e^{-\tau} d\tau} = 1 - e^{-\tau_0} = \xi. \tag{2.27}$$

The sampling function for optical depths thus becomes:

$$\tau_0 = -\log(1-\xi), \tag{2.28}$$

In which the distance L travelled can be calculated from the following relation:

$$\tau_0 = \int_0^L n\sigma dl. \tag{2.29}$$

Once distance L has been travelled the photon is scattered or absorbed. The interaction being set probabilistically according to the scattering and absorption cross sections of the particles that make up the medium, gives as the albedo, a:

$$a = \frac{n_s\sigma_s}{n_s\sigma_s + n_a\sigma_a} \tag{2.30}$$

With the subscripts representing scattering and absorption. These cross sections are wavelength dependent, with an absorption event generally resulting in thermal emission of a photon of different wavelength and direction, a topic that will not be covered here.

Consider now the simplest form of scattering, isotropic scattering, in which the direction is drawn uniformly over the 4π steradians. We require two random values, ξ_1 and ξ_2 between 0 and 1, to sample the angles θ and ϕ, which become

$$\theta = \arccos(2\xi_1 - 1), \qquad \phi = 2\pi\xi_2 \tag{2.31}$$

Reproducing radiative transfer using Monte Carlo methods becomes a relatively straightforward process, i.e:

(i) Emit N photon packets.

(ii) Sample the optical depth for each photon packet to determine its point of interaction.

(iii) Sample the albedo to determine the interaction type.

(iv) Sample the scattering functions to determine photon packets path.

(v) Repeat the sampling process (i-iv) until the photon exits the medium.

By considering enough photon packets one can build an accurate representation of the object as governed by the radiative transfer equation. From these simulations spectrums and images can be calculated, and hence one needs only compare the modelled outputs with the objects data products. However, we are again faced with an inverse type problem, and the search space has now greatly expanded. Radiative transfer can for example require dozens of parameters for accurate representation. In the following section we introduce post-AGB environments and the parameters necessary to describe them in the context of radiative transfer models. As well as the radiative transfer code adopted for the remainder of the analysis of this thesis. For a more comprehensive introduction to Monte Carlo

radiative transfer see for example Wood et al. (2001), Ercolano et al. (2003) or Whitney (2011). For a more general overview of the physics that govern radiative transfer see Chandrasekhar (1960).

2.5 Radiative transfer of post-AGB environments

2.5.1 RADMC-3D

RADMC-3D (Dullemond, 2012) is a general purpose 3-D Monte Carlo radiative transfer code based on RADMC (Dullemond, 2011). The code is very versatile, being applicable to dust continuum RT, molecular and/or atomic line transfer and gas continuum transfer in 1-D, 2-D and 3-D geometries. RADMC-3D was adopted in this thesis for its ability to create intensity distributions (images) and spectral energy distributions quickly and efficiently. In an optimisation approach, in which potentially thousands of RT models are necessary, simulation efficiency is paramount. RADMC-3D offers a range of RT approximation methods that save precious computational seconds. Such methods include, modified random walk, weighted photon package mode and simplified random walk. These techniques, in addition to controlling the number of photons and model resolution, allows for a balance between simulation speed and accuracy to be obtained easily. Additionally, RADMC-3D was chosen for its excellent, and comprehensive documentation.

High angular resolution infrared interferometry is sensitive to the innermost circumstellar dusty regions. In this section we introduce the model parameters required to model such an environment.

2.5.2 Modelling post-AGB environments

In creating a model of our post-AGB environments we begin with the stellar source. The input consists of a file describing the flux as a function of wavelength (normalised for a distance of 1 parsec). This file is created by our Python module to be a blackbody of given temperature and luminosity.[4] The stellar object has the option to be set as a point source, i.e., a single photon packet source, or as a more complex 3-D structure. The main difference is that the photons for the three-dimensional case are able to heat the top and bottom surfaces of the disc structure directly (i.e., in the 3-D case the photons can be emitted onto the disc surfaces directly. A point heat source can however only emit directly onto the inner disc rim, heating of the top and bottom of the disc in the point source case is thus achieved through second order effects). Surrounding the star we build our dust structure. For simulation efficiency and the avoidance of potential model degeneracies (which will be considered in later chapters), we rely on a simple 2-D axial symmetric geometry.

[4] The RADMC-3D default is a stellar blackbody, we rely on our own module to create this table as it allows us to include reddening, or the additional of a second blackbody source etc.

2.5.2.1 The disc

The study of post-AGB discs presently remains in its infancy, with only fragmented information across a number of object classes. Ultimately, understanding a discs origin depends on the determination of their characteristics. With little knowledge of the structures, we rely on the relatively simple azimuthally symmetric disc, as first described by Shakura & Sunyaev (1973).

This disc structure, though not observed directly, is common to many post-AGB modelling studies (e.g., Chesneau et al., 2007b, 2009; Lykou et al., 2011; Bright, 2013). The simple nature of the structure satisfies maximum entropy arguments, that is, we are selecting from a high entropy uninformative distribution (i.e. a simple and reasonable structure), that does not assume information currently unknown (i.e. low entropy distribution). Yet, the number of parameters allows for a broad range of simple and unique dust density distributions. In cylindrical coordinates (r, z), we have:

$$\rho(r,z) = \rho_0 \left(\frac{R_\star}{r}\right)^{h_\alpha} \exp\left(-\frac{z^2}{2h(r)^2}\right), \tag{2.32}$$

where ρ_0 is a normalisation constant, $R_\star$ is the stellar radius, h_α is an exponent controlling the density as a function of radius along the mid-plane and $h(r)$ is the disc scale height, increasing with radius as

$$h(r) = h_0 \left(\frac{r}{R_\star}\right)^{h_\beta}, \tag{2.33}$$

where h_0 is the scale height for a given radial distance and h_β is the vertical density parameter. We also define an inner and outer disc radius ($r_{\rm in}$ and $r_{\rm out}$). The mid-plane density factor h_α, controls the density fall off in the mid-plane. Values in the range $1.5 < h_\alpha < 2.5$ are typical. A small h_α results in large extended discs. Alternatively, a large h_α results in small compact density structures. The parameter controlling the density in the vertical plane, h_β, controls the flaring in the disc, with larger values being highly flared. h_β is generally limited to $1.0 < h_\beta < 4.0$. The scale height controls the vertical thickness of the disc, typical values limit h_0 as 5.0 AU $< h_0 <$ 25.0 AU. The effect of the parameters is illustrated in a plot of disc density profiles in Figure 2.15.

2.5.2.2 Dust

AGB stars are broadly categorised as either carbon or oxygen rich depending on the carbon to oxygen ratio in the photosphere. The theory explaining the elemental abundances of the AGB photosphere, has all giants existing initially as O-rich stars (caused by the O-rich ISM). It is found that carbon and oxygen atoms in the photosphere becomes readily tied up in CO molecules, such that the more abundant of the two elements will exist independently, and thus characterise the stars chemical composition. Younger AGB stars are typically O-rich, some will however become C-rich following carbon dredge-up as part of the the thermal pulse cycle phase (i.e. see Section 1.1.1), the stars that don't introduce carbon in

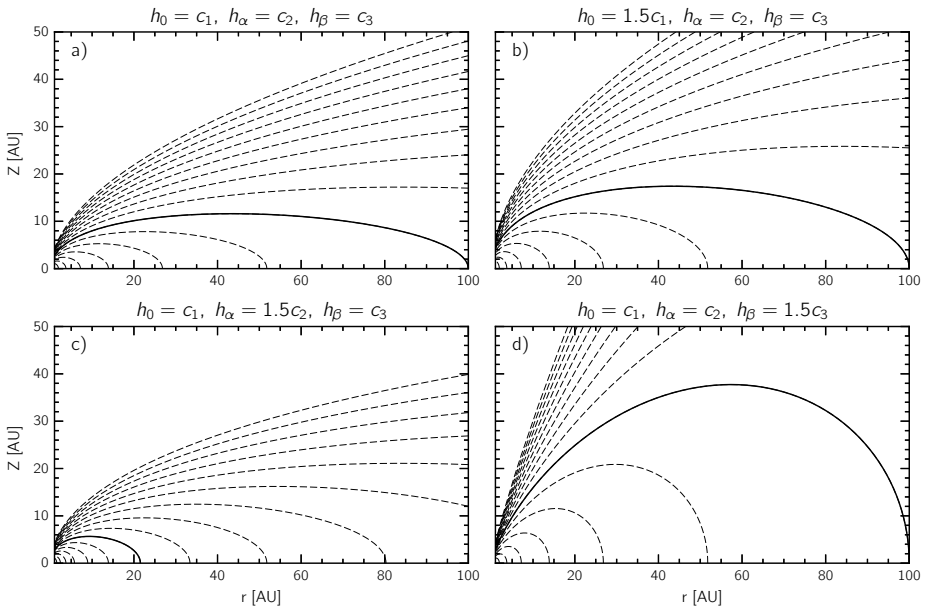

Figure 2.15: Contours of density for the stratified disc: a) represents a disc structure for comparison. b) is simply a 50% increase in h_0, c) a 50% increase in h_α and d) a 50% increase in h_β. Contour steps are represented in log scale, such that every 4 steps represents a factor of 10 change in density. The solid line represents an equivalent density contour for comparison.

sufficient quantity to rise the C/O ratio above unity, however, remain O-rich (hot bottom burning can turn C-rich stars to O-rich).

At infrared wavelengths emission from the post-AGB objects is dominated by thermal dust emission, and the stellar composition can be determined by the dust emission signatures. O-rich stars for example, have silicate-rich dust that exhibit its own unique features. The Si-O bonds that make up the silicate grains create vibrational transitions which result in two main observable features, one located at $\sim 10\mu$m, the other at 20μm. The ordered structure of the crystalline silicates generally result in more complex and subtle features than their amorphous counterparts. The C-rich giants, on the other-hand, display features unique to the carbonaceous solids, in the case of a crystalline dust structure a 11.3-μm SiC feature. Amorphous carbon or graphite on the other-hand display much more simple, often featureless continuum.

Consideration of the dust properties is necessary for successful modelling of post-AGB environments. Dust species, sizes, structure, temperature and density, for example, all influence greatly the resulting spectral energy distributions and wavelength-dependent intensity distributions. Dust in many environments, however, cannot be so easily defined. Firstly, numerous dust species exist: common types include olivine or pyroxene silicates, and carbonaceous forms such as polycyclic aramotic hydrocarbons (PAHs) or complex organic compounds (an image of a typical crystalline olivine dust particle is presented in Figure 2.16). Second, the dust can often exist as a composite of a number of such dust species. Ultimately, dust type is an important consideration in RT models.

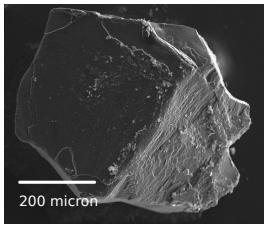

Figure 2.16: Crystalline olivine dust particle from Timmerman et al. (2015).

2.5.2.3 Opacities

The effect of dusty media in a radiative transfer context can be complex. For example, to fully describe the interaction one is in fact required to solve Maxwell's equations both internal to, and external of each individual dust grain, whose geometry, structure, etc must be accounted for. Fortunately, simplifications can be made. Yet, the dependence on the light's wavelength, the particle size and shape, and the dust species remains non-trivial.

Following interaction with gas and dust, radiation is either scattered or absorbed. Interaction with a transparent particle for example, will lead to photon deflection as determined by the medium's index of refraction. On the other-hand, the interaction with a non-transparent solid will result in absorption, ultimately heating the particle. A grain's absorption and emission properties are qualitatively represented by their absorption and emission coefficients. It is not difficult to realise why such interactions become complicated in a RT situation, the thermal emission from the newly heated grain, for example must be accounted for.

The difficulties of RT modelling in dusty environments are further compounded as complex dependencies arise between the particle's size a, and the photon's wavelength. Photon-gas/dust interaction is generally considered in three regimes, the first is small particle size relative to the wavelength (i.e. $\lambda \gg 2\pi a$). This arrangement is known as the Rayleigh scattering regime, the result is that the shorter light wavelengths are more efficiently scattered. In the RT context, this system of scattering can be easily approximated, and simulated. However, as the grain size increases ($\lambda \simeq 2\pi a$), more complex interactions arise, and a complete description requires Maxwell's equations to be solved fully. The third regime, sometimes known as the geometric optics regime, occurs when the photons interact with large grains (i.e. $\lambda \ll 2\pi a$), this too can be difficult to simulate. Fortunately, computationally-efficient approximate solutions can be found when treating dust particles as spherical (or cylindrical or elliptical) grains. Mie theory (Mie, 1908) is a statistical approach that provides a series approximations to Maxwell's equations in the case of homogeneous spherical particles. However, the geometric simplification can result in significant differences in the resulting absorption and scattering coefficients. The statistical approaches, however, arise out of computational necessity. Alternative statistical approaches to Mie theory exist, but Mie theory remains a common approximation method, in part due to its simplicity and ability in handling the most difficult interaction regime when $\lambda \simeq 2\pi a$. However, in the large grain case ($\lambda \ll 2\pi a$), better alternatives exist.

To compute the absorption and scattering coefficients of a dust species, we rely on the DIANA opacity code (Woitke et al., 2016) based on third party software of Toon & Ackerman (1981). Coefficients need to be determined for each dust species from lab-derived refractive index values and cross sections. In this thesis we use the amorphous silicate dust (astronomical silicates) of Weingartner & Draine (2001), the crystalline silicates of Jaeger et al. (1994), and unless otherwise mentioned the amorphous carbon dust grains of Hanner (1988). We do not consider individual dust particles, but approximate a distribution of grain sizes according to the MRN distribution law (Mathis et al., 1977). Hence we are required to define a minimum and maximum grain size ($a_{\rm min}$ and $a_{\rm max}$, respectively) and a dust size power law index ($a_{\rm pow}$), which defines the grain size distribution i.e. $n(a) \propto a^{-a_{\rm pow}}$. Typical grain size in AGB environments are of the order 0.01-5μm, however larger

grains, of the order of millimetres have been adopted, following for instance the ALMA observation of the Boomerang PPN (Sahai et al., 2013), or the the disc surrounding PPN M 1-92 Murakawa et al. (2010).

We provide absorption coefficients for amorphous silicates as a function of a number of MRN parameters in Figure 2.17. There we see that as the grain distribution a_{pow} is increased, the opacities increase. When varying a_{min} we see changes in the short wavelength opacities: higher values reduce opacity at shorter wavelengths in addition to suppressing the 10μm and 20μm silicate features. The opacity changes in the a_{max} case show us that the opacities reduce almost universally across the spectrum as a_{max} increases. This is a result of a_{max} acting in a similar fashion to a_{pow} as the ratio of small to large grains is very high.

The relative featurelessness of carbon can be seen in comparison to amorphous silicates. These outcomes agree with (Woitke et al., 2016), who in a similar fashion present opacity tables in the case of Dorschner et al. (1995) silicates. We adopt this dust in the construction of a post-AGB disc,[5] with similar variation in the MRN parameters we present the resulting model's SED and visibilities in Figure 2.18 and 2.19 respectively.

In the case of our post-AGB environment we see that the SED is reduced as a_{min} is increased in addition to the loss of the silicate features. The effect on the visibility shows us that as the a_{min} is increased the object becomes smaller. This is similarly seen as a_{max} is increased, but emphasised between 1 and $\sim 10\mu$m. While the effect of the maximum grain size on the SED has the larger grain size display a decrease in flux at lower wavelengths, with more subtle changes seen beyond $\sim 40\mu$m. a_{pow} shows very consistent changes across both the spectrum and visibility curves, with higher values resulting in higher fluxes, but lower spatial dimensions. The carbon and silicate comparison shows contrasting distributions for both the SED and visibility.

[5] The input parameters are those used in the synthetic test object in Section 3.4, i.e. Table 3.2.

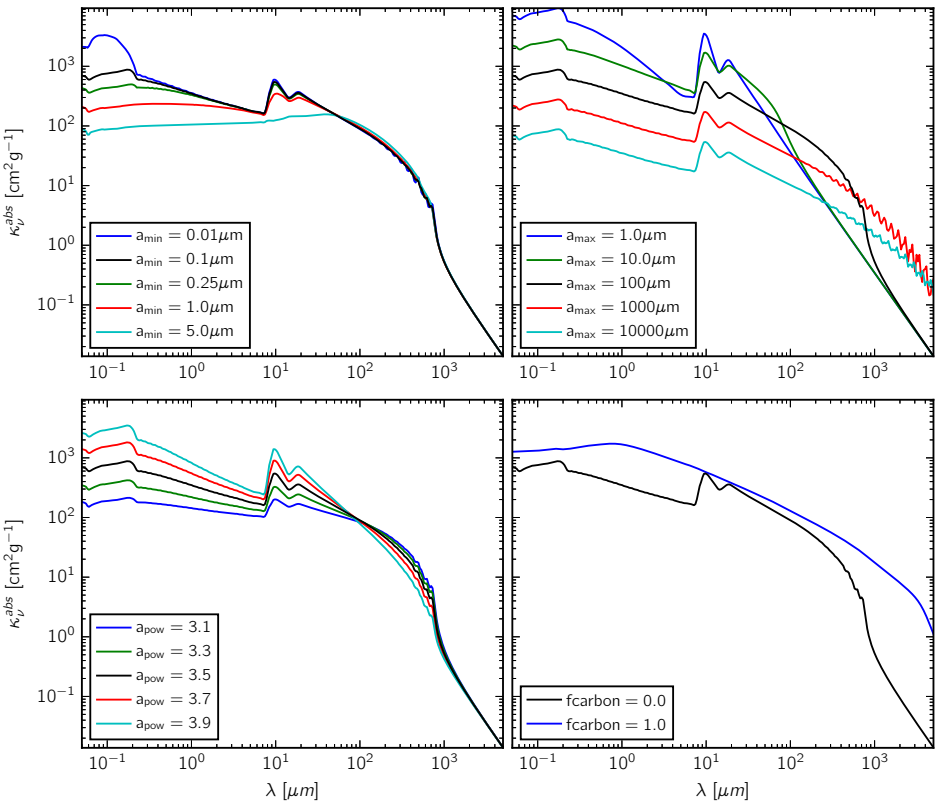

Figure 2.17: Opacity functions for the Weingartner & Draine (2001) amorphous silicates, as a function of the MRN parameters. In addition to the amorphous carbon of Zubko et al. (1996). For comparison purposes, the black line remains consistent between plots.

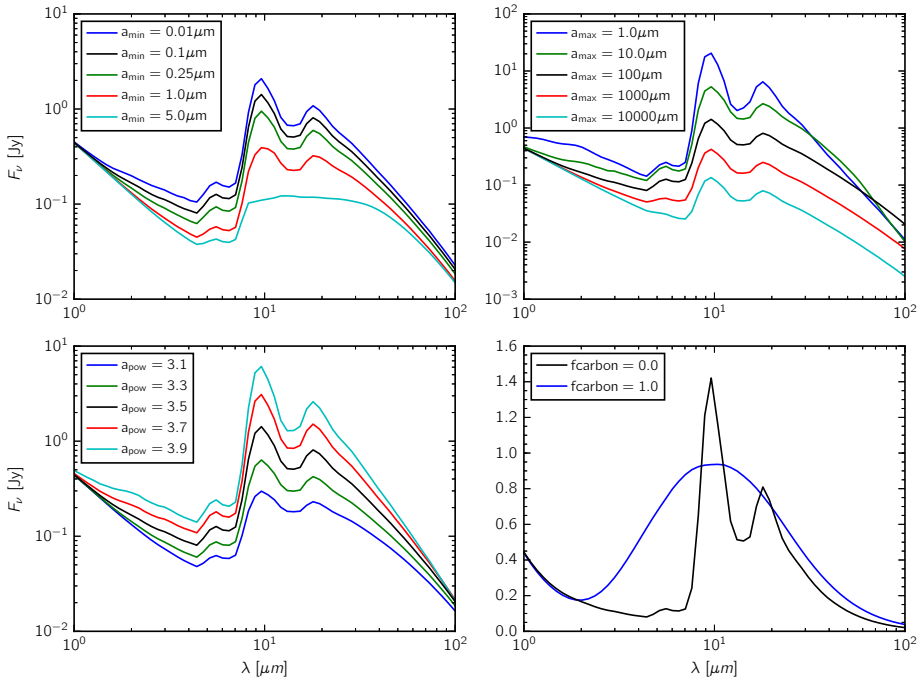

Figure 2.18: Spectral energy functions as a function of MRN parameters, for the amorphous silicates of Weingartner & Draine (2001) and amorphous carbon of Zubko et al. (1996). For comparison purposes, the black line remains consistent between plots.

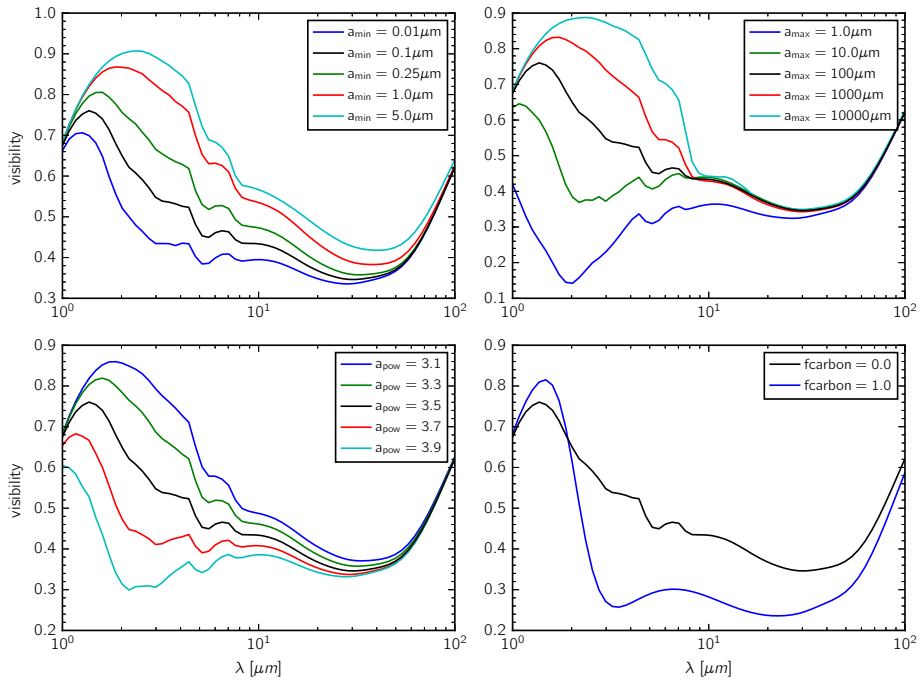

Figure 2.19: Visibility as a function of MRN parameters. For comparison purposes, the black line remains consistent between plots.

Chapter 3

Genetic Algorithm Driven RADiative transfer (GADRAD) code

"The solutions all are simple – after you have arrived at them. But they're simple only when you know already what they are."

R.M. Pirsig – 1974

Material in this chapter is based on an article submitted to MNRAS Apr. 2017. Macdonald D., De Marco O., Lagadec E., Ma J., Chesneau O.

In this chapter we present GADRAD, a Python module that adopts a search heuristic in the form of numerous genetic algorithms to efficiently model post-AGB disc environments. GADRAD systematically constructs the multi-dimensional parameter probability density functions that arise from the fitting of radiative transfer and geometric models to optical interferometric data products. The result provides unbiased descriptions, for a given model class, of an object's potential morphology, component luminosities and temperatures, dust composition, disc density profiles and mass. Correlation in the estimated environment parameters as well as potential degeneracies are revealed. Distributions of the estimated parameters provide insight into the shaping processes that may occur in the transition from the post-Asymptotic Giant Branch to the planetary nebula phase.

In Section 3.1 we briefly discuss the need for applying a mathematical optimisation method in the search for good numerical model representation of optical interferometric data products. In Section 3.2 we introduce the theoretical underpinnings of the genetic algorithm as a search heuristic. In Section 3.3 we test genetic algorithm convergence on a standard test function. Finally (Section 3.4) we proceed to test radiative transfer parameter recovery on simulated artificial data products of a typical post-AGB environment.

3.1 The case for mathematical optimisation methods in numerical model reconstruction

The discs of interest to this thesis are those large enough to be detected by the high spatial resolution of optical interferometers (a few milliarcseconds). They are not the smaller accretion discs that sometimes form around one of the stars in a close binary system. These larger (AU-scale), cool and dusty discs, likely form due to a binary interaction process during the AGB and may play an active role in shaping the subsequent outflows. Alternatively they may not directly play a role in shaping the outflow, but may form as a byproduct of the shaping mechanism: for example, jets may inflate lobes that in turn compress material on the equatorial plane forming large disc-like structures (Akashi & Soker, 2008). The disc's parameters, such as its geometry, orientation, mass and chemical makeup (i.e., Balick & Frank, 2002) may give us enough information to determine their origin and whether the disc played an active role in shaping the nebula or if it was itself an outcome of the nebula formation process (e.g., Bright, 2013).

However, the study of these discs remains challenging. As addressed in the previous chapter, direct observation is not typically achievable, with even the closest objects remaining near the limit of current instruments' spatial resolution. The required resolution, however, can be obtained via optical interferometric techniques, but, as discussed, such options present their own challenges. For example, the number of interferometric measurements necessary for full image reconstruction is presently unfeasible, because post-AGB discs tend to be far and faint and large telescopes are typically required, limiting the observing time that can be dedicated to individual objects.

In the more complex objects, numerical modelling via radiative transfer (RT) has become common practise. The models, are typically dependent on numerous input parameters. The simplest environments, for example, can often require parameters describing the stellar properties such as luminosity and temperature, disc density profiles and mass, as well as dust composition. Modelling the discs thus becomes a problem of optimisation, with potentially complex and non-linear dependencies between the parameters. This problem is all too often solved in an *ad-hoc*, non-systematic fashion, leaving the possibility that better global solutions exist (e.g., Chesneau et al., 2007b; Lykou et al., 2011; Bright et al., 2012; Bright, 2013). Human parameter choice for example, often considers only small fractions of parameter space. The level of potential under-sampling is evident when considering the number of models required to sample an n-dimensional space. For example, consider just a sparsely sampled brute-force approach, with just four models sampling a two-dimensional space (i.e., two values per parameter, with a single model sampling each quadrant). To similarly sample the *quadrants* of an n dimensional space, 2^n models are necessary. In the case of RT models of post-AGB objects, where models can require 16 parameters, this (very low) level of sampling would require upwards of 65 000 models! Reducing parameter space by fixing variables to literature values reduces the number of models, but this often further degrades the final solutions as this form of parameter limitation necessitates *a priori* sampling (and with incorrect parameter adoption) introduces bias. Furthermore, the χ^2 fitting approach adopted in these studies only give little indication of whether a given parameter set is better than another, they do not for instance, provide insight into the underlying parameter interaction,

nor indicate the range of acceptable parameter values that represent good model solutions.

Determining RT models solutions that result in the interferometric data products observed, is an ill-posed, general inverse type problem. It is an inverse type problem as we have to transform the interferometric data products to a set of model parameters, as opposed to the more commonly found forward problem, were the transformation direction is reversed (i.e., given the model parameters, calculate the result). As with many inverse type problems, our problem is also ill-posed, for example the parameters we wish to determine are poorly constrained by the data and many potential solutions exist. The number of parameters available in constructing a RT model though finite, can be numerous, and there is likely non-uniqueness in the solution space (especially when considering the stochastic noise introduced to each model as a result of Monte-Carlo RT simulation). Model approximations need to be made, where the model class adopted hopefully generalises well enough to represent the main characteristic features of the observed object. In determining ranges of acceptable parameter values from such a model, we explore the objective function (the function that maps the parameter input values to the resulting model's 'fitness'). Minimisation of the objective function results in good model representations of the object (known as a *quasi-solution*), the multi-dimensional non-linear nature of the function however, typically requires the application of robust optimisation techniques. This optimisation task was approached with the use of the genetic algorithm, which form the basis of `GADRAD` (Genetic Algorithm Driven RADiative transfer).

3.2 The genetic algorithm

3.2.1 Biological evolutionary processes

The genetic algorithm (GA) is an evolutionary search heuristic inspired by concepts of natural selection and biological evolution. Its goal is the minimisation of the objective function, which is the function that maps a number of input parameter values to the output value one wishes to minimise. In our case the parameters are those that describe the post-AGB model environment, and the objective function is the resulting *fitness landscape* as it relates to the interferometric data products. The global minimum of the objective function represents a good solution, in this instance is a quasi-solution, which is a solution that represents the optimum (or near optimum) model candidate for a given model class. In cases where model overfitting is avoided, a good representation of the observed interferometric data products leads to a model environment that characterises the true environment. Optimising the objective function is a challenging task, as complex parameter interactions can occur over a multi-dimensional space.

In the attempt of determining the global minimum of a given model class we turn to the processes of biological evolution for inspiration. Biological evolution for example does a remarkable job at optimising its extremely complex objective function. In a biological setting the objective function can be thought of as the resulting *fitness* from the input of the parameters which constitute the genetic structure of the chromosome (where the parameters are the genes that makeup the chromosome). The search domain is truly enormous, as it represents all potential

lifeforms described by a chromosome of any possible length. The objective function, or *fitness landscape*, harbours the fittest individuals in the highest regions of the terrain, and the non-successful organisms located in the the landscape's minima (e.g., Grant, 1985; Haupt & Haupt, 2004). In this description the evolutionary process is the movement of individuals to higher levels of the fitness landscape, thus optimising (maximising in this case) the objective function with each successive generation. Despite the complex solutions that can arise genetically, and the dynamic nature of the fitness surface (for example evolution considers the interaction of individuals on generational timescales), the evolutionary process seemingly depends on relatively simple rules which can be implemented computationally in a relatively straightforward manner.

By encoding these evolutionary concepts into a computational setting we can reproduce, even if crudely, the optimisation process seen in genetic evolution. This is the task of the GA. First to be considered is a population of candidate solutions (inter-breeding individuals) found in biological evolution. Populations of solutions provides a unique depth and breadth in the exploration of the objective function. The task is then to understand how genetic material is passed on to the next generation. At its most simple, the parent of a unicellular organism, for example, will pass on genetic information to its offspring asexually by replication, or cell division, in which the chromosome is simply duplicated gene for gene. Such a process, without gene mutation or natural selection, will see an isolated population of such organisms result in what is known as a Hardy-Weinberg equilibrium, in which evolution (optimisation) does not occur.[1] At the genetic level, a Hardy-Weinberg equilibrium, sees the the genotype frequency (i.e. number of individuals in the population with a specific genotype, or chromosome), and allele frequency (where the allele is the gene values that makeup the chromosome) remain constant over a the generations. However, a population exposed to selection, recombination and mutation allows for the introduction of new genotype and allele forms to the next generation, and evolution proceeds through this genetic interaction.

The evolutionary process becomes apparent when considering the more complex, multicellular organisms, in which sex (genetic recombination), acts to increase the genetic variation of the following generation. Recombination allows, through a process known as chromosomal crossover, the exchange of genetic material between parents, such that the inherited genotype can be unique to that of both parents. Recombination thus allows not only the hereditary traits of fit individuals be passed on to next generation, but also acts to introduce potentially fit and novel genotype combinations to future gene pools. This however one of many mechanisms available for introducing genetic variation, mutation, typically a spontaneous or error induced change of an individual gene of the chromosome may also occur. Other mechanisms that make up the evolutionary process include: genetic drift, in which the genotype (chromosomal makeup) of a species is changed by a random, typically external process, that would favour the "lucky" individuals as opposed to the fittest ones. Gene flow (migration) is another such process, in which genetic material is carried from one group of individuals to another. However, in this thesis we rely on the the three genetic processes that constitute the canonical genetic algorithm: selection, recombination and mutation. By encoding these evolutionary concepts into a computational setting we can reproduce the

[1] The Hardy-Weinberg condition additionally requires: an infinitely large population, all individuals of the population to breed with random selection, and the number of offspring is equal for all population members.

optimisation process seen in genetic evolution. This is the task of the GA, which is the topic of the following section.

3.2.2 The canonical GA

The theoretical framework of the GA was developed by John Holland (1975). Mathematical optimisation methods of the time were typically task specific, Holland, with the development of the GA, set about developing a more universally applicable optimisation technique. The innovation came in the form of the genetic based operators that acted to converge a population of candidate solutions. The technique was later popularised in collaboration with a student (David Goldberg, 1989). A population based optimisation approach, as introduced by Holland (1975), has defined a broader category of evolutionary based algorithms, and has been the inspiration for many other optimisation techniques. In this section we introduce what is sometimes known as the canonical GA, the algorithm as first introduced by Holland. The algorithm is known to exhibit a number of qualities and advantages with regard to mathematical optimisation that include:

- The ability to handle a large number of variables.
- Its suitability to highly, complex non-linear cost surfaces.
- The ability to handle multiple local optima (multimodal surfaces).
- The handling of noisy cost surfaces.
- Provides a broad sampling of parameter space.
- Returns a population of optimum solutions, i.e. as opposed to a single best fit solution.
- Does not require calculation of derivatives.
- Well suited to parallel computational facilities.
- Easily implemented computationally.
- Ability to handle both continuous and discrete variables.
- Broadly applicable to many areas of research.

The versatility of the GA is well known, take for example just a small selection of scientific areas in which the GA (and its numerous forms) has been successfully applied: Astronomy, physics, chemistry, molecular biology, chemical engineering, medicine, climatology and the social sciences (e.g., Charbonneau, 1995; Deaven & Ho, 1995; Hibbert, 1993; Levin, 1995; Hanagandi & Nikolaou, 1995; Dybowski et al., 1996; Li et al., 2010; Hosseinzadeh & Roghanian, 2012, respectively). The GA has also been used for tasks including: timetabling and scheduling, design, quality control, classification, image processing, automatic programming, machine learning and code breaking.

The GA is also found to work well in many situations, however, as common to many search heuristics, it is likely that a more efficient and effective algorithm exists for the specific problem at hand. For example, derivative-based search methods are much more efficient in low dimensional analytical function optimisation applications. One also has to consider the fitness evaluation cost. For example, a task that requires the computation of intensive simulations for each of the potential thousands (or hundreds of thousands) of candidate solutions (such as radiative transfer models), may be outperformed by more specific calculus-based methods, in which the objective function can instead be derived. However, in most problems

the objective function is not so well understood, and form of search heuristics are often required. Heuristics, however, often provide no guarantee the global maximum or minimum has been found. The question then becomes which optimisation algorithm to use. Many non-deterministic algorithms have arisen and been applied successfully, and may be well suited to the problem addressed in this thesis, e.g., memetic algorithms (Moscato et al., 1989), swarm algorithms such as Ant-colony optimisation (Dorigo et al., 1996), particle swarm optimisation (Kennedy & Eberhart, 1995), simulated annealing (Kirkpatrick et al., 1983), evolutionary algorithms, hill climbing algorithms (e.g., Goldfeld et al., 1966).

The GA was, however, chosen in this thesis for its robustness in the handling of complex and un-explored search space. Additionally, the GA provides a number of 'tuning' parameters which can be customised to the problem at hand. In future development, the algorithm also has the potential of being combined with with other search algorithms to form what is known as the hybrid GAs. Importantly, the GA has also been found to perform well in determining solutions from noisy objective functions, a situation that may arise from the stochastic nature of the radiative transfer models performed. There is also a case to be made for the successful application of GAs to radiative transfer codes in astronomical settings (Baier et al., 2010; De Geyter et al., 2013; Menu et al., 2014). De Geyter et al. (2013), for example, upon comparing the GA to the Levenberg-Marquardt method and Downhill simplex method (Nelder & Mead, 1965), found the GA to perform well, and in general, out-perform the other methods in convergence to the the global minima. However, no formal algorithm comparison tests were completed. We should however consider some of the disadvantages that may arise when adopting a GA:

- The GA is non-deterministic, such that there is no guarantee of finding the global minima. However, this is common to many such algorithms that do not rely on brute force approaches.
- The stochastic nature of the algorithm, for example it is very sensitive to the initial population, i.e., non-reproducible.
- Generally requires a long training time, convergence time is thus limited. Large populations are required etc.
- Requires parameter 'tuning'. The solution quality is thus not only dependent on the problem size, but the chosen mutation rate, crossover rate, and choice of fitness, choice of selection operator type, elitism etc. Refinements are typically made on a trial and error basis, and are generally found to be problem specific.

For a more in depth introduction and overview of the GA, and its numerous forms, see for example Holland (1975); Goldberg (1989); Davis (1991); Whitley (1994) and Mitchell (1998).

3.2.3 The GA operators and process

In this section we will introduce the fundamental genetic operators of the canonical GA as introduced by Holland (1975), and develop the GA process. The genetic algorithm, at its core, relies on three genetic operators: selection, crossover and mutation. The algorithm proceeds as follows:

(i) Initialisation. Initialise the population, that is create $n_{\rm pop}$ parameter sets, known as chromosomes, by selecting random values from within given parameter domain ranges. The parameters in this instance will describe the post-AGB environment, disc scale height, inner-disc radius, etc.

(ii) Evaluation. Evaluate the quality (*fitness*) of the parameter sets that make up the population, based on a goodness of fit criteria (such as χ^2).

(iii) Selection. Select individuals (sets of parameters) to *breed* from the given population.

(iv) Recombination. Combine (*breed*) individuals to form the next generation.

(v) Mutation. Randomly adjust given parameters of the individuals.

(vi) Repeat steps (ii)-(v) until termination criterion has been met, at which point the solution set is obtained. Each iteration is known as a generation.

The initial step (step i) taken in the GA is to produce a population of parameter sets. These parameter sets are known as candidate solutions, or *chromosomes*. The parameter values that make up the parameter sets are known as *genes*. For example, a three-dimensional optimisation problem would require a population ($n_{\rm pop}$) of chromosomes with just three genes. This could be a fit with only 3 free parameters, say, stellar temperature, disc's inner-radius and its scale height, where say, 100 combinations of these 3 parameters are chosen as the initial population, the allowable parameter values (gene values) are known as *alleles*.

A number of methods exists in the creation of the initial population, such as random sampling, uniform sampling and complementary sampling. In `GADRAD` we adopt random sampling positions, in which allele values are selected from a defined search range, resulting in the occupation of $n_{\rm pop}$ random positions located on the objective function. We select values based on a uniform flat sampling distribution i.e.,

$$P(x) = \begin{cases} \frac{1}{b-a}, & \text{where } a \leq x \leq b \\ 0, & \text{otherwise,} \end{cases} \tag{3.1}$$

where a and b are the domain limits of each parameter (allele limit), based upon literature values where available.

Following initialisation we evaluate the candidate solution (step ii). Determining the fitness of a candidate solution is generally the most computationally expensive task (here it is the radiative transfer simulation). How the fitness is evaluated is also very important, a fitness function that does not relate directly to the objective function will result in poor solutions, for example. We adopt the following weighted function as a fitness measure:

$$\Theta = \frac{w_1}{N_1}\sum_{i_1=1}^{N_1}\left(\frac{x_{i_1}-\mu_{i_1}}{\delta_{i_1}}\right)^2 + \frac{w_2}{N_2}\sum_{i_2=1}^{N_2}\left(\frac{x_{i_2}-\mu_{i_2}}{\delta_{i_2}}\right)^2 + \cdots \tag{3.2}$$

$$+\frac{w_n}{N_n}\sum_{i_n=1}^{N_n}\left(\frac{x_{i_n}-\mu_{i_n}}{\delta_{i_n}}\right)^2, \tag{3.3}$$

where x_i is the model value as obtained by the RT simulation, μ_i is the observed data product value and δ_i the error or uncertainty in the observed value. The

function is the sum of the data products (i.e. the visibility, spectrum, etc.), where $w_i \geq 0$ is the assigned data product weight. If, for example, the spectrum was known to better describe the object than the visibilities, one would set $w_{\rm sed} > w_{\rm visibility}$.

Once the population has been evaluated, we apply the first of the GA operators (step iii). The selection operator acts to determine the candidate solutions (parameter solutions) to be kept, and those that will be discarded. It is thus the job of the selection operator to mimic natural selection processes in which the fitter individuals are kept in the population and allowed to breed. A good selection operator will however, not remove unfit solutions from the gene pool entirely. For example fit offspring have been shown to not necessarily result from fit parents. However, a selection operator that does not favour the fit chromosomes over the un-fit solutions to some degree, may provide premature, and potentially local minima convergence (or no convergence at all). Ultimately, selection acts under the notion that fit solutions will create better ones. Selection operators are further discussed in Section 3.2.3.1.

Once the candidate solutions have been selected, the second operator is introduced (step iv). The task of the crossover operator (or recombination operator) is to *breed* the selected solutions to create offspring. This is done by exchanging parameter values (alleles) between parents. The crossover operator introduces new genotype material to the population. In this way the genetic building blocks of fit members of a generation can be passed onto the next. Crossover occurs with probability p_c, thus $(1 - p_c)n_{\rm pop}$ members of a given generation will remain unmodified, and pass their genetic material intact on to the next stage of the GA process. The crossover operator is further discussed in Section 3.2.3.2.

The final genetic operator to apply is the mutation operator (step v). The task of the mutation operator is to introduce new allele values into the population. The mutation operator prevents a loss of diversity (Holland, 1975). Without mutation, for example, an allele value may come to dominate the population, and once such a state is reached, no new allele values can be introduced to following generations. This is particularly detrimental to algorithm convergence if good allele values weren't introduced into the original population. Without mutation, solutions can potentially converge to, and be trapped in, local minimum. It is with the introduction of new genetic building blocks that the genetic structures can be disturbed, and ultimately prevent local minima convergence. The mutation operator is generally applied by giving each gene a low probability (p_m; typically between 0.001 and 0.10) of obtaining a new allele value. The mutation operator is further discussed in Section 3.2.3.3.

3.2.3.1 Selection

The canonical GA of Holland adopted a fitness-proportionate selection operator, in which the more fit candidate solution benefited from a higher selection chance than that of a less fit candidate. This type of selection operator has come to be known as roulette wheel sampling. Three selection operators are briefly discussed below (see also Bäck, 1994; Hancock, 1995; Mitchell, 1998).

Roulette wheel selection The process behind roulette wheel selection, is easily visualised when considering the casino's roulette wheel, in which each candidate occupies a portion of real-estate on the wheel. Being a fitness-proportionate operator, the area occupied by the parent is scaled to be directly representative of their fitness, with the fittest chromosome controlling the largest area. The wheel is spun n_{pop} times, and with each spin, a candidate solution is selected to become a parent for the next generation.

Rank selection Rank selection, as its name indicates, uses a ranking approach to select the parent population pool. Rank selection does not rely on any scaling of the candidate solution fitness's, but ranks (linearly) the chromosomes from fittest to least fit. The approach was proposed by Baker (1985), in an attempt to reduce premature convergence. The assumption was that by not giving a small set of very fit individuals significant ownership of the offspring, early convergence could be avoided. As Mitchell (1998) notes, however, it may be valuable in some cases to have knowledge of the large fitness discrepancies between fit and unfit individuals.

Tournament selection Tournament selection is based on rank selection, but the ranking exists on a smaller scale. In tournament selection two or more individuals are picked at random from the population. The individuals compete for selection, with a selection bias favouring the fittest of the tournament group. All individuals from the tournament are returned to the population and the selection continues until n_{pop} individuals have been selected. Tournament selection works well for large populations when sorting the entire population is computationally intensive. In this thesis we adopt the tournament selection based operator.

Elitism Elitism, as introduced by DeJong (1975), is not a global selection operator, but a process that aims to keep already fit solutions in the population. Losing fit solutions to the following crossover and mutation operators, for example, can be disadvantageous. By selecting a small percentage of the fittest solutions to remain in the gene pool, algorithm efficiency has, in many cases, been shown to improve.

3.2.3.2 The crossover operator

The crossover operator is considered by many as the operator that uniquely defines the GA. Crossover attempts to simulate the genetic recombination in single-chromosome organisms. Genetic material is exchanged between two (or more) parents, by switching allele values. In this way the genetic building blocks of fit members of a generation can be passed onto the next. As mentioned, crossover occurs with probability p_c, thus $(1 - p_c)n_{\text{pop}}$ members of a given generation will remain unmodified, and pass their genetic material intact on to the next stage of the GA process. The crossover operator can also sometimes be avoided entirely (i.e., with $p_c = 0$), a case known as the asexual GA (e.g., Cantó et al., 2009). In the case of floating point variables the asexual GA has been suggested by some authors to be an applicable algorithm simplification (e.g., Golub, 1996).

[2]

K-Point crossover K-point crossover (Holland, 1975) is perhaps the most common form of crossover, where $K=1$ is known as single-point crossover, and $K=2$ two-point crossover. In K-point crossover parental genotypes are passed to the following generations by exchanging allele values between parents, before and after a randomly selected crossover (locii) point(s). For instance, with single point crossover ($K = 1$), two parents each with six genes, and the following allele values 101010 and 111111, would result in following offspring 101011 and 111110 (if the locii point was between the fourth and fifth gene). Single point crossover is illustrated in Figure 3.2.

Uniform crossover Uniform crossover exchanges individual alleles between parents with some probability (typically 0.5). Uniform crossover is considered a more exploratory form of crossover than more traditional single-point or two-point crossover forms. This is due to the opportunity for parents to contribute individual genes to the offspring. However, by destroying the genetic segments of the parents, fit genotype forms may become lost.

Three parent crossover In this form of crossover the offspring is derived from three parents (i.e., Eiben et al., 1994). In three parent crossover the allele values are compared between the first two parents, and the values that are common to each parent are passed directly to the child. The remaining values that are make up the offspring chromosome (i.e. the allele values not shared) are taken from the third parent. For instance, three parents with the following structure $\text{parent}_1 = 101010$, $\text{parent}_2 = 110110$ and $\text{parent}_3 = 000000$, would result in the following offspring structure: 100010.

3.2.3.3 The mutation operator

As mentioned the mutation operator is generally applied by giving each gene a low chance (typically between 0.001 and 0.10) of obtaining a new allele value. The choice of value can be selected from a uniform distribution, or it can be determined from a normal distribution about the original allele value. Dynamic mutation rates can also be adopted, for example the variance of the normal distribution can be set as a function of generation, such that early populations are given a large variance distribution which encourages parameter exploration, while in the latter generations, narrower searches are likely preferred (i.e., when nearing the global minima). Similar ideas form the basis for the hybrid GAs, in which the GA is combined with local optimiser algorithms. The local optimiser is used when in the vicinity near the global minimum. Numerous hybrid GAs forms have been developed since Holland first introduced his algorithm. Hybrid GAs have for example combined basic ideas of the GA with particle swarm optimisers (Kao & Zahara, 2008), and simulated annealing (Thangiah et al., 1994). In this work however, reasonable success was found in the adoption of the canonical algorithm

[2] In the case of float variables, which is yours, some authors claim that the crossover operator can be avoided or that is can be used on the basis of exponential coding of the genes: http://zemris.fer.hr/ golub/clanci/iti96.pdf

with dynamic mutation. Normal (Gaussian) dynamic mutation is introduced in the following manner:

$$x_j^{'} = x_j + \sigma N_j, \tag{3.4}$$

where x_j is the original value, $x_j^{'}$ is the mutated value, σ the standard deviation and N_j the normal distribution. Cauchy distributions can be implemented in a similar manner (i.e. Yao et al., 1999)

$$x_j^{'} = x_j + \sigma_j C_j. \tag{3.5}$$

Where C_j is defined as

$$P(\zeta) = \frac{1}{\pi}\frac{t}{t^2 + \zeta^2}, \tag{3.6}$$

where t is the scaling parameter (with $t > 0$). As can be seen in in Figure 3.1, the Cauchy distribution (with $t = 1$) introduces a wider mutation scale than the normal distribution, immunising one somewhat against early local convergence.

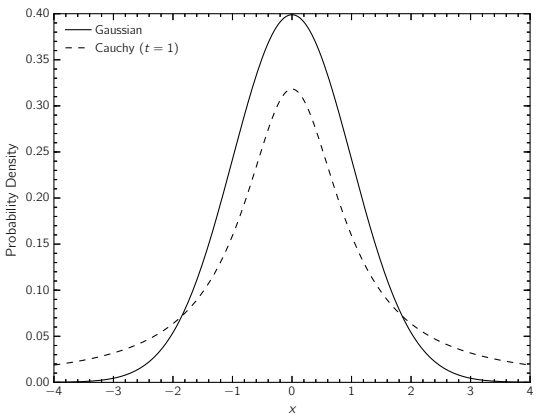

Figure 3.1: Cauchy function The dotted line represent the Cauchy function with $t = 1$, while the solid line represents the normal distribution. The wide tails of the Cauchy distribution prevent early convergence when guiding mutation convergence in GAs.

By iterating the three genetic operators we form GA convergence. The solution set is obtained once the termination criteria has been met (step vi), whether based on a specific fitness criteria or on a number of iterations (generations; n_{gen}). A good GA ultimately relies on a correctly balanced contribution from the selection, crossover and mutation operators. Despite numerous studies, seeking an optimum balance seems to remain problem specific. It should be noted, however, that the GA, similar to most other non-brute force techniques, is non-deterministic, such that there is no guarantee that the global minima has been found. The GA is also

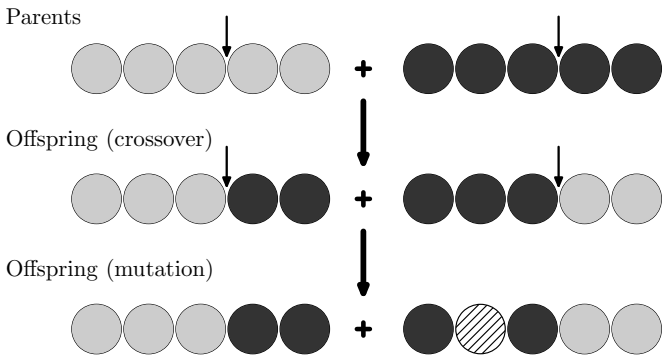

Figure 3.2: Typical process of the GA we represent parent chromosomes in which the allele values (in this instance black and white) are exchanged through K=1 point crossover and mutation to create the offspring.

sensitive to the initial population, such that solution sets are non-reproducible and, as mentioned, parameter *tuning* is necessary, with the solution quality dependent on the types and implementation of the genetic operators.

The population size, for example, has been identified in many instances to alter GA efficiency. For instance, it is generally considered that small population sizes lead to poor solutions, with the trade-off for large populations being computational expense. Refinement of the population size for reasons of efficiency and performance is thus generally considered important. In what is considered the first study on the topic, DeJong (1975) sought to analyse and optimise the GA parameters. In his dissertation, DeJong introduced two GA performance measures. The first, known as the on-line measure, is the average of all costs up to the current generation. By its nature it is a measure that awards algorithm efficiency but penalises deep exploration. The second measure, known as the off-line measure, is defined as the running average of the best cost found for each generation, it is a measure of algorithm performance more tolerant to exploration. DeJong (1975) found that small population sizes improved initial performance, while long-term performance was improved by larger populations. In regard to the GA parameters, DeJong (1975) found that high mutation rates drive good off-line performance while low mutation rates improve on-line performance.

In applying a more thorough search of GA tuning parameters Grefenstette (1986) applied a so-called *meta*-genetic algorithm in which a GA was used to derive the tuning parameters of a second GA with reference to both on-line and off-line performance. It was found that low crossover rates and larger population sizes tended to improve off-line performance, while high crossover rates and smaller populations increased the on-line performance. However, it was noted that good performance in general can be obtained for many instances and ranges of GA tuning parameters. Haupt & Haupt (2004), for example in varying population sizes and mutation rates on test cost surfaces, found the optimum GA operator parameters were problem dependent. They also found for a range of problems the crossover type and rate as well as the method of selection had little impact in terms of overall efficiency. Population size and mutation rates on the other hand were found to heavily influence the algorithms overall ability. It was also found that the type of crossover had little impact overall. These sentiments agree with DeJong

(1975), who indicated that the type of crossover had limited influence overall. Bäck & Schütz (1996) regarded these GA operators as secondary operators, and of little importance.

Following these principles, we develop our own GA, which forms the basis of GADRAD. This algorithm provides seamless interfacing between the Python modules that govern the operation of RADMC-3D. The GA is parallelised to run using the OpenMPI library, with each RT simulation run on a separate computational thread. Following some preliminary results, the GA that drives GADRAD was found to perform best with the adoption of tournament selection, elitism, three-point crossover and dynamic Cauchy mutation. GA tuning parameters were found to be problem specific and are given where relevant.

3.3 Testing GA convergence to an optimisation test function

To determine whether the algorithm is converging efficiently we apply the GA to the Rastrigin function (Rastrigin, 1974). The function is frequently used as a test function for optimisation algorithms due to its many local minima and large search space, its multimodal nature combined with the relatively small contrast between global and local minima make it demanding for any optimisation algorithm (especially more classical, gradient-based optimisation methods). The Rastrigin function also benefits from its ability to be scaled to include as many dimensions as is necessary. Its general form is presented in Equation 3.7, where the global minima occurs at $\mathbf{x} = \mathbf{0}$, with $f(\mathbf{x}) = 0$.

$$f(x) = An + \sum_{i=1}^{n} [x_i^2 - A\cos(2\pi x_i)]. \tag{3.7}$$

We consider the two-dimensional case, with $A = 10$.

$$f(x_1, x_2) = 20 + x_1^2 + x_2^2 - 10(\cos 2\pi x_1 + \cos 2\pi x_2). \tag{3.8}$$

The resulting function is plotted (with $x_i \in [-5.12, 5.12]$) in Figure 3.3. We demonstrate the GA's convergence in this case by plotting the spatial distribution of the individual search results for the given generations with respect to the function's contours in Figure 3.4. The GA was run for $n_{\text{gen}} = 100$ generations with a population of $n_{\text{pop}} = 100$ individuals. In this test we adopt tournament selection, with 2-point crossover (of frequency $p_c = 0.65$), and a mutation rate of $p_m = 0.05$. These operator values where selected to closely match the values as adopted in similar 2-D GA convergence tests carried out by Charbonneau (1995) and De Geyter et al. (2013).

The initial population (Figure 3.4a), is randomly sampled across the search domain. By $n_{\text{gen}} = 25$ (Figure 3.4d) the population can be seen to centre about the global minima. This convergence continues right through to $n_{\text{gen}} = 100$ (Figure 3.4f) at which point we obtain a final result of $(x_1, x_2) = (0.00205, -0.0037)$, with $f(x_1, x_2) = 0.0037$ (where the solution is $f(0, 0) = 0$).

To test the convergence properties more thoroughly we repeat the GA 100 times ($N_{\rm GA} = 100$). We find that the result above is not atypical. After 100 runs we find the average result to be close to the global minima, and with relatively small standard deviation across the solutions, i.e.

$$x_1 = 0.0006 \pm 0.0036,\ x_2 = 0.0004 \pm 0.0032. \tag{3.9}$$

It should be noted that due to the low dimensionality of the function, an increase in the mutation rate was found to improve convergence. We now compare the convergence efficiency of our algorithm with the `Pyevolve` Python package, after 100 such runs, and following the same GA operator parameters, `Pyevolve` obtains a result of

$$x_1 = 0.0001 \pm 0.0048,\ x_2 = -0.0004 \pm 0.0040. \tag{3.10}$$

The similarity is evident, we conclude that our GA is converging in a similar fashion to that of `Pyevolve` in this instance.

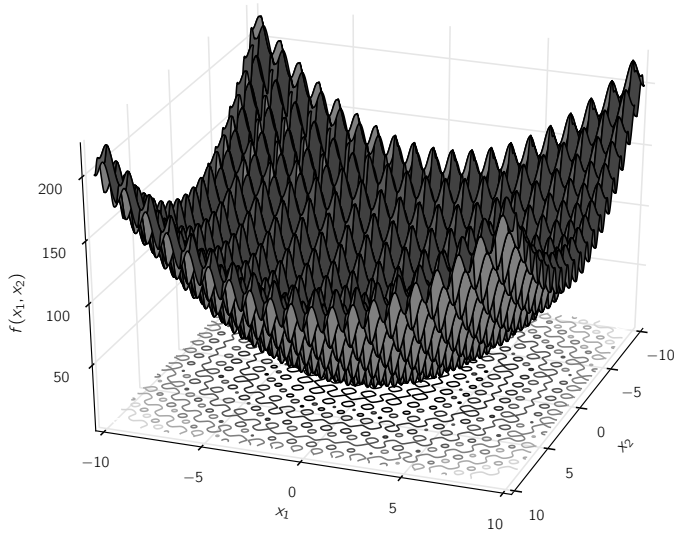

Figure 3.3: The 2-D Rastrigin test function, with A=10 (i.e. Equation 3.8).

3.3.1 Parameter inference

As indicated, the purpose of GADRAD is not simply the determination of good fitting post-AGB disc solutions to the interferometric data products, but the construction of the multi-dimensional parameter probability density functions that arise in the fitting of these solutions (RT models) to the interferometric data. It is with knowledge of these parameter density distributions, that we can begin to constrain the object's physical characteristics in the context of an unbiased parameter space. GADRAD allows us to better explore and understand areas of the objective function of interest (i.e., the areas that return *fit* RT solutions).

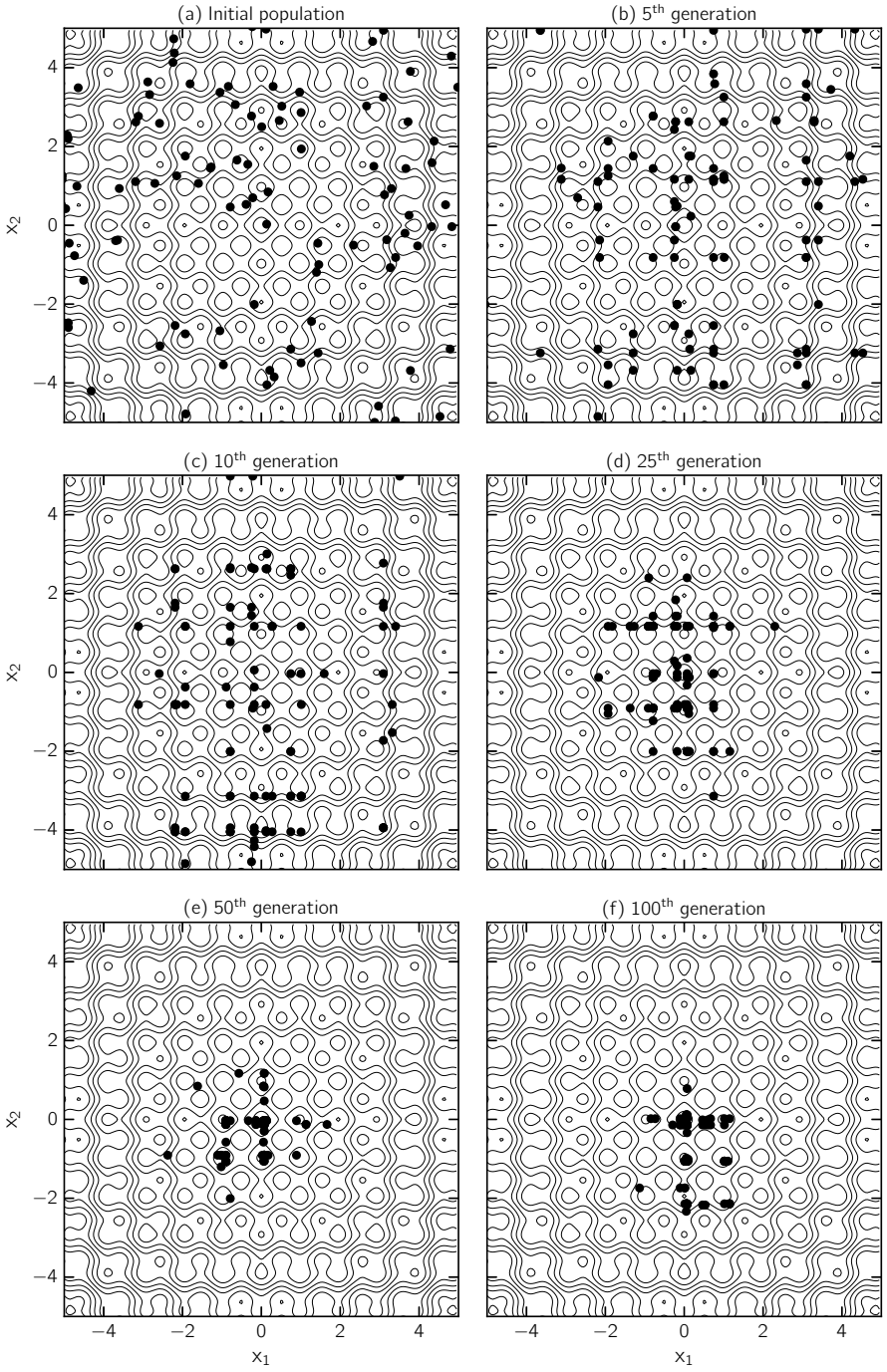

Figure 3.4: Plots of GA convergence for 100 individuals as applied to the 2-D Rastrigin function (Equation 3.8). The initial random population is illustrated in (a) with the generational convergence seen through to the 100^{th} generation (f).

The GADRAD process relies on a number, $N_{\rm GA}$, of independent GAs to search a prescribed regions of parameter space of a given model class. The fittest solution from each GA provides a single independent, but stochastic, probe of the underlying objective function. When these solutions are considered collectively we gain some understanding of the objective function (hopefully) near the global minimum.

To represent our parameter probability density function we adopt a kernel density estimation (KDE), which similar to the frequency histogram, is an estimator to the density function of a given variable. KDE overcomes two major shortcomings of the common histogram (i) the ability to produce a continuous and differentiable function, and (ii) forgives the requirement of defining the histogram bin edge.

The resultant parameter probability density function is a representation of good areas of parameter determined by our search heuristic. It is hence the probability density function that best illustrated our understanding, however, this is not always practical and a description of the parameter density, summarised as a best estimate or confidence interval is sometimes necessary. This is known as point and interval estimation, and it can be done in a number of ways, for example we can calculate the posterior mean, which minimises the mean squared error, i.e.,

$$\textsc{mmse}(\hat{\theta}) = \int (\theta - \hat{\theta})^2 \; g(\theta|y_1, ..., y_n) d\theta, \tag{3.11}$$

where $\hat{\theta}$ is the estimator, θ the true value and $g(\theta|y_1, ..., y_n)d\theta$ is the posterior density i.e.

$$\int_{-\infty}^{\infty} g(\theta|y_1, ..., y_n) d\theta = 1. \tag{3.12}$$

In GADRAD, however, we adopt the posterior median absolute deviation, the value that minimises the median absolute error, i.e.

$$\textsc{mmae}(\hat{\theta}) = \int |\theta - \hat{\theta}| \; g(\theta|y_1, ..., y_n) d\theta. \tag{3.13}$$

The posterior median occurs at the mid-point of the posterior distribution (i.e. half the distribution located above the point, while half are located below), to calculate the posterior median $\tilde{\theta}$, we solve

$$\int_{-\infty}^{\tilde{\theta}} g(\theta|y_1, ..., y_n) d\theta = 0.5. \tag{3.14}$$

In addition to our point estimate, we can select values from the the underlying probability density function that represent confidence intervals. The interval extremes are determined by solving in a similar fashion that above, but for the the 95% confidence interval, i.e., setting equation 3.14 to 0.025 and 0.975. However, in some instances the probability density function cannot be represented by a handful of statistical values. For instance multimodal probability density functions are in many instances best described by the distribution itself.

3.4 Algorithm convergence to an astrophysical synthetic test object

In this section we test convergence efficiency and overall algorithm performance by applying the GA to a synthetic post-AGB test object. We proceed to test the algorithm in a similar to fashion as De Geyter et al. (2013), by setting a sample of the RT parameters fixed to their respective synthetic input value (see Table. 3.2), while allowing the remaining parameters to freely converge. This approach allows us to identify convergence irregularities and detect potential parameter degeneracies.

Problems of degeneracy in GA solutions to RT problems have been investigated before (e.g., Hetem & Gregorio-Hetem, 2007; Schechtman-Rook et al., 2012; De Geyter et al., 2013). It is known that global optimisers such as a GA, when applied to inverse problems of this type, can result in model degeneracies. This is especially true in our case, where complex parameters interactions can exist, and where the stochastic noise from Monte-Carlo RT can complicate the objective function (i.e., the objective function becomes dynamic). Interferometrically limited coverage of the *uv*-plane also introduces model degeneracies. For example astrophysically distinct objects can provide non-distinct data product results. That is, one-to-one mapping of the model to its resulting data product is not necessarily always the case. The analysis of these data outputs however, whether they represent over- or under-simplified approximations of the true astronomical source, is beneficial. Parameter correlations and interactions will after all allow us to probe potential parameter degeneracies.

3.4.1 The model

In testing our synthetic model we apply a simple, azimuthally symmetric stratified disc density structure (e.g., Shakura & Sunyaev, 1973), a disc structure common to many similar post-AGB studies (e.g., Chesneau et al., 2007b, 2009; Lykou et al., 2011; Bright, 2013). In cylindrical coordinates (r, z), we have:

$$\rho(r,z) = \rho_0 \left(\frac{R_\star}{r}\right)^{h_\alpha} \exp\left(-\frac{z^2}{2h(r)^2}\right), \tag{3.15}$$

where ρ_0 is a normalisation constant, $R_\star$ is the stellar radius, h_α is the mid-plane's density factor and $h(r)$ is the disc scale height, increasing with radius as

$$h(r) = h_0 \left(\frac{r}{R_\star}\right)^{h_\beta}, \tag{3.16}$$

where h_0 is the scale height for a given radial distance and h_β is the vertical-plane density factor. We also define an inner and outer-disc radius ($r_{\rm in}$ and $r_{\rm out}$). We adopt the dust grain size distribution of Mathis et al. (1977). in which the dust grains are considered homogeneous spheres, and are distributed between a minimum and maximum grain size ($a_{\rm min}$ and $a_{\rm max}$) as $\frac{{\rm dn(a)}}{{\rm da}} \propto a^{-b}$ (the exponent b is henceforth known as $a_{\rm pow}$). The disc, of mass $m_{\rm disc}$, is thus characterised by a total of nine parameters.

The stellar component is approximated as a blackbody, of given temperature and luminosity (T and L respectively). While three final parameters describe the positional properties of the object: distance (d), positional angle (p) and inclination (i). The model thus requires a total of fourteen free parameters. The values adopted were chosen to reflect an object similar in nature to those considered in previous studies (e.g., Chesneau et al., 2007b; Lykou et al., 2011), and the orientation of the object was chosen to provide a contrast in resulting visibilities.

In testing our algorithm we adopt typically large parameter ranges and choose non-informative uniform sampling distributions about the input value (i.e. Equation 3.1). We adopt a non-symmetric sampling distribution with respect to the synthetic input values (for example we test convergence to the vertical disc density parameter, with $h_{\beta_{\rm min}} = a = 1.0$, $h_{\beta_{\rm max}} = b = 2.0$ where $h_{\beta_{\rm orig.}} = 1.2$). Such a distribution, allows us to analyse the performance of the algorithm in a more realistic setting. In testing convergence we also include low level Gaussian noise equivalent to SNR=200 (i.e., add noise to the data x_i from a normal distribution where $\sigma = x_i/200$) to the resulting images and spectral energy distributions. By doing so we test convergence in a more realistic and rigorous manner. Input values and sampling search spaces are presented in Table. 3.2.

3.4.2 Results

3.4.2.1 Three-parameter test

We begin by considering the objective function of the two-parameter interaction as revealed by a brute-force grid search over the selected domain. We then analyse the convergence of three free parameters with respect to these contours. Parameters are chosen to represent all model categories, i.e., the stellar parameters, orientation, disc characteristics and dust properties. As mentioned, non-symmetric sampling distributions (with respect to the synthetic input values) were chosen.

We test convergence over wide parameter ranges for the following six parameter groups: (i) distance, inclination and mid-plane density factor; (ii) luminosity, vertical-plane density factor and outer-disc radius; (iii) temperature, disc scale height and dust size distribution; (iv) inner-disc radius, luminosity and maximum grain size in disc; (v) vertical-plane density factor, minimum grain size and distance, and finally (vi) disc scale height, position angle and inclination.

Algorithm convergence for the parameter groups is presented in Figure 3.5, for a GA with $n_{\rm pop} = 100$ and $n_{\rm gen} = 25$, where we adopt a crossover rate of $p_c = 0.65$ and mutation rate of $p_m = 0.035$. The GA solutions are represented as dots, with the darker dots representing later generations. It can be seen that the three-parameter GA converges to the synthetic solution efficiently and without too much difficulty. Final best fit solutions, for example, converge to parameter values within 0.1% of their original input values. The argument can be made however (for this single GA run instance) that the following parameter pairings: position angle - scale height, minimum grain size - vertical-plane density factor, and vertical-plane density factor - luminosity, converge quicker than the other parameter pairings (evident in the fact that the mutation operator is constrained to searching parameter space in the region near the synthetic input value in earlier generations when compared to other parameter pairs). However, this is likely

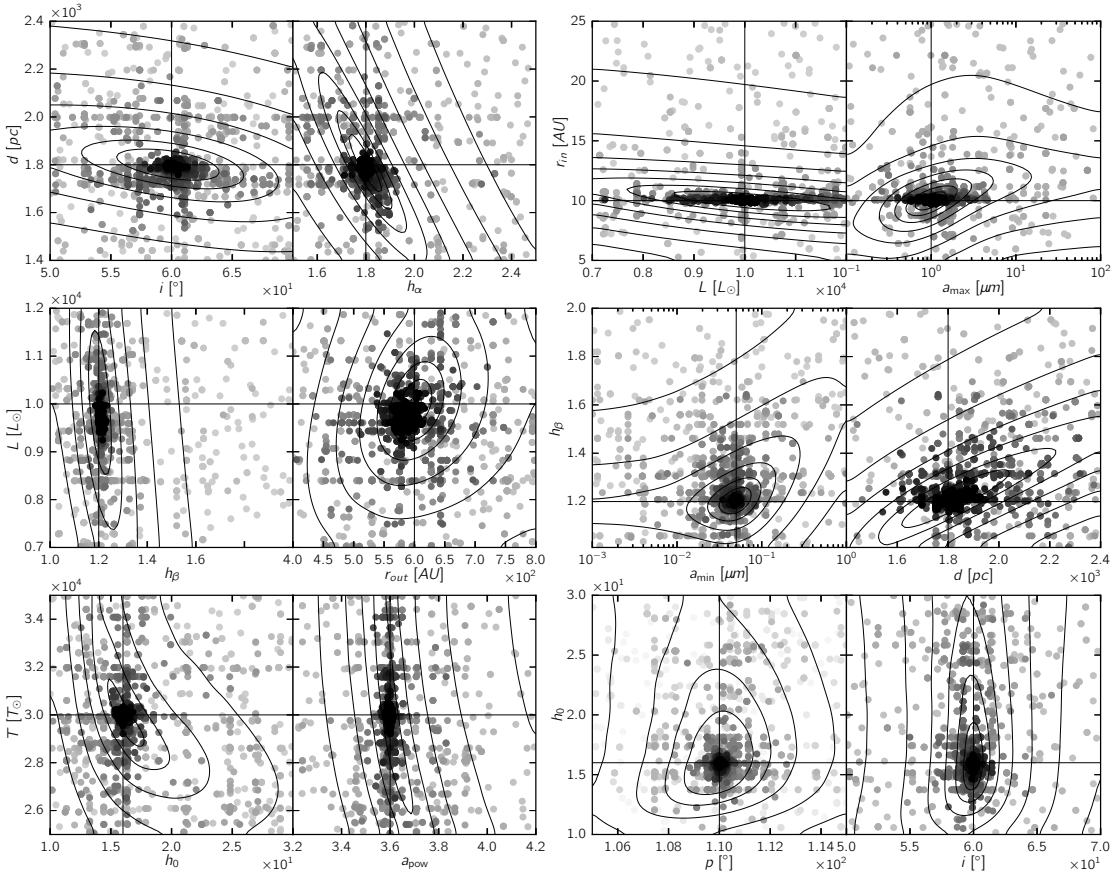

Figure 3.5: Illustration of convergence to the two dimensional objective function for a three dimensional genetic algorithm. The solid vertical and horizontal lines represent the input parameters while the contour levels represent the dimensional objective function (contour lines are equal between plot pairs). Convergence is represented as a scatter plot, with the darker symbols representing later generations. All solutions are shown for the genetic algorithm with $n_{\rm pop} = 100$ and $n_{\rm gen} = 25$.

Table 3.1: Synthetic model parameters.

Parameter		Input[a]	GA Prior (Min., Max.)
Stellar parameters			
Temperature (T_1)	10^3K	30	(25,35)
Luminosity (L_1)	$10^3 L_\odot$	10	(7,12)
Distance (d)	kpc	1.8	(1.4,2.4)
Orientation			
Inclination (i)	deg	60	(50,70)
Position angle (PA)	deg	110	(105,115)
Disc characteristics			
Inner radius ($r_{\rm in}$)	AU	10	(5,25)
Outer radius ($r_{\rm out}$)	AU	600	(400,800)
Mid-plane density factor (h_α)	-	1.8	(1.5,2.5)
Vertical-plane density factor (h_β)	-	1.2	(1.01,2.0)
Scale height (h_0)	AU	16	(10,30)
Dust mass ($m_{\rm disc}$)	$M_\odot$	10^{-7}	$(10^{-8},10^{-6})^\dagger$
Dust properties			
Minimum grain size ($a_{\rm min}$)	μm	0.05	$(10^{-3},10^{-1})^\dagger$
Maximum grain size ($a_{\rm max}$)	μm	1.0	$(10^{-1},10^{2})^\dagger$
Size distribution ($a_{\rm pow}$)	-	3.6	(3.0,4.2)

[a]test model input parameter; [†]log sampling.

explained by the stochastic nature of a single GA run. Additional runs are needed to clarify the situation, but in general, no large scale systematic problems relating to convergence, such as pre-mature convergence (i.e., local minima convergence), or other biases or anomalies are evident. Also of note is the horizontal and vertical clustering of the population across the generations. These observed concentrations are an artefact of the GA process. As the basis of a given offspring solution is its parental chromosomes, those that do not undergo mutation will copy directly the parental gene values. In this 2-D example, this so called gene pool clustering results in observed horizontal and vertical artefacts. Similar behaviour in GA convergence is seen in De Geyter et al. (2013), for example. We conclude that in this low-dimension problem, the algorithm performs as well as one would expect for a typical global optimisation algorithm, we therefore proceed to apply the algorithm to the higher dimensional cases.

3.4.2.2 Ten-parameter test

To test further algorithm performance, we apply the GA to 10 of the 14 parameters. The 10 parameters searched by the GA are those describing the stellar parameters, orientation and disc characteristics only. We fix the parameters which control the distance, minimum and maximum dust grain size and dust size distribution. We set the crossover and mutation rate to the same values as in the three free parameter example above (i.e. $p_c = 0.65$ and $p_m = 0.035$), but increase the population size and generation number. After a number of trial runs the population size was set to $n_{\rm pop} = 600$, with a resulting generation number $n_{\rm gen} \sim 400$ (dependent on the computational time of the RT runs that made up the specific GA, but in general within 5% of this value).

In this test, we begin to see the underlying statistical discrepancies present in

parameter space. As discussed, to build an understanding of the underlying probability density distribution of individual parameters we run N_{GA} such GAs. In this test we run $N_{\mathrm{GA}} = 100$ GAs. A histogram of the best individuals of each GA (i.e. 100 final solutions) is constructed using kernel density estimation.

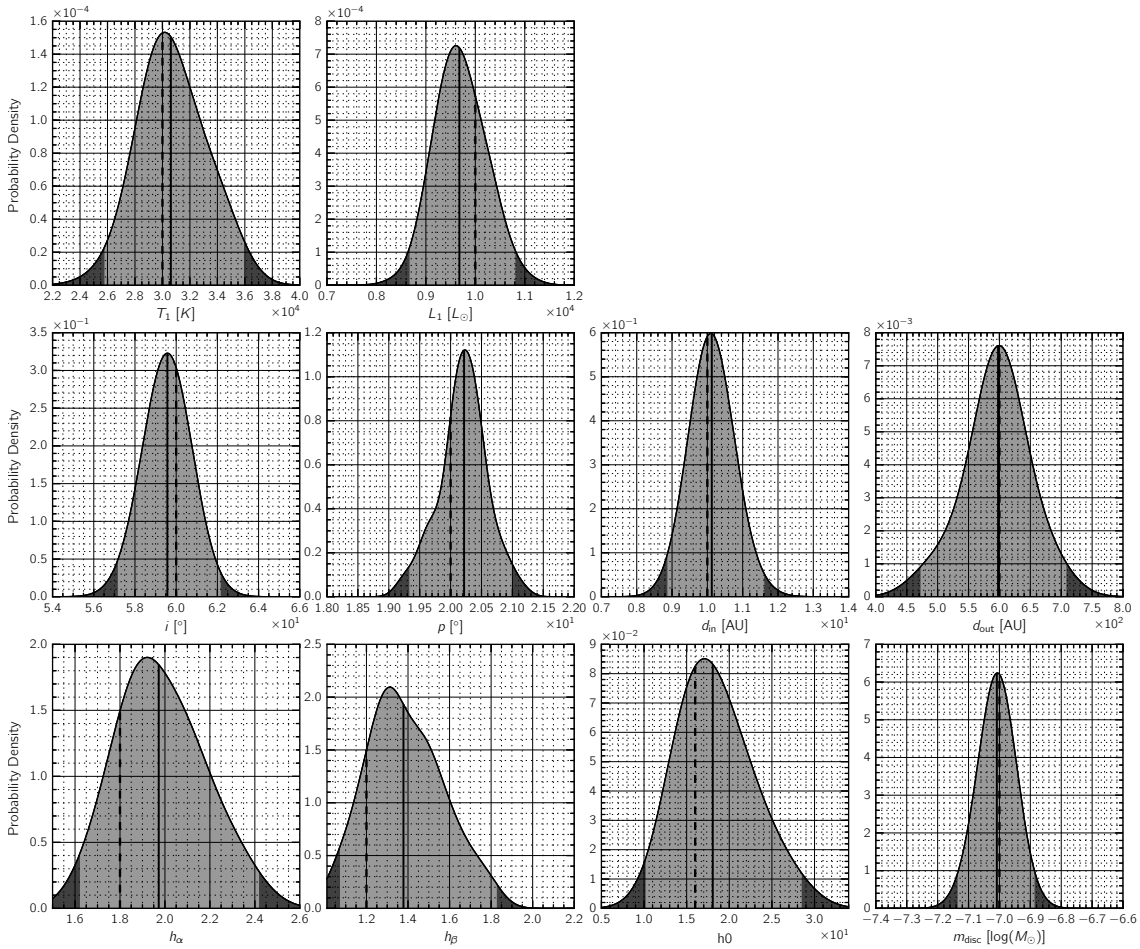

Figure 3.6: The parameter probability density functions for the GA as applied to 10 of the possible 14 free parameters. The solid black vertical line represents the distribution mean, with the light grey region representing the 95% confidence interval. The dark regions represent the 2.5% distribution tail. For comparison the synthetic input values are represented by the dashed vertical lines.

The resulting parameter solution is found by taking the median point estimate of the distribution, and an estimate to the parameter error is provided by the 95% confidence intervals. The mean parameter values, confidence intervals, and standard deviations with respect to the original input values are presented in Table. 3.2. Final solutions are deemed acceptable. For example, the mean of all parameter standard deviations is respectable ($\sim 0.41\sigma$), and reassuringly, median point estimates are found to lie within $\sim 1\sigma$ of their synthetic values. All estimates are also found to lie within the 95% confidence interval range.

Parameter analysis reveals that the disc's vertical-plane density factor is the most difficult to constrain, closely followed by the mid-plane density factor with resulting uncertainty of 1.0σ and 0.87σ respectively. This is however not surprising,

upon deeper consideration, correlation between model parameters reveals a very strong positive correlation ($r = 0.99$) between the mid-plane disc density factor (disc compactness; h_α) and the vertical-plane density factor (or disc flaring parameter; h_β). Some level of degeneracy is thus proposed to exist for the two parameters (at least in the case of near edge-on discs). Physically, this is not surprising. For example, at this orientation it can be seen that similar discs result from high h_α - high h_β values and their low h_α - low h_β counterparts. We conclude that in modelling an edge on disc, h_α and h_β parameters may potentially be replaced by a single parameter. Interestingly however, efficient convergence of the h_β parameter, as found in the three parameter test, was not replicated in this larger 10-parameter study. This may be explained by, again, the stochastic nature of the GA. As in the three parameter test, the algorithm was only run once and with additional runs, degeneracies of the h_β and h_α parameter may begin to surface.

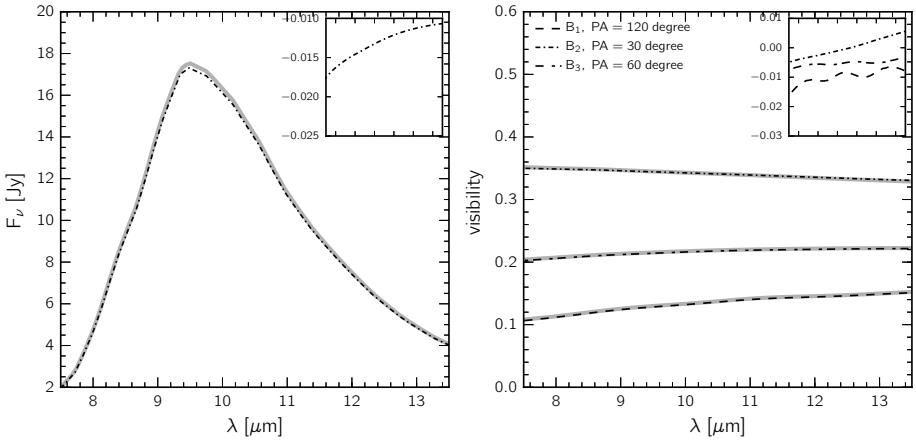

Figure 3.7: A comparison between the 10-parameter GA SED and visibility solution, with the synthetic input model equivalent. The solid grey line represents the synthetic model, and the dotted lines represent the GA solution. The residuals are plotted in the inset as percentages.

The resulting visibilities and SED are presented in Figure 3.7, in which residuals for both the SED and visibilities do not exceed 2% of the original values. Considering that the additional artificial noise had to be overcome (noise which extends beyond the 2% level), the convergence accuracy of the GA is quite impressive. We compare images of the reference synthetic source at 8.0μm and 13.0μm, with the final GA solution equivalents in image Figure 3.8. Alongside these images, we also estimate the image residuals as the fraction of total flux between the two objects (i.e fit/reference). It is evident that the flux difference between the two images are within 30%, however, the important flux to consider is that focused in the image centre, near the central star. These inner-disc regions are many orders of magnitude more luminous than the outer disc regions.[3] A good solution, is thus expected to show good agreement with these inner brighter regions, of which small differences are seen (sub 2%). However, higher differences (at the 25% level) are seen between a some pixels at the inner-disc rim.

[3] Images are log-scaled, of which the artefacts seen in the outer disc regions are a direct result.

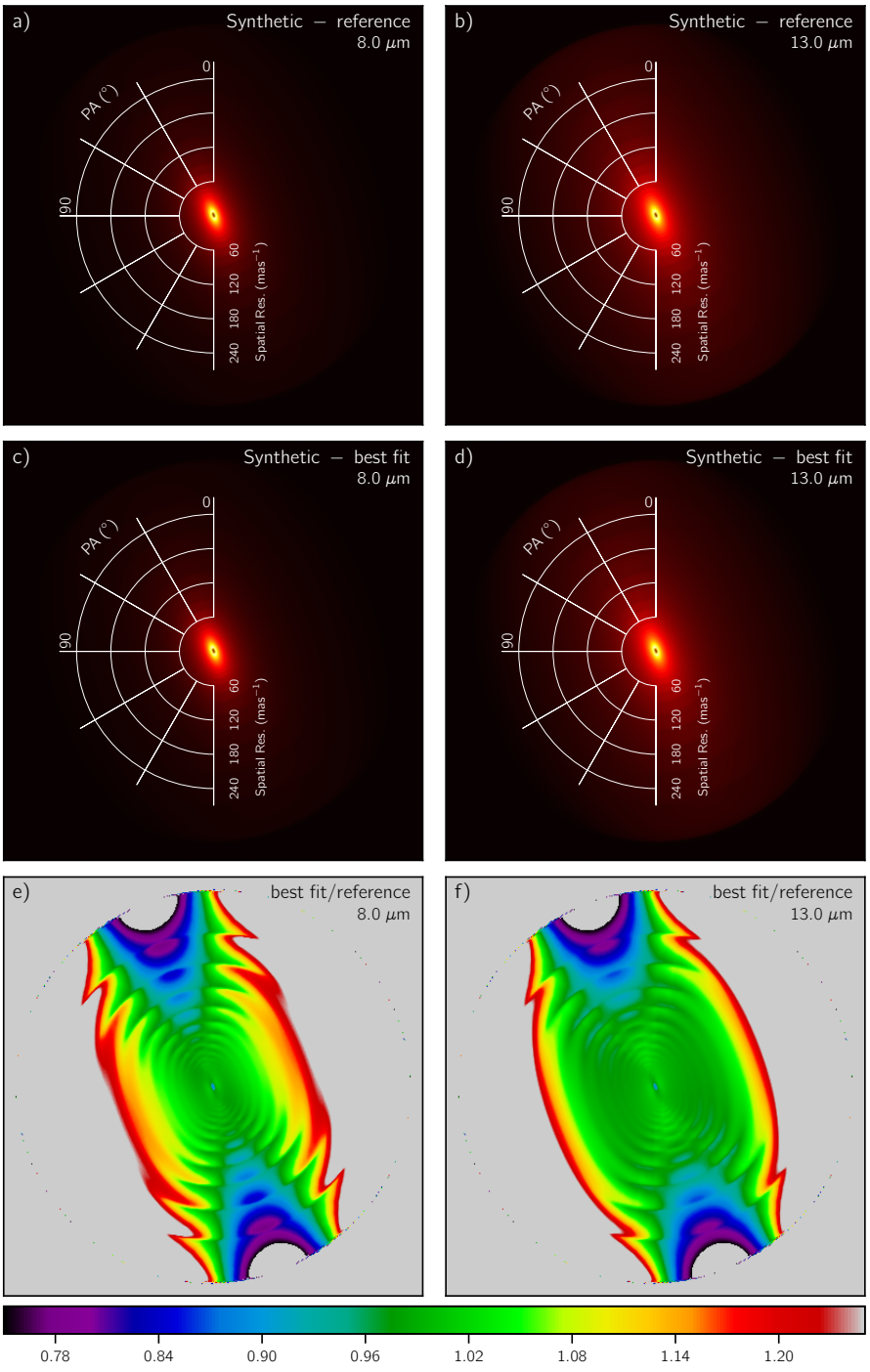

Figure 3.8: A comparison of the reference synthetic intensity distribution with the 10 parameter GA radiative transfer solution. In a) we can compare the 8 micron reference distribution with the 8 micron 10 parameter GA equivalent in c) the residuals (as a percentage) are plotted in e). Similarly the distribution comparison is made at 13 microns in b) d) and f). In e) and f) grey represents values outside the dynamic range of the colour map.

It is evident in all resulting measures, that the GA is doing a good job at reproducing the 10-parameter synthetic astrophysical object well. With confidence in our method, we extend the algorithm to the task of constraining all 14 model parameters.

3.4.2.3 Fourteen free parameters

In this section we test algorithm performance as applied to all 14 parameters. The crossover and mutation parameters remain unchanged, however the population size was increased to $n_{\rm pop} = 750$. Again, approximately $n_{\rm gen} \sim 400$ generations resulted, and the task of constructing an underlying probability density distribution was procured with $N_{\rm GA} = 100$ runs. The resulting functions are represented in Figure 3.9, in which the 10-parameter solutions are also presented for comparison. Final parameter results are presented in Table. 3.2.

Algorithm performance in the 14-parameter case is naturally less efficient than the 10-parameter case. For example the average standard deviation between the reference parameter value and the solution value is 0.55σ, (as opposed to 0.41σ in the 10-parameter case). In the 14-parameter case three parameters however exceed 1.0σ, notably the distance, the inner-disc radius and the disc vertical density. The dust grain size distribution is also very close to the 1.0σ level, and the mid-plane density factor displays similar high variance to the 10-parameter example.

In the 14-parameter case there are signs of degeneracies. For example, the high standard deviation of the inner-disc radius and distance parameters reflected in the strong correlation ($r = 0.79$). This degeneracy however may arise from the simple fact that the inner-disc radius was well constrained in the 10-parameter case (i.e., when distance wasn't considered). Finally it is clear that the correlation makes sense physically: a change in the distance would result in a perceived geometric change to the inner-disc radius. As can observed in the correlation matrix in Figure 3.12, the 10 parameter test shows a very strong correlation between disc compactness (h_α) and disc flaring (h_β) exists (with $r = 0.96$). We conclude again (at least for the case of near edge-on discs) that h_α and h_β may be replaced by a single parameter; this correlation is also evident with paired interactions with other parameters, the disc position angle for example (with $r = 0.83$ and $r = 0.8$ respectively), this is also evident in the 10-parameter case (with $r = 0.87$ and $r = 0.89$).

No perceived strong correlation between the dust distribution parameter ($a_{\rm pow}$) and any other parameter is observed, with an average correlation coefficient magnitude of only 0.18. Though a moderate positive correlation ($r = 0.64$) between the maximum grain size may exist. This finding can be understood. For example, as we increase the maximum grain size, the ratio of large to small grains increases, and an increase in the dust grain distribution $a_{\rm pow}$, will see this somewhat compensated for, though with more complex higher order effects, the correlation is not strong enough to indicate degeneracy. Another correlation worth noting is the outer-disc radius and disc mass interaction, which is strong in both the 10 and 14-parameter case ($r = 0.89$ and $r = 0.79$ respectively), this correlation can be explained, however, as a more massive disc will be larger for a given density. This effect however is expected to not be as strong in non-edge on discs, in which visibility results are likely be affected, and at this point conclude that their inclusion as separate parameter inputs is necessary. Finally we note the result in

which the inner-disc radius and inclination correlation changes from 0.84 to -0.51 between the 10- and 14-parameter result respectively. In this instance a positive correlation is perhaps expected. For example, to reveal similar levels of luminosity from the central source directly, a higher inclination is expected to accompany a larger inner disc radius. The 14-parameter case, is thus suggested to be the product of higher order parameter correlations, or perhaps simply be statistically insignificant. Further analysis would be required to understand both the direction and magnitude of the correlation.

The resulting visibilities and SED for the 14 parameter case is presented in Figure 3.10. Similarly to the 10 parameter case, the residuals of the SED and visibilities are small (sub 2%). Again we compare images of the reference synthetic source at 8.0μm and 13.0μm with the final GA solution equivalents in image alongside the residual image (i.e., fit/reference) in Figure 3.11. Flux differences again do not exceed 30%, with the largest discrepancy between models appearing in the outer-disc region. A larger discrepancy in the inner region is seen in the 14 parameter sample than was observed in the 10 parameter case. However this does not seem to effect the SED or visibilities significantly.

Table 3.2: Synthetic model parameters and GA convergence for the 10 and 14-parameter cases.

Parameter		Input.[a]	GA Range (Min., Max.)	10 param.	σ	14 param.	σ
Stellar parameters							
Temperature (T)	10^3K	30	(25,35)	$30.6^{+5.5}_{-4.9}$	0.22	$30.0^{+5.3}_{-4.2}$	0.03
Luminosity (L)	10^3L$_\odot$	10	(7,12)	$9.67^{+1.10}_{-1.00}$	0.55	$9.65^{+1.30}_{-1.50}$	0.53
Distance (d)	kpc	1.8	(1.4,2.4)	-	-	$1.93^{+0.33}_{-0.22}$	1.04
Orientation							
Inclination (i)	deg	60	(50,70)	$59.6^{+2.6}_{-2.4}$	0.33	$59.6^{+1.9}_{-1.8}$	0.44
Position angle (PA)	deg	110	(105,115)	$110.2^{+0.8}_{-0.9}$	0.58	$110.2^{+0.5}_{-0.7}$	0.60
Disc characteristics							
Inner radius ($r_{\rm in}$)	AU	10	(5,25)	$10.1^{+1.5}_{-1.3}$	0.18	$10.75^{+1.50}_{-1.30}$	1.12
Outer radius ($r_{\rm out}$)	AU	600	(400,800)	598^{+110}_{-130}	0.03	614^{+130}_{-120}	0.23
Mid-plane density factor (h_α)	-	1.8	(1.5,2.5)	$1.97^{+0.45}_{-0.35}$	0.87	$1.95^{+0.34}_{-0.31}$	0.86
Vertical density factor (h_β)	-	1.2	(1.01,2.0)	$1.38^{+0.45}_{-0.31}$	1.00	1.37 ± 0.27	1.15
Scale height (h_0)	AU	16	(10,30)	$18.1^{+10.5}_{-8.0}$	0.44	$16.7^{+9.8}_{-7.2}$	0.17
Mass ($m_{\rm disc}$)	10^{-8}M$_\odot$	10	$(1, 100)^\dagger$	$9.8^{+3.3}_{-2.5}$	0.11	$9.5^{+3.9}_{-2.8}$	0.31
Dust properties							
Minimum size ($a_{\rm min}$)	μm	0.05	$(10^{-3},10^{-1})^\dagger$	-	-	$0.05^{+0.04}_{-0.03}$	0.03
Maximum size ($a_{\rm max}$)	μm	1.0	$(10^{-1}, 10^2)^\dagger$	-	-	$1.08^{+0.94}_{-0.66}$	0.22
Size distribution ($a_{\rm pow}$)	-	3.6	(3.0,4.2)	-	-	3.83 ± 0.46	0.98

[a]test model input parameters, [†]log sampling.

The resulting probability density functions (Figure 3.9) show striking similarities between the 10 and 14-parameter test. Perhaps the only parameter to show a difference of note is the inner-disc radius. For example in the 14 parameter case we determine a radius of $10.75^{+1.50}_{-1.30}$ au, versus $10.1^{+1.5}_{-1.3}$ au in the 10-parameter case. Interestingly, however, this result reinforces the strong positive correlation between inner-disc radius and distance ($r = 0.79$). For example, the 10-parameter test did not include distance; as such, it was set to its original input parameter in all GA runs (d = 1800 pc). As a free parameter in the 14-parameter case, a higher distance parameter resulted ($1.93^{+0.33}_{-0.22}$ kpc), such a result is expected to permeate, and in some sense corrupt the other parameters, in particular the strong positive correlation will result in an overestimate of the inner-disc radius.

The resulting visibilities and spectrums for the 14-parameter case is presented in Figure 3.10, residuals for both the spectrum and visibility are found to lie within 3% of the original model. We conclude the GA has performed well in this full model reconstruction, and proceed to apply GADRAD to VLTI data products of a post-AGB object.

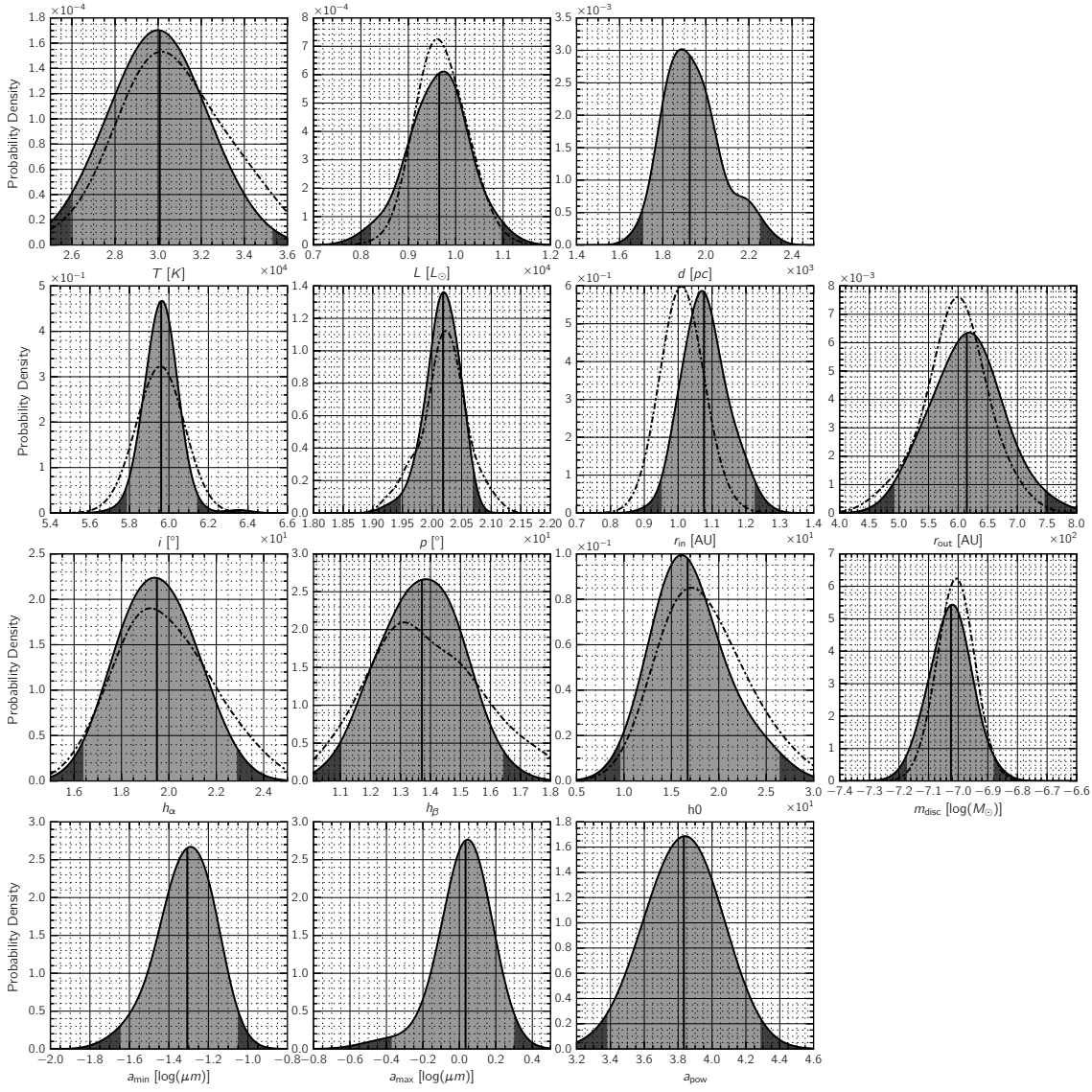

Figure 3.9: Parameter probability density functions for the 14-parameter GA for the synthetic object. The solid vertical line represents the median, with the grey area depicting the 95% confidence interval. The dark regions represent the 2.5% distribution tail. For comparison the probability distribution for the 10-parameter GA is plotted as the dot dash line.

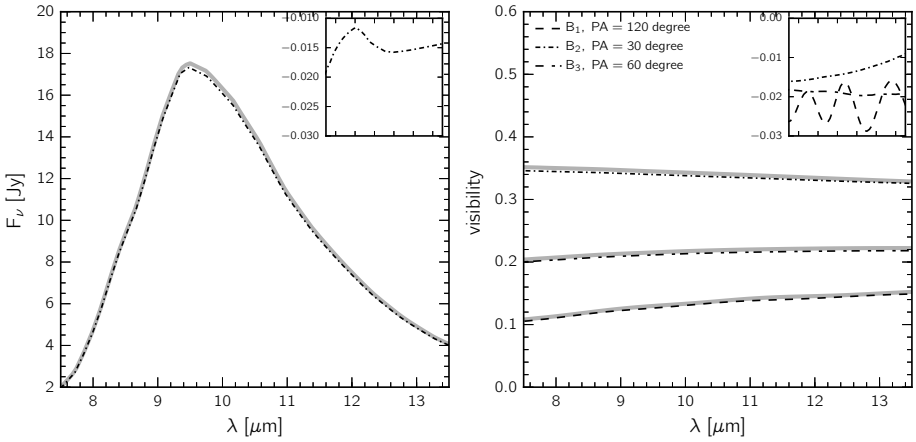

Figure 3.10: A comparison between the 14-parameter GA spectrum and visibility solution, with the synthetic input model equivalent. The solid grey line represents the synthetic model, and the dotted lines represent the GA solution. The residuals are plotted in the inset as percentages.

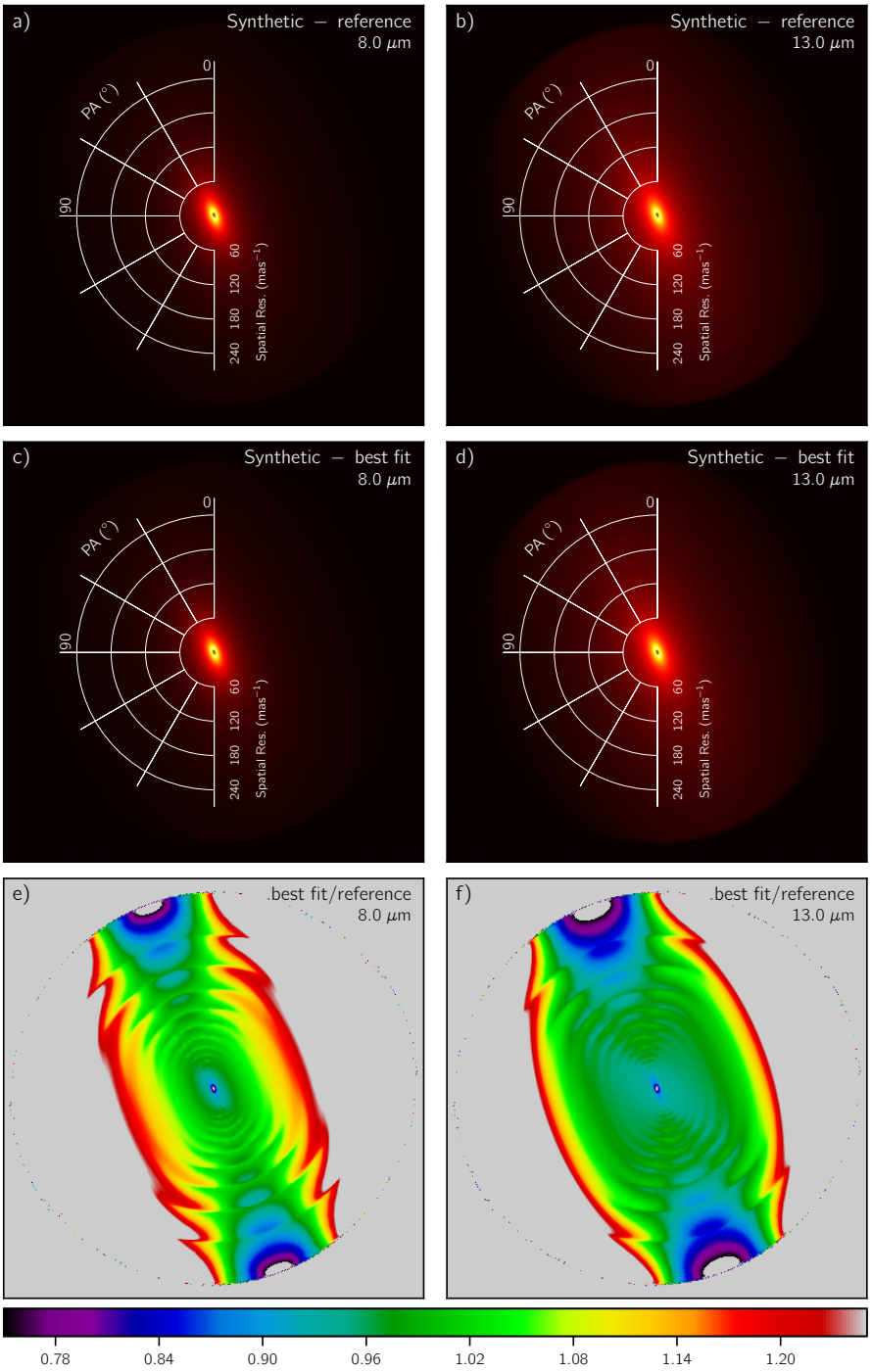

Figure 3.11: A comparison of the reference synthetic intensity distribution with the 14-parameter GA radiative transfer solution. In a) we can compare the 8 micron reference distribution with the 8 micron 14- parameter GA equivalent in c) the residuals (as a percentage) are plotted in e). Similarly the distribution comparison is made at 13 microns in b) d) and f). In e) and f) grey represents values outside the dynamic range of the colour map.

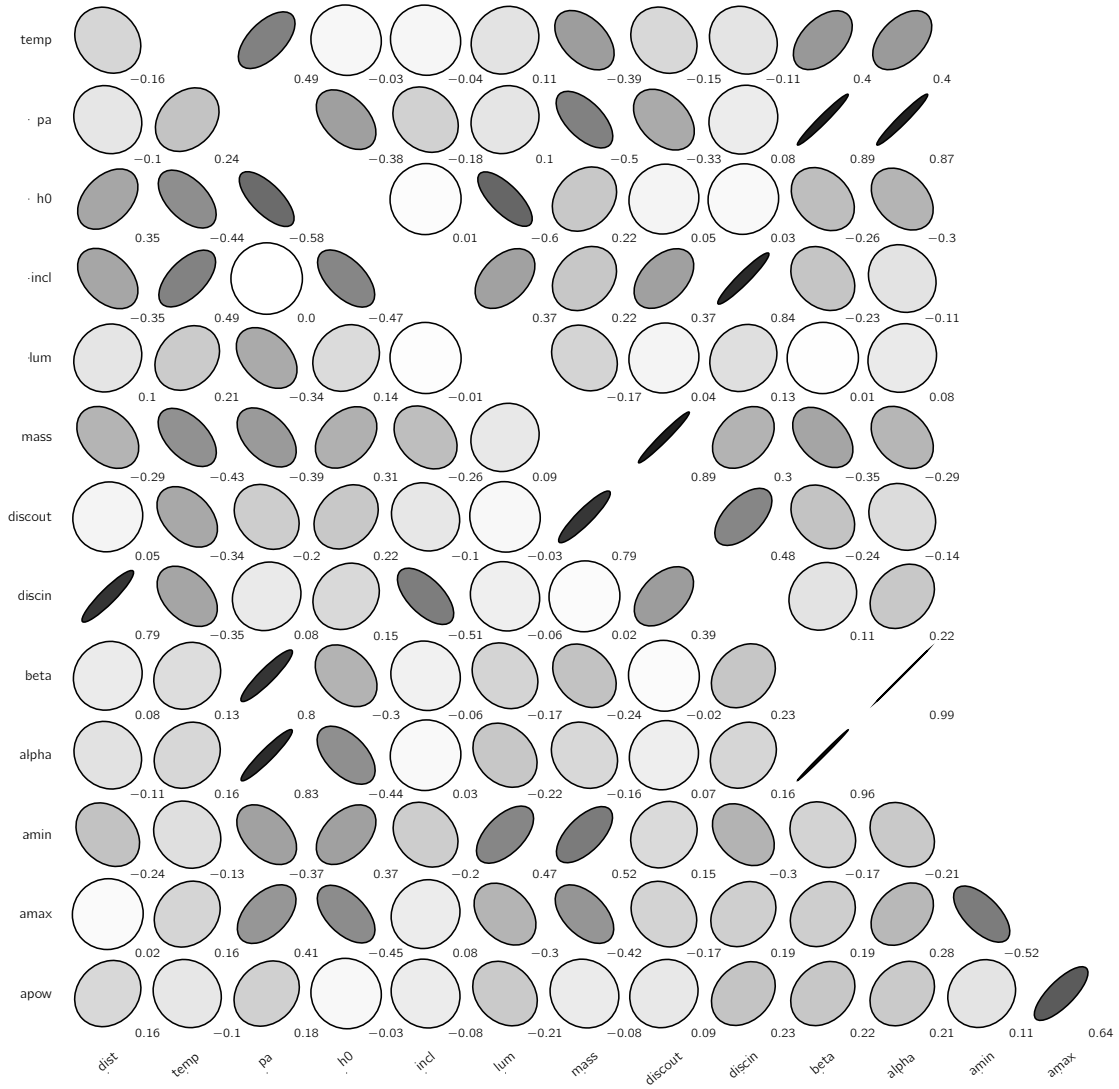

Figure 3.12: Visualisation of the correlation matrix depicting the correlation coefficient, r, for the synthetic test object. The correlation coefficient is presented in the bottom right corner of each parameter correlation. Darker, more elliptical ellipses indicate a stronger correlation, and less correlated parameters are lighter in colour and more circular. The 10-parameter correlations are presented in the top right corner, while the full 14 parameter simulation is located in the bottom left.

Chapter 4

Menzel 3

"Essentially, all models are wrong, but some are useful"

G.E.P. Box – 1987

Material in this chapter is based on an article submitted to MNRAS Apr. 2017. Macdonald D., De Marco O., Lagadec E., Ma J., Chesneau O.

In this chapter we apply GADRAD to the MIDI data products of the young bipolar nebula Menzel 3 (henceforth Mz3), from which we obtain parameter probability density estimates for the given radiative transfer input variable. Mz3 is a good candidate for initial application of GADRAD, as simple and good fitting radiative transfer models have already been determined (e.g., Chesneau et al., 2007b). These solutions provide context in which we can compare directly the performance of GADRAD.

4.1 Background

The Ant Nebula, Mz3 (Menzel, 1922), is a young nebula with numerous large, and highly collimated bipolar outflows (see Figure 4.1a). At the object's core resides a proposed symbiotic binary system (e.g., Calvet & Peimbert, 1983; Smith, 2003), the exact nature of which is however still to be determined. Evidence for a symbiotic Mira core has been suggested (e.g., Schmeja & Kimeswenger, 2001; Zhang & Liu, 2006), but on constraining the inner dust regions, Chesneau et al. (2007b) speculated on the existence of a less luminous, cooler star with a white dwarf companion. As indicated by Guerrero et al. (2004), a symbiotic core would explain the spectacular multipolar structures observed, with the expansion regions being caused by episodic events due to accretion type outbursting. Ages of the outbursts, as estimated by Santander-García et al. (2004), supported this line of thinking. The innermost lobes are proposed to be the youngest outburst region (670 year kpc^{-1}), while the extended column type structure is estimated to have been ejected earlier in the object's history (875 year kpc^{-1}). Finally, the larger cone structure was found to be older still (1600 year kpc^{-1}). Guerrero et al.

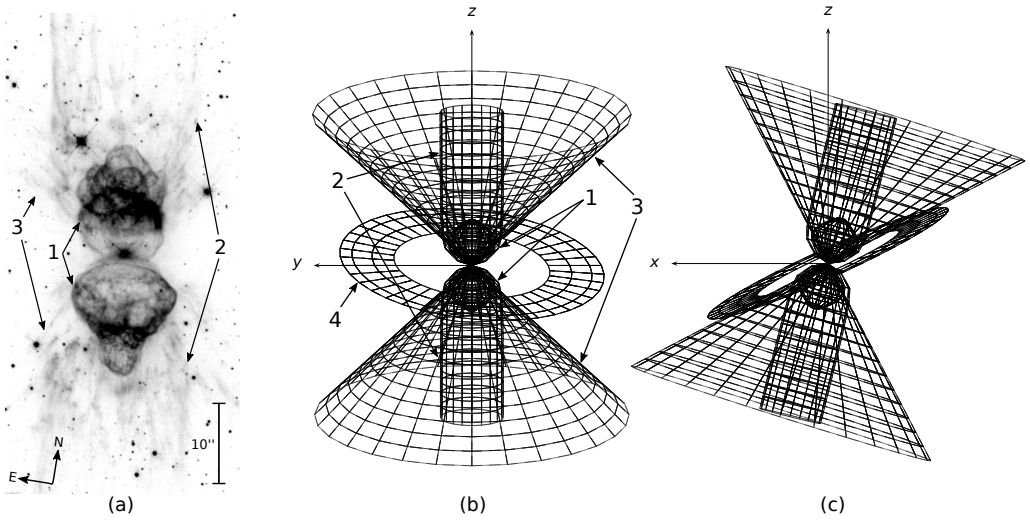

Figure 4.1: Composite HST image (a), in reference to a schematic depicting the outflow regions (adapted from spatiokinematical modelling from Santander-García et al.); front view (b) and side view (c) where the x axis is directed towards the observer. Images are not of shared scale. The four regions are: 1. the inner lobe core 2. the column structure 3. the steep angled rays, and 4. the chakram ring structure. The chakram is not easily discerned in image (a), outflows 1,2 and 3 are orientated with an inclination between 68° and 78° (the angle between the line of sight and the symmetry axis of the structure). With reference to (c), the chakram (outflow 4) inclination is orientated in the opposite direction (Northern symmetry axis towards the observer) with $i \sim 115°$, and with reference to (b) the chakram symmetry axis is rotated ∼9° clockwise with respect to the projected symmetry axis z of the nebula.

(2004) concluded we could be witnessing ongoing evolution, driven by the complex interactions of a binary system.

Spatio-kinematic modelling of the object (e.g., Santander-García et al., 2004; Guerrero et al., 2004) identified a fourth, previously unnoticed structure. The feature, known as the 'chakram' (a large flattened disc), is interesting due to its peculiar orientation. The nested pairs of bipolar lobes already mentioned are estimated to sit at inclination angles between 68° and 78° to the line of sight. The axis perpendicular to the plane of the chakram, in contrast, is inclined in the opposite direction, sitting at an inclination of 115°. The chakram's axis was also found to have a ∼9° clockwise rotation with respect to the projected symmetry z-axis of the nebula (see Figure 4.1; the projected z-axis has a position angle of ∼5°). The origin of the chakram is unknown, but unlike the other outflow structures, is proposed to have been ejected over a long time period, in a 'non-explosive' type event.

Looking at the core more closely, infrared measurements indicate the presence of a circumstellar dust and gas disc that obscures the inner stellar region to direct imaging (e.g., Cohen et al., 1978; Meaburn & Walsh, 1985). In agreement with the gas-phase detected in the nucleus (e.g., Zhang & Liu, 2002), a second, flat silicate disc located close to the stellar surface (i.e., well within the chakram structure) was proposed. Chesneau et al. (2007b), henceforth C07, observed the inner dust region with the mid-infrared interferometer MIDI at the VLTI. They witnessed a strong dependence on the visibility magnitude with position angle, indicating a disc structure was likely being seen close to edge on. The MIDI spectrum exhibited amorphous silicate signatures, suggesting the structure to be

quite young (older, more processed discs tend to show crystalline features). RT modelling was employed in an attempt to constrain the disc geometry further. The disc modelled was simple in nature, but it proved to fit the interferometric data products reasonably well. It was proposed a disc was likely sitting at an inclination of $75° \pm 3°$ to the line of sight, with a position angle $5° \pm 5°$, parameters that would make the disc's major symmetry axis aligned with the lobes' major axis. For the exhaustive list of the disc and environment parameters derived by C07, see Table. 4.3.

C07 believed the disc to be of too low a mass to cause collimation, and instead favoured a collimation scenario where a jet shaped the outflow, and where the disc may have resulted as the aftermath of the jet action. A similar ejection process was also supported by Smith & Gehrz (2005), who compared the inner dust mass (and later ascribed to the disc observed by C07) with the inner bipolar lobes' mass. The bipolar lobes' mass was found to be many orders of magnitude greater than the disc's mass. They concluded the momentum of the outflows that formed the lobes could not be diverted by such a disc.

Many of the environmental parameters of the C07 study, however, were not explored, and instead were fixed to literature values only. The stellar temperature, luminosity and object's distance, for example, were fixed, as was the outer-disc radius. Just seven free parameters were explored, and only a small area of parameter space was considered, and as mentioned, such *by-eye* methods are inclined to bias introduced by human intervention (see Table. 2 in C07 for the parameter range explored). In terms of the literature values (see Table. 4.1) the C07 study was small in scope, despite the fact that it was indicated that a *'good fit was found rapidly'*. What is not so clear is whether a more comprehensive study of parameter space would be beneficial to the overall understanding of Mz3 and its disc structure and origin. Exploring parameter space further will additionally reveal possible model degeneracies. The simple nature of the C07 model and the impressive data product fits obtained, however, make Mz3 a prime candidate for initial testing of the GADRAD algorithm on an astronomical source. This is the topic of this section.

4.2 Observations

The Mz3 data products were obtained with the MIDI instrument (Leinert et al., 2003) of the VLTI, in May and June 2006 by C07. With MIDI being able to combine light from just two telescopes, and with the high sensitivity required, Mz3 was observed with two of the four 8.2m UTs. The measurements were taken in SCI_PHOT mode, such that fringe measurements were taken concurrently with the photometric information. The lower resolution prism mode (R=25) was used. Data reduction was additionally performed by C07, in which MIA and EWS software packages were used. The resulting flux and visibilities measurements are presented in Figure 4.3. The observation log is presented in Table. 4.2 as well as the source calibrators used. For more information regarding the observations see section 2 of C07.

Table 4.1: Menzel 3 literature parameter values alongside the initial GA search domain.

Parameter		Lit. Values	Ref.	GA Samp. (Min., Max.)
Stellar Parameters				
Temperature (T)	10^3K	31.5, 35, 39.3	a,b,c	(20,45)
Luminosity (L)	$10^3 L_\odot$	5.7, 9.1, 10	a,c,b	(5,16)
Distance (d)	kpc	1, 1.3, 1.4, 1.8 2.6, 2.7, 2.85	d,(c,e),b,a f,g,g	(1.0,2.8)
Orientation				
Inclination (i)	deg	74	b	(55,85)
Position angle (PA)	deg	5	b	(0,10)
Disc Characteristics				
Inner radius ($r_{\rm in}$)	AU	9	b	(4,25)
Outer radius ($r_{\rm out}$)	AU	500	b	(150,600)
Mid-plane density factor (h_α)	-	2.4	b	(1.5,6.0)
Vertical density factor (h_β)	-	1.02	b	(1.0,2.5)
Scale height(h_0)	AU	17	b	(5,35)
Mass ($m_{\rm disc}$)	$10^{-5} M_\odot$	0.1, 0.9	f,b	(0.01,100)†
Grain Parameters				
Minimum size ($a_{\rm min}$)	μm	0.05	b	(0.001,1)†
Maximum size ($a_{\rm max}$)	μm	0.2, 1	f,b	(1,10^4)†
Size distribution ($a_{\rm pow}$)	-	3.5	b	(3,6.0)

[a]Cohen et al. (1978); [b]Chesneau et al. (2007b); [c]Pottasch & Surendiranath (2005); [d]Lopez & Meaburn (1983); [e]Cahn et al. (1992); [f]Smith & Gehrz (2005); [g]Kingsburgh & English (1992); †log sampling.

Table 4.2: Menzel 3 observing log.

OB	Time	Base	Baseline	
			Length (m)	PA (°)
Mz3-1	2006-06-11T23	U2 – U3	46.3	1.5
Mz3-2	2006-05-15T04	U2 – U3	45.4	30.5
Mz3-3	2006-05-15T08	U2 – U3	31.4	73.8
Mz3-4	2006-05-14T08	U3 – U4	60.6	149.2
Mz3-5	2006-06-11T01	U3 – U4	52.0	77.2
Mz3-6	2006-05-17T06	U3 – U4	62.5	122.1

Calibrators: HD 151249 5.42 ± 0.06 mas, HD 160668 2.22 ± 0.1 mas, HD 168723 2.87±0.13 mas, HD 188512 1.98±0.1 mas.

4.3 Reproducing the Chesneau et al. model and applying the search heuristic

We begin by attempting to reproduce the Mz3 results as determined in the analysis of C07. The C07 model was obtained with the Monte-Carlo RT code `MC3D` (e.g., Wolf, 2003; Wolf et al., 1999), a different RT code from the one we use. Therefore, before blaming result differences on the fitting technique, we compare the two RT codes. The C07 input parameters can be found in Table. 4.1. We adopt the amorphous silicates of Weingartner & Draine (2001) in all subsequent models. The resulting `RADMC-3D` spectrum and visibilities were found to agree very closely

(with differences smaller than 4%) Results are presented in Figure 4.3. With confidence in our RT code implementation, we initiate the search heuristic. We begin by first testing for the presence of a possible disc aligned with the Santander-García et al. (2004) chakram.

4.3.1 Potential disc-chakram alignment

Santander-García et al. (2004) indicated that Mz3 contains a large chakram or flattened disc surrounding the outflow regions, with an inclination of 115° and a position angle of 9°. What can be considered a '*mis-alignment*' of the chakram structure may in fact be evidence of some complex physical process that may in the same way affect the orientation of a smaller silicate disc structure. In either case, we feel there is enough evidence to begin searching for a small circumstellar disc with a similar orientation to the larger chakram.

In performing a preliminary search of parameter space we set the population size $n_{\rm pop} = 1200$, and iterate for approximately $n_{\rm gen} = 500$ generations. We adopt the stratified disc structure (Equation 3.15), however, following 4 GA searches we find only poor fitting results (see Figures 4.3 and 4.5). We conclude that the chakram orientation is likely not mirrored in a smaller internal disc structure. We instead start searching for a disc alignment closer to that suggested by C07. Preliminary attempts suggest that this area of parameter space is more encouraging. We thus apply `GADRAD` in a similar manner to the synthetic test case as presented in Section 3.4, and test for convergence of a sample of parameters.

4.3.2 Ten-parameter search

In this section we explore parameter space for only 10 of the 14 simulation parameters. These include: the stellar effective temperature, stellar luminosity, inclination and position angle, inner and outer-disc radii, mid-plane density factor, vertical-plane density factor, scale height and disc mass. By setting the remaining 4 values to the C07 values, we are able to explore parameter space in a similar fashion to C07 (though in this instance we additionally explore the stellar luminosity and effective temperature search space). Underlying differences in the resulting parameter density distributions between this sample of parameters and full model exploration (i.e. all 14 parameters in Section 4.3.3), will additionally reveal any potential local minima convergence. Parameter correlations can also be compared between the two searches, which may reveal potential degeneracies.

To avoid premature convergence to local minima, and ensure a broad search of parameter space, we set the population size to $n_{\rm pop} = 750$. Through trial and error, optimal algorithm performance was found with a mutation rate $p_m = 0.035$, in combination with a crossover rate $p_c = 0.65$. An acceptable level of convergence was reached after approximately $n_{\rm gen} = 450$ generations. Running `GADRAD` in parallel on 48 CPUs, resulted in a runtime of approximately 24 hours for each GA. As discussed in Sect. 3.3.1, in the attempt to gain statistical inference, we construct confidence distributions by running a number of such GAs, in this instance we employ $N_{\rm GA} = 100$ GAs.

It is evident that a number of parameter distributions are non-uniform, and non-normal, with, for example, a selection of skewed and bimodal results. The dis-

tributions were again calculated using a kernel density estimator. The resulting distribution variance was estimated using the median absolute deviation (MAD) measure ($\hat{\sigma}$).[1] The MAD measure of variance provides an indication to how well the parameters are constrained, with the parameter displaying the broadest relative distribution having the higher $\hat{\sigma}$ value. The largest variance was observed in the parameter controlling the stellar effective temperature ($\hat{\sigma} = 0.104$), closely followed by the outer-disc radius ($\hat{\sigma} = 0.101$, though this is likely due to the MAD estimator being ill-suited to heavy-tailed data sets, as evident in this distribution). The mid-plane density factor was additionally ill-constrained with $\hat{\sigma} = 0.090$. The best constrained parameter was found to be the parameter controlling the inclination angle, with $\hat{\sigma} = 0.007$. Remaining MAD values are presented in Table. 4.1.

As in the case of the synthetic GA test of Section 3.4, the 10-parameter case here (Figure 4.7) shows that a positive correlation exists between the mid-plane density factor (h_α, the parameter that controls disc compactness) and the vertical-plane density factor (h_β, the parameter that controls disc flaring). This result is not surprising, as was discussed previously. For a near-edge on disc at this orientation similar intensity distributions result from a highly flared compact disc (i.e. high h_β, high h_α), and a low flaring larger disc (i.e. low h_β, low h_α). In this instance, however, the correlation is moderate to strong ($r = 0.58$), as opposed to a very strong correlation as found in the synthetic test case ($r = 0.99$). The difference is likely due to more complex underlying parameter interaction, that may be expected from the data products of a real object. Support for correlation between h_α and h_β, is reinforced by the very strong positive correlation existing between the disc scale height (h_0) and h_α ($r = 0.87$), which is mirrored in the scale height and vertical-plane density factors ($r = 0.65$). However, the argument for degeneracy is weakened by the strong correlations that exist between the luminosity and vertical-plane density factor ($r = -0.77$), and the inner-disc radius and vertical-plane density factor ($r = 0.65$), a result not seen in the mid-plane density factor (with $r = -0.1$ and $r = 0.29$ respectively). Additionally, the vertical-plane density factor, in contrast to mid-plane density factor, was found to be one of the best constrained parameters with $\hat{\sigma} = 0.016$. Contrary to the 10-parameter synthetic case, we conclude that degeneracy is unlikely to exist between the mid-plane and vertical-plane density factors, and propose they remain independent parameters. Other correlations of note is the moderate to strong positive correlation that exists between the inclination angle and luminosity ($r = 0.58$), and the luminosity and inner-disc radius ($r = -0.57$). Parameter correlations are presented in Figure 4.7.

As mentioned previously in this section, the stellar effective temperature was difficult to constrain. We determine the RT model is not particularly sensitive to this parameter. A bimodal distribution is suggested for example. The importance of this is yet to be determined. However, correlations between the temperature parameter and other parameters are weak, suggesting the bimodal structure may be important, we however only provide a single point estimate to represent the distribution, as we feel the distribution's median does an adequate job of representing the probability density function. The outer-disc radius is another instance of a non-normal distribution, yet only very few samples are contained within the

[1] MAD is a measure of the deviation of the residuals, from the distributions median, more specifically the median of the deviation, i.e., $\hat{\sigma} = \mathrm{med}_i(|x_i - \mathrm{med}_j(x_j)|) \cdot b$, where b is a normalisation factor, which we set to the inverse of the 50th percentile of the distribution.

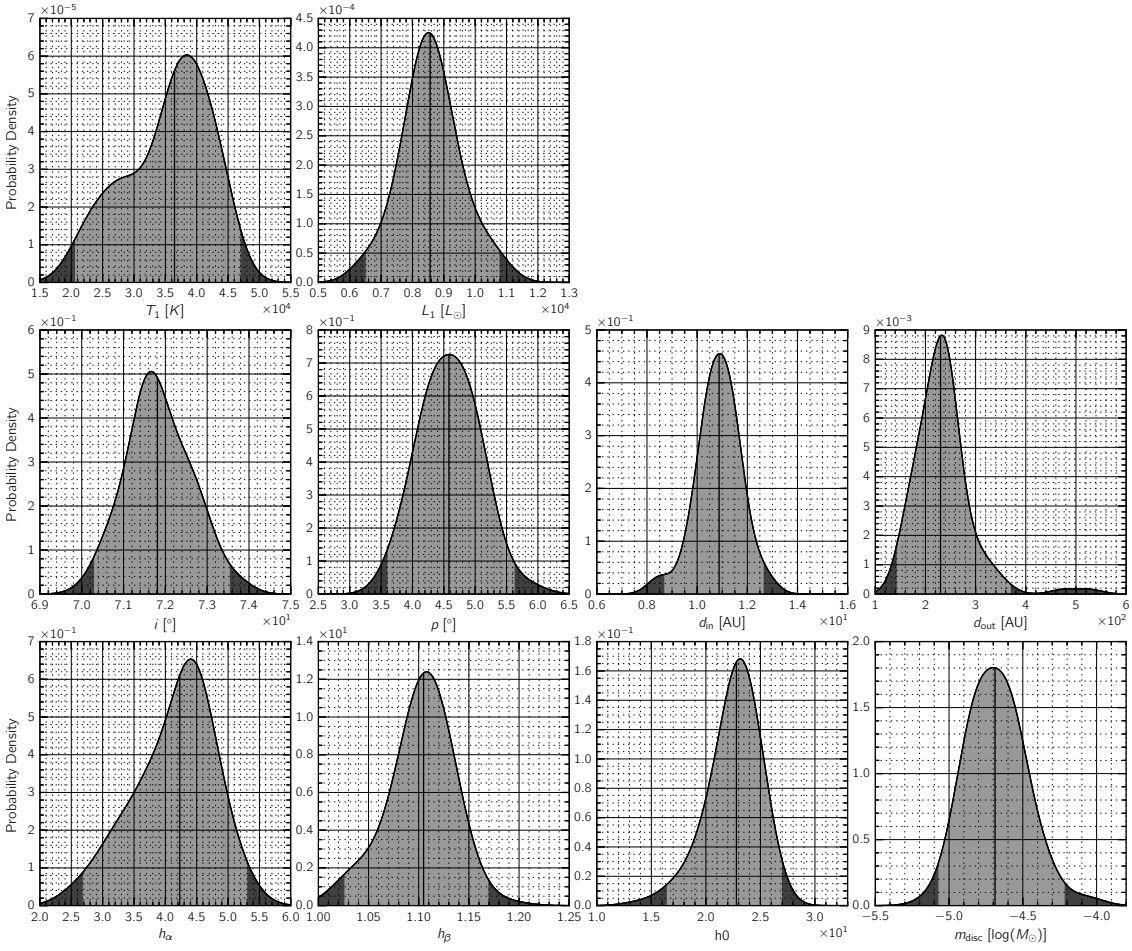

Figure 4.2: Parameter probability density distributions for the 10-parameter GA. The solid vertical line represents the median, with the grey area depicting the 95% confidence interval. The dark regions represent the 2.5% distribution tail.

tail (i.e. less than 2%). The result could arise due to outlying fitness runs, but with the median appearing very close to the mode the result seems to be of little consequence.

At this point our findings show reasonable agreement with the C07 result. Only the outer-disc radius, mid-plane density factor and disc mass parameters display discrepancies beyond our error estimates. Our model favours a smaller more compact disc than that determined by C07 with an outer-disc radius of $r_{\rm out} = 230^{+140}_{-90}$ au, and mid-plane density factor of $h_\alpha = 4.2^{+1.0}_{-1.5}$. The disc is also suggested to be more massive than that determined by C07 ($m_{\rm disc} = 2.1^{+4.2}_{-1.2} \times 10^{-5}$ M$_\odot$ vs 9×10^{-6} M$_\odot$ in C07).

4.3.3 The fourteen-parameter fit

We now apply GADRAD to all 14 of the model parameters, by introducing the distance, minimum dust grain size, maximum dust grain size and size distribution parameters. With the additional search parameters we increase the GA population size to $n_{\rm pop} = 850$. The mutation and crossover rates of the previous section are maintained and, again, sufficient convergence was found after $n_{\rm gen} \sim 450$ generations. However, with the dust parameters requiring additional computational time for the necessary calculation of the dust opacity tables, and with the larger population size, the computational time increased to approximately 36 hours on 48 CPUs. In constructing the parameter confidence distributions we again rely on $N_{\rm GA} = 100$ runs. The resulting distributions are presented in Figure 4.6, with the point estimates presented alongside the 10-parameter result for comparison, in addition to the MAD values in Table. 4.3.

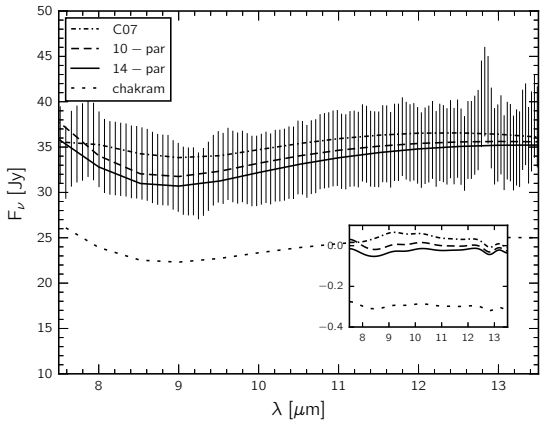

Figure 4.3: The MIDI spectrum is represented by the vertical error bars. The resulting flux for the Chesneau et al. model is represented by the dot dash line, the long dash line is the 10 parameter GA solution and the solid line represents the full 14-parameter solution. The chakram aligned disc best fit is additionally provided as the short dash line. The corresponding residuals are presented in the inset as percentages.

Differences in the resulting spectrums and visibilities become evident when comparing the final 14-parameter GADRAD solution with the 10-parameter result (Figure 4.3 and 4.5). The most notable differences are seen in the parameter controlling the stellar luminosity and inner-disc radius. This however may be explained by

the moderate, positive correlation existing for both parameters with the distance parameter ($r = 0.51$, $r = 0.71$ respectively). For example, in the 10-parameter case distance was set to the C07 value of 1.4 kpc. The 14-parameter model however favoured a higher value ($1.8^{+0.2}_{-0.3}$ kpc). With the object located at a closer distance, the correlation suggests that the luminosity and inner-disc radius would likely decrease, and better match the data than 10-parameter distributions.

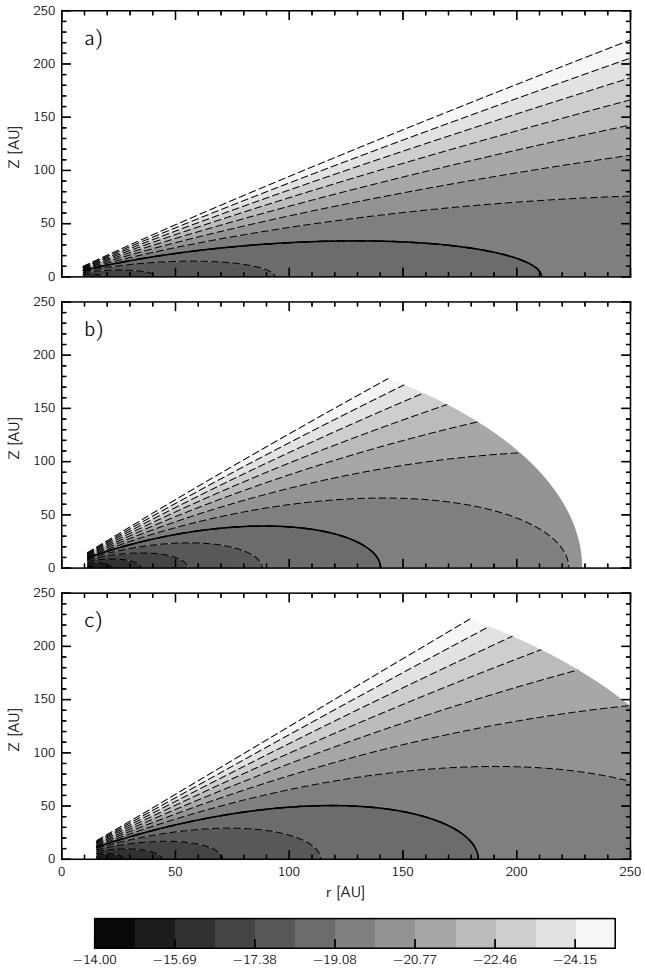

Figure 4.4: Contours of density for the stratified disc: a) represents the Chesneau et al. (2007b) disc, b) is the GADRAD 10-parameter disc and c) the 14-parameter version. Densities are presented in log-base 10, with the solid line representing an equivalent density contour for direct comparison. Disc parameter values are presented in Table. 4.3.

With GADRAD exploring much more of parameter space, and at a much higher resolution than considered C07, we favour this 14-parameter result, and conclude that Mz3 is likely located at a distance of $1.8^{+0.2}_{-0.3}$ kpc, which falls within literature limits. Additionally, we propose that Mz3 has a more luminous star at it's core ($12\,000^{+3500}_{-4000}$ $L_\odot$ vs. $10\,000$ $L_\odot$), surrounded by a smaller and more compact disc (with $r_{\rm out} = 290^{+220}_{-100}$ au vs. 500 au and $h_\alpha = 4.1 \pm 1.0$ vs 2.4, respectively). However, our model favours a larger inner-disc radius, with $r_{\rm in} = 15^{+3}_{-4}$ au, versus $r_{\rm in} = 9.0$ au. To better visualise the differences and similarities seen in the

disc structure between that determined by C07 and that found by the GADRAD 10- and 14-parameter fit, a visualisation of the disc densities are compared in Figure 4.4.

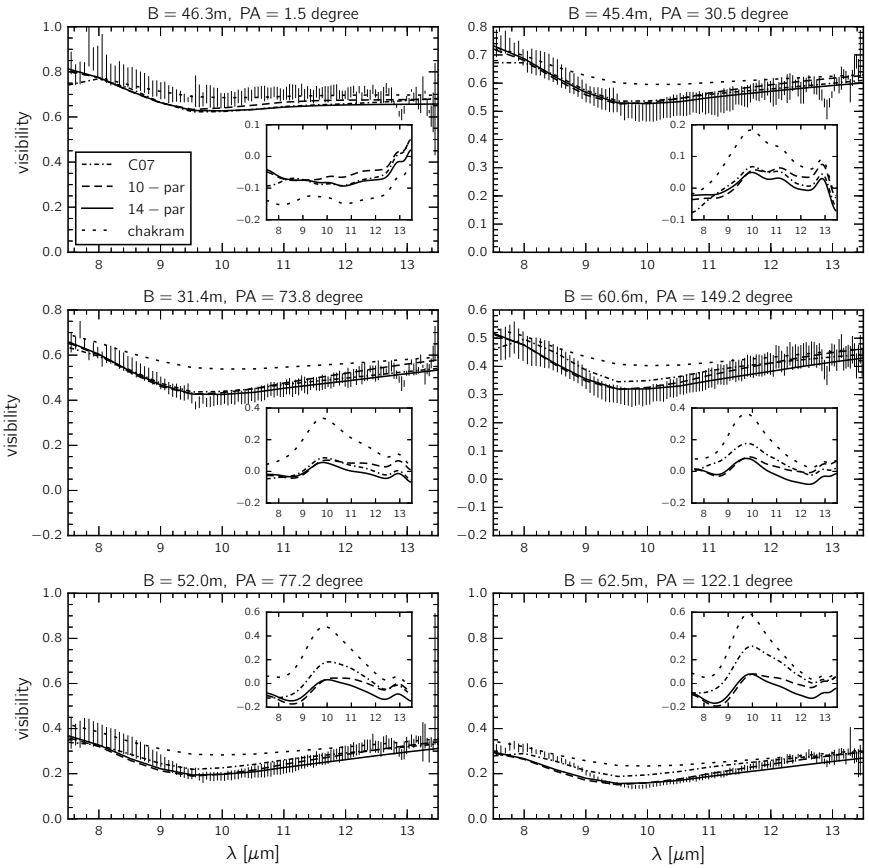

Figure 4.5: The MIDI visibilities are represented by the vertical error bars. The resulting visibilities for the Chesneau et al. model is represented by the dot dash line, the large dashed line is the 10 parameter GA solution and the solid line represents the full 14-parameter solution. The chakram aligned disc best fit is additionally provided as the small dashed line. The corresponding residuals are presented in the inset as percentages.

Despite the fact that our 14-parameter model seems to constrain the parameters better, it is evident that parameters controlling the dust properties are ill-constrained. For example, we determine a MAD value for the minimum and maximum dust grain radius of 0.301 and 0.328, respectively. The grain size distribution parameter fairs a little better with $\hat{\sigma} = 0.127$, but of the 14 parameters, it still remains one of the poorest constrained. The sensitivity of the model to the dust parameters may be questioned, and the exact bearing they have on the overall parameter distributions is unknown. It is possible that in future GA attempts, the dust parameters can be fixed, this will for one eliminate the need to create opacity tables that require additional computational time. Exploring the parameter correlations further, we find moderate negative correlation ($r = -0.61$) between the minimum grain size and disc inclination, as well as the particle size distribution and inclination angle ($r = -0.53$). Moreover, the dust parameters seem to have

little influence on the well constrained inclination parameter ($\hat{\sigma} = 0.007$), further supporting the argument that fixed dust values may suffice. At worst the inclusion of GA-derived dust parameters acts to increase the variance of the remaining parameters. This, however, does not seem to be of concern as the MAD values determined are similar to the 10-parameter MAD variances.

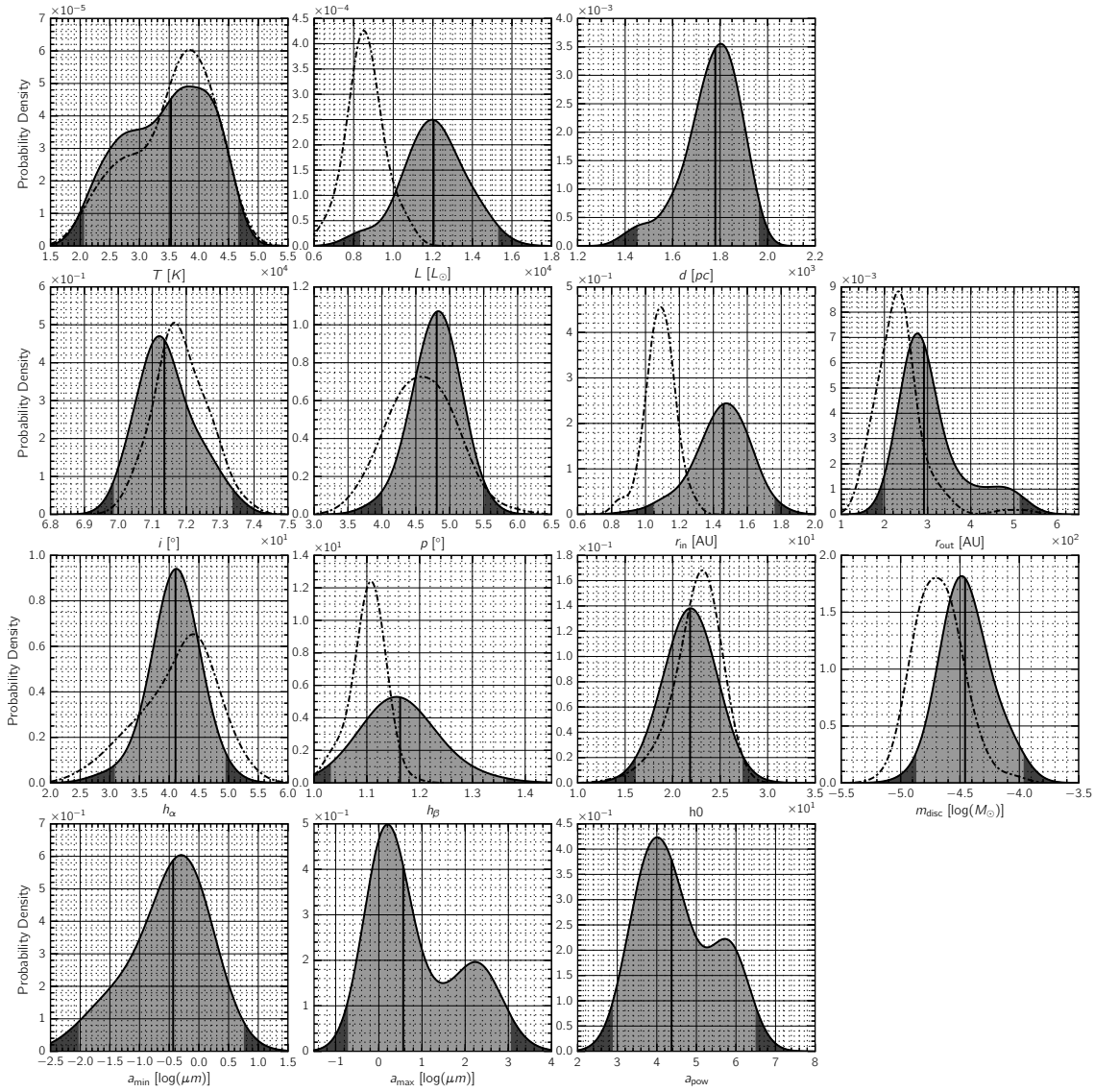

Figure 4.6: Parameter probability density distributions for the 10-parameter GA. The solid vertical line represents the median, with the grey area depicting the 95% confidence interval. The dark regions represent the 2.5% distribution tail. For comparison the confidence distribution for the 10 parameter GA is plotted as the dot dash line.

Similar to the 10-parameter case, the temperature and luminosity were difficult to constrain, and as mentioned the inclination was well defined. The bimodal nature of the effective temperature distribution, similar to the 10-parameter case, is again evident in the 14-parameter example. Additionally the effective temperature again displays only weak correlations (with an average correlation coefficient magnitude

of 0.105). We conclude that our parameter distribution identifies a statistically significant bimodal nature of this parameter, the cause of which is however not known, and would require further analysis. The heavy-tailed distribution of the outer-disc parameter is similarly reproduced here in the 14-parameter solution, though in this instance with more substantive weight, with the median somewhat differing to the mode. However, as was found by Bright (2013) (see also Lykou et al., 2011; Werner et al., 2014), at these inclinations, models are found to be only moderately sensitive to the outer-disc radius, which is evident in the parameter's MAD measure.

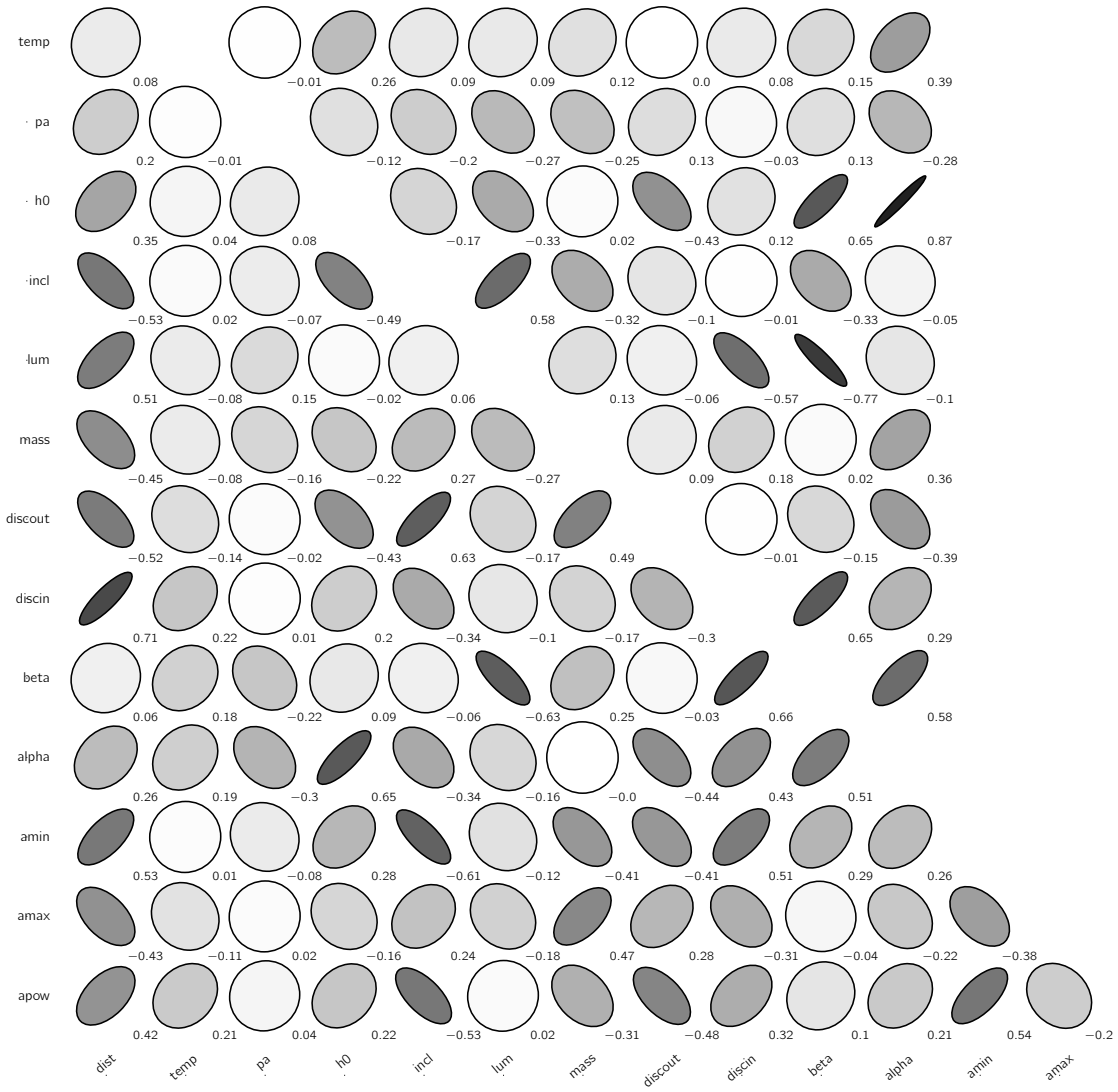

Figure 4.7: Visualisation of the correlation matrix depicting the correlation coefficient, r. The correlation coefficient is presented in the bottom right corner of each parameter correlation. Darker, more elliptical ellipses indicate a stronger correlation, and less correlated parameters are lighter in colour and more circular.

Table 4.3: The Chesneau et al. (2007b) Mz3 parameters vs. GADRAD point estimates for the 10 and 14-parameter GA fits.

Parameter		C07	10 param.	$\hat{\sigma}_{10}{}^{*}$	14 param.	$\hat{\sigma}_{14}{}^{*}$
Stellar Parameters						
Temperature (T)	10^3K	35	36^{+11}_{-16}	0.104	35^{+12}_{-15}	0.161
Luminosity (L)	10^3L$_\odot$	10	8.6 ± 2.1	0.056	12 ± 4	0.075
Distance (d)	kpc	1.4	-	-	$1.8^{+0.2}_{-0.3}$	0.039
Orientation						
Inclination (i)	deg	74	72 ± 2	0.007	71 ± 2	0.007
Position angle (PA)	deg	5	5 ± 1	0.067	5 ± 1	0.038
Disc Characteristics						
Inner radius ($r_{\rm in}$)	AU	9	11 ± 2	0.046	15^{+3}_{-4}	0.071
Outer radius ($r_{\rm out}$)	AU	500	230^{+140}_{-90}	0.101	290^{+220}_{-100}	0.093
Mid-plane density factor (h_α)	-	2.4	$4.2^{+1.0}_{-1.5}$	0.090	4.1 ± 1.0	0.041
Vertical density factor (h_β)	-	1.02	1.1 ± 0.1	0.015	1.15 ± 0.2	0.023
Scale height(h_0)	AU	17	23^{+4}_{-7}	0.053	22 ± 6	0.038
Mass ($m_{\rm disc}$)	10^{-5}M$_\odot$	0.9	$2.1^{+4.1}_{-1.2}$	0.026	$3.5^{+7.5}_{-2.2}$	0.025
Grain Parameters						
Minimum size ($a_{\rm min}$)	μm	0.05	-	-	$0.4^{+5.0}_{-0.35}$	0.301
Maximum size ($a_{\rm max}$)	μm	1	-	-	$4^{+1280}_{-3.5}$	0.328
Size distribution ($a_{\rm pow}$)	-	3.5	-	-	$4.5^{+2.0}_{-1.5}$	0.127

*MAD value.

4.4 Foreground extinction

The MIDI N-band spectrum has a small wavelength coverage ($\lambda \simeq 8\mu$m-13^{-}m) and is virtually independent of reddening. A self-consistent result however requires a model that agrees with the Mz3 spectrum over a broader wavelength range. Literature flux measurements are plotted alongside the MIDI spectrum in Figure 4.8, and the extended GADRAD 14-parameter SED.

The GADRAD result is seen to agree closely with the TIMMI2 flux (Smith & Gehrz, 2005). However, it is evident that at shorter wavelengths (i.e. the 2MASS data) the observations are fainter than the model. This can be explained by foreground extinction. We approximate the reddening effect using the Cardelli et al. (1989, CCM) extinction law. An extinction value $E(B-V) = 0.625$ provides convincing SED fits, where we have reddened the fit rather than de-reddening the data. Much of the reddening has been shown to occur local to Mz3 (i.e., Smith, 2003). Interstellar reddening limits can be calculated from the reddening value estimated of the debris surrounding the outer lobe structures, our adopted reddening value of $E(B-V) = 0.625$ is below this limit $E(B-V) = 0.85$ (Smith, 2003).

Additional energy is thought to be provided to the spectrum due to extended structure that is not captured by MIDI, because MIDI spectra only see the flux that can be resolved by the interferometer, effectively simulating a much smaller aperture. However, modelling the extended structure (as seen by 2MASS for example) would require too many additional parameters. Additionally, the MIDI visibilities are essentially insensitive to the over-resolved structure. A fully self-consistent model would however require a much more thorough multi-wavelength study.

Table 4.4: Menzel 3 aperture photometry.

Instrument/ Reference	Wavelength (μm)	Flux (Jy)	Aperture
2MASS	1.235	0.29	$4''$
	1.66	1.17	$4''$
	2.16	3.81	$4''$
MSX6C	8.28	38.79	$18.3''$
	12.13	80.40	$18.3''$
TIMMI2	8.7	34.3	$4''$
	11.6	36.9	$4''$
	12.8	45.8	$4''$
	17.0	45.7	$4''$
IRAS	12	88.8	$0.75' \times 4.5'$
	25	343	$0.75' \times 4.6'$
	60	277	$1.5' \times 4.7'$
	100	113	$3.0' \times 5.0'$

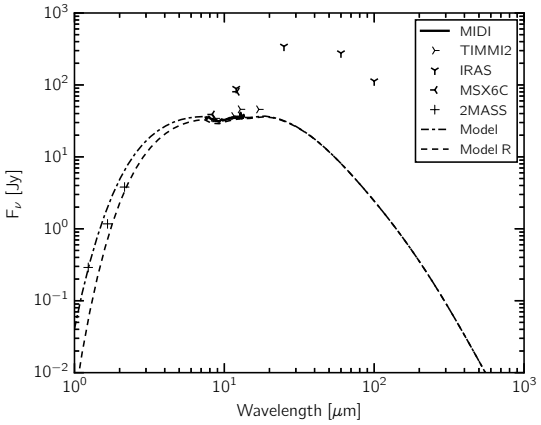

Figure 4.8: Spectral energy distribution of Menzel 3, the dashed and dot-dashed lines represent the modelled RT flux for the 14-parameter solution. The dot-dashed line is non-reddened, and the dashed line is reddened with $E(B-V) = 0.625$.

4.4.1 Solution interpretation

As indicated, the Mz3 GADRAD solutions are represented by parameter probability density functions, which approximate the underlying objective function near the global minima. The final solution is represented by the median point estimate of the distribution (which approximates the global minima). However, the result is in fact only a quasi-solution, representing an approximate solution of a model class or family only. The model class in this instance represents only a subset of all potential models, in which the GADRAD solution provides an estimate to the good fitting solutions of the model in question. The chosen model however, is formed from empirical prior knowledge (which introduces biasness), that may in fact represent a model class far removed from that that describes the true object.

Evidence of model differences have been acknowledged, for example the systematic differences observed between the model and the observational data products (differences which are similarly seen in C07). However, with the existence of noise, an exact solution to an inverse type problem is inconsequential, as an infinite number of solutions exist. In this instance a better approximation of the true object is a solution that discourages model complexity and avoids data product overfitting, ideas which stem from regularisation theory and maximum entropy arguments. It should also be noted that there is the potential of the GADRAD solution to be reflective of the termination criteria or irregularities of the given GA, rather than the underlying parameter distribution. Estimations to the scale of the effect would require more rigorous analysis, but is worth pursuing. The models chosen to represent Mz3 though not ideal, evident in the systematic differences observed, as well as the introduction of modest parameter degeneracies (the dust parameters for example), is proposed to be simple enough to avoid overfitting, yet represents a model class that generalises well.

4.5 Discussion

4.5.1 Comparing the results with Chesneau et al.

In comparing residuals of the visibility and spectrum fits of the 10-parameter GA, 14-parameter GA and the C07 RADMC-3D implementation result, no significant differences are seen, though a slight improvement to the fit is observed in both the 10- and 14-parameter cases. However, it is important to stress the fundamental difference between our approach and that of C07. Our results are estimated using the median point estimate of the $N_{\mathrm{GA}} = 100$ density distributions, and this measure, while not necessarily being the best solution in terms of the overall χ^2, ultimately provides a better representation of the areas of parameter space that provide acceptable model solutions. When considering an ill-posed inverse type problem of this type, in which many reasonable solutions exist, it is important to estimate the acceptable parameter ranges via the resulting parameter probability density function and the error bars which they represent.

Of additional importance are the *systematic* similarities that exist between the C07 result, and the 10 and 14-parameter GADRAD findings, because, it is evident, there exist some similarities between the residuals. With similar disc environments

results, we conclude that the structures adopted (the model class) are likely too simple an approximation. After all, the perfect symmetry of the disc and the environment adopted, are unlikely to accurately represent the post-AGB object. Introducing more parameters to overcome these systematic differences, such as removing symmetry or adding more complex structure or dust distributions, however, will most likely provide no further information pertaining to the object, but instead result in overfitting of the data products.

Our modelling shows that an inner silicate disc is unlikely to share the alignment (i.e., inclination of $i \sim 115°$, and position angle of $-4°$) of the much larger chakram structure inferred by Santander-García et al. (2004) and Guerrero et al. (2004), and instead favour a disc closely aligned with the equatorial symmetry of the lobes (i.e., with a position angle of 5°). Our model shows close agreement with the environment described by C07. The distance, outer-disc radius and mid-plane density factor in particular, however, show some level of disagreement, with the C07 equivalent values falling outside the 95% confidence ranges determined here. Overall however, our findings closely agree with those of C07, we confirm that an amorphous circumstellar or circumbinary silicate disc likely resides at the core of Mz3, although our analysis suggests that it is likely more compact (with a smaller outer-disc radius and larger mid-plane density factor), but with a larger inner-disc radius. We also determine that the disc is likely 4 times more massive than what was determined by C07, and the system is overall located farther than the value adopted by C07.

4.5.2 The shaping history of Mz3

The question of whether Mz3 is a symbiotic nebula is central, because the symbiotic binary is a wide binary and the shaping opportunities it affords are fundamentally different from those of other binary configurations. We argue here, as did C07 based on a different line of reasoning, that the central star is not a giant (RGB nor AGB) and that the system, if indeed a binary is still present at the core of the nebula today, is not a symbiotic. We argue that our star is a post-AGB star, based on the parameters derived from this study and their confidence intervals.

The star was found here to be a 35 000-K, 12 000-$L_\odot$ (3-$R_\odot$), post-AGB star on its way to the white dwarf cooling track. The mass of the star, comparing its luminosity to the stellar evolutionary tracks of Miller Bertolami (2016) should be just larger than 0.66 $M_\odot$. However, this star would, according to the same tracks, reach a temperature of 35 000 K in less than 100 years, making the nebular kinematic ages all too large by approximately one order of magnitude. To reconcile our results with the Miller Bertolami (2016) tracks, we would have to assume that the central star has a luminosity at the lower end of its error range, namely $\sim$8000 $L_\odot$ and a temperature of 55 000 K, which exceeds our upper error bar (47 000 K). In that case the time to transition between the AGB and the current location on the HR diagram would be of the order of 1000 years, more in line with the measured nebular ages. We therefore conclude that our derived parameters are somewhat inconsistent with AGB to post-AGB transition of a single star, though not right outside the domain of possibility.

We now consider the possibility that the ejection may have been due to a close binary interaction, which would have disturbed the regular AGB evolution. In par-

ticular, taking as an example a common envelope interaction (Ivanova et al., 2013; Paczynski, 1976), we know that the envelope removal is almost instantaneous, as is the orbital reduction (e.g., Iaconi et al., 2017), something that would accelerate the left-ward evolution on the HR diagram. This would give us a younger nebula compared to what is inferred using single-star tracks, the opposite of what is observed.

In order to observe a nebula that looks *older* than explained by the evolution of the central star, the only possibility we are aware of is that the binary interaction caused some post-interaction material fall-back, leading to accretion onto the post-AGB star. This is hypothesised to be able to slow the evolution of post-AGB stars allowing the nebula to expand while the star does not move towards the white dwarf cooling track as quickly (van Winckel et al., 2009).[2]

The considerations above leave the original question wide open. What collimated the outflow? C07 and, before them, Smith & Gehrz (2005) argued that the small disc at the core of Mz3 is of too low a mass to have influenced the much more massive outflow. Smith & Gehrz (2005) measured the total mass of the dust in the lobes of Mz3 to be 2.6×10^{-3} $M_\odot$, which should be compared to our measured disc dust mass of 3.5×10^{-5} $M_\odot$ (see Table. 4.1).

On the other hand, the estimated densities and velocity contrast of the outflow, assuming typical AGB mass-loss parameters (i.e., an AGB mass loss rate of 10^{-5}-10^{-4} $M_\odot yr^{-1}$, and a velocity of 10-20 km s^{-1} Renzini 1981; Bloecker 1995), is estimated to be ∼100 times larger than that of the disc's inner rim (3.3×10^{-15} g cm^{-1} for the outflow, 2.7×10^{-15} g cm^{-1} for the disc, where we have used a gas-to-dust ratio of 100).[3] If so, then the argument can be made that such a disc, if formed before the outflow event, may perhaps play some role as a collimating agent.

As an alternative to the collimation-by-disc scenario both Smith & Gehrz (2005) and C07 suggested that the ejection was already bipolar and launched via jets, similar to the scenario described by Sahai & Trauger (1998), Soker & Rappaport (2000) and García-Arredondo & Frank (2004). The problem with this scenario is that a jet launched magneto-centrifugally via an accretion disc (Blandford & Payne, 1982), presumably formed around the companion during the AGB, needs an accreted mass that is 2.5 to 10 times larger than the mass ejected by the jet. So if the jet launches 0.6 $M_\odot$ (Smith & Gehrz, 2005), 1.5-6.0 $M_\odot$ must have been accreted onto the companion. Assuming the original companion to be a low mass main sequence star (∼0.5 $M_\odot$), accretion would have made it into a 2-6.5 $M_\odot$ star (where the lower efficiencies are preferred, making the higher masses more likely). While hiding a six-solar-mass main sequence companion may not be out of the question inside the very optically thick disc, another argument against this scenario presents itself.

The accretion rate needed to eject the massive jets is high and such large values are unlikely to be achieved in a wind accretion or even in a Roche-lobe over-

[2] The post-AGB binaries for which accretion has been hypothesised to have slowed down their evolution tend not to have a visible nebula, and are always in binaries with periods of the order of 100-2000 days. Exceptions exist, for example the Red Rectangle (Bujarrabal et al., 2016). It maybe problematic to suggest that Mz3 belongs to this class because many of its characteristics are quite different from those of these post-AGB objects.

[3] The outflow density is the calculated instantaneous density at the disc's inner rim following isotropic mass-loss over the period $t = r_{in}/v_{wind}$. I.e., not accounting for mass accumulation.

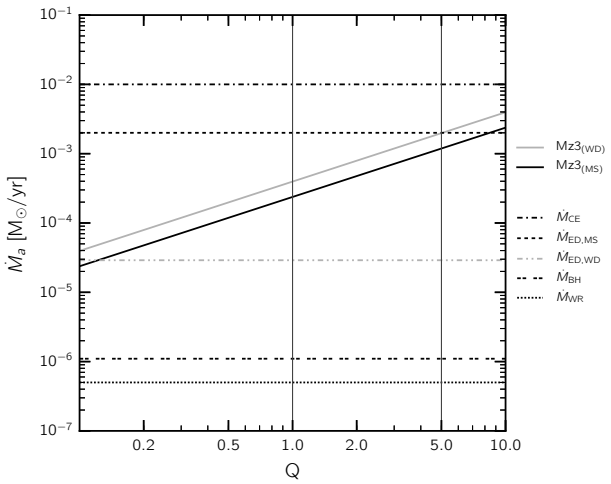

Figure 4.9: Theoretical mass accretion rate onto a putative companion versus efficiency parameter Q for Menzel 3 and Minkowski 2-9 following Blackman & Lucchini. The accretion mechanisms (horizontal lines; from top to bottom) for a 1-$M_\odot$, 1-$R_\odot$ main sequence (MS) star and a 0.6-$M_\odot$, 0.014-$R_\odot$ white dwarf (WD) star represent: common envelope accretion ($\dot{M}_{CE}=10^{-2}$ $M_\odot yr^{-1}$ with $\dot{M}_{CE,MS}=\dot{M}_{CE,WD}$); Eddington accretion for a MS star ($\dot{M}_{ED,MS}=2\times10^{-3}$ $M_\odot yr^{-1}$); Eddington accretion for a WD star ($\dot{M}_{ED,WD}=2.9\times10^{-5}$ $M_\odot yr^{-1}$); Bondi-Hoyle accretion ($\dot{M}_{BH}=1.1\times10^{-6}$ $M_\odot yr^{-1}$ with $\dot{M}_{BH,MS}=\dot{M}_{BH,WD}$) and, finally, accretion caused by wind Roche lobe overflow ($\dot{M}_{WR}=5\times10^{-7}$ $M_\odot yr^{-1}$, where again $\dot{M}_{WR,MS}=\dot{M}_{WR,WD}$). The Mz3 WD and MS accretion cases are plotted as the grey and black solid lines respectively, M2-9 equivalents are represented by the long dashed lines. For a given Q value, viable accretion mechanisms are those found above the object's estimated accretion.

flow scenario. We have here used equation 6 of Blackman & Lucchini (2014) to determine the minimum accretion rate required to form the lobes of Mz3:

$$\dot{M}_{\rm a} \geq 10^{-4} \left(\frac{Q}{2}\right) \left(\frac{M_{\rm a}}{\rm M_\odot}\right)^{-1/2} \left(\frac{R_{\rm a}}{\rm R_\odot}\right)^{1/2} \times \left(\frac{M_{\rm j,ob}}{0.1\dot{\rm M}_\odot}\right) \left(\frac{v_{\rm j,ob}}{100\ {\rm kms}^{-1}}\right) \left(\frac{t_{\rm acc}}{500\ {\rm yr}}\right)^{-1}, \qquad (4.1)$$

where Q is an efficiency parameter typically between 1 and 5 (Blandford & Payne, 1982), $M_{\rm a}$ is the accretor's mass, $R_{\rm a}$ is the accretor's radius, $M_{\rm j,ob}$ is the observed outflow mass, $v_{\rm j,ob}$ is the observed outflow velocity and $t_{\rm acc}$ is the timescale of the accretion event. Using an outflow mass of 1.9 $\rm M_\odot$, $v_{\rm j,ob}$ = 90 km s^{-1} and accretion time of 1800 yr (e.g., Santander-García et al., 2004; Smith & Gehrz, 2005), we obtain the minimum accretion rate that can cause the observed jets. This is plotted as a function of Q in Figure 4.9, which is equivalent to figure 1 of Blackman & Lucchini (2014).

As we can see from Figure 4.9, we obtain a limiting value that is only consistent with a common envelope accretion scenario or Roche lobe overflow accretion onto a main sequence star. In fact the value for Mz3 is comparable to the largest value obtained for the objects tested by Blackman & Lucchini (2014), though we note that our adopted outflow mass is derived from the dust mass rather than from molecular lines probing the gas mass more directly and maybe more uncertain. However, even arguing for a dust mass 10 times lower, still leaves the common envelope as the preferred scenario.

This type of argument gives us a clue that a common envelope must have taken place. However, one more ingredient is needed, because a non-magnetic common envelope ejects mass preferentially along the equatorial plane (e.g., Passy et al., 2012), contrary to the clearly bipolar ejection characterising Mz3. We would therefore have to invoke a magnetic common envelope winding the field to cause a magnetically-driven explosion (Nordhaus et al., 2007). The winding of the magnetic field associated with the giant may have lead to intensification (Regős & Tout, 1995; Nordhaus & Blackman, 2006; Tocknell et al., 2014) and final ejection in a polar direction via a magnetic tower (Huarte-Espinosa et al., 2012). While this may be the underlying mechanism for one or more of the ejections (if indeed there are separate ejections as suggested), there are clearly further complexities.

The observation of an X-ray point source as well as diffuse X-ray emission in Mz3 by Kastner et al. (2003) is not inconsistent with this scenario, which could have left a close binary in the core of this nebula, where the companion accretion of gas may have spun it up rejuvenating the corona (as likely observed in other post-common envelope binaries by Montez et al., 2010, 2015).

In conclusion, while a magneto centrifugal launch in a strong binary interaction seems to be implied by the outflow power of many collimated objects classified as PPN, the broad variety of many of the characteristics of these objects leave many questions to be answered. It is likely that the VLTI dusty discs still have something to tell us, particularly when their kinematics, rotation properties and angular momenta are surmised by observations such as those achievable with ALMA.

Chapter 5

Minkowski 2-9

5.1 Background

Minkowski 2-9 (henceforth M2-9) or Minkowski's Butterfly Nebula (Minkowski, 1947; Acker et al., 1992), is a young bipolar nebula with a tightly-pinched waist and stunning, highly collimated axisymmetric outflows (see the Hubble image of M2-9 in Figure 5.1). M2-9 shows many similarities with the bipolar nebula Mz3, in both outflow energy and morphology, as well as spectral energy contributions. The objects are sometimes described as spectroscopic twins. MIRLIN infrared images for example (e.g., Smith & Gehrz, 2005), show the central source contribution from the two objects is comparable, with an N-band flux of $\sim$30 Jy found in both instances. This similarity is also seen in the high resolution MIDI spectrums. There does however, exist some differences. IR emission of molecular hydrogen for example is seen in Mz3, but not observed in M2-9 (Smith, 2003). Additionally, the contribution to the spectral energy distribution from the extended dust in the lobes is lower in M2-9 than in Mz3 (e.g., Smith & Gehrz, 2005).

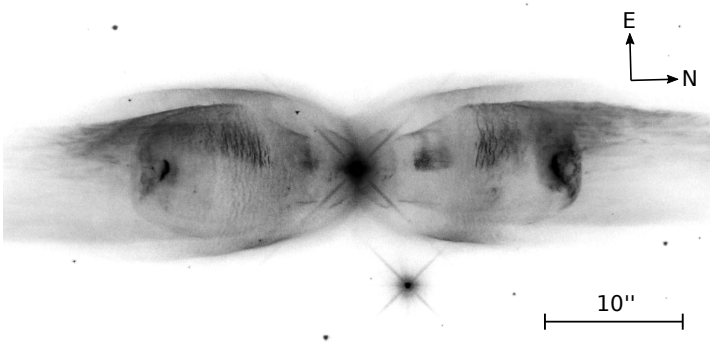

Figure 5.1: Composite 502-673nm HST grey-scale image of Minkowski 2-9.

Despite no direct detection of binarity in M2-9, much evidence has been presented in the literature that supports a binary central star. For example, optical emission

line ratios (i.e., λ4363/Hγ vs. λ5007/Hβ; e.g., Gutierrez-Moreno et al., 1995) as well as NIR colour-colour diagrams, which act as diagnostics to differentiate symbiotic systems from single ionising PN sources (Schmeja & Kimeswenger, 2001), suggest M2-9 is a D-type symbiotic (e.g., Clyne et al., 2015). Something that would indicate the preference of an AGB star and a WD companion. Double-peaked Hα emission is also observed in the central region (e.g., Clyne et al., 2015), suggesting energetic (high-mass loss and fast) stellar winds. The spectral flux peak observed at $\sim$19μm (e.g., Lykou et al. 2011, henceforth L11; see also the SED in Figure 5.8) is also found to be common to the D-type symbiotic systems (e.g., Clyne et al., 2015). Similar conclusions were made by Schmeja & Kimeswenger (2001).

Perhaps the most persuasive argument of binarity is however seen in the *lighthouse* beams (e.g., Allen & Swings, 1972) that are seen to rotate with a period of $\sim$90 years within the bipolar lobes. The lighthouse effect is thought to be created either directly (e.g., Corradi et al., 2011) or indirectly from bipolar jets (e.g., Livio & Soker, 2001). It is thought that such jets would interact with the lobe walls, or the jets would act to clear a path to the inner lobe walls allowing for beams of ionising radiation (originating from a white-dwarf) to reach the inner walls (e.g., Livio & Soker, 2001). Jet rotation is likely caused by the orbital motion of a binary system.

The high level of collimation seen in M2-9's lobes is thought to originate from two equatorial rings. Castro-Carrizo et al. (2017), in modelling the structure of molecular gas in M2-9 from ALMA observations, found evidence of these two structures of cool molecular gas with mass of $\sim 5\times10^{-3}$ M$_\odot$. Their origin is postulated to be two separate binary ejection events, the first $\sim$1400 yr ago, and a second some $\sim$900 yr ago. Higher resolution infrared VLTI MIDI observations of M2-9 (e.g., L11), reveal a similarly orientated, but much smaller circumstellar disc. The disc was found to be similar in nature to that found in Mz3, and because of its silicate composition it is suggested that it too may have originated from the envelope of an AGB star. The role the disc plays in nebula collimation is however uncertain. The question is whether disc structures collimated the bipolar outflow or whether they are the by-product of a different mechanism itself responsible for the collimation.

Similar to many early attempts to constrain radiative transfer models to interferometric data products, the L11 analysis relies on *ad-hoc* fitting, in which only a few environmental parameters are explored. In the following sections we apply `GADRAD` to the VLTI MIDI data products of M2-9 present by L11 study. As has been seen in the previous chapter in the analysis of Mz3, `GADRAD` is well suited to the task of systematically fitting radiative transfer models to interferometric data products.

5.2 Observations

Measurements of M2-9 were taken with the MIDI instrument at the VLTI. Observations were taken in April, June and August 2007 and March 2008, final data products adopted here are those found in L11 (the observing log is presented in Table 5.1). Data was reduced using the MIA and EWS software packages. Observations were taken with two Unit Telescopes in the `SCI_PHOT` mode and the

low spectral resolution mode was chosen (R = 30; see Section 2.3.1). Four visibilities resulted. Errors were estimated to be of the order of 5-10%, while spectrum uncertainties were found to be larger (10-13%). For more information regarding the observation and data reduction process see section 2.1 of L11.

Table 5.1: Minkowski 2-9 observing log.

Label	Date	Baseline (UTC)	Projected Baseline Length (m)	PA (°)
B_1	2007-04-11	UT2 – UT3	40.2	107.3
B_2	2007-06-28	UT2 – UT3	47.3	126.0
B_3	2007-08-28	UT2 – UT3	39.7	44.0
B_4	2008-03-28	UT3 – UT4	45.1	39.0

Calibrators: HD 116870 K5III 2.44±0.12 mas, HD 163917 G9III 2.75±0.11 mas, HD 167618 M3.5III 11.33±0.1 mas, HD 175775 G9III 3.26±0.23 mas, HD 152820 K5III 2.57±0.34 mas.

5.3 Reproducing the Lykou et al. model

The disc model adopted in the L11 analysis is the simple, azimuthally symmetric disc density structure of Shakura & Sunyaev (1973; this disc is introduced in Section 2.5.2.1). We begin by attempting to reproduce the M2-9 results as presented in the L11 study. The L11 model was obtained with a different Monte-Carlo RT code, `MC3D` (e.g., Wolf, 2003; Wolf et al., 1999), than the one we adopt here (`RADMC-3D`), this confirmation step will allow us to determine potential differences between the two codes.

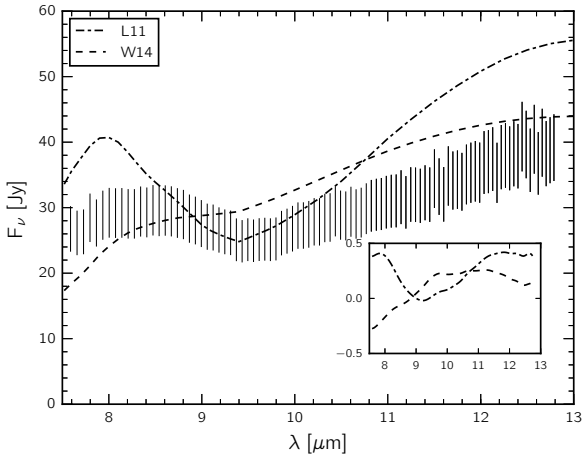

Figure 5.2: The MIDI spectrum is represented by the vertical error bars. The resulting flux modelled by the `RADMC-3D` code using the Lykou et al. (2011) parameters, is represented by the dot dash line. The resulting flux modelled by the `RADMC-3D` code using the parameters of Werner et al. (2014) are represented by the dashed line. Corresponding residuals are presented in the inset as percentages.

The L11 input parameters are presented alongside other literature values in Table 5.3 (for direct comparison see Table 5.4). The resulting MIDI spectrum and

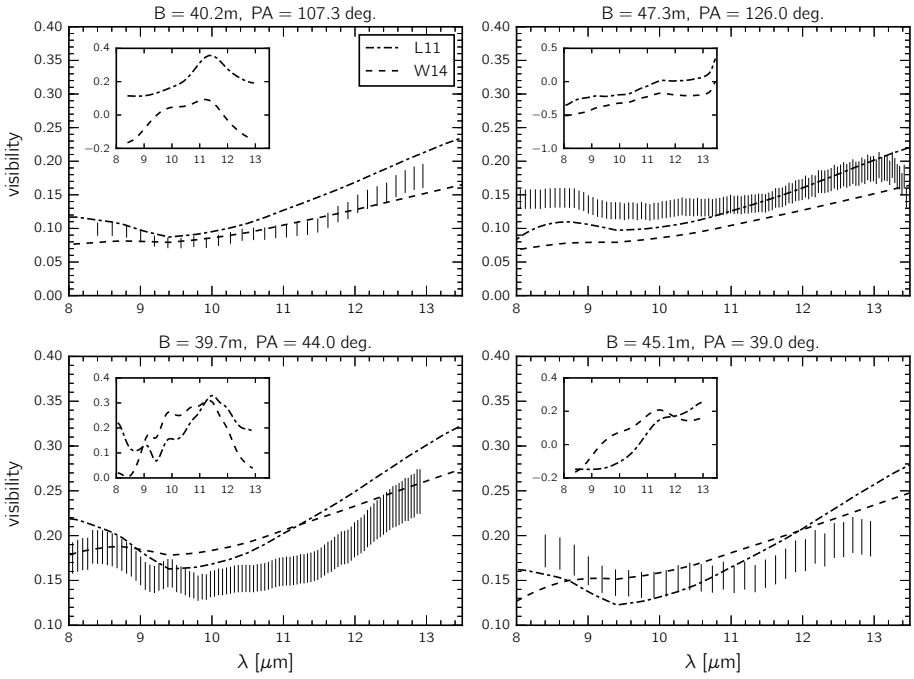

Figure 5.3: The MIDI visibilities are represented by the vertical error bars. The resulting visibilities modelled by the RADMC−3D code using the Lykou et al. (2011) parameters, is represented by the dot dash line. The resulting flux modelled by the RADMC−3D code using the parameters of Werner et al. (2014) visibilities are represented by the dashed line. The corresponding residuals are presented in the inset as percentages.

visibilities determined using the RADMC−3D code and the parameters of L11 are presented in Figures 5.2 and 5.3 respectively. It can be seen that the resulting RADMC−3D L11 parameter implementation produces MIDI visibilities and spectrum (between 8 and 20 μm) that agree closely with the results presented in L11 (differences are of the order of $\lesssim$6%). However, the resulting RADMC−3D L11 implementation's spectrum, at shorter wavelengths, shows some discrepancy to that presented in L11. This is observed in the both the un-reddened and reddened spectral energy distributions presented in Figure 5.4. We redden the RADMC−3D L11 disc according to the extinction values presented in L11 e.g., A_v=2.5 following (Torres-Peimbert & Arrieta 1998; we thus adopt $E(B-V) = 0.81$ assuming $R_v = 3.1$). The reddened model result however shows an energy excess when compared to the literature flux measurements between 3 and 5 μm (see Figure 5.4). A discrepancy that is not seen in the model presented in L11.

Table 5.2: Minkowski 2-9 aperture photometry.

Instrument/ Reference	Wavelength (μm)	Flux (Jy)	Aperture
2MASS	0.053	4.6	4″
	1.662	0.219	4″
	2.159	1.06	4″
SOFIA	6.6	24	3.68″
	11.1	32	3.85″
	19.7	58	3.76″
	24.2	55	4.19″
	33.6	63	4.42″
	37.1	48	4.51″

There are many potential reasons that could explain the differences seen between the L11 fits and the RADMC−3D L11 implementation. We consider the following four: (i) using two different radiative transfer codes (a scenario we feel is unlikely, considering that we successfully reproduced the Mz3 environment of Chesneau et al. 2007b which was similarly modelled with RADMC−3D). (ii) a difference in the dust used between the two simulations (dust files are not disclosed in L11 for example; we adopt the amorphous silicates of Weingartner & Draine 2001), though we would perhaps expect differences in selected dust composition to result in changes to the resulting spectrums and visibilities across the entire bandwidth (something that is not seen), (iii) our incorrect assumption on the R_v value adopted by L11, which again is not presented by them and (iv) a difference in the reddening technique adopted, for example we rely on the Cardelli et al. (1989) relationship with updated near-IR coefficients from O'Donnell (1994), while L11 adopt the reddening following the Savage & Mathis (1979) law. The determination of the source of the discrepancy(ies) would require confirmation steps beyond the scope of this study. Despite the differences seen at the shorter wavelengths, we have confidence in our radiative transfer implementation evident in the successful reproduction of the MIDI visibilities and spectrum.

Table 5.3: Minkowski 2-9 literature parameter values.

Parameter		Lit. Values	Ref.	GA Range (Min., Max.)
Stellar Parameters				
Temperature (T)	10^3K	5, 15, 30	e,d,c	(4, 32)
Luminosity (L)	$L_\odot$	2500	e,d	(1500, 6000)
Distance (D)	kpc	0.64, 0.65, 1.0, 1.2, 1.3	a,f,(b,c),(e,d),g	(0.6, 1.5)
Orientation				
Inclination (i)	deg	72, 73, 74, 75, 79	g,(h,f),d,a,i	(70, 90)
Position angle (PA)	deg	-3, -2	f,d	(-12, 0)
Disc Characteristics				
Inner radius ($r_{\rm in}$)	AU	15	e,d	(5, 40)
Outer radius ($r_{\rm out}$)	AU	800, 900	e,d	(500, 1000)
Mid-plane density factor (α)	-	2.0, 2.2	d,e	(1.5, 5.0)
Vertical-plane density factor (β)	-	0.9, 1.23	d,e	(0.6, 1.5)
Scale height (h_0)	AU	36, 37	d,e	(10, 40)
Dust mass ($m_{\rm disc}$)	$M_\odot$	4.0×10^{-6}, 1.5×10^{-5}	c,d	$(10^{-7}, 10^{-4})$
Dust Parameters				
Minimum grain size ($a_{\rm min}$)	μm	0.01, 0.05	e,d	(0.005, 5)
Maximum grain size ($a_{\rm max}$)	μm	1.0, 5	d,e	(0.5, 1000)
Size distribution ($a_{\rm pow}$)	-	3.5	d,e	(2, 6)

[a]Schwarz et al. (1997); [b]Hora & Latter (1994); [c]Smith & Gehrz (2005); [d]Lykou et al. (2011); [e]Werner et al. (2014); [f]Castro-Carrizo et al. (2017); [g]Corradi et al. (2011); [h]Clyne et al. (2015); [i]Goodrich (1991).

Following the L11 disc model, measurements of the central region of M2-9 was taken with SOFIA's FORCAST instrument (e.g., Werner et al. 2014; henceforth W14). It was found that the L11 models were brighter than the SOFIA data at 19.7 and 24.2μm (see Table 5.2). In attempting to reconcile the disparity, W14 attempted to fit their own stratified disc model to M2-9. The W14 disc parameters can be found in Table 5.4. The W14 model however, did not attempt to fit the L11 MIDI visibilities. Similarly, the MIDI spectrum was not prioritised. We re-implement the W14 model parameters with `RADMC-3D`, it is evident that although the model fits the SOFIA flux data well (the resulting SED is presented in Figure 5.4), it poorly fits the MIDI data products (see the resulting N-band spectrum and MIDI visibilities in Figure 5.2 and 5.3 respectively).

These inconsistencies make M2-9 a good candidate for application of `GADRAD`, which allows us to thoroughly explore parameter space in an unbiased and self-consistent fashion. We initiate the search of parameter space to determine whether better self-consistent descriptions of the disc structure in M2-9 can be determined by applying the GA.

5.4 Application of the GA parameter search to M2-9

A total of 14 parameters describe the radiative transfer environment, these parameters include: the stellar effective temperature, stellar luminosity, inclination and position angle, inner and outer-disc radii, mid-plane density factor, vertical plane density factor, scale height and disc mass. We also explore parameters controlling

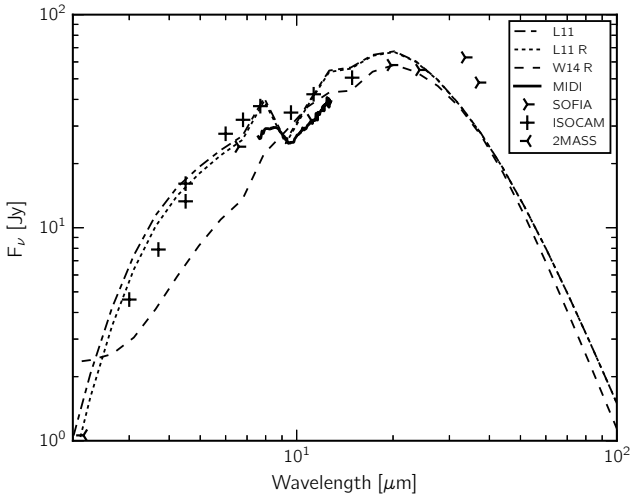

Figure 5.4: Spectral energy distribution of Minkowski 2-9, the dot-dashed and dotted lines represent the modelled RT flux for the Lykou et al. (2011) solution. Flux discrepancies are seen between both the Lykou et al. (2011) reddened model (L11 R; dotted line) and un-reddened model (L11; dot-dashed line) and the ISOCAM measurements. We also present the resulting SED from the disc presented in Werner et al. (2014) (W14 R; dashed line). Both reddened models adopt $E(B-V)=0.82$. This model is seen to fit well the SOFIA measurements at 19.7 and 24.2μm as it was designed to do.

the object's distance, minimum and maximum dust grain sizes and the grain size distribution within the disc.

We begin our genetic algorithm by initialising a search within parameter ranges as determined in the literature. The initial sampling distribution is flat and the search domain is presented in Table 5.3. Based on our successful models of the similar post-AGB object Mz3 (see Section 4.3) we adopt similar GA operator parameters, that is: a mutation rate $p_m=0.035$, a crossover rate $p_c=0.65$, and a population size $n_{\rm pop}=850$, we iterate for approximately $n_{\rm gen}=400$ generations (GA parameters are listed/explained in Section 3.2.3). Following the application of 12 initial GAs, no anomalies or problems with convergence are seen. We proceed to construct parameter probability density functions from $N_{\rm GA}=100$ algorithms. The probability density functions are calculated from the fittest solution from each GA. The resulting parameter density functions are presented in Figure 5.7.

5.4.1 Results

The radiative transfer model solution is calculated from the median point estimate of the resulting probability density distributions (see Section 3.3.1). Similarly to the analysis of Mz3, better solutions in terms of the overall χ^2 measure exist, but they provide little information regarding model confidence. Final parameter values and errors (estimated from the 95% confidence interval of the distributions) are presented in Table 5.4. We also quantify the variance of the parameters by calculating the distributions' resulting MAD measure ($\hat{\sigma}$), where higher $\hat{\sigma}$ values indicate higher parameter variance. The MAD value is introduced in Section 4.3.2, and is essentially a measure of how well constrained a parameter

is. For example, an ill-constrained parameter shows a broad probability density function and returns a high value $\hat{\sigma}$. On the other hand, well constrained parameters (non-degenerate) show a low value $\hat{\sigma}$. We present the resulting MAD values in Table 5.4.

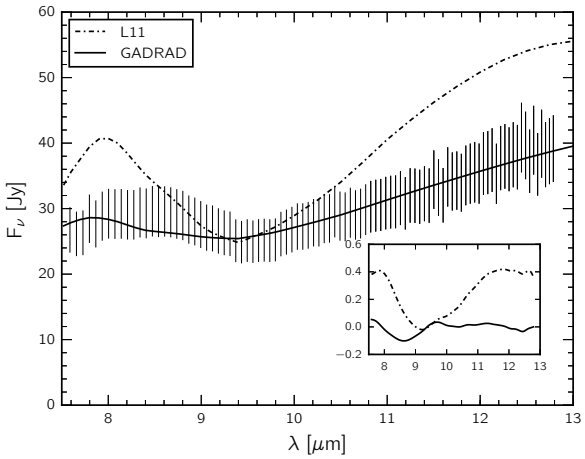

Figure 5.5: The MIDI spectrum is represented by the vertical error bars. The resulting flux for the GADRAD model (solid line) is presented alongside the RADMC3D Lykou et al. (2011) parameter implementation (dot dash line) for comparison. The corresponding residuals are presented in the inset as percentages.

We present the MIDI spectrum, and visibilities of the resulting median point estimate model (Table 5.4) in Figures 5.5 and 5.6, respectively. In both instances it can be seen that our model better represents the MIDI data products than the RADMC−3D L11 model implementation. Additionally the model is found to not exceed the energy constraints of the SOFIA flux measurements. This result affirms the benefits of model fitting through application of an optimisation algorithm. The result is perhaps expected however, as the ad-hoc approach of the L11 model was found by favouring good visibility fits over a well represented spectrum. Similar approaches were used to determine the W14 model, which was constructed to satisfy flux measurements observed at 19.7 and 24.2μm.

GADRAD affords us the ability of finding the best fitting model solution that falls within such a set of constraints. However, in this instance no such constraints were necessary as good representations were found of MIDI data products, and other data. A plot of the flux values for GADRAD model SED and the L11 RADMC−3D model implementation are compared in Figure 5.5.

It is evident that some discrepancies exist between the parameters derived in our model and the L11 and W14 models (i.e., see Table 5.4). Most noteworthy are the differences in stellar luminosity. The central source described by our model is significantly more luminous than that found in L11 and W14 (i.e., 2500 L$_\odot$ vs. $3960^{+0.9}_{-0.8}$). Following integration over the IRAS measurements of M2-9 between 2.5-120μm, W14 estimated the total isotropic luminosity to be ∼1530 L$_\odot$. This finding however assumes that all the stellar luminosity is being captured within the dusty disc and re-emitted in the IR. However, when there exists a non-isotropic distribution about the star, such as a disc for example, stellar luminosity will escape and this method underestimates the true stellar luminosity. Thus, we find

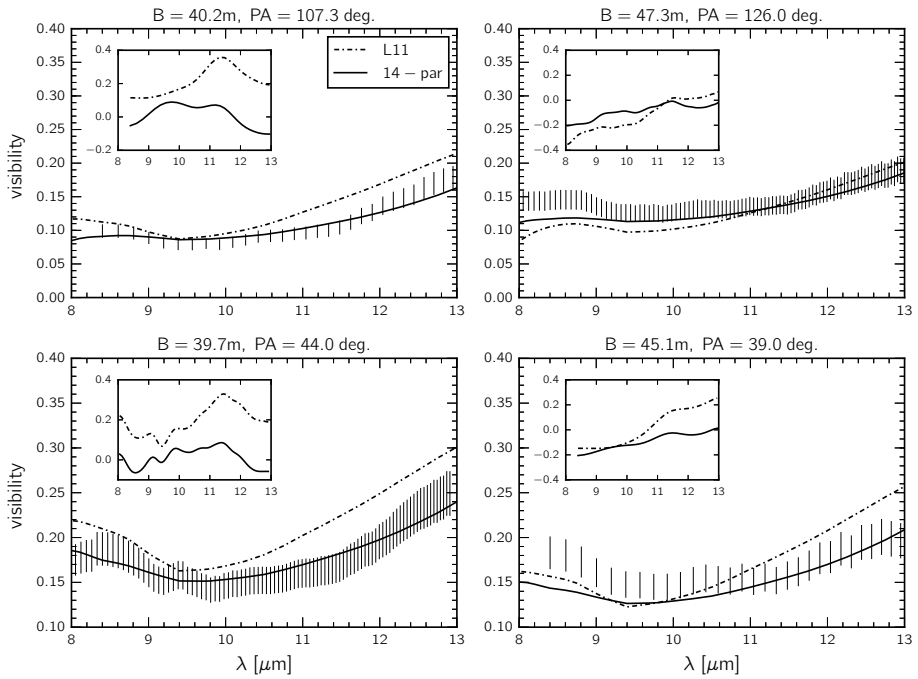

Figure 5.6: The MIDI visibility is represented by the vertical error bars. The resulting visibilities for the GADRAD model (solid line) is presented alongside the RADMC3D Lykou et al. (2011) parameter implementation (dot dash line) for comparison. The corresponding residuals are presented in the inset as percentages.

Table 5.4: Minkowski 2-9 - Lykou et al. (2011), Werner et al. (2014) and GADRAD model comparison.

Parameter		W14	L11	GADRAD	$\hat{\sigma}$
Stellar Parameters					
Temperature (T)	K	5,000	15,000	$12,700^{+13,400}_{-7,000}$	0.167
Luminosity (L)	$L_\odot$	2,500	2500	$3,960^{+900}_{-800}$	0.062
Distance (D)	pc	1,200	1,200	$1,400^{+100}_{-200}$	0.029
Orientation					
Inclination (i)	deg	74	74 ± 1	79^{+6}_{-3}	0.010
Position angle (PA)	deg	-2	-2 ± 2	-7 ± 2	0.026
Disc Characteristics					
Inner radius ($r_{\rm in}$)	AU	15 ± 1	15 ± 1	18 ± 5	0.072
Outer radius ($r_{\rm out}$)	AU	800 ± 100	900	540^{+260}_{-230}	0.140
Mid-plane density factor (α)	-	2.2 ± 0.05	2.0 ± 0.1	2.9 ± 0.9	0.083
Vertical-plane density factor (β)	-	1.23 ± 0.02	0.9 ± 0.1	$1.1^{+0.2}_{-0.25}$	0.046
Scale height (h_0)	AU	37 ± 3	36 ± 2	28 ± 6	0.063
Dust mass ($m_{\rm disc}$)	$10^{-6}M_\odot$	10 ± 1	15 ± 5	$4.6^{+5.3}_{-1.9}$	0.010
Grain Parameters					
Minimum grain size ($a_{\rm min}$)	μm	0.01	0.05	$1.0^{+3.4}_{-0.9}$	0.280
Maximum grain size ($a_{\rm max}$)	μm	5.0	1.0	$3.0^{+60}_{-2.8}$	0.290
Size distribution ($a_{\rm pow}$)	-	3.5	3.5	$3.5^{+3.0}_{-2.2}$	0.292

that a higher luminosity is not inconsistent with their estimate.

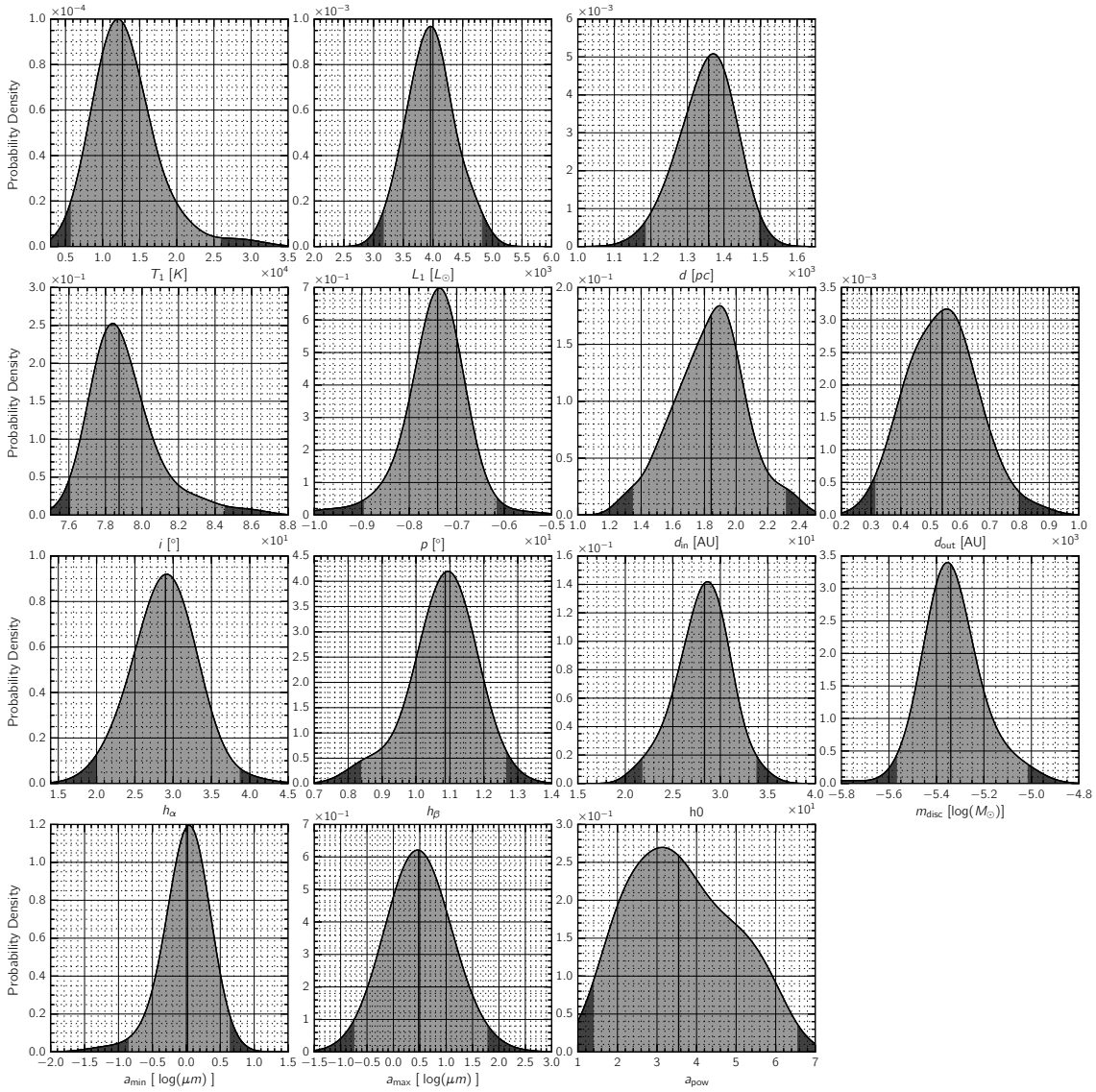

Figure 5.7: M2-9 parameter distribution functions. The solid vertical line represents the median point estimate of the distribution, with the grey area depicting the 95% confidence interval. The dark regions represent the 2.5% distribution tail.

Our parameters also shows a large discrepancy with the primary source temperature as estimated by W14. The temperature preferred by GADRAD is much hotter ($12,700^{+13,400}_{-7000}$K) than the stellar temperature $T = 5000$K of W14. Despite the high variance of the parameter ($\hat{\sigma} = 0.167$; a similar value to that found in the case of Mz3), the W14 value falls outside the resulting 95% confidence interval.

Similarly to the L11 findings, the shorter distance estimations of Schwarz et al. (1997, see also Castro-Carrizo et al. 2017; i.e., $\sim$ 650pc), proved difficult to fit, with the area of parameter quickly rejected by the search heuristic. The shortest allowable distance in this instance is found to be over 1100 pc. Interestingly, GADRAD

prefers slightly larger estimates for the object's location to that described by the literature 1400^{+100}_{-200}pc vs. 1300 ± 120pc (e.g., Corradi et al., 2011), though the distance value adopted by L11 (1200pc) falls within the GADRAD error estimates. We also find the disc orientation to be somewhat different than suggested by L11. We find a steeper, more inclined disc with $i = 79^{+6}_{-3}$ vs. $i = 74$, and a different position angle PA=-7 ± 2 vs. PA=-2 ± 2. We find our derived inclination to fit within the upper limits of the literature constraints. The resulting position angle, however, is unexpected. One would expect for instance that the disc would be aligned equatorially with respect to the nebula outflows which is estimated to lie between -3 and -2 degrees (e.g., Castro-Carrizo et al. 2017, L11). The best fitting position angle derived from the GADRAD model is however -7±2 degrees. The angle is found to be well supported, as very little variance is seen in the parameter as evident in the resulting MAD measure ($\hat{\sigma} = 0.026$). Sampling limitations cannot be blamed for the result either, as a large initial sampling domain was available to the parameter (i.e., 0, -12). When considering parameter correlations (as presented in the correlation coefficient matrix presented in Figure 5.9), we see that the position angle shows very little correlation with the other parameters, suggesting that the result is unlikely to be dependent on the influence of a second parameter. Further, high resolution measurements will be necessary to confirm the disc's true position angle.

We also find significant differences between the GADRAD outer disc radius and the L11 and W14 result. The GADRAD result of 540^{+260}_{-230} AU is smaller than that estimated by L11 and W14. However, the high MAD value ($\hat{\sigma} = 0.140$) confirms again (i.e., see Section 4.3) that the parameter is likely difficult to constrain. The outer-disc radius was also found to be ill-constrained in both the L11 and W14 models. Another disc parameter discrepancy of note is the disc mass, with a less massive disc favoured in our analysis (i.e., $1.5 \pm 0.5 \times 10^{-5}$ $M_{\odot}$ and $1.0 \pm 0.5 \times 10^{-5}$ $M_{\odot}$ vs. $4.6^{+5.3}_{-1.9} \times 10^{-6}$ $M_{\odot}$). It should be noted that the disc mass is found to be one of the best constrained parameters, with an estimated MAD value $\hat{\sigma} = 0.010$, suggesting we can be confident in our less massive disc mass estimate.

The minimum grain size was found to be much larger than that adopted in both the L11 and W14 studies. This larger minimum grain size is expected to reduce the overall energy of SED, which would explain the more luminous central source estimated, though a correlation between the minimum grain size and primary luminosity is not witnessed ($r = -0.17$). The only correlation of note in regards to the minimum grain size is the moderate negative correlation between the inclination angle with $r = -0.53$. This correlation, however, does not explain the higher inclination favoured by our model ($i = 78.8^{+5.8}_{-2.7}$ vs. $i = 74$ degrees) and larger minimum grain size ($1.0^{+3.4}_{-0.9}$ vs. 0.05 microns). Further analysis is required to determine the grain sizes and distributions that make up the silicate disc at the heart of M2-9. Yet, in describing the dust makeup of the outer lobes W14 finds comparable masses of small (radii $< 0.1\mu$m) and large (radii $> 1\mu$m) grains. W14 postulate, following the description of Jura et al. (2001), that the disc is likely made up of large grains with grain-grain collisions resulting in small grains that are driven with a higher ratio (but comparable masses) to the large grains, (from the disc) to the lobes by radiation pressure. The large minimum dust grain estimated by GADRAD is supportive of such a scenario.

The grain size distribution was poorly constrained (with $\hat{\sigma} = 0.292$), yet the

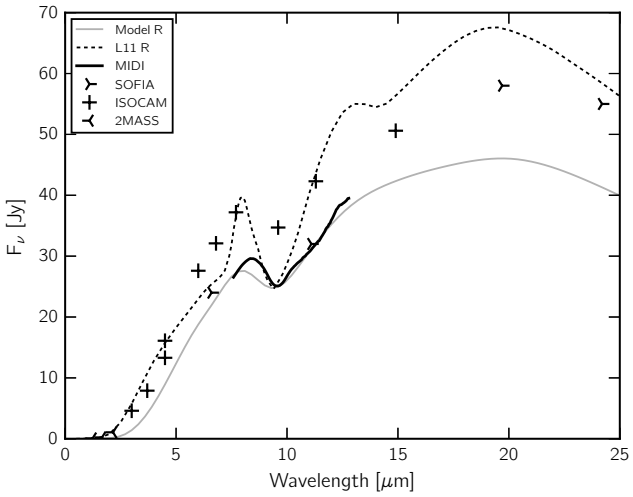

Figure 5.8: Spectral energy distribution of Minkowski 2-9, the solid grey line is the GADRAD model, for comparison we plot the RADMC-3D produced Lykou et al. (2011) implementation model in the dashed lines. The Lykou et al. implementation, shows a small excess with relation to ISOCAM data, and SOFIA flux measurements. Peak flukes in both instances are near $\sim$20μm.

resulting median was found to be close to that adopted by L11 and W14, though the result is perhaps more likely a product of the initial sampling symmetry of the parameter domain than an explicit description of an inherent property of the objects disc. Similar to the Mz3 analysis, we find the parameters controlling the dust grain sizes show high levels of variance. For example, we determine a MAD value for the minimum and maximum dust grain radius of $\hat{\sigma} = 0.280$ and $\hat{\sigma} = 0.290$ respectively. Similar to our Mz3 analysis, a quantification of the exact effect on the density functions of the remaining parameters is unknown. Qualitatively however we are likely to see the variance of the parameter solutions increase. The dust parameter's high MAD measures are however not too dissimilar to those found in the Mz3 model, in which degeneracy was found to have little effect on overall findings (when comparing the 10-parameter case with the 14-parameter case i.e., see Section 4.3.2 and 4.3.3).

To quantify potential model degeneracies we consider parameter correlations. Strong negative correlation ($r = -0.71$), is seen between the inner-disc radius and disc inclination. The inclination also shows a strong negative correlation ($r = -0.72$) with the vertical-plane density factor (h_β). Interestingly both these correlations are not seen in the case of Mz3 (with $r = -0.34$ and $r = -0.34$ respectively). Other correlations of note are those that exist between the mid-plane and vertical-plane density factors (i.e., h_α and h_β). They show strong positive correlation with $r = 0.65$, with the correlation re-reinforced through the respective positive correlations with the inner-disc radius, i.e., α–$r_{\rm in}$, $r = 0.83$ and β–$r_{\rm in}$, $r = 0.68$. Potential differences however, may exist in the correlation direction with the object's position angle (negative in the case of β with $r = -0.13$ and positive in the case of α with $r = 0.23$), which gives us enough evidence to suggest that parameter space should not be reduced through the adoption of a combined α and β parameter. A final correlation of note is the negative correlation that exist between the minimum grain size radii and disc inclination angle ($r = -0.53$)

which is similar to that found for Mz3 ($r = -0.61$). This correlation suggests that a more inclined disc has a similar effect to increasing the minimum grain size, both of which are expected to increase the disc opacity, for example.

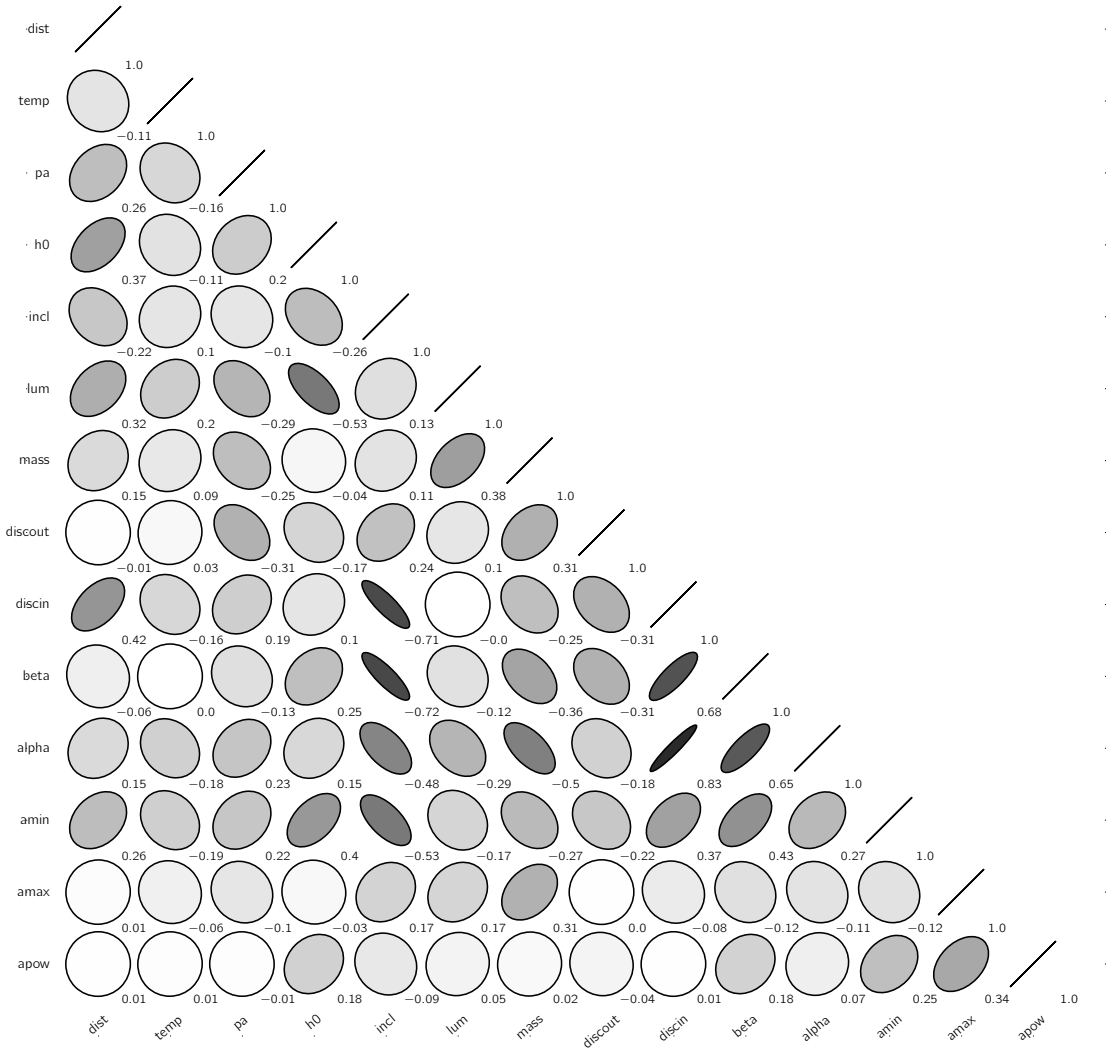

Figure 5.9: Visualisation of the correlation matrix depicting the correlation coefficient, r. The correlation coefficient is presented in the bottom right corner of each parameter correlation. Darker, more elliptical ellipses indicate a stronger correlation, and less correlated parameters are lighter in colour and more circular.

5.5 Summary and discussion

We have successfully found a self-consistent model that represents the MIDI spectrum and visibilities of M2-9. Similar to both L11 and W14, we propose that a silicate disc lies at the heart of the central source of M2-9. By employing a search

heuristic, we have fitted models to the MIDI data products as obtained by L11. Following the L11 study, W14 found the L11 model showed an energy excess with the SOFIA flux measurements at 19.7 and 24.2μm. In reconciling the disparity, W14 suggested an alternative disc, the main difference being a lower temperature central source (5000 K vs 15,000 K). The construction of the W14 disc however only considered the resulting SED measurements, and did not fit the initial visibilities presented in L11. The model found by GADRAD is found to be a good representation of the the MIDI measurements of L11 and the SOFIA flux values of W14.

The resulting GADRAD model shows some differences with both L11 and W14 models. For instance, we suggest a more distant and more luminous central source is likely. Disc orientation is also found to be more inclined, and the position angle of the disc is suggested to potentially lie at an angle slightly mis-aligned with respect to the outflows. For instance a disc aligned equatorially is estimated to be oriented with a position angle of -3 or -2 degrees (i.e., Castro-Carrizo et al. 2017, L11), which potentially falls outside the error estimates calculated by GADRAD (i.e., -7 ± 2 degrees). Further, high angular resolution observations are required to clarify the true orientation and the minor disparity. Our disc is also found to be less massive than both the L11 and W14 models.

We also determine that a larger minimum dust grain size is favoured, this is in accordance to the W14 analysis, in which the equal minimum to maximum grain mass ratio seen in the lobes is explained by a larger than typical grain radii in the disc (it is suggested that grain-grain collisions in a large grain disc create small grains which are blown out of the disc in higher proportion to the large grains by radiation pressure, resulting in the minimum to maximum grain mass ratio observed). We also find the grain size distribution parameter to be ill-constrained (in fact it showed the highest MAD value $\hat{\sigma} = 0.292$), suggesting, possibly in agreement with W14 that the grain distribution in the disc is not standard (i.e., not described by the standard Mathis et al. 1977 law). The high variance of the parameter is possibly testament to this. Or it may suggest we simply did not explore a broad enough range of the parameter and have not found a representative value (though the parameter domain is relatively broad with initial sampling of $a_{\rm pow}$ between 2 and 6). It may be that a different grain size distribution law to that of Mathis et al. (1977) is necessary to describe M2-9's circumstellar disc. Additionally it could be evidence of dust processing, or crystalline silicates, the latter of which has been detected (e.g., L11). Further observations will likely be required to determine which is the case.

5.5.1 Comparison with Mz3 and further considerations

Many characteristics identified in M2-9 are common to the bipolar nebula Mz3. These similarities are seen in both the morphological structures of the large scale outflows and their spectroscopic properties (e.g., Lykou et al., 2011). In comparison, Mz3 displays evidence of an equatorially-orientated amorphous silicate disc structure similar to that detected in M2-9. Similar inner-disc radii are also found (15^{+3}_{-4} AU for M2-9, and 18 ± 5 AU for Mz3), though in the case of M2-9 the disc is purportedly more extended ($\sim$ 540 AU vs. $\sim$290 AU). Traces of crystalline silicates may however be present in the case of M2-9 (e.g., Lykou et al., 2011), which is typical of longer lived discs surrounding post-AGB stars (e.g., Deroo

et al., 2007a), suggesting Mz3's disc may be more recently formed.

We find a similar SED flux peak at 19μm to that of L11, which fits with the D-type symbiotic description of Clyne et al. (2015). However, fitting potential symbiotic orbits within the inner-disc rim proves difficult. Though the orbital separation requirements of a symbiotic may be met (i.e., 10-15 AU; Gromadzki et al. 2009), relatively low-mass objects (a white dwarf with mass 0.5 $M_\odot$ and a companion of mass $\sim$0.25 $M_\odot$) are needed to explain the ($\sim$90 year) orbital period of the the *lighthouse* beam. Whether the orbital period is longer, however, and the lighthouse beams observed are an effect from jets, unrelated to the binary orbit is yet to be determined.

However, the stellar temperature and luminosity determined from our analysis, may exclude the symbiotic scenario (white dwarf and giant companion; e.g., Clyne et al. 2015). We consider the Miller Bertolami (2016) stellar evolutionary tracks, a 12,700-K 3960-$L_\odot$ post-AGB star would likely be of mass 0.55 $M_\odot$, which may support the hypothetical orbit described above. The central source of M2-9 is seen to reach this temperature within $\sim$1000 years of leaving the AGB. A value that may agree with the kinematical age of the outflow (i.e., 1200-2000 yr), single star transition from AGB to post-AGB can thus not be ruled out. Explaining the observed light curve, in addition to the energetic outflows in a single star context, however, becomes problematic. If we were to exclude a symbiotic binary as the cause of the accretion and outflow in the case of M2-9, we would have to invoke a triple star system, where one companion entered a common envelope and one remained farther out.

Finally, we determine potential routes of outflow formation, we again consider the Blackman & Lucchini (2014) formula (Equation 4.1). Following Smith & Gehrz (2005) and Clyne et al. (2015), we adopt a jet mass of 1.5 $M_\odot$, and an ejection timescale of 2000 yr with velocity of 30 km s^{-1}. The limit obtained indicates that the ejecta of M2-9 are not consistent with Bondi-Hoyle accretion nor with wind-Roche lobe overflow, the two mechanisms that would operate in a symbiotic binary. They are consistent, however, with Roche lobe overflow, implying a close binary, which may have after a brief phase of Roche-lobe overflow entered a common envelope. In any case, the outflow of M2-9 appears to have less momentum than that of Mz3, but still requires an energetic event.

Similarly to the analysis of Mz3 we find that despite the relatively low mass of the disc, M2-9's disc may be able to exert the required ram pressure on the stellar wind and potentially cause some level of collimation in the resulting outflow. Consider for example a typical mass loss rate and velocity of a post-AGB wind 10^{-8} $M_\odot$ yr^{-1} and 1000 km s^{-1} respectively, (e.g., Cerruti-Sola & Perinotto, 1989; Patriarchi & Perinotto, 1991). Assuming an isotropic outflow throughout a spherical volume with the same radius as the inner-disc ($\sim$18 AU) we estimate the resulting density at the inner-disc rim to be $\sim 6.9 \times 10^{-21}$ g cm^{-3}, the disc density (when considering a gas ratio of 100) at the inner rim is however much greater with $\sim 2.6 \times 10^{-15}$ g cm^{-3}. Considering a radially stationary disc, linear momentum arguments suggest the disc is maybe dense enough to have some influence in disrupting the outflow direction, if formed prior to the outflow event.

In conclusion, we favour an outflow description similar to Mz3, that a magnetically assisted centrifugal launch from a binary interaction during the common envelope, is required to emit the high mass lobes apparent. Further kinematical descriptions

will, however, likely be necessary to determine the exact nature of the collimating engine in M2-9.

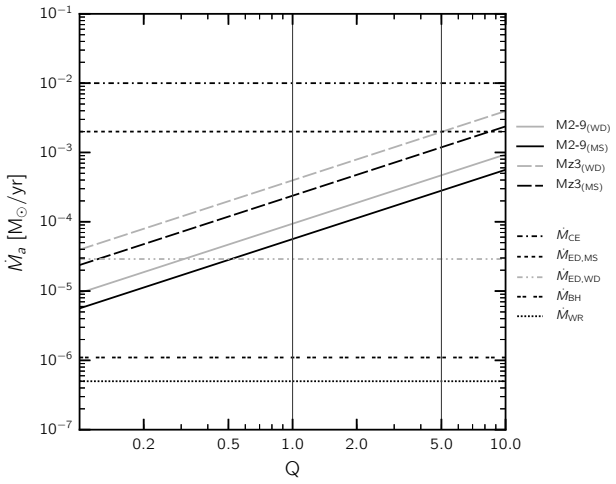

Figure 5.10: Theoretical mass accretion rate onto a putative companion versus efficiency parameter Q for Menzel 3 and Minkowski 2-9 following Blackman & Lucchini (2014). The accretion mechanisms (horizontal lines; from top to bottom) for a 1-$M_\odot$, 1-$R_\odot$ main sequence (MS) star and a 0.6-$M_\odot$, 0.014-$R_\odot$ white dwarf (WD) star represent: common envelope accretion ($\dot{M}_{CE}$=10^{-2} $M_\odot yr^{-1}$ with $\dot{M}_{CE,MS}$=$\dot{M}_{CE,WD}$); Eddington accretion for a MS star ($\dot{M}_{ED,MS}$=2×10^{-3} $M_\odot yr^{-1}$); Eddington accretion for a WD star ($\dot{M}_{ED,WD}$=2.9×10^{-5} $M_\odot yr^{-1}$); Bondi-Hoyle accretion ($\dot{M}_{BH}$=1.1×10^{-6} $M_\odot yr^{-1}$ with $\dot{M}_{BH,MS}$=$\dot{M}_{BH,WD}$) and, finally, accretion caused by wind Roche lobe overflow ($\dot{M}_{WR}$=5×10^{-7} $M_\odot yr^{-1}$, where again $\dot{M}_{WR,MS}$=$\dot{M}_{WR,WD}$). The Mz3 WD and MS accretion cases are plotted as the grey and black solid lines respectively, M2-9 equivalents are represented by the long dashed lines. For a given Q value, viable accretion mechanisms are those found above the object's estimated accretion.

Chapter 6

IRAS 08005-2356

"The purpose of models is not to fit the data but to sharpen the questions"

S. Karlin – 1983

6.1 Background

The source known as IRAS 08005-2356 (hereafter IRAS08005) has a high velocity ($V \sim$200 km s^{-1}) outflow bipolar nebula (e.g., Sahai & Patel, 2015; Sahai et al., 2007). The object's central source, V510 Pup, first observed by Slijkhuis et al. (1991), is likely a F5Ie type supergiant. IRAS08005 has been shown to share many observational characteristics with the post-common-envelope-evolution binary system HD 101584 (e.g., Bakker et al., 1996, 1997; Olofsson et al., 2015; Sahai & Patel, 2015). Similarities are seen between these objects' spectral energy distributions, emission signatures, outflow momenta and expansion velocities. In fact, the infrared spectral energy distribution of IRAS08005 is often associated to binary systems (e.g., Waters et al. 1993; HD 101584 for example).

It is thus likely that IRAS08005, like HD 101584 harbours a binary at its core. Binarity is also suggested by the All Sky Automated Survey (ASAS) light-curve data (see Figure 6.1). Hrivnak (2017; private communication) calculates an observed period in the range 6.0-6.3 years, and suggests the periodicity is caused by partial occultation by a disc due to binary motion with period $P_{\rm orb} \sim 6$ yr. This light-curve was also considered by Bright (2013), who suggested that its lopsided nature may indicate an eccentric binary orbit, potentially caused by an interaction between a circumbinary disc and a stellar companion to the post-AGB primary star.

The high mass loss rate (10^{-6} M$_{\odot}$yr^{-1}) and high expansion velocities observed are known to be too energetic for the radiation pressure of an AGB star alone (e.g., Sahai & Patel, 2015). These energy considerations lead Zijlstra et al. (1991) to suggest that IRAS08005's outflows may result from an interaction between a post-AGB star and a companion, in which jets or collimated fast winds (CFWs) may arise from an accretion disc. Support for such a scenario was presented by Bakker et al. (1997), who interpreted chromospheric emission lines of neutral and singly ionised metals as evidence of a such an accretion disc. Evidence of an accretion

disc was additionally presented by Sahai & Patel (2015), who upon observing broad Hα photons in the IRAS08005's lobes, suggested it was a consequence of Raman-scattering of Lyman-β emission from such a structure. It was concluded however, that a revolving disc, if in Keplerian rotation about a star of V510 Pup's size, would be too slow to account for the Hα line broadening, while a disc in rotation about a smaller main sequence star, for example, could cause the observed spectra.

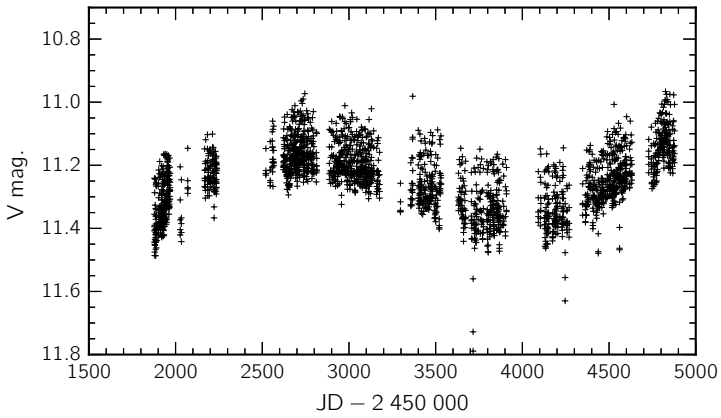

Figure 6.1: The light-curve of V510 Pup from the ASAS photometric catalogue. ASAS data ranges from A (best) to D (worst). This plot comprises the A grade data, from which Hrivnak (2017; private communication) calculates a period of ∼6.0 years.

Interestingly, in studying C_2 absorption (an indicator of carbon-rich gas), and OH maser emission (an indicator of oxygen-rich gas) in the lobes, Bakker et al. (1997) determined the absorption and emission regions within the outflows to have similar radial velocities. In explaining this finding, it was proposed that V510 Pup had recently made the transition from an oxygen-rich mass ejection object to a carbon rich one, a scenario perhaps common to other dual chemistry PNe (e.g., IRAS 10197-5750; Zijlstra et al. 1991; Zijlstra et al. 2001). It was also suggested the ejection may be shared between stellar components, with one star potentially ejecting the carbon-rich material, and the other the oxygen-rich for example. Detection of C_2 and CN lead them to propose that the object is a C-rich PPN, despite the fact that IRAS08005 does not displaying the 21-μm feature common to carbon-rich post-AGBs (e.g., Kwok et al., 1995).

Radiative transfer modelling of IRAS08005 was completed by Oppenheimer et al. (2005), in which disc models were constructed under the assumption that the transition from carbon- to oxygen-rich dust was complete. The result was a hypothesised inner carbon disc extending from ∼24-780 AU, surrounded by a second, predominantly silicate shell extending from ∼780-2730 AU. However, visibility and spectrum measurements obtained from the much higher resolution MIDI combiner at the VLTI (e.g., Bright 2013; henceforth B13), indicated the presence of a circumstellar silicate disc (this is further discussed in Section 6.3). Following radiative transfer models of the object it was found that IRAS08005 had a morphologically complex inner structure. A relatively simple flat silicate disc extending from ∼5-780 AU was modelled, but ultimately provided a poor representation of the interferometric data products. The slope of the spectrum in the N-band is

too high and negative to be explained by warm dust with a single temperature (the MIDI spectrum in relation to the literature flux measurements of I08005 is presented in Figure 6.4). The presence of hot gas with a temperature of ∼2000 K was hypothesised and additional blackbody curves were added to the fit in an *ad-hoc* manner. Fitting these curves however proved difficult, with only moderate quality fits resulting.

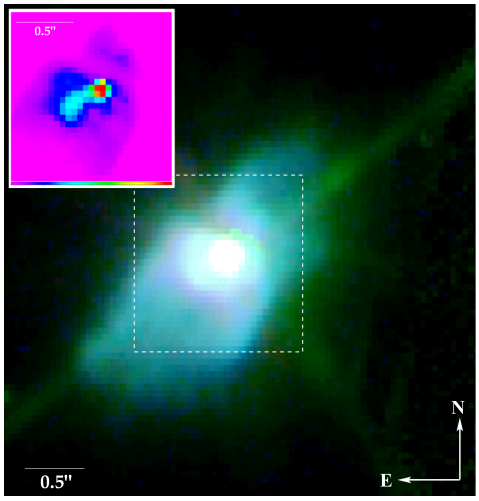

Figure 6.2: HST color-composite of IRAS 08005-2356 from Sahai & Patel. The inset is a false-color representation of the intensity distribution, which depicts a jet-like feature at the object's core.

The flat Keplerian nature of the disc detected in the B13 models, was suggested to meet the criteria of an oxygen remnant disc. For example Zijlstra et al. (2001) postulated the OH emission observed in IRAS08005 may originate from a long lasting circumstellar oxygen reservoir. With such a disc additionally suggested to cause the less defined collimated outflows observed in IRAS08005.

In this section we aim to characterise IRAS08005's disc structure further with application of `GADRAD`. We construct radiative transfer models from the MIDI data products, in addition to measurements taken with the AMBER instrument.

6.2 Observations

Interferometric observations of IRAS08005 where taken with the MIDI instrument at the VLTI in December 2011 and February 2012 under programme 088.D-0586 (P.I. Bright, S.N.; see B13 for full account of observational procedure). Three unit telescopes were used in different telescope pairings, with one measurement taken in February 2011, followed by five measurements taken in February 2012. MIDI observations were made in `HIGH_SENS` mode, with the lower resolution but higher sensitivity (R=30) NaCl prism chosen. Good *uv*-coverage was provided by baselines both perpendicular and parallel to the object's outflows, and measurements were taken over a range of baseline lengths (∼37-62m). MIDI observation logs and the calibration source can be found in Table 6.1. A map of *uv*-coverage is presented in Figure 6.3. Similarly to B13 , we discard the baseline measurements

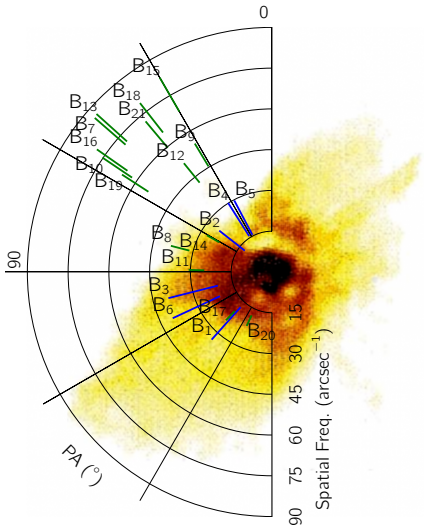

Figure 6.3: Illustration of the interferometric *uv*-coverage of IRAS 08005-2356. Projected baselines are shown in geometric reference to the HST image of Ueta et al. (2000). The blue lines represent the MIDI baselines (for λ range 7.5-14μm). Green lines depict baseline coverage of the AMBER measurements (for λ range 2-2.4μm). Baseline parameters correspond to those presented in Table 6.1.

B_2 and B_6. B_2 for example displays visibilities in excess of 1, while the 2011 observation B_6 shows large discrepancies in resulting flux measurements with the other measurements.

Following MIDI analysis of 08005 (e.g., B13) evidence of a disc became apparent and higher resolution measurements were subsequently taken with the AMBER instrument in April 2013 under programme 091.D-0030 (P.I. Bright, S.N.). These measurements were taken in the attempt of gaining additional information at closer proximity to the central source. Observations were taken predominantly perpendicular to the objects outflows in the *J*-, *H*- and *K*-bands. Five baseline triplets were taken resulting in fifteen baselines measurements over a range of projected baseline lengths (∼8-36m), and position angles (from ∼-150 to -155°). The observation log with calibration sources is presented in Table 6.1, a map of *uv*-coverage can be found alongside those of MIDI in Figure 6.3. Measurements were taken in low resolution mode (R=30), in good conditions with average seeing over the three nights of ∼1.2". Data was reduced with the standard AMBER reduction software (`amdlib`, e.g., Tatulli et al., 2007; Chelli et al., 2009b). However we find the *J*-band data to be unusable and the *H*-band unreliable. We proceed to model IRAS08005 with reference to the *K*-band data only.

Table 6.1: IRAS 08005-2356 observing log.

Label	Date	Time (UTC)	Baseline	Projected Baseline Length (m)	PA (°)
MIDI					
B_1	2012-02-04	06:52	UT2 – UT3	51.1	138.3
B_2	2012-02-05	07:21	UT2 – UT3	37.6	51.9
B_3	2012-02-05	02:34	UT3 – UT4	60.3	104.2
B_4	2012-02-04	02:44	UT2 – UT3	46.0	32.4
B_5	2012-02-04	02:11	UT2 – UT3	45.5	27.8
B_6	2011-12-13	07:56	UT3 – UT4	61.8	115.0
AMBER					
B_7	2013-04-15	23:51	D0-A1	35.5	-131
B_8	2013-04-15	23:51	A1-C1	15.7	75.5
B_9	2013-04-15	23:51	C1-D0	22.6	-149
B_{10}	2013-04-16	01:56	D0-A1	30.9	-124
B_{11}	2013-04-16	01:56	A1-C1	12.5	88.6
B_{12}	2013-04-16	01:56	C1-D0	21.1	-141
B_{13}	2013-04-14	23:40	D0-A1	35.7	-132
B_{14}	2013-04-14	23:40	A1-B2	11.2	119.4
B_{15}	2013-04-14	23:40	B2-D0	33.9	-150
B_{16}	2013-04-15	01:35	D0-A1	32.3	-125
B_{17}	2013-04-15	01:35	A1-B2	10.0	136.4
B_{18}	2013-04-15	01:35	B2-D0	32.4	-142
B_{19}	2013-04-15	02:56	D0-A1	27.0	-123
B_{20}	2013-04-15	02:56	A1-B2	8.9	154.9
B_{21}	2013-04-15	02:56	B2-D0	29.7	-140

Calibrators: MIDI: HD 63700 3.81 ± 0.01 mas; AMBER (B_7-B_{12}): HD 63660, HD 108530, HD 130518, HD 52265; AMBER (B_{13}-B_{21}): HD 64616, HD 52265, HD 54990, HD 63660, HD 130518.

6.3 Preliminary analysis

B13 analysed the MIDI observations of IRAS08005 and concluded that a silicate disc resides at the centre of the nebula. Simple considerations of MIDI visibilities for example indicate that a non-circular elongated body is detected (see Figure 6.5). For example, the MIDI baselines orientated parallel to the nebula's minor axis (B_4, B_5), display visibilities of similar magnitude to the baselines taken along the object's major axis (B_1 and B_3). If for example we detected a circular distribution interferometrically, we would expect the longer baselines (B1 and B3) to display a lower overall visibility indicative of the higher resolution. The visibility similarities seen in this instance thus demonstrate that an elongated disc type structure is being observed, in particular, a body that is extended equatorially with respect to the outflows. We additionally confirm that the inner rim of a disc is not likely detected by the MIDI instrument, as a resolved inner rim would result in a larger visibility signal at $\sim$ 8-9μm. Without this feature, we suggest if an inner-disc rim is present, it is likely smaller than the resolution capabilities of the MIDI instrument of $\sim$10 mas, thus constraining the inner-disc rim to scales smaller than $\sim$30 AU (at a distance of $\sim$2.85 kpc; see also B13). Visibilities are also found to give guidance to the disc's dust composition. For instance, the common silicate feature at $\sim$9.8μm, is detected in the MIDI visibilities, the negative gradient at $\sim$10μm suggest the object is larger or denser when observed at these wavelengths.

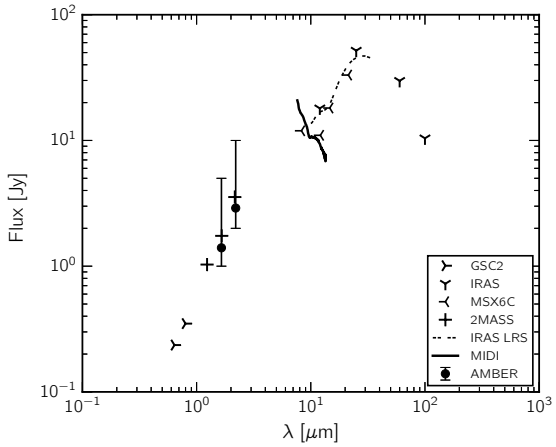

Figure 6.4: MIDI spectrum (solid line) and AMBER fluxes (tilled circular symbols) of IRAS 08005-2356 in relation to the literature spectral energy distribution (values are listed Table 6.3).

Information pertaining to the disc environment about IRAS08005 is more difficult to decipher from the AMBER measurements, however. The closure phase measurements for instance are clearly centred about zero, which would indicate that no asymmetries are being detected. Baselines along the minor axis of the object (i.e., the disc's major axis; as detected by B13) correspond (on average) to longer projected baseline lengths. One would thus expect much lower visibility signals than those observed parallel to the disc minor axis (objects major axis; i.e., baselines B_{20} and B_{17}). The differences observed between the minor and major axis of the object, suggest we are not observing a well defined elongation in the object being resolved.

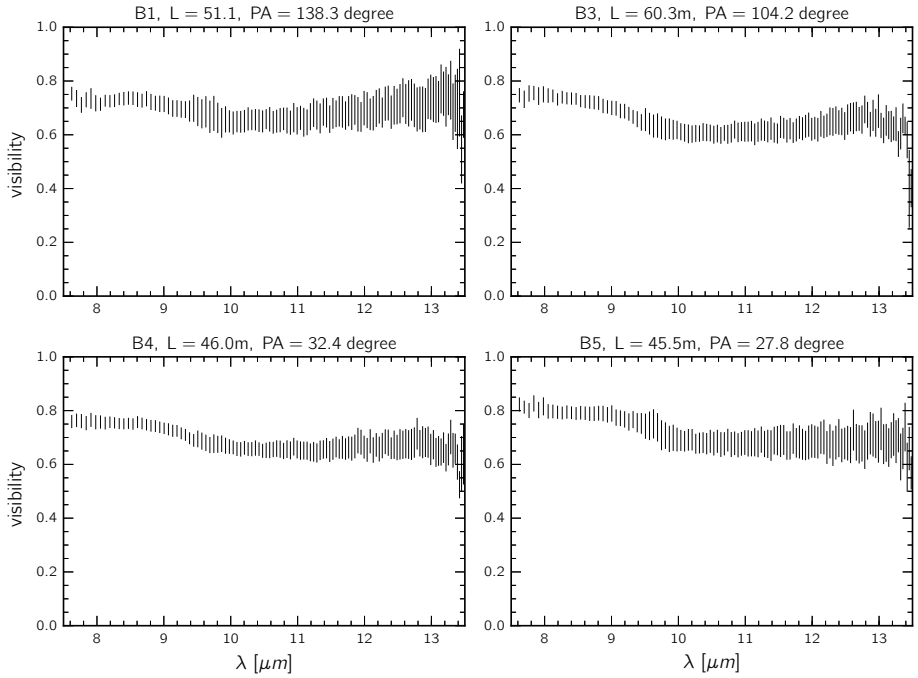

Figure 6.5: The MIDI visibilities of IRAS 08005-2356. The similar magnitudes, but differing baseline lengths support the detection of an elongated distribution.

6.4 Radiative transfer modelling

In this section we employ GADRAD to constrain IRAS08005's disc characteristics further. We begin by considering the early radiative transfer modelling attempts of IRAS08005 by B13. The structure observed with MIDI is likely complex, with numerous blackbodies seemingly necessary for appropriate SED fitting. B13 for example suggested 4 blackbodies are likely needed: a 7000-K blackbody representing the observed stellar spectral energy distribution of the primary, a 1200-K shell or disc representing a hot gaseous structure (which fits the near-IR observations of Slijkhuis et al. 1991), a circumstellar/circumbinary disc (500 K) and a cool surrounding dust distribution (150 K). The need for a 1200-K blackbody stems from the fact that the MIDI spectrum has a negative slope that is not reproducible with any choice of dust temperature.

The task of fitting the MIDI data products with this combination of blackbodies however proved challenging. For instance, the radiative transfer models resulted in non-self-consistent findings. The inner hot shell for example, was found to extend to 6 AU, while the inner disc radius was only determined to extend to 5 AU. Additionally, the models of the outer structures were calculated including only the central star without the warm gas shell (the 1200-K source). Instead radiative transfer models were selected to *under-fit* the MIDI spectrum, so as to allow the addition of the 1200 K blackbody. Such scenarios did not for example account for dust emission and absorption that would occur due to the surrounding disc. How this affected the objects morphology and spectrum with regard to the MIDI visibility and flux measurements could only be approximated. As has also

been mentioned previously, the B13 analysis was done in a *by-eye* ad-hoc fashion, with limited search of parameter space. For example, of the 12 parameters in the B13 model 7 were set to literature values, and only parameters controlling the disc were explored.

With GADRAD however, we are able to carry out a systematic exploration of parameter space, and consider resulting fits to both the MIDI and AMBER data products. We adapted GADRAD to account for a multi-temperature central source. Despite the fact that little is known about the morphological structure of IRAS08005's central regions, we expect that the 1200 K gas shell or disc to be located near the central source and interior to the modelled dust disc. For simplicity and computational efficiency we approximate the the central source as a point source with an energy distribution equivalent to that of a multi-temperature structure. This approximation forgoes the need of parameters controlling relative positioning of the sources and their respective size, both of which would likely be under-resolved by MIDI and AMBER. The potential inaccuracy of such a scenario is however clearly evident. For example we cannot account for asymmetries, and a point source approximation removes the ability of the source to emit directly onto the top and bottom surfaces of the disc. Additionally radiation transfer effects of the source caused by emission through the likely surrounding gas structure are ignored. However, without more knowledge of the hot gas structure, better approximations cannot be made without additional information. Given the central object is only partially obscured (e.g., Ueta et al., 2000), we expect the morphological simplicity of the 2-D stratified disc model class (see Section 3.4.1) to potentially result in systematic problems in the visibility representation. We apply GADRAD to the fitting of 5 VLTI data products, the MIDI visibilities and SED as well as the AMBER equivalents in addition to the AMBER closure phases.

6.5 Preliminary search of parameter space

As has been previously indicated, parameter space can quickly become very large when modelling interferometric observations of post-AGB environments. For this reason preliminary searches of parameter space are heavily guided by parameters derived in the literature. An overview of previous IRAS08005 constraints is presented in Table 6.2. At this early stage of parameter exploration we use broad, course sampling, that provide solutions that favour parameter exploration and avoid higher resolution searches of small regions of parameter space. Broad sampling is achieved by initiating GAs that explore large areas of parameter space, we consider flat initial sampling (see Equation 3.1) in our algorithm search with wide parameter ranges (see Table 6.2). To achieve course sampling we select a relatively low sampling value of 100. We select a large population size (adopt $n_{\rm pop} = 1200$). Exploration is further assisted by allowing a generous number algorithm iterations $n_{\rm gen} \sim 500$.[1]

We begin by applying 4 initial GA searches. It becomes quickly apparent, however, when comparing the resulting model's SEDs with flux measurements taken in the K-band, that most models produce too much flux at wavelengths short-ward of the N-band. The AMBER fluxes for example, with their large respective errors,

[1] These parameters are explained and defined in Section 3.2.3.

Table 6.2: IRAS 08005-2356 literature parameter values.

Parameter		Lit. Values	Ref.	GA Range (Min., Max.)
Stellar Parameters				
Temperature (T_1)	10^3K	6.5, 6.8, 7, 15	a,g,b,h	(6.0,16.0)
Luminosity (L_1)	$10^3 L_\odot$	6, 6.3, 6.98	a,b,d	(5.5, 12.5)
Distance (D)	kpc	2.85, 4.0	b,(c,g)	(2.6, 4.2)
Secondary Source				
Temperature (T_2)	kK	1200	f	(600,4000)
Luminosity (L_2)	$10^3 L_\odot$	-	-	(500,8000)
Orientation				
Inclination (i)	deg	60	(b,f)	(55, 80)
Position angle (PA)	deg	42, 141	b,f	(130, 155)
Disc Characteristics				
Inner radius ($r_{\rm in}$)	AU	5, 24	f,b	(2, 40)
Outer radius ($r_{\rm out}$)	AU	780	(b,f)	(400, 1000)
Mid-plane density factor (α)	-	2.6, 2.8	f,f	(2,8)
Vertical-plane density factor (β)	-	0.3	f	(0.2,1.5)
Scale height (h_0)	AU	25, 28	f,f	(5, 50)
Dust mass ($m_{\rm disc}$)	$M_\odot$	6.9×10^{-7}, 1×10^{-5}	b,f	$(1\times10^{-7}, 1\times10^{-4})$
Grain Parameters				
Grain chemistry	AS:AC[†]	0:1, 1:0	b,f	0:1,1:0
Minimum grain size ($a_{\rm min}$)	μm	0.018, 0.05	b,f	(0.005, 1.0)
Maximum grain size ($a_{\rm max}$)	μm	1.0	(b,f)	(1.0, 100)
Size distribution ($a_{\rm pow}$)	-	3.5, 6.0	f,b	(2,6.5)

[a]Slijkhuis et al. (1991); [b]Oppenheimer et al. (2005); [c]Klochkova & Chentsov (2004); [d]Sahai & Patel (2015); [e]Trammell et al. (1994); [f]Bright (2013); [g]Clayton et al. (2014); [h]Zijlstra et al. (2001); [†]Amorphous silicates and amorphous carbon.

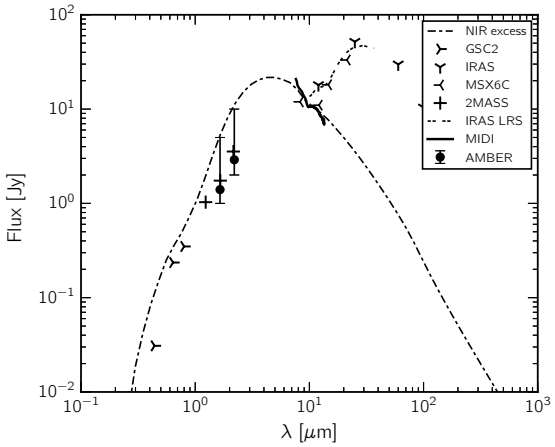

Figure 6.6: Typical initial model found in parameter exploration, which displays a clear energy excess at wavelengths short-ward of the N-band. The model is reddened with $E(B-V)=0.5$.

Table 6.3: IRAS 08005-2356 aperture photometry

Instrument/Reference	Wavelength (micron)	Flux (Jy)	Aperture
Photometric Data			
GSC-II	0.44	0.031	$1''$
	0.7	0.218	$1''$
2MASS	1.235	1.03±0.02	$4''$
	1.66	1.74±0.07	$4''$
	2.16	3.55±0.07	$4''$
MSX6C	8.28	1.19	$18.3''$
	12.13	11.0	$18.3''$
	14.65	18.1	$18.3''$
	21.34	33.1	$18.3''$
IRAS	12	18.0	$0.75' \times 4.5'$
	25	51.8	$0.75' \times 4.6'$
	60	29.8	$1.5' \times 4.7'$
	100	10.4	$3.0' \times 5.0'$
Spectroscopic Data			
IRAS LRS	8-13	8.97-46.7	$5.0'$
	11-23	8.97-46.7	$7.5'$

did not constrain the models energy distribution well. Better fits of the steepness of the N-band spectrum was seemingly at the expense of fitting the K-band data, with large energy excesses resulting in all 4 searches (a typical model SED from the initial searches is presented in Figure 6.6). Before increasing the AMBER flux weighting parameter, we turn to the literature for guidance. We present literature flux measurements in Table 6.3. Comparing fluxes, however, proved difficult in practise as one has to consider the different beam sizes. For example, the $4''$ aperture of the 2MASS instrument likely observes much larger structures than that resolved by MIDI. With the larger beam collecting more photons due to the extended nature of the object, when compared to MIDI, and expects higher SED fluxes. The visibilities are, however, in general, insensitive to the extended structures seen by the larger apertures. It remains evident, however, that we are still observing flux excesses below the N-band. Based on these considerations, we increase the AMBER spectrum weight in future models.

With a better constraint now applied to the radiative transfer's resulting SED, we initiate a further 12 GA searches. Resulting solutions indicate that the objective function is potentially very complex, with resulting solutions showing only moderately good fitness values (suggesting our simple disc is not a good representation of the true object). Following this small number of GAs however, it quickly becomes apparent that solution sets from these 12 GAs, are seemingly divided into two groups controlled by the parameter describing the primary stellar effective temperature.[2] This bimodal nature is evident in the resulting parameter histogram presented in Figure 6.7. As it can be seen, a first group tends to focus about a primary stellar effective temperature of $T_1 \sim 7500$ K which is in line with an F5I type central source (e.g., Klochkova, 2014). The second group is seen to favour hotter primary temperatures with $T_1 > 11,000$ K. Interestingly both temperature ranges are encountered in the literature. For example Bakker et al. (1997) sug-

[2] Initial models also tested disc composition. Silicate discs resulted in solutions with much better fitness values than the carbon counterparts.

gested IRAS08005's primary may be in an eccentric orbit with a close companion. A scenario similar to HD 101584, that could potentially result in high-mass loss winds that would accumulate about the primary. The resulting material is suggested to obstruct the central source, and hide the spectral signatures of a hotter star.

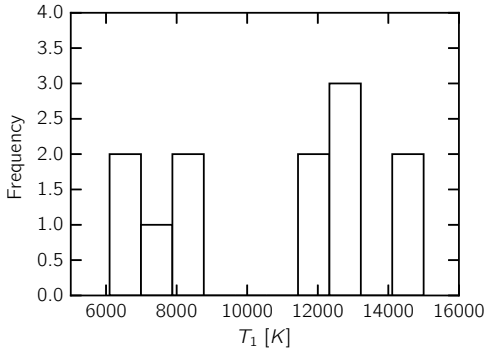

Figure 6.7: Density histogram of the primary stellar effective temperature parameter suggesting that a potential bimodal nature is evident i.e., a group about $T_1 \sim 7500$ K and a second with $T_1 > 11,000$ K. Both temperature domains have been presented to the literature, we proceed to fit models representative of both regions. More models would however be required to confirm the distribution.

Due to the similarity in resulting fitness between these seemingly independent scenarios, we proceed to apply GADRAD to these two regions of parameter space independently. Two scenarios are proposed and explored, we run an additional 12 GAs in each of the following potential scenarios: (i) a F5I type supergiant with temperature $T_1 \sim 7000$ K and (ii) a hotter primary ($T_1 > 10,000$ K), obstructed by wind material. We refer to these two models as the *cool-star model* and the *hot-star model* respectively.

6.6 Results

6.6.1 Cool-star model

We apply GADRAD to the aforementioned cool-star model, this model was found from initial searches of parameter space in which the central source is chosen to be an F5I type supergiant. Except for the primary's effective temperature, which is limited to the parameter range $6000 \geq T_1 \geq 9000$, we run 12 GAs with a full search of parameter space (see Table 6.4). As indicated by our preliminary searches, the MIDI spectrum was found difficult to reproduce. For this reason we increased the fitness weighting parameter to better constrain the N-band spectrum.

Parameter space is again found to be complex, with the resulting parameter solutions showing high levels of variance. For example, the fit using a radiative transfer model of the disc with parameters corresponding to the mean parameter values of the 12 GA solutions, is found to be significantly worse ($\Theta \sim 260$; this measure is related to χ^2; see Equation 3.2) than the mean fitness value across the

Table 6.4: IRAS 08005-2356 cool-star models

Parameter		Model		
		C-MSW	C-MVW	C-SC
Stellar Parameters				
Temperature (T_1)	10^3K	7.2 ± 1.7	-	-
Luminosity (L_1)	$10^3 L_\odot$	9.2 ± 1.6	-	-
Distance (D)	kpc	3.1 ± 1.2	-	-
Secondary Source				
Temperature (T_2)	K	780 ± 100	790 ± 120	1240 ± 200
Luminosity (L_2)	$10^3 L_\odot$	5.4 ± 1.5	5.35 ± 1.80	5.5 ± 2.4
Orientation				
Inclination (i)	deg	74 ± 2	-	-
Position angle (PA)	deg	134 ± 4.2	-	-
Disc Characteristics				
Inner radius ($r_{\rm in}$)	AU	8.7 ± 2.2	6.4 ± 1.2	10 ± 0.8
Outer radius ($r_{\rm out}$)	AU	700 ± 80	850 ± 30	760 ± 110
Mid-plane density factor (α)	-	6.6 ± 1.3	3.5 ± 0.3	5.0 ± 0.8
Vertical-plane density factor (β)	-	0.93 ± 0.16	1.3 ± 0.05	1.12 ± 0.08
Scale height (h_0)	AU	15.7 ± 6.5	14.3 ± 6.0	25.6 ± 3.2
Dust mass ($m_{\rm disc}$)	$10^{-7} M_\odot$	2.0 ± 1.8	187 ± 60	3.7 ± 2.0
Grain Parameters				
Minimum grain size ($a_{\rm min}$)	μm	0.9 ± 0.4	0.9 ± 0.7	$1.1^{+1.2}_{-0.2:}$
Maximum grain size ($a_{\rm max}$)	μm	$4.3^{+7.4}_{-0.0:}$	4.2 ± 4	$2.0^{+6}_{-0.8:}$
Size distribution ($a_{\rm pow}$)	-	2.1 ± 0.4	2.0 ± 0.2	2.6 ± 0.4
Fitness measure				
MIDI spectrum ($\Theta_{\rm ms}$)	-	1.05	10.4	14.9
AMBER spectrum ($\Theta_{\rm as}$)	-	0.04	0.08	0.004
MIDI visibility ($\Theta_{\rm mv}$)	-	34.7	1.25	20.0
AMBER visibility ($\Theta_{\rm av}$)	-	12.5	36.4	8.8
Closure Phase ($\Theta_{\rm cp}$)	-	0.09	0.15	0.14
Total (Θ)	-	48.3	48.3	43.9

The errors are calculated from the standard deviation of the parameters of N_{GA} GAs. Where the standard deviation is larger than the parameter value we provide it as a positive upper limit, the lower limit (followed by :) is the lowest value in the model sample.

12 GA models ($\Theta \sim 60$; with max $\Theta \sim 80$). It is thus evident that the mean solution of the adopted model class provides a poor description of the observed data products. The solution we adopt is therefore the model with the lowest fitness value. This model is presented in Table 6.4; resulting parameter errors are calculated from the standard deviation of the 12 models. This initial model in henceforth referred to as the 'cool-star, MIDI spectrum-weighted model' (C-MSW; see Table 6.4).

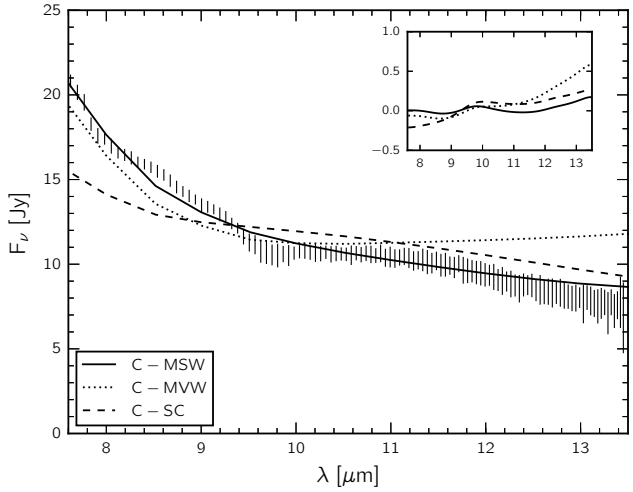

Figure 6.8: The MIDI spectrum is represented by the vertical error bars, to which we compare the resulting flux of the three cool-star (C-) models considered. The full model (C-MSW) is represented by the solid line, the midi visibility weighted model (C-MVW) is represented by the dotted line, and the self-consistent (C-SC) model is depicted as the dashed line. The corresponding residuals are presented in the inset as percentages.

In the C-MSW model, we find the resulting N-band spectrum matches the MIDI spectrum very well (see Figure 6.8). However, the goodness of the fit (with $\Theta_{\rm ms} \sim 1.05$) seemingly comes at the expense of the MIDI and AMBER visibilities (e.g., $\Theta_{\rm mv} \sim 34.7$, $\Theta_{\rm av} \sim 12.5$, respectively). The resulting fit to the MIDI visibilities is poor (Figure 6.9), with the result suggesting that a smaller object is being modelled than is observed. It is interesting, however, that the resulting AMBER visibilities fair better (see Figure 6.10), suggesting that a close likeness is present between the observed and modelled disc at high spatial frequencies (higher resolutions). This is supported by the resulting closure phase, which shows good agreement with that observed (see Figure 6.11). The discrepancy between the N- and K-band spectra again suggests that the object is structurally more complex than our 2D-symmetric model class adopted.

Constraining the object's SED provides further information on the disc structure. We modify `GADRAD` to reject radiative transfer models that show large energy excesses compared with the SED (see Table 6.3). The task, however, is non-trivial as aperture sizes must be considered. We first apply reddening to the models' SED. To allow less stringent constraint on our resulting model fits (and allow for the additional reddening caused by unresolved nebula contributions), we adopt an interstellar extinction value higher than that adopted by (Oppenheimer et al. 2005; i.e., $E(B-V) = 0.5$ vs $E(B-V) = 0.16$). The resulting C-MSW

model SED shows good agreement with the flux measurements presented in the literature (see Figure 6.12).

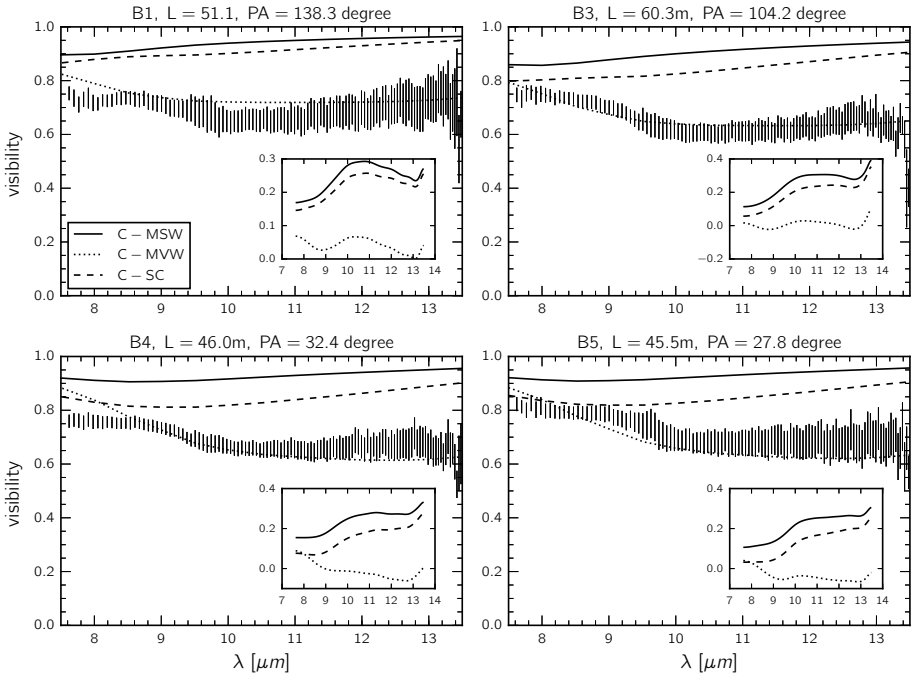

Figure 6.9: The MIDI visibilities are represented by the vertical error bars, in which we compare the resulting visibilities of the three cool-star (C-)models considered. The full model (C-MSW) is represented by the solid line, the midi visibility weighted model (C-MVW) is represented by the dotted line, and the self-consistent (C-SC) model is depicted as the dashed line. The corresponding residuals are presented in the inset as percentages.

However, similar to the B13 analysis, we find that our model is not self-consistent. For example, the temperature and luminosity values chosen for the warm gas structure result in an overall size of ∼18 AU, so that this gaseous distribution would extend beyond the inner-disc rim radius of only ∼ 8.7 AU. In an attempt to, (i) constrain better the MIDI visibilities and (ii) to determine a self-consistent model that describes the VLTI data products, we continue searching the parameter space and construct models with higher weighting for the MIDI visibilities. We have already gained a lot of information about parameter space, and with many of the data products well described, we restrict our parameter space search. We fix 5 parameters to the values determined in the C-MSW model, as we are focused on fitting the MIDI visibilities and improving the disc description, as well as finding a model in which the gaseous distribution is contained within the inner-disc rim. We therefore only explore the parameters controlling the disc characteristics, dust grain parameters, and gaseous source. We explore parameter space with the application of a further 8 (limited parameter) GA searches.

Similar to the C-MSW model, we adopt the fittest GA solution from the 8 GAs as our model, this model is presented in Table 6.4, we refer to this model as the 'cool-star, MIDI-visibility-weighted model' (C-MVW). Also similar to the C-MSW model, the fitting of one data product has come at the significant expense of a second. In this instance the good MIDI visibility fit ($\Theta_{\rm mv} \sim 1.25$; see Figure 6.9),

is at the expense of the poor N-band spectrum fit ($\Theta_{\rm ms} \sim 10.4$; see Figure 6.8). Following the C-MVW model, it becomes further apparent that our model class is likely an inaccurate representation of the true source.

However, such models may yet provide some constraint on potential structures. To fit the MIDI visibility, for example, it is apparent that a more compact disc is needed than the one that fits the N-band spectrum (i.e., $h_\alpha \sim 3.5$ vs. $h_\alpha \sim 6.6$). The biggest difference between a model that fits the N-band spectrum and one that fits the N-band visibility the disc mass. For example, in the C-MSW we determine a disc mass of $\sim 2 \times 10^{-7}$ $M_\odot$, while in the C-MVW model we find a disc mass of $\sim 2 \times 10^{-5}$ $M_\odot$. This suggest that a more opaque disc is required to fit the MIDI visibilities. The AMBER visibilities fit for the C-MVW model are poorer than for the C-MSW one ($\Theta_{\rm mv} = 36.4$ vs $\Theta_{\rm mv} = 12.5$ and $\Theta_{\rm cp} = 0.15$ vs $\Theta_{\rm cp} = 0.09$ respectively), and the C-MVW model additionally shows an energy excess at shorter wavelengths (see Figure 6.12). Once again, however, we find that the gaseous distribution again extends well beyond the inner-disc rim (i.e., $\sim$18 AU vs $\sim$6.4 AU respectively).

With these two cool-star models, we have found reasonable fits to the observed VLTI data products, though only when considered in isolation. Of particular concern, however, is these models predict a very large and cool central source unlikely to coexist with the implied dusty disc. We adapt `GADRAD` to limit parameter space to models that result in solutions, in which the central source is contained within the inner-disc rim. We refer to these set of models as the 'cool-star self-consistent' model (C-SC). For this last model we fix the stellar temperature, luminosity, distance, inclination and position angle. We apply a further 8 GAs, to these regions of parameter space. The final solution is the fittest of these results and is presented in Table 6.4. The errors provided are again calculated from the standard deviation of the 8 GAs.

The C-SC model is the poorest fitting model when considering the N-band spectrum. It is clear that the MIDI spectrum steepness is not reproduced, for example. The C-SC model however shows a better fit with literature flux measurements at lower wavelengths, i.e., no energy excess. The agreement seen between C-SC model with the other VLTI data products, seems a good compromise. The fitness values seen in the AMBER visibilities are in fact better than both previous models. Interestingly, the parameters controlling the disc's characteristics (excluding the dust composition) determined for the C-SC model are close to the average of the C-MSW and C-MVW. With only the scale height and inner disc radius being larger. The larger inner disc radius likely results from how the self-consistent model was constructed. It was noticed that smaller inner-disc radii were quickly removed from the population, suggesting the algorithm favoured fitting the spectral result (temperature and luminosity) over the spatial result (smaller inner disc radius favoured by the N-band spectrum and visibilities). Overall the C-SC showed the lowest fitness value, for this reason in addition to the disc model allowing enough space for the gas distribution (i.e., an extent of less than $\sim$10 AU), we propose that the C-SC model is the best model description so far determined, although the poor fit of the N-band spectrum suggests that we have not fully described the disc that is located at the core of IRAS08005. In Section 6.6.2, we continue searching for a better model model by investigating models with a hotter stellar temperature.

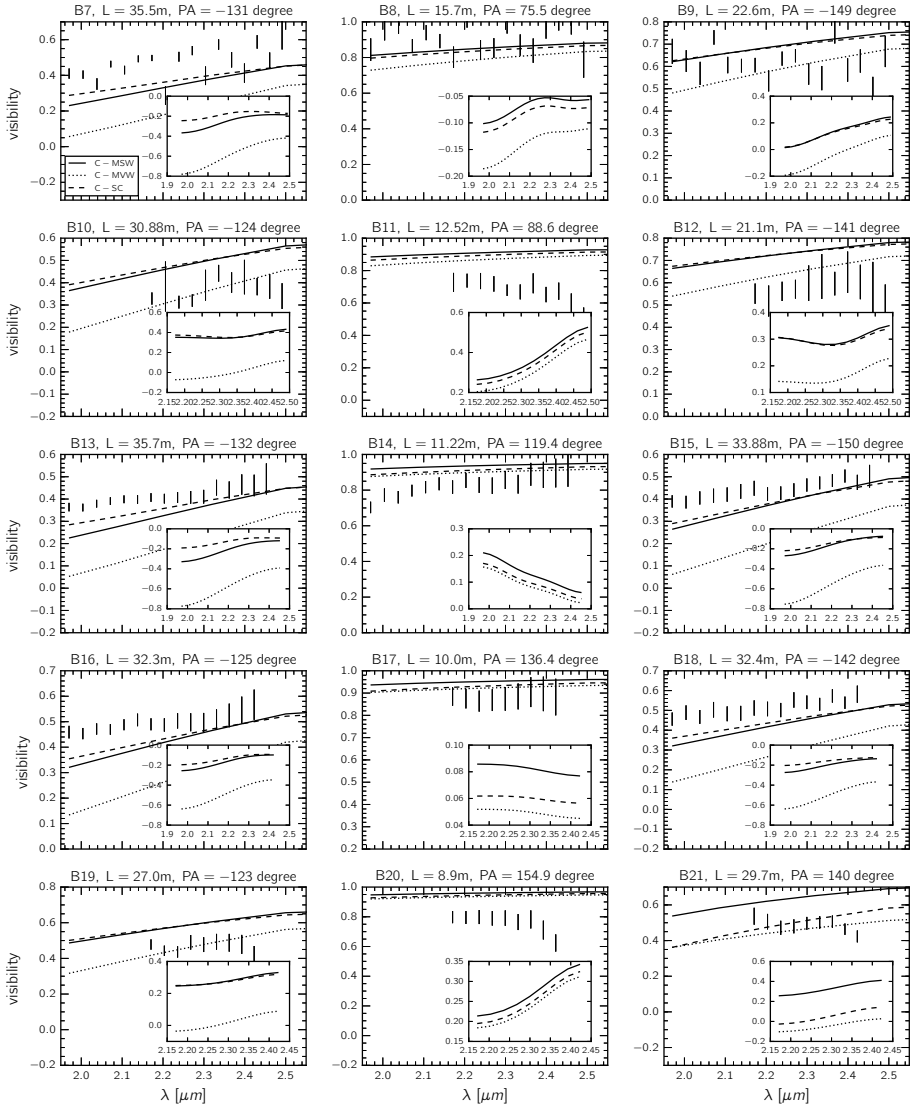

Figure 6.10: The AMBER visibilities are represented by the vertical error bars, to which we compare the visibilities of the three cool-star (C-) models considered. The full model (C-MSW) is represented by the solid line, the midi-visibility-weighted model (C-MVW) is represented by the dotted line, and the self-consistent (C-SC) model is depicted as the dashed line. The corresponding residuals are presented in the inset as percentages.

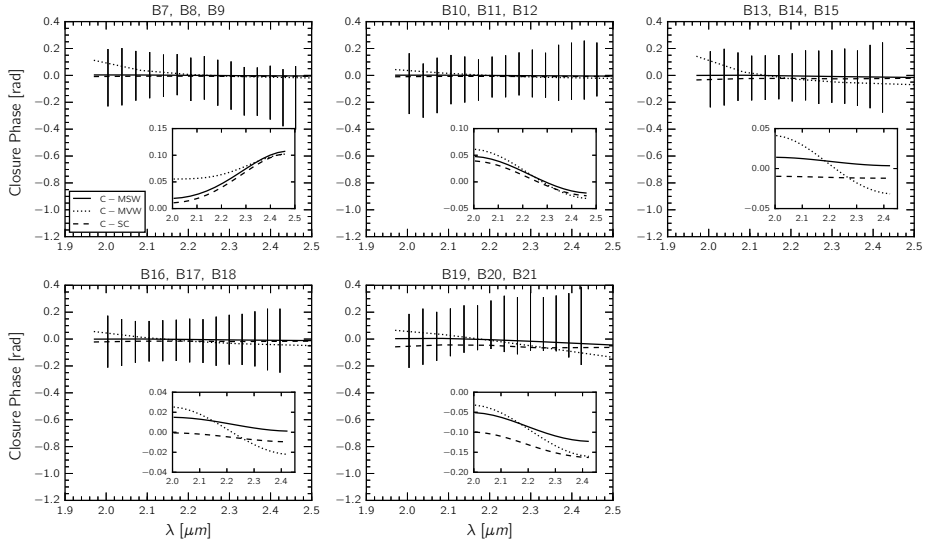

Figure 6.11: The AMBER closure phases are represented by the vertical error bars, in which we compare the resulting closure phases of the three cool-star (C-)models considered. The full model (C-MSW) is represented by the solid line, the midi visibility weighted model (C-MVW) is represented by the dotted line, and the self-consistent (C-SC) model is depicted as the dashed line. The corresponding residuals are presented in the inset.

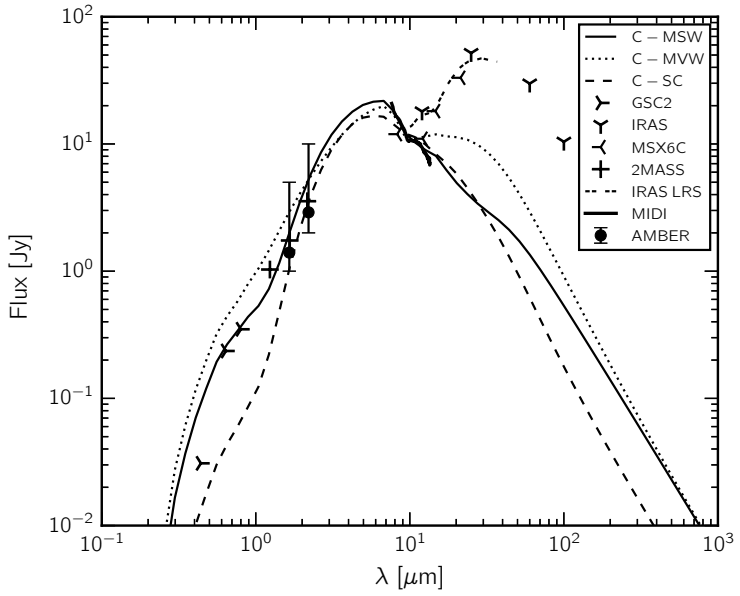

Figure 6.12: The IRAS 08005-2356 spectral energy distribution, in relation to the resulting RT flux from the three three cool-star (C-)models considered. The full model (C-MSW) is represented by the solid line, the midi visibility weighted model (C-MVW) is represented by the dotted line, and the self-consistent (C-SC) model is depicted as the dashed line. Note the AMBER flux values and the MIDI spectrum.

Table 6.5: IRAS 08005-2356 hot-star models

Parameter		Model		
		H-MSW	H-MVW	H-SC
Stellar Parameters				
Temperature (T_1)	10^3K	13 ± 1.2	-	-
Luminosity (L_1)	$10^3 L_\odot$	7.85 ± 1.6	-	-
Distance (D)	kpc	2.9 ± 0.8	-	-
Secondary Source				
Temperature (T_2)	K	875 ± 80	890 ± 110	1250 ± 130
Luminosity (L_2)	$10^3 L_\odot$	5.7 ± 2.0	5.5 ± 2.2	5.55 ± 0.4
Orientation				
Inclination (i)	deg	73 ± 3	-	-
Position angle (PA)	deg	141 ± 2.5	-	-
Disc Characteristics				
Inner radius ($r_{\rm in}$)	AU	7.3 ± 1.8	4.8 ± 2.4	8.25 ± 0.9
Outer radius ($r_{\rm out}$)	AU	650 ± 50	710 ± 30	670 ± 90
Mid-plane density factor (α)	-	6.45 ± 0.9	3.1 ± 0.7	4.2 ± 0.25
Vertical-plane density factor (β)	-	1.13 ± 0.1	1.25 ± 0.1	0.9 ± 0.2
Scale height (h_0)	AU	25 ± 6.5	26 ± 4.7	14 ± 6.8
Dust mass ($m_{\rm disc}$)	$10^{-8} M_\odot$	21 ± 15	170 ± 36	40 ± 20
Grain Parameters				
Minimum grain size ($a_{\rm min}$)	μm	0.5 ± 0.3	$0.1^{+0.4}_{-0.05:}$	$1.0^{+2.5}_{-0.2:}$
Maximum grain size ($a_{\rm max}$)	μm	$5.0^{+8.0}_{-2.0:}$	4.0 ± 1.5	3.0 ± 2.5
Size distribution ($a_{\rm pow}$)	-	2.2 ± 0.5	2.35 ± 0.3	4.5 ± 0.5
Fitness measure				
MIDI spectrum ($\Theta_{\rm ms}$)	-	1.0	12.45	7.86
AMBER spectrum ($\Theta_{\rm as}$)	-	0.09	0.05	0.08
MIDI visibility ($\Theta_{\rm mv}$)	-	38.1	1.83	23.6
AMBER visibility ($\Theta_{\rm av}$)	-	11.36	13.4	9.23
Closure Phase ($\Theta_{\rm cp}$)	-	0.12	0.20	0.14
Total (Θ)		50.7	27.9	40.9

The errors are calculated from the parameter sample standard deviation over the N_{GA} GAs. Where the standard deviation is larger than the parameter value we provide it as a positive upper limit, the lower limit (followed by :) is the lowest value in the model sample.

6.6.2 Hot-star model

The hot-star model follows the hypothesis of Bakker et al. (1996), in which a hot star is hidden by a circumstellar envelope. Similar to the cool-star model, a full search of parameter space is undertaken, with the exception of the primary's effective temperature, which we limited to $11,000 \geq T_1 \geq 20,000$ K. We run 12 GAs, and proceed in a similar fashion to that in the exposed star model, by increasing the fitness weighting parameter that controls the N-band spectrum. These models are henceforth referred to as the 'hot-star, MIDI-spectrum-weighted' model (H-MSW). The fittest H-MSW model is presented in Table 5.4, with the errors again calculated from the standard deviation of the parameters over the 12 GAs.

As expected, the H-MSW model describes well the N-band spectrum obtained by MIDI (see Figure 6.13). However, again it seems that this fit comes directly at the expense of the MIDI visibilities, which are equally poor (see Figure 6.14). Also,

similarly to the C-MSW model, we see that this model results in a smaller structure than is observed. The implied disc is similar to that obtained in cooler exposed-star model, with only the scale high showing significant levels of disagreement, with a more vertically extended disc seen in the H-MSW model. The gaseous structure contribution is also found to be relatively similar, though a slightly hotter structure is favoured (∼875 vs ∼780 K). Similar to the C-MSW model, the AMBER visibilities and closure phases are a reasonable fit to those observed. The SED and AMBER flux fits, however, show some improvement over those of the C-MSW model. Once again, however, we see that this model has a gaseous source that extends beyond the inner-disc radius (∼15 vs 7.3 AU). It is evident that similarities between the H-MSW and C-MSW models exists. This is perhaps not unexpected, for example previous models of other objects (Mz3 and M2-9 in Chapters 4 and 5, respectively), showed the stellar temperature parameter to be one of the most difficult parameters to constrain. However, this does not explain the bimodal nature seen in parameter space following the preliminary analysis (i.e., see Figure 6.7). Regardless, it is evident that the resulting visibility shows poor agreement with the MIDI data. Similarly to what was done in the previous section, we attempt to improve the fits using our GA to model the data with a weighted MIDI visibility. We refer to this model as the 'cool-star, MIDI-visibility-weighted' (H-MVW) model.

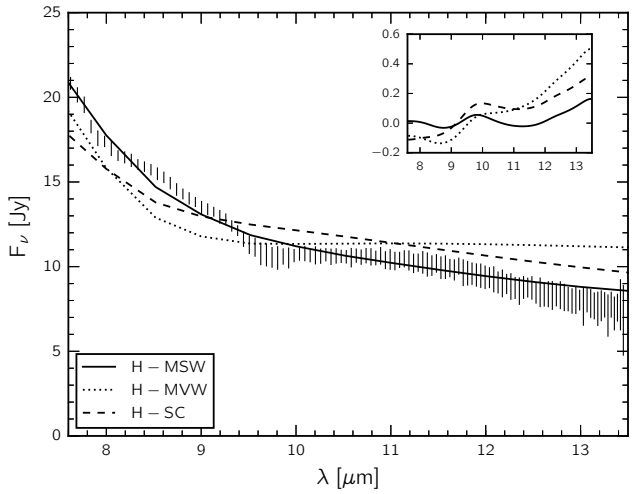

Figure 6.13: The MIDI spectrum is represented by the vertical error bars, in which we compare the resulting flux of the three hot-star (H-)models considered. The full model (H-MSW) is represented by the solid line, the midi visibility weighted model (H-MVW) is represented by the dotted line, and the self-consistent (H-SC) model is depicted as the dashed line. The corresponding residuals are presented in the inset as percentages.

The H-MVW model is carried out in a similar fashion to the C-MVW model, i.e., we fix 5 of the parameters to the values obtained in the H-MSW model, and further explore parameters controlling only the disc characteristics, disc grain composition and secondary source temperature and luminosity. We run a further 8 GAs, the best fitting solution is presented in Table 5.4.

Once again the fitting of one data product is done at the expense of another. It is evident, for instance, the H-MVW does a poor job at fitting the N-band spectrum

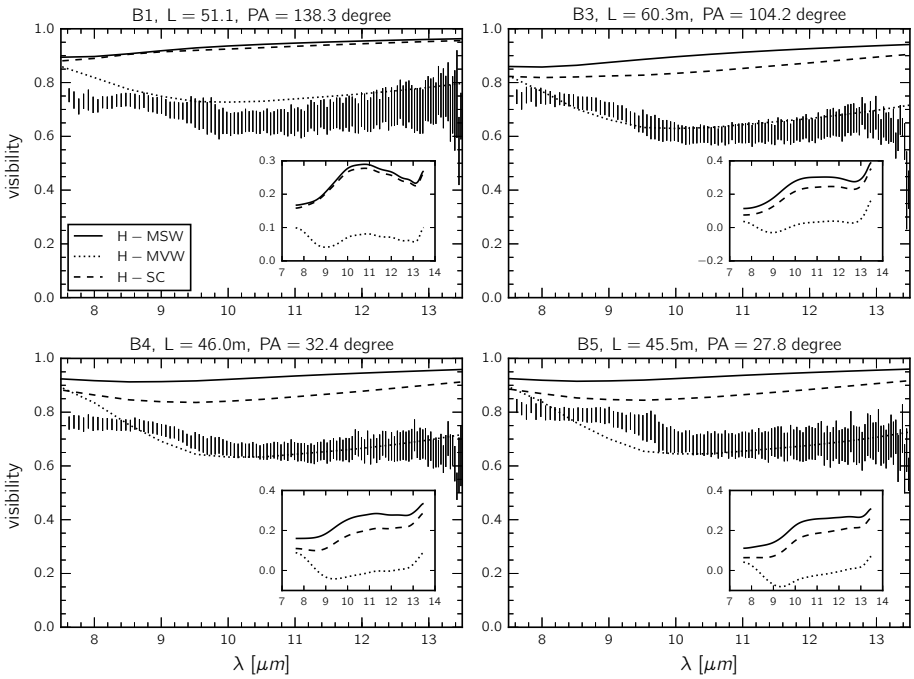

Figure 6.14: The MIDI visibilities are represented by the vertical error bars, in which we compare the resulting visibilities of the three hot-star (H-)models considered. The full model (H-MSW) is represented by the solid line, the midi visibility weighted model (H-MVW) is represented by the dotted line, and the self-consistent (H-SC) model is depicted as the dashed line. The corresponding residuals are presented in the inset as percentages.

($\Theta_{\rm ms} = 12.45$). The parameters of the H-MVW show that a more massive and more extended (less compact) disc, with smaller inner radius, is necessary to fit the spatial constraints of the MIDI visibilities. The H-MVW solution provides the fittest solution so far determined of either the cool or hot-star models. However, once again the model suggests a gaseous source extending some 15 AU (vs. an inner disc radius of only ∼4.8 AU).

Finally, as was done for the cool star model family, we calculate a hot star model that ignores solutions that allow the large gas component to extend beyond the inner disc radius. We run a further 8 GAs in the region of parameter space constrained by the inclination and position angle determined in the C-MSW model, in addition to the parameters controlling the primary's temperature and luminosity. The fittest solution for this region of parameter space is henceforth described as the 'hot-star, self-consistent' (H-SC) model.

The H-SC (see Table 5.4) model, though not as good a representation of the N-band spectrum as the H-MSW model, shows improvement over the H-MVW model, and additionally shows a good compromise to the MIDI visibility fits between the H-MVW and H-MSW models. Similarly the model shows compromise between both the weighted models with regards to the AMBER data products. This is reflected in the final fitness parameters, which though not as good as the overall value of the H-MVW, is an improvement to the H-MSW model. The disc in this model differs to the previous two in only the level of disc flaring and scale height. Despite the better fit of the H-MVW we prefer the H-SC as a description of the 'hot'-star model class, not only for its self consistent nature, but for its lower energy SED at shorter wavelengths (see Figure 6.17).

6.7 Summary and discussion

In the analysis of IRAS08005 we have run 6 different model sub-classes with (a total of 68 GAs) on the stratified disc density environment. Two primary star scenarios were considered, a cool-star model with a primary central star temperature of $6000 \geq T_1 \geq 9000$ and a hot-star model with $T_1 > 11,000$ K. In both scenarios systematic differences between our adopted 2D-symmetric stratified disc model class and the true object is apparent. It was evident, for example, that the fitting of one data product came often directly at the expense of a second. Thorough searches of parameter space were carried out, however, a model that showed good representation across all interferometric data was not obtained. We propose that the 2-D disc model adopted, is perhaps too simple an approximation of IRAS08005, and that the model does not generalise well enough to determine a model representative of the true object in this instance. We suggest the systematic differences between models and data products likely stem from the unrealistic 2D-symmetric nature of our model class, and the treatment of the two blackbody objects as a single point source.

In our analyses we did not expand parameter space to include more complex asymmetric features. We propose that other, relatively simple 2-D disc model classes can however be considered (more complex 3-D, non-symmetric, models will most likely require addition observations, or risk overfitting the data products available). The chosen model in this instance was a point source at the centre of a simple 2-D disc structure, with the central source comprised of the

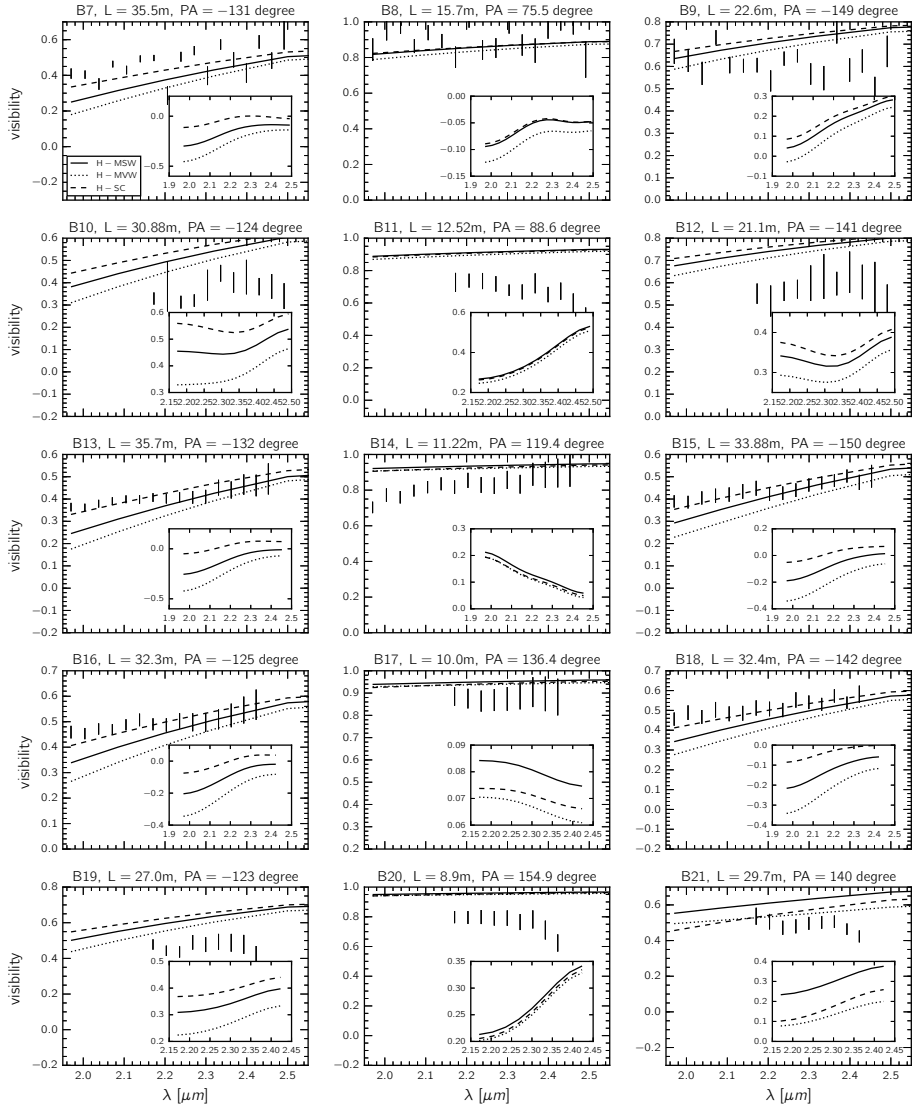

Figure 6.15: The AMBER visibilities are represented by the vertical error bars, in which we compare the resulting visibilities of the three hot-star (H-)models considered. The full model (H-MSW) is represented by the solid line, the midi visibility weighted model (H-MVW) is represented by the dotted line, and the self-consistent (H-SC) model is depicted as the dashed line. The corresponding residuals are presented in the inset as percentages.

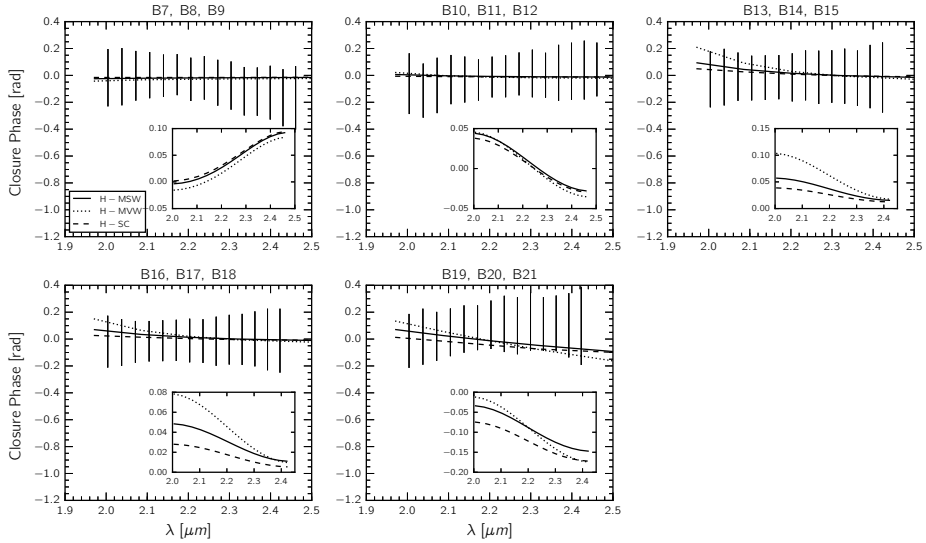

Figure 6.16: The AMBER closure phases are represented by the vertical error bars, in which we compare the resulting closure phases of the three hot-star (H-)models considered. The full model (H-MSW) is represented by the solid line, the midi visibility weighted model (H-MVW) is represented by the dotted line, and the self-consistent (H-SC) model is depicted as the dashed line. The corresponding residuals are presented in the inset.

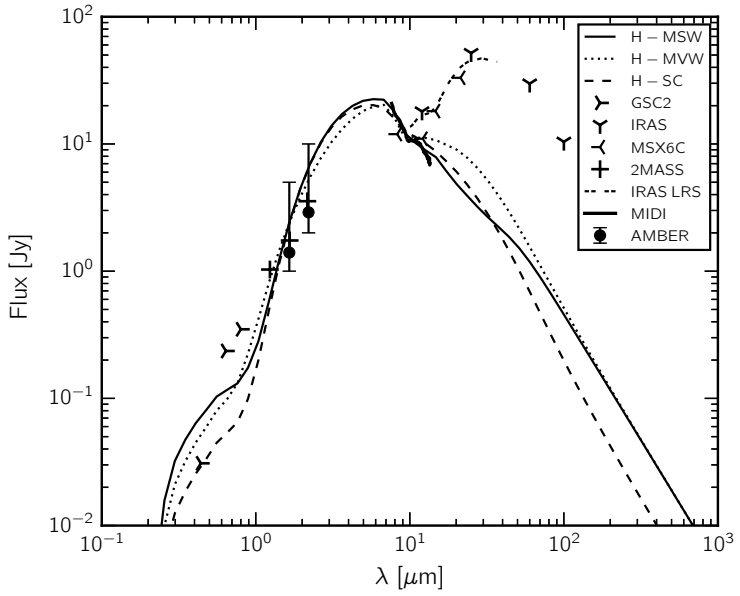

Figure 6.17: The IRAS 08005-2356 spectral energy distribution, in relation to the resulting RT flux from the three three hot-star (H-)models considered. The full model (H-MSW) is represented by the solid line, the midi visibility weighted model (H-MVW) is represented by the dotted line, and the self-consistent (H-SC) model is depicted as the dashed line. Note the AMBER flux values and the MIDI spectrum.

temperature and luminosity of two given blackbodies. This model, though simple geometrically, proved to be a poor estimate of the true object as the warm gaseous structure was found to extended beyond the disc rim. Though our models provide good spectral constraints on the object, the extended structure seemingly preferred, would most likely result in differing visibilities than those determined. Interestingly however, the adopted model class showed better agreement with the higher resolution AMBER visibility and closure phase data than that of MIDI (see Table 6.6). Suggesting that the smaller scale inner regions are better represented geometrically than the larger regions as resolved by MIDI. We however recommend implementing an extended inner cool structure in future modelling attempts. Other model classes worth considering may be a second, larger carbon disc structure, that surrounds the regions so far discussed. This would build on the structure put forward by Oppenheimer et al. (2005).

Object complexity is evident in the literature flux values, which show differences in the resulting energies as a function of aperture, suggesting multiple separate regions are being resolved. This complexity is also seen in the the case of our simple disc model, which reveals a complex parameter space. Consider, for example, the large differences seen between the respective model parameter averages and the observed data products. In the C-MSW model, for instance, 12 independent attempts were made at optimising the objective function (through the 12 GAs applied). The mean of the parameter values returned from the 12 GAs, results in a a very poor solution when compared to the individual solutions (i.e., $\theta \sim 260$ vs. $\theta \sim 60$).

By modelling with our relatively simple model structures we have however gained some knowledge of the spectral energies requirements, in addition to potential disc orientation and size. We have also shown that a relatively hot ($T_1 \sim 13{,}000$ K) star may reside at the centre of IRAS08005, and that the disc modelled may act as a shield to the central star, similar to that described by Bakker et al. (1996). Despite running two model sub-classes with differing stellar temperatures, it is evident that similar solution models result. This finding supports previous analyses in which the effective temperature was often found to be ill-constrained (e.g., see the synthetic model in Section 3.4, Mz3 in Chapter 4 and M2-9 in Chapter 5). Further analyses would be required to determine the true nature of the bimodal structure seen in the effective temperature parameter.

We found that in general, relatively low temperature extended central structures are preferred (i.e., $\sim$800K). However, by limiting our GA searches to areas of parameter space that accommodate a secondary source within the inner-disc radii, higher temperature sources were preferred over a larger inner-disc size. Similar to B13 we find that an amorphous silicate disc was preferred to one composed of amorphous carbon as proposed by Oppenheimer et al. (2005). The disc scale is however very comparable to the inner disc determined by Oppenheimer et al. (2005) which was found by them to extend from 24-780 AU. We also find that the disc is relatively flat (low h_β) and compact (high h_α), though not as flat as that determined by B13. Possibly indicating that the disc we are observing does not fit within the framework of Waters et al. (1998), in which the oxygen rich material observed dual-dust chemistry of these objects is stored within a disc from an earlier O-rich mass loss phase in the AGBs past. Other similarities with the B13 disc are however observed, in the cool-star model for example the primary temperatures are comparable (T_1=7200$\pm$1.4 K vs. T_1=7000 K in B13). Considering both hot-

star and cool-star models however, we determine a more luminous primary with L_1 ranging from 7850-9200 $L_\odot$ vs. 6300 $L_\odot$ in B13. Disc inner- and outer-radii are however relatively comparable ($r_{\rm in}$ = 5 and $r_{\rm out}$ = 780 AU respectively for B13 and a disc size ranging from $r_{\rm in}$ of ∼5 to 10 AU to $r_{\rm out}$ of 700 to 850 AU determined here). We further suggest that the disc is seen more edge on than estimated by B13, for example we determine an inclination of ∼ 73 vs. ∼ 60 degrees in B13.

To gain a better overview of the 6 GADRAD models, we compare their goodness of fit to the data in Table 6.6. Rather arbitrarily, we assign a check-mark (✓) to the models that display 'good-fitness', with a fitness measure of between 0 and 2, a cross-checkmark (×✓) to the 'moderate-fitness' models with fitness ranging from 2 and 15, and finally a cross (×) to the 'poor-fitness' models with measures above 15. Only the AMBER spectrum, and AMBER closure phases were well reproduced by all models. The MIDI visibility proved the hardest data product fit, with four poor fitting models. Following consideration of Table 6.6, the hot-star MIDI-visibility-weighted model shows the best agreement with the data, this model also shows best agreement in terms of the overall fitness measure. However, in determining a representation of IRAS08005's true environment parameters we prefer to rely on a parameter range estimated from across the 6 resulting models. As indicated previously for instance, it is unlikely that we have adopted a model class representative of IRAS08005, and generous parameter ranges give us the best chance of defining a 'suitable' quasi-solution of this model class, that represents 'good' fitness areas of parameter space.

Table 6.6: IRAS 08005-2356 model overview: MS and AS represent the MIDI and AMBER spectrums respectively, AV and AC represent the AMBER visibility and closure phase data products respectively. Check-marks in the SED column are awarded to the models that do not show any energy excess with regards to the literature.

	MS	AS	MV	AV	AC	SED
C-MSW	✓	✓	×	×✓	✓	×✓
C-MVW	×✓	✓	✓	×	✓	×✓
C-SC	×✓	✓	×	×✓	✓	✓
H-MSW	✓	✓	×	×✓	✓	×✓
H-MVW	×✓	✓	✓	×✓	✓	×✓
H-SC	×✓	✓	×	×✓	✓	✓

With regards to the formation history of IRAS08005, we again see high levels of outflow momenta, clearly exceeding the available radiation pressure of the central star (e.g., Sahai & Patel, 2015). Considering the Sahai & Patel (2015) scalar momentum (2.8×10^{39} g cm s^{-1}; similar to that of HD 101584 with 1.5×10^{39} g cm s^{-1}; i.e., Bujarrabal et al. 2001) and accretion time of 190 years, we determine, following the Blackman & Lucchini (2014) equation (i.e., Equation 4.1), the required accretion rate mechanism (see Figure 6.18). We find, similarly to Mz3 and M2-9, that the outflow momentum is only consistent with accretion values achieved during common envelope or Roche lobe overflow phases.

The detection of a $\sim$6 yr photometric period, if interpreted as an orbital period, however, complicates the outflow formation scenarios. For instance, assuming a $\sim$0.5 M$_\odot$ companion, a total mass of $\sim$1.0 M$_\odot$, would result in an orbital diameter $\sim$3 AU (assuming a circular orbit). Though this would likely fit within the disc, the orbit is too wide for the binary to be post common envelope (e.g., Passy et al., 2012), yet too small to have accommodated an inner binary in the past. The possible scenarios are then a Roche lobe overflow that ejected the lobes very efficiently (in a short time) and avoided common envelope all together, or a triple system whose inner binary went through a common envelope (with the companion undetected today or merged) and the tertiary's orbit subsequently decreased. Olofsson et al. (2015) similarly suggest that the nebula mass gives evidence of a capture event in which a companion has spiralled inside the giant.

It is unclear however, when the detected disc formed. it is possible that a gas outflow from L_2 at the time of Roche lobe overflow may have formed a disc before the common envelope ejection. Alternatively, fall-back of gas that was not fully ejected during the common envelope may result in a circumbinary disc. If the disc was formed during an L_2 outflow we suggest that it may have played a small role as a collimating agent in IRAS08005. For example, assuming a minimum outflow mass loss rate of 5.8×10^{-4} M$_\odot$ with velocity of up to 200 km s^{-1} (e.g., Sahai & Patel, 2015), we estimate the wind density to be of the order of 7×10^{-15} to 3×10^{-14} g cm^{-3}, depending on the inner disc radius. This is perhaps lower than the disc density of 5×10^{-15} to 1×10^{-12} g cm^{-3} depending on the disc model adopted (where we have assumed a gas-to-dust ration of 100).

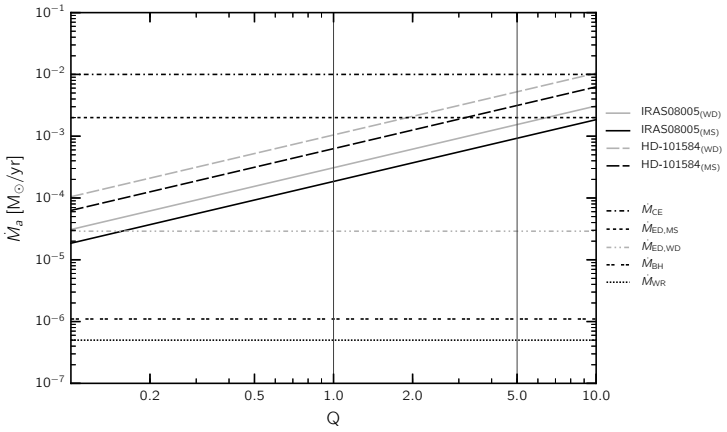

Figure 6.18: Theoretical mass accretion rate onto a putative companion versus efficiency parameter Q for IRAS 08005-2356 and HD 101584 following Blackman & Lucchini. The accretion mechanisms (horizontal lines; from top to bottom) for a 1-$M_\odot$, 1-$R_\odot$ main sequence (MS) star and a 0.6-$M_\odot$, 0.014-$R_\odot$ white dwarf (WD) star represent: common envelope accretion ($\dot{M}_{CE}$=10^{-2} $M_\odot yr^{-1}$ with $\dot{M}_{CE,MS}$=$\dot{M}_{CE,WD}$); Eddington accretion for a MS star ($\dot{M}_{ED,MS}$=2×10^{-3} $M_\odot yr^{-1}$); Eddington accretion for a WD star ($\dot{M}_{ED,WD}$=2.9×10^{-5} $M_\odot yr^{-1}$); Bondi-Hoyle accretion ($\dot{M}_{BH}$=1.1×10^{-6} $M_\odot yr^{-1}$ with $\dot{M}_{BH,MS}$=$\dot{M}_{BH,WD}$) and, finally, accretion caused by wind Roche lobe overflow ($\dot{M}_{WR}$=5×10^{-7} $M_\odot yr^{-1}$, where again $\dot{M}_{WR,MS}$=$\dot{M}_{WR,WD}$). The IRAS08005 WD and MS accretion cases are plotted as the grey and black solid lines respectively, HD 101584 equivalents are represented by the long dashed lines. For a given Q value, viable accretion mechanisms are those found above the object's estimated accretion.

Chapter 7

IRAS 16279-4757

7.1 Background

IRAS 16279-4757 (hereafter IRAS16279) is a bipolar nebula around a presumed post-AGB star that displays complex large-scale S-shaped outflows (see the Lagadec et al. 2011 VISIR image in Figure 7.1). The central star has been classified as both a M3 and G5 spectral type star (e.g., Suárez et al., 2006; Hu et al., 1993, respectively). IRAS16279 is an interesting candidate for study, as evidence for both polycyclic aromatic hydrocarbon (PAH) and crystalline silicates are observed in the object's envelope, making the object a member of the so-called mixed-chemistry post-AGB stars (e.g., Matsuura et al., 2004). This group of objects are poorly understood. Few objects are seen to display oxygen-rich silicates and carbon-rich PAHs. The explanation for the observed dual-dust chemistry (as presented in the case of IRAS08005), may be a recent transition from an O-rich AGB to star to a carbon-rich one, in which a circumbinary or circumstellar disc would form during the O-rich AGB, allowing the amorphous silicates to crystallise upon cooling, storing the oxygen-rich material of the star's initial oxygen phase (e.g., Waters et al., 1998). Following the third dredge-up, the object would become carbon rich, and a C-rich outflow would lead to PAH molecules forming, resulting in a mixed-chemistry object.

Such a long-lived disc, in which crystalline silicates are stored, may however be at odds with the estimated disc size. The Red Rectangle, which is the prototypical mixed-chemistry post-AGB object (e.g., Waelkens et al., 1996), for example is thought to store its crystalline silicates in a compact and dense disc. One-dimensional radiative transfer models applied to IRAS16279 (e.g., Matsuura et al., 2004), however, revealed that a two-shell model best fit their data, with an inner carbon shell extending from ~ 650 to ~ 3400 AU, and a larger oxygen-rich shell extending from ~ 2700 to ~ 5300 AU, sizes which are several times larger than the disc found in the Red Rectangle. Further radiative transfer models, applied to the higher angular resolution VLTI interferometric observations from both the MIDI and AMBER instruments, (e.g., Bright 2013; henceforth B13), were made in the attempt of constraining the inner circumstellar region at angular resolutions beyond that provided by the 3.6m telescope used by Matsuura et al. (2004). The B13 models revealed a carbon disc extending from approximately 60 AU to

3000 AU. Models including a compact silicate disc were additionally made, but ultimately the carbon disc was favoured. Without evidence of a silicate storage disc, B13, similarly to the conclusions of Matsuura et al. (2004), favoured the alternative hypothesis of (Waters et al., 1996) to explain IRAS16279's dual dust chemistry, in which the crystalline silicates form as a result annealing during the strong, high-temperature post-AGB winds. The task of constraining the inner region of IRAS16279 and determining the disc's composition is one well suited to GADRAD, in which thorough searches of parameter space can be carried out. This is the topic of this chapter.

7.2 Observations

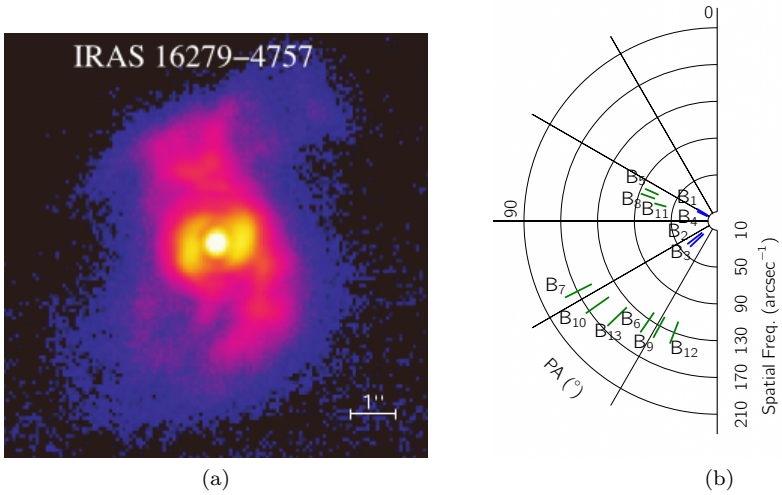

(a) (b)

Figure 7.1: (a) VISIR image of IRAS 16279-4757 from Lagadec et al. (2011). (b) illustration of interferometric *uv*-coverage, where blue lines represent the MIDI baselines. (for λ range 7.5-14μm). Green lines depict baseline coverage of the AMBER measurements (for λ range 2-2.4μm). Baseline characteristics correspond to those presented in Table 7.1.

Interferometric observations of IRAS16279 were taken with the MIDI and AMBER instruments in April 2011 and May 2011 under programme 087.D-0656 (P.I. Bright, S.N.; see B13 for a full account of the observational procedure).[1] The observation log is presented in Table 7.1. Four MIDI measurements were taken in HIGH_SENS mode, with the lower resolution but higher sensitivity (R=30) NaCl prism chosen. Good *uv*-coverage was provided by baselines both perpendicular and parallel to the objects outflows, with measurements taken over a range of baseline lengths (∼39-62m). A map of the MIDI *uv*-coverage spatial frequencies is presented in Figure 7.1b.

Three AMBER measurements were additionally taken of IRAS16279, resulting in 9 baseline measurements (see again Table 7.1). Observations were taken perpendicular and parallel to the object outflows in the *J*-, *H*-, and *K*-bands, with good levels of *uv*-coverage acquired (again see Figure 7.1b). Similar to IRAS08005

[1] Note data was re-reduced by A. Spang.

however, the larger errors observed in the J- and H-band AMBER data indicate it is likely unreliable. We proceed to model with reference to the K-band data only.

Table 7.1: IRAS 16279-4757 observing log.

Label	Date	Time (UTC)	Baseline	Projected Baseline Length (m)	PA (°)
MIDI					
B_1	2012-04-15	09:42	UT2 – UT3	39.0	59.1
B_2	2012-04-17	09:13	UT3 – UT4	62.1	127.8
B_3	2012-04-19	09:34	UT3 – UT4	61.5	133.6
B_4	2012-08-17	02:11	UT2 – UT3	36.0	64.4
AMBER					
B_5	2012-05-17	08:26	UT2 – UT3	35.0	65.9
B_6	2012-05-17	08:26	UT3 – UT4	60.3	145.4
B_7	2012-05-17	08:26	UT2 – UT4	76.0	116.7
B_8	2012-05-17	09:01	UT2 – UT3	36.0	70.3
B_9	2012-05-17	09:01	UT3 – UT4	59.3	151.3
B_{10}	2012-05-17	09:01	UT2 – UT4	71.6	125.1
B_{11}	2012-05-17	09:32	UT2 – UT3	28.9	74.3
B_{12}	2012-05-17	09:32	UT3 – UT4	58.5	158.9
B_{13}	2012-05-17	09:32	UT2 – UT4	67.7	133.7

7.3 Preliminary analysis

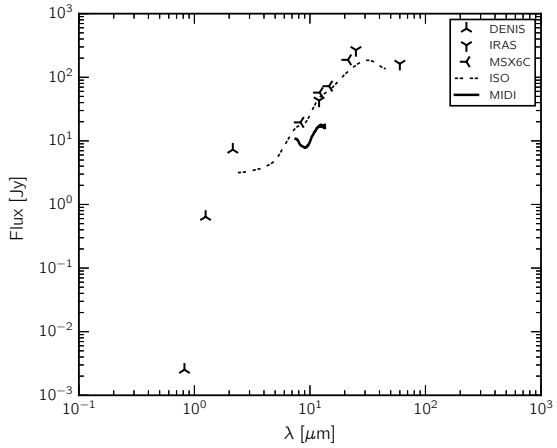

Figure 7.2: The IRAS 16279-4757 spectral energy distribution. The MIDI spectrum is represented by the solid black line.

There is clear evidence of a $\sim$9μm feature observed in the MIDI spectrum (see Figure 7.2). As B13 indicated, the feature may be the result of a silicate disc, or alternatively, the result of a crossover point of two blackbody curves. The analysis of B13 revealed that the latter option is more likely. However, in the context of the literature flux measurements the object is perhaps more complex. For

Table 7.2: IRAS 16279-4757 aperture photometry.

Instrument/Reference	Wavelength (micron)	Flux (Jy)	Aperture
Photometric Data			
DENIS	0.82	2.5×10^{-3}	$4.5''$
	1.25	0.64	$4.5''$
	2.15	7.28	$4.5''$
MSX6C	8.28	1.95	$18.3''$
	12.13	57.4	$18.3''$
	14.65	72.4	$18.3''$
	21.34	188	$18.3''$
IRAS	12	4.3	$0.75' \times 4.5'$
	25	268	$0.75' \times 4.6'$
	60	163	$1.5' \times 4.7'$
Spectroscopic Data			
ISO SWS	2.4-45	3-210	$4.7''$

example, to explain the energy discrepancies, the telescopes' aperture sizes must be considered, which suggests separate extended structures are being resolved in each observational case (see Table 7.2). In the B13 analysis of IRAS16279, the AMBER and MIDI data products were considered separately, and the models that lead to the B13 conclusions considered the MIDI data products only. With GADRAD we set out to construct a fully self-consistent radiative transfer model that accounts for both the K- and N-band interferometric observations. This multi-wavelength approach provides additional constraints on which radiative models can be based, making use of all available data products in this way is important in finding solutions to inverse type problems and thus gives us the best chance of determining a suitable representation of the object.

The sinusoidal shape seen in the visibilities of baselines B_2 and B_3 lead B13 to propose a resolved ring like structure with an inner radius of 75 AU. This pattern is, however, not seen in B_1 and B_4, suggesting that if the inner rim is indeed the cause of these features, that it only being resolved at the longer baselines of B_2 and B_3 (62.1m and 61.5m respectively vs. B_1 and B_4 of 39m and 36m respectively). The MIDI visibilities may also provide guidance to IRAS16279's disc's dust composition. For instance, the common silicate feature at $\sim 9.8\mu$m may be present in baselines B_2 and B_3, where the disc is seen to be larger at these wavelengths. An accurate depiction of the structure, and its inner radius will however require further analysis.

If similar to the post-AGB objects modelled previously, a disc is expected to lie perpendicular to the outflows of the nebula (i.e., with position angle of ∼10 degrees in this instance), and assuming it to be symmetric, a similar sized disc-cross section will be resolved for the baselines orientated at ∼60 degrees (e.g., B_1 and B_4) as for those orientated at ∼130 degrees (e.g., B_2 and B_3). Considering the additional resolving power of the latter baselines, and the similar visibility levels seen, we suggest that the object is not circular. Further modelling is necessary to determine suitable disc models. MIDI visibilities are presented in Figure 7.3.

Similar to IRAS08005, information pertaining to IRAS16279's disc environment in is difficult to decipher from the AMBER measurements. The closure phase measurements in the K-band for instance are clearly centred about zero (see Fig-

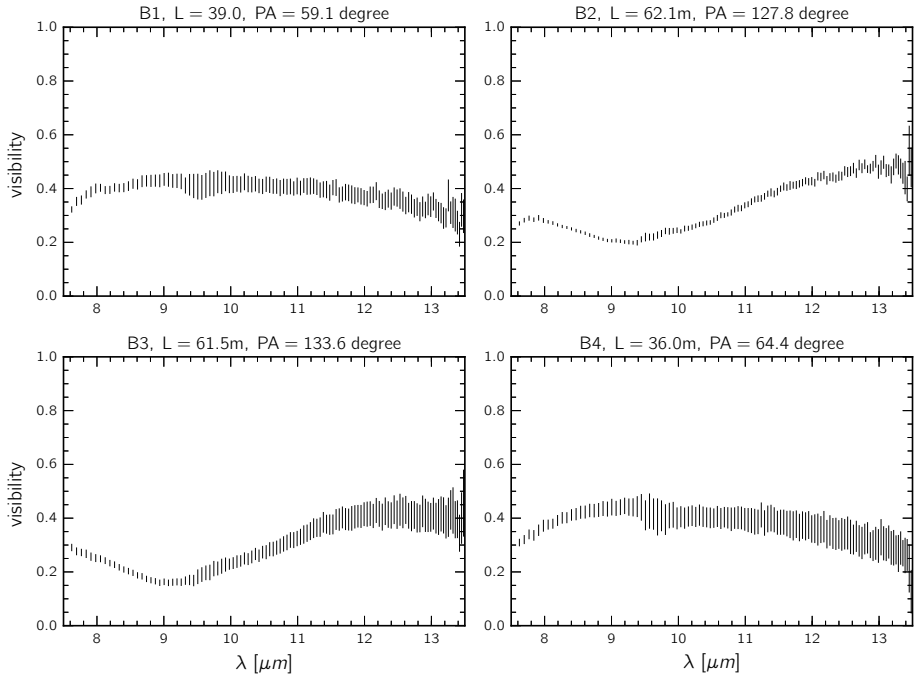

Figure 7.3: MIDI visibilities are represented by the vertical error bar.

ure 7.7), and perhaps contradictory to the MIDI data, suggests that no asymmetries are being detected. The K-band visibilities for the 9 baselines all show similar flat contributions at $\sim$0.4, suggesting no significant change in source morphology is seen over the K-band (see Figure 7.6).

7.4 Radiative transfer modelling

A self-consistent model that accounts for the multi-wavelength observations of IRAS16279 has not yet been determined. Geometric modelling determined from the VLTI AMBER measurements, 2D radiative transfer models of the MIDI measurements (e.g., B13) and 1D radiative transfer models of the thermal infrared (TIMMI-2 ESO instrument of the La Silla 3.6m telescope Matsuura et al. 2004) all present different findings. Insight into the formation history of the dual dust-chemistry object IRAS16279 will come from better understanding and constraining the inner regions of this elusive object. We begin by consulting the literature parameters in the constraint of our initial exploratory `GADRAD` models.

7.5 Preliminary search of parameter space

In the attempt to constrain the parameter space in this exploratory stage, we (similarly to the case of IRAS08005), select large population sizes ($n_{\rm pop} = 1200$), and rely on a generous number of algorithm (iterations; $n_{\rm gen} \sim 500$ see Section 3.2.3 for

a description of these parameters). We again select flat initial sampling domains based on those presented in the literature (see Table 7.3).

We begin by applying 12 initial GA searches, 4 amorphous carbon dust disc models (with adoption of the Hanner 1988 grains), 4 amorphous silicate dust disc models (amorphous silicates of Weingartner & Draine 2001) and finally crystalline silicate equivalents (with grains from Jaeger et al. 1994). To represent the object we again adopt the simple stratified disc model (see Equation 3.15). Though simple in nature, the model class has generalised reasonably well to the post-AGB object so far explored (the limits of the model were however probably met in the case of IRAS08005, see Chapter 6). We favour the simple nature of the disc structure in the case of IRAS16279, as any potential model class irregularities (as seen in the case IRAS08005) can likely be more easily traced, and provides a good basis from which to build upon in future modelling attempts.

The three model sub-classes (amorphous carbon, amorphous silicates and crystalline silicates) result in different disc morphologies, though display similar levels of fitness. In contrast to the conclusions of B13 and Matsuura et al. (2004), in which inner silicate disc/torus were rejected, preliminary GADRAD findings show silicate fitness levels to be promising. However, both silicate model types display some level of energy excess when compared to the ISO spectrum (see Figure 7.13), this excess will be further considered in Section 7.6.2. It should also be noted however, that both carbon and silicate models result in poorly reproduced MIDI visibilities (Figures 7.5, 7.10, respectively). Due to the similarity in resulting fitness between the compositionally different disc models, we proceed to apply GADRAD to the carbon disc models and two silicate disc models independently.

7.6 Results

7.6.1 Carbon dust

We begin by initiating GADRAD with an amorphous carbon dust disc model. Following 6 models, it becomes quickly apparent, that the MIDI visibilities are poorly reproduced. Similar to what we did in the case of IRAS08005, we adopt the fittest model of the 6 GADRAD models as the solution model (see Table 7.4). This solution similarly to B13, was unable to reproduce the $\sim$9μm feature in the MIDI spectrum (see Figure 7.4). Differences between this model and the models presented in B13 are however evident. For example, the inner-disc radius in the B13 model is much larger (60 AU vs. 14 ± 6 AU), and the disc mass is substantially less massive (2×10^{-3} M$_{\odot}$ vs. $3.4 \pm 1.2 \times 10^{-5}$ M$_{\odot}$). Interestingly, this initial model shows good agreement with the AMBER data products (see the AMBER visibilities and closure phases in Figures 7.6 and 7.7 respectively), suggesting, similarly to IRAS08005, the model does a good job of representing the object at high angular resolutions. The discrepancy between the N- and K-band data products, may suggest the object may be more complex than can be generalised by our disc model class.

This initial model's (henceforth referred to as the 'carbon-equal-weight' model; C-EW) SED, shows no excess with the literature (see Figure 7.8). The reason for the $\sim$9μm MIDI spectrum feature not being reproduced however, is unclear,

Table 7.3: IRAS 16279-4757 literature parameter values.

Parameter		Lit. Values	Ref.	GA Range (Min., Max.)
Stellar Parameters				
Temperature (T_1)	10^3K	3.0, 5.7, 6, 10	a,b,c,d	(4,16)
Luminosity (L_1)	$10^3 L_\odot$	10	c	(1,14)
Distance (D)	kpc	1.7, 2.0	a,(e,f,g)	(1.6,2.5)
Secondary Source				
Temperature (T_2)	10^3K	1.5	g	(0.6,4.0)
Luminosity (L_2)	$10^3 L_\odot$	-	-	(1.0,4.0))
Orientation				
Inclination (i)	deg	45	g	(40,90)
Position angle (PA)	deg	10	g	(0,20)
Disc Characteristics				
Inner radius ($r_{\rm in}$)	AU	60, 670*, 1500*	g,c,a	(4,80)
Outer radius ($r_{\rm out}$)	AU	3000, 3350	g,c	(80,4000)
Mid-plane density factor (α)	-	2.0	g	(1.0,5.0)
Vertical-plane density factor (β)	-	0.9, 1.5	g,g	(0.6,2.5)
Scale height (h_0)	AU	6, 15	g,g	(5,40)
Dust mass ($m_{\rm disc}$)	$M_\odot$	2×10^{-3}, 3×10^{-3}	g,c	(10^{-7},10^{-2})
Grain Parameters				
Minimum grain size ($a_{\rm min}$)	μm	0.05	f	(0.001,1000)
Maximum grain size ($a_{\rm max}$)	μm	1.0	f	(1.0,1000)
Size distribution ($a_{\rm pow}$)	-	3.5	f	(2.0,5.0)

[a]van der Veen et al. (1989); [b]Clayton et al. (2014); [c]Matsuura et al. (2004); [d]Silva et al. (1993); [e]Hu et al. (1993); [f]Van de Steene et al. (2000); [g]Bright (2013); *larger surrounding disc; †Amorphous silicates - crystalline silicates - amorphous carbon.

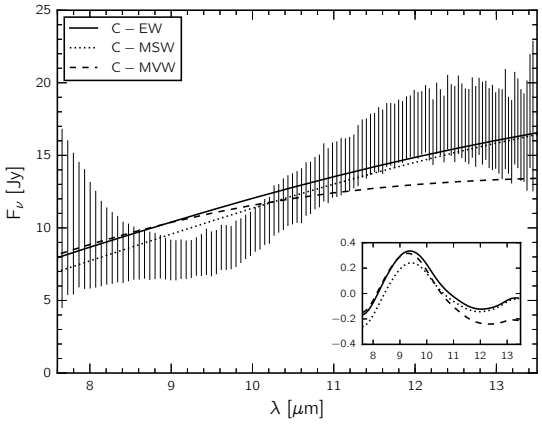

Figure 7.4: The MIDI spectrum is represented by the vertical error bars, to which we compare the resulting flux of the three carbon dust models considered. The equal-weight carbon model (C-EW) is represented by the solid line, the MIDI-spectrum-weighted model (C-MSW) is represented by the dotted line, and the MIDI-visibility-weighted (C-MVW) model is depicted as the dashed line. The corresponding residuals are presented in the inset as percentages.

but may suggest the two blackbody argument as a cause for the feature is weak. For this reason, we continue to explore parameter space, by applying a further 6 GADRAD models, this time with a weighted MIDI spectrum data product (henceforth referred to as the 'carbon MIDI-spectrum-weighted' model; C-MSW). The fittest C-MSW model is presented alongside the C-EW model in Table 7.4.

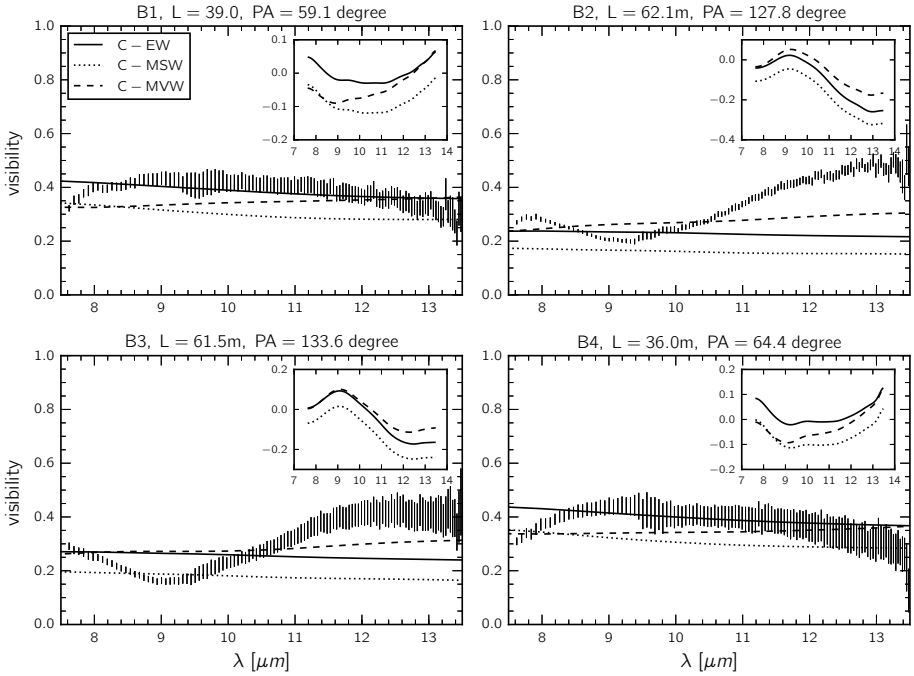

Figure 7.5: The MIDI visibilities are represented by the vertical error bars, in which we compare the resulting visibilities of the three carbon dust models considered. The equal-weight carbon model (C-EW) is represented by the solid line, the MIDI spectrum weighted model (C-MSW) is represented by the dotted line, and the MIDI visibility weighted (C-MVW) model is depicted as the dashed line. The corresponding residuals are presented in the inset as percentages.

As illustrated in Figure 7.4, the C-MSW model indeed provides a marginally better representation to the MIDI spectrum when compared to the C-EW model, reflected in the fitness value ($\Theta_{\rm ms} = 0.70$ vs. $\Theta_{\rm ms} = 0.97$). However, the $\sim$9μm feature in the MIDI spectrum is again not reproduced, perhaps indicating the feature cannot be reproduced by a blackbody crossover. The improved spectrum fit in the C-MSW model however, is seen to come at the expense of the MIDI visibility (see Figure 7.6; with $\Theta_{\rm mv} = 26.6$ vs. $\Theta_{\rm mv} = 56.9$) and the AMBER equivalent (see Figure 7.6; with $\Theta_{\rm av} = 3.43$ vs. $\Theta_{\rm av} = 1.69$). Though the C-MSW model could be classified as a much poorer fit to the resulting AMBER and MIDI data products overall (i.e., with $\Theta_{\rm mv} = 61.5$ vs. $\Theta_{\rm mv} = 29.5$), little difference is seen between model parameters. Other than the dust parameters, which have shown to be ill-constrained in many prior GADRAD implementations, only the dust mass ($34 \pm 12 \times 10^{-6}$ M$_\odot$ for C-EW and $9 \pm 6 \times 10^{-6}$ M$_\odot$ for C-MSW) shows substantial differences, though even here the parameter is found to fall within the errors estimated for the two model types (errors are estimated from the standard deviations of the 6 GADRAD models for each model sub-class).

Both model types evidently do a poor job at accounting for the MIDI visibilities.

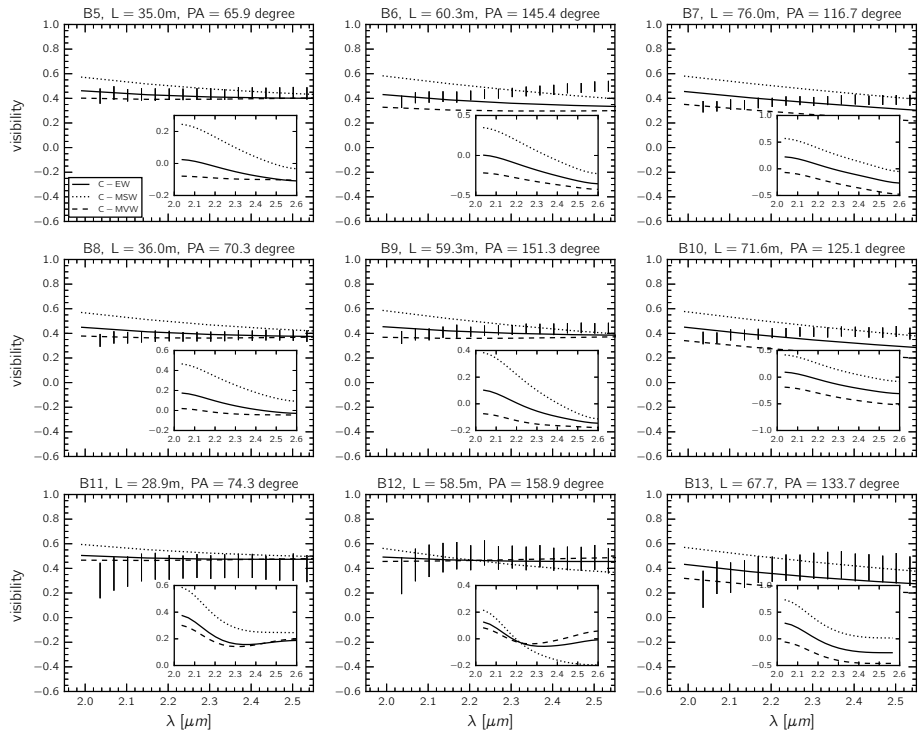

Figure 7.6: The AMBER visibilities are represented by the vertical error bars, to which we compare the resulting visibilities of the three carbon dust models considered. The equal-weight carbon model (C-EW) is represented by the solid line, the MIDI-spectrum-weighted model (C-MSW) is represented by the dotted line, and the MIDI-visibility-weighted (C-MVW) model is depicted as the dashed line. The corresponding residuals are presented in the inset as percentages.

In an attempt of determine a model that better represents all interferometric data products, we initiate a further 6 GADRAD models, this time with weight placed on the MIDI visibility. These models are henceforth referred to as the carbon MIDI-visibility-weight models (C-MVW). The best fitting C-MVW model (presented in Table 7.4), as expected, displays an improved MIDI visibility fit (see Figure 7.5; $\Theta_{\rm mv} = 16.2$ vs. $\Theta_{\rm mv} = 56.9$ and $\Theta_{\rm mv} = 26.6$), and in fact shows a lower cumulative fitness value over all data products. This however is more an indication of the poor job our simple stratified disc model class likely does at accounting for the MIDI visibilities than representation of an improved model solution. The better fitness is also likely a direct result of the fitness measure, which is based on a square value of the error and hence biased towards large discrepancies which is seen in the MIDI visibility. It is evident once more that our model class does not represent the characteristic features found in the true object. The C-MVW model, for example does not match the features seen in each baseline, but instead 'averages' over the observed characteristics, with a flat visibility contribution across all wavelengths. Despite GADRAD exploring regions of parameter space that included models similar to the carbon disc presented by B13, we suggest that carbon dust cannot reproduce the features. Additionally, as seen in IRAS08005, it is evident that the fitting of one interferometric data product is done at the expense of the second, something that is not expected of a more representative model class.

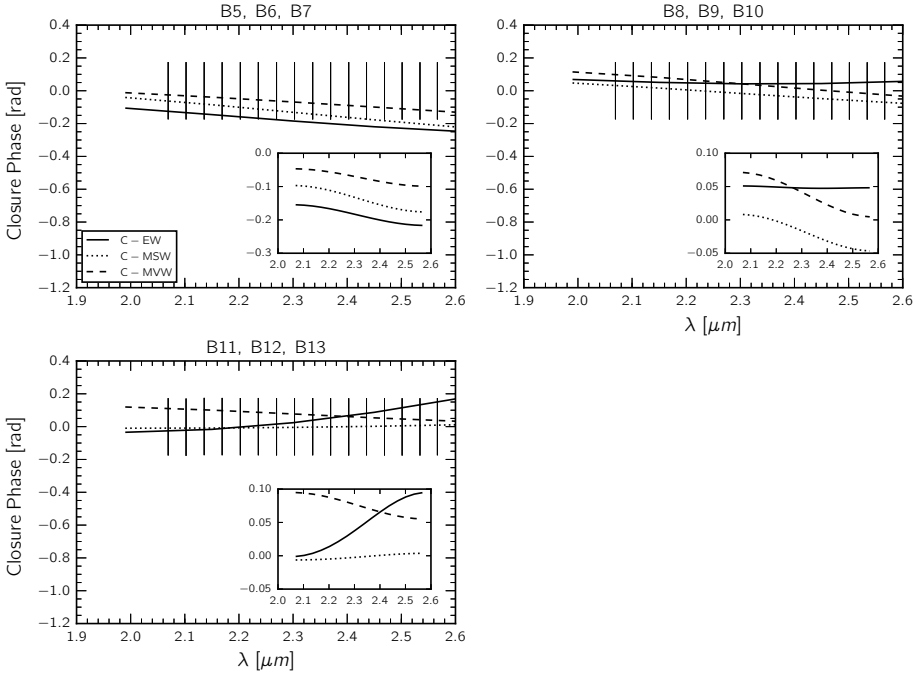

Figure 7.7: The AMBER closure phases are represented by the vertical error bars, to which we compare the resulting closure phases of the three carbon dust models considered. The equal-weight (C-EW) is represented by the solid line, the MIDI-spectrum-weighted model (C-MSW) is represented by the dotted line, MIDI-visibility-weighted model (C-MVW) model is depicted as the dashed line. The corresponding residuals are presented in the inset.

The C-MVW does display some small differences to the C-EW and C-MSW mod-

els, most notably a more compact disc structure, with larger mid-plane density factor and smaller outer-disc radius. Suggesting, in contrast to B13 and Matsuura et al. (2004), that a relatively small disc could reside at the heart of IRAS16279. Overall, however, not much difference is seen between the three carbon disc subclasses. Of note is perhaps the more massive disc in the case of the C-EW model ($34 \pm 12 \times 10^{-6}$ $M_\odot$ vs. $9 \pm 6 \times 10^{-6}$ $M_\odot$ and $5 \pm 4 \times 10^{-6}$ $M_\odot$; though all values fall within each parameters error ranges), and the larger grain size preferred for the C-EW model (80 ± 60 μm vs. 9^{+30}_{-6} μm and $1.25^{+6}_{-0.5}$ μm).

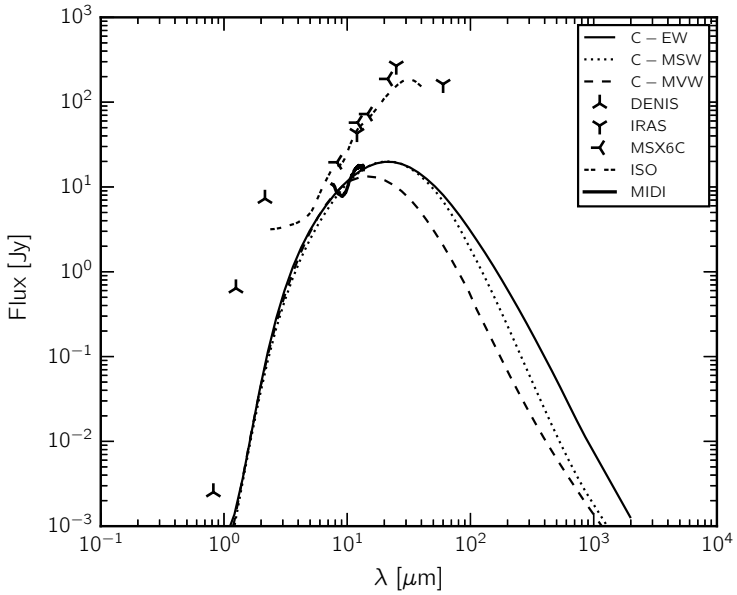

Figure 7.8: The IRAS 16279-4757 spectral energy distribution, in relation to the resulting RT flux from the three carbon models considered. The equal-weight carbon model (C-EW) is represented by the solid line, the MIDI-spectrum-weighted model (C-MSW) is represented by the dotted line, and the MIDI-visibility-weighted model (C-MVW) model is depicted as the dashed line.

It should be noted that all carbon models show good agreement with the AMBER data products, suggesting the model class generalises well enough to represent the object at higher spatial resolutions. Model generalisation to one set of data products in this instance may suggest the model class adopted is unlikely to contain the *true* solution. However, in determining a model to represent IRAS16279, the fitter C-EW and C-MVW models are preferred over the C-MSW. Despite the fitter C-MVW model ($\Theta = 22.6$ vs. $\Theta = 29.5$), the better MIDI spectrum and AMBER visibility representation have us favour the C-EW model. Perhaps, however, a silicate model will provide better representation across the interferometric data products.

7.6.2 Silicate dust disc

A silicate dust disc at the heart of IRAS16279 supports the Waters et al. (1998) hypothesis, in which dual-dust chemistry observed in post-AGB objects is the result of a long-lived crystalline storage disc surviving the transition from the O-rich phase of the host star to the carbon-rich one. Promisingly, in contrast to the

Table 7.4: IRAS 16279-4757 carbon models.

Parameter		Model		
		C-EW	C-MSW	C-MVW
Stellar Parameters				
Temperature (T_1)	10^3K	10.4 ± 2.6	9.85 ± 2.4	10.9 ± 1.5
Luminosity (L_1)	$10^3 L_\odot$	2.6 ± 1.2	2.45 ± 1.0	3.25 ± 0.9
Distance (D)	kpc	2.1 ± 0.2	2.3 ± 0.1	2.3 ± 0.2
Secondary Source				
Temperature (T_2)	10^3K	1.2 ± 0.4	1.3 ± 0.4	1.3 ± 0.3
Luminosity (L_2)	$10^3 L_\odot$	2.2 ± 1.0	3.4 ± 0.8	3.0 ± 0.8
Orientation				
Inclination (i)	deg	75 ± 7	77 ± 5	79 ± 2
Position angle (PA)	deg	3 ± 3	5 ± 3	3 ± 3
Disc Characteristics				
Inner radius ($r_{\rm in}$)	AU	14 ± 6	16 ± 4	17 ± 3
Outer radius ($r_{\rm out}$)	AU	230 ± 40	240 ± 60	150 ± 40
Mid-plane density factor (α)	-	1.7 ± 0.4	1.7 ± 0.5	2.4 ± 0.3
Vertical-plane density factor (β)	-	1.1 ± 0.2	1.2 ± 0.2	1.4 ± 0.1
Scale height (h_0)	AU	22 ± 4	21 ± 5	12 ± 4
Dust mass ($m_{\rm disc}$)	$10^{-6} M_\odot$	34 ± 12	9 ± 5	5 ± 4
Grain Parameters				
Minimum grain size ($a_{\rm min}$)	μm	$0.07^{+0.5}_{-0.03:}$	$0.005^{+0.3}_{-0.003:}$	$0.004^{+0.1}_{-0.002:}$
Maximum grain size ($a_{\rm max}$)	μm	80 ± 60	$9^{+30}_{-6:}$	$1.25^{+6}_{-0.5:}$
Size distribution ($a_{\rm pow}$)	-	3.4 ± 0.3	3.2 ± 0.2	2.8 ± 0.7
Fitness measure				
MIDI spectrum ($\Theta_{\rm ms}$)	-	0.97	0.702	1.69
MIDI visibility ($\Theta_{\rm mv}$)	-	26.6	56.9	16.2
AMBER visibility ($\Theta_{\rm av}$)	-	1.69	3.43	4.50
Closure Phase ($\Theta_{\rm cp}$)	-	0.26	0.52	0.18
Total (Θ)	-	29.5	61.5	22.6

The errors are calculated from the parameter sample standard deviation over the N_{GA} GAs. Where the standard deviation is larger than the parameter value we provide it as a positive upper limit, the lower limit (followed by :) is the lowest value in the model sample.

carbon discs of the previous section (including the MIDI-spectrum weighted GA searches), preliminary exploration of parameter space, shows both amorphous and crystalline silicate discs reproduce the $\sim 9\mu$m feature in the MIDI spectrum (see for example Figure 7.9).

We proceed to model the amorphous and crystalline disc types separately. Though the disc is perhaps more likely composed of a fraction of amorphous and crystalline components (with a likely higher fraction of crystalline dust; i.e., Waters et al. 1998), determining a composition ratio will likely be difficult. As was evident from preliminary analyses for example, very similar discs result from both amorphous and crystalline silicate dust compositions. Discerning between these, will most likely necessitate additional spectroscopic data products. By instead focusing on the two silicate compositions independently, limitations on disc parameters can be determined for each model sub-class, and more broad and inclusive parameter constraints can be drawn.

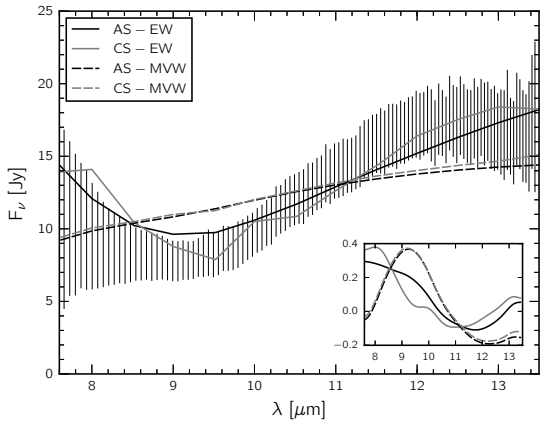

Figure 7.9: The MIDI spectrum is represented by the vertical error bars, to which we compare the resulting flux of the three amorphous silicate dust models considered. The equal-weight amorphous silicate model (AS-EW) is represented by the solid dark line, the equal-weight crystalline silicate model (CS-EW) is represented by the solid grey line, the amorphous silicate MIDI-visibility-weighted model (AS-MVW) is depicted as the dark dashed line, finally the crystalline silicate MIDI-visibility-weighted model (CS-MVW) is represented by the grey dashed line. The corresponding residuals are presented in the inset as percentages.

We begin by applying 12 GADRAD models, 6 amorphous silicate models and 6 crystalline silicate. These models are henceforth referred to as the amorphous and crystalline silicate, equal-weight models (AS-EW and CS-EW respectively), with the best fitting model for each dust type presented in Table 7.5, errors are again calculated from the parameter standard deviation. Differences between the disc environments determined in the case of the AS-EW and CS-EW models are again determined to be relatively small. The largest difference between these 2 model sub-classes, is the hotter secondary source favoured by the CS-EW model (2300 ± 400K vs. 1300 ± 400K) and larger disc mass mass ($3.2 \pm 1.1 \times 10^{-5}$ M$_\odot$ vs. $1.1 \pm 0.5 \times 10^{-5}$ M$_\odot$).

Perhaps more noteworthy, however, is the similarity seen between the models resulting data product fits. As evident in Figure 7.9 for example, both the AS-EW and CS-EW models show good agreement with the N-band spectrum, and the SED more generally (see Figure 7.13), and both models show good agreement

with the K-band data products.

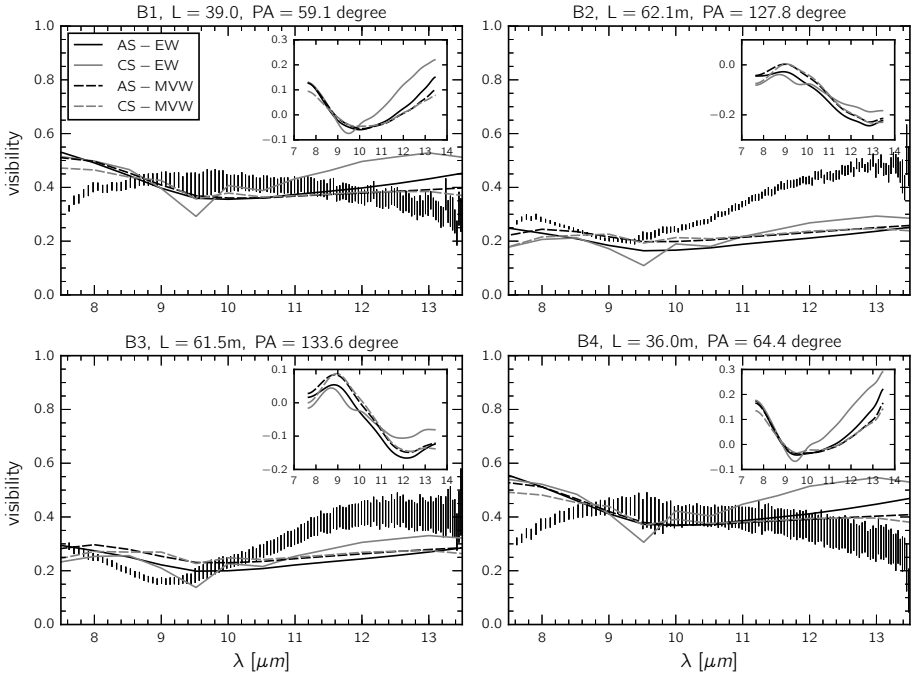

Figure 7.10: The MIDI visibilities are represented by the vertical error bars, in which we compare the resulting visibilities of the three amorphous silicate dust models considered. The equal-weight amorphous silicate model (AS-EW) is represented by the solid dark line, the equal-weight crystalline silicate model (CS-EW) is represented by the solid grey line, the amorphous silicate MIDI-visibility-weighted model (AS-MVW) is depicted as the dark dashed line, finally the crystalline silicate MIDI-visibility-weighted model (CS-MVW) is represented by the grey dashed line. The corresponding residuals are presented in the inset as percentages.

We should however note the AS-EW and CS-EW models SED contribution between $\sim$4μm and $\sim$7μm, in which both models show an energy excess with relation to the ISO spectrum. This however is likely caused by fitting the MIDI spectrum feature at $\sim$9μm. A model tasked with providing good representation of both the MIDI and ISO spectrums, for example, would require a very abrupt drop in energy contributions below $\sim$7μm. Though such an SED is possible, we suggest that there is support for the 'continuous' distribution seen in both the AS-EW and CS-EW models. We suggest instead that the ISO spectrum, observed with a different aperture, is resolving a feature that provider a lower energy contribution to the MIDI instrument. The model SEDs presented in Figure 7.13 are reddened with $E(B-V) = 1.0$, It is however clear that the spectrum is poorly reproduced at short wavelengths. Further model exploration will likely be necessary to fit the wavelengths in the K- and I-bands.

Though both the AS-EW and CS-EW show improvements to the MIDI spectrum, as well as the AMBER visibilities and AMBER closure phases compared to the carbon disc (see Figures 7.11 and 7.12 respectively). The MIDI visibilities, are again poorly reproduced (see Figure 7.10). In an attempt to reconcile this discrepancy, we run a further 12 GADRAD models, 6 amorphous silicate, MIDI-visibility-weighted models (AS-MVW), and 6 crystalline silicate equivalents (CS-MVW).

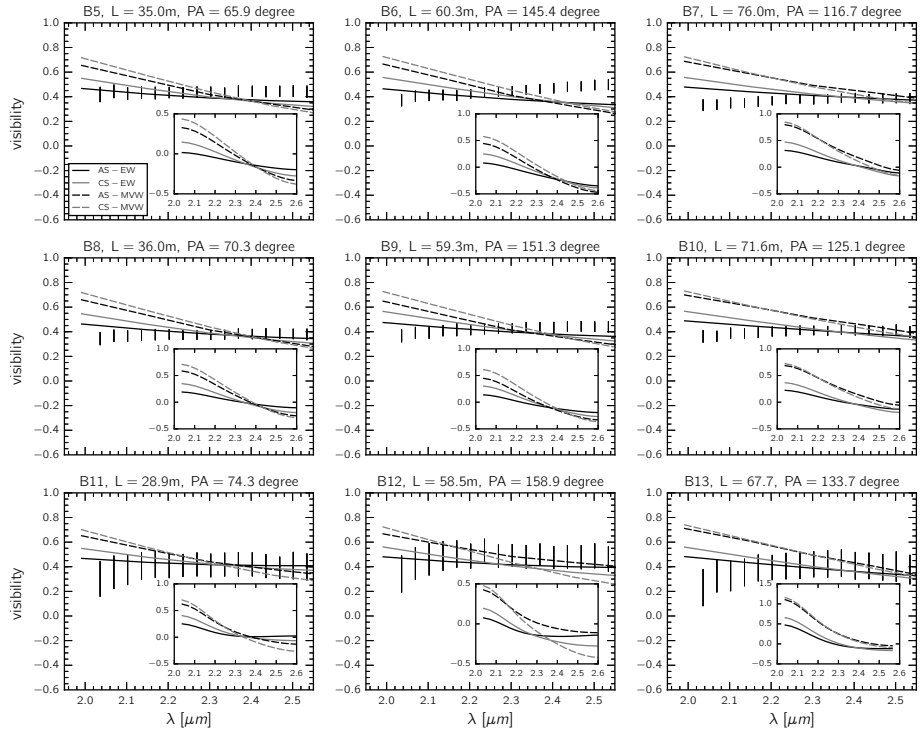

Figure 7.11: The AMBER visibilities are represented by the vertical error bars, to which we compare the resulting visibilities of the three amorphous silicate dust models considered. The equal-weight amorphous silicate model (AS-EW) is represented by the solid dark line, the equal-weight crystalline silicate model (CS-EW) is represented by the solid grey line, the amorphous silicate MIDI-visibility-weighted model (AS-MVW) is depicted as the dark dashed line, finally the crystalline silicate MIDI-visibility-weighted model (CS-MVW) is represented by the grey dashed line. The corresponding residuals are presented in the inset as percentages.

The fittest AS-MVW and CS-MVW models are presented in Table 7.5, errors are similarly calculated from the parameter's standard deviation.

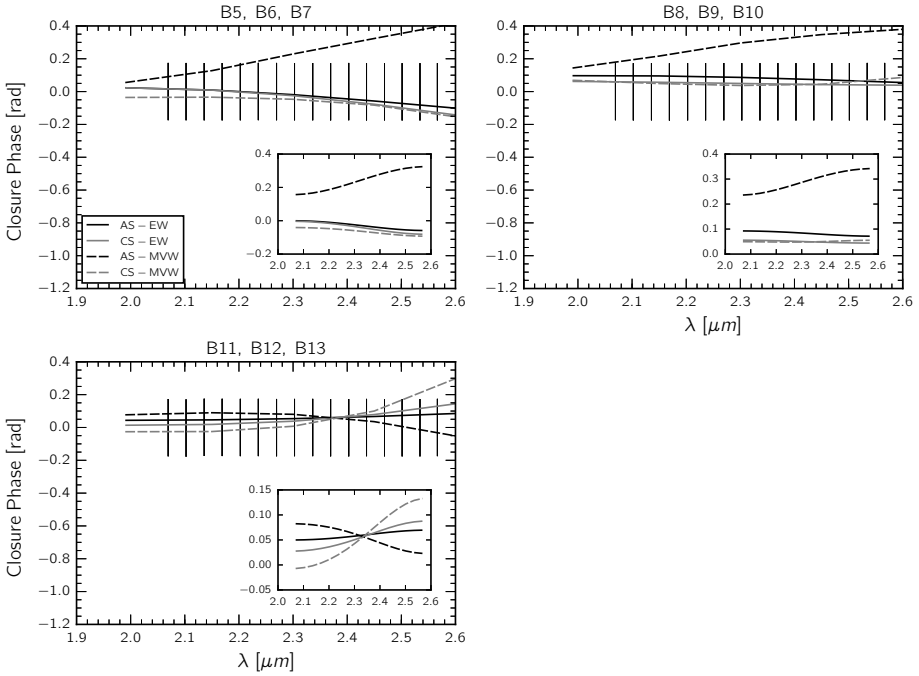

Figure 7.12: The AMBER closure phases are represented by the vertical error bars, in which we compare the resulting closure phases of the three amorphous silicate dust models considered. The equal-weight amorphous silicate model (AS-EW) is represented by the solid dark line, the equal-weight crystalline silicate model (CS-EW) is represented by the solid grey line, the amorphous silicate MIDI-visibility-weighted model (AS-MVW) is depicted as the dark dashed line, finally the crystalline silicate MIDI-visibility-weighted model (CS-MVW) is represented by the grey dashed line. The corresponding residuals are presented in the inset as percentages.

Differences of note between the resulting disc environment between the EW model sub-classes and the MVW models is the increased primary temperature and luminosity. With the object up to twice as luminous and almost double the temperature of the EW equivalent. The disc mass in the CS-MVW model was also determined to be up to ten times that of the other models in some cases. There is also a noticeable reduction in the scale height. Perhaps most notable, however, is the similarity seen between the parameters. The inner and outer-disc radius are seemingly well constrained to values between 20-23 AU. Disc compactness and flaring were also found to be comparable across the models.

Though both the AS-MVW and CS-MVW show improved MIDI visibility fits, they are again achieved at the expense of the other data products. For example the improved AS-MVW and CS-MVW MIDI visibilities (with $\Theta_{\rm mv} = 27.9$ and $\Theta_{\rm mv} = 27.1$, vs. $\Theta_{\rm mv} = 35.4$ and $\Theta_{\rm mv} = 29.8$ for AS-EW and CS-EW respectively), result in poorer overall MIDI spectrum representation, in addition to AMBER visibilities and closure phases. In Figure 7.9, for example the $\sim 9\mu$m feature in the MIDI spectrum is not fitted. The AMBER visibilities model is steeper than the observations, suggesting the modelled object in both instances is smaller at shorter wavelengths than the true object. While the AMBER closure

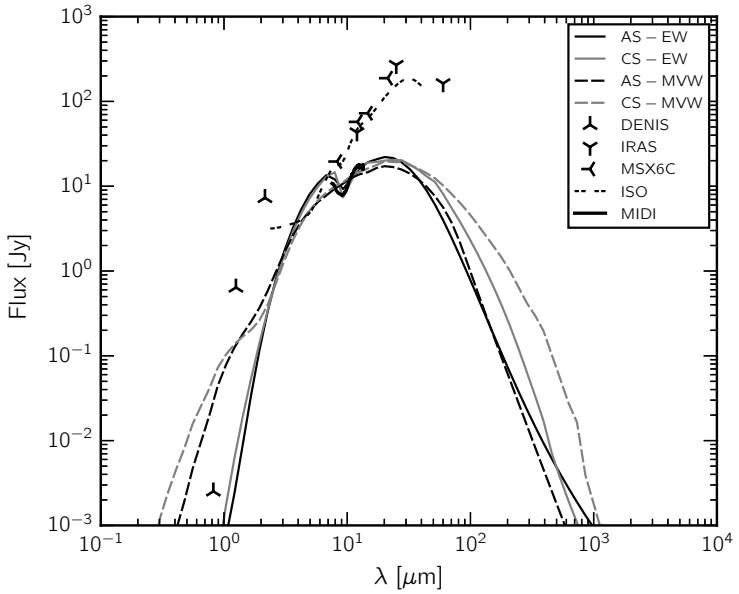

Figure 7.13: The IRAS16279 spectral energy distribution, in relation to the resulting RT flux from the three amorphous silicate models considered. The equal-weight amorphous silicate model (AS-EW) is represented by the solid dark line, the equal-weight crystalline silicate model (CS-EW) is represented by the solid grey line, the amorphous silicate MIDI-visibility-weighted model (AS-MVW) is depicted as the dark dashed line, finally the crystalline silicate MIDI-visibility-weighted model (CS-MVW) is represented by the grey dashed line. The corresponding residuals are presented in the inset as percentages.

Table 7.5: IRAS 16279-4757 silicate models

Parameter		Model			
		AS-EW	CS-EW	AS-MVW	CS-MVW
Stellar Parameters					
Temperature (T_1)	K	9.9 ± 2.9	8.7 ± 1.6	14.8 ± 2.7	14.0 ± 1.4
Luminosity (L_1)	$10^3 L_\odot$	3.2 ± 1.4	2.6 ± 0.3	5.2 ± 2.7	6.6 ± 1.1
Distance (D)	kpc	2.3 ± 0.2	2.2 ± 0.2	2.1 ± 0.1	2.2 ± 0.2
Secondary Source					
Temperature (T_2)	10^3K	1.3 ± 0.4	2.3 ± 0.4	3.4 ± 0.8	0.83 ± 1.1
Luminosity (L_2)	$10^3 L_\odot$	2.0 ± 0.5	2.3 ± 0.6	$1.2^{+1.6}_{-0.4}$	2.2 ± 0.1
Orientation					
Inclination (i)	deg	74 ± 3	73 ± 2	77 ± 3	78 ± 3
Position angle (PA)	deg	2.5 ± 4	3 ± 1	2 ± 2	1 ± 2
Disc Characteristics					
Inner radius ($r_{\rm in}$)	AU	20 ± 5	20 ± 2	20 ± 6	23 ± 5
Outer radius ($r_{\rm out}$)	AU	280 ± 150	210 ± 50	240 ± 120	230 ± 100
Mid-plane density factor (α)	-	2.7 ± 1.4	2.2 ± 0.3	2.4 ± 1.1	2.9 ± 0.4
Vertical-plane density factor (β)	-	1.1 ± 0.3	1.0 ± 0.2	1.3 ± 0.2	1.4 ± 0.1
Scale height (h_0)	AU	26 ± 7	24 ± 7	14 ± 9	14 ± 7
Dust mass ($m_{\rm disc}$)	$10^{-6} M_\odot$	11 ± 5	32 ± 11	14 ± 4	155 ± 50
Grain Parameters					
Minimum grain size ($a_{\rm min}$)	μm	$0.09^{+0.2}_{-0.04:}$	0.07 ± 0.05	$0.004^{+0.4}_{-0.002:}$	$0.006^{+0.08}_{-0.0:}$
Maximum grain size ($a_{\rm max}$)	μm	$3^{+20}_{-1:}$	60 ± 30	$10^{+40}_{-5:}$	120 ± 40
Size distribution ($a_{\rm pow}$)	-	3.6 ± 0.9	3.9 ± 0.3	3.4 ± 1.5	3.0 ± 0.3
Fitness measure					
MIDI spectrum ($\Theta_{\rm ms}$)	-	0.53	0.42	1.56	1.43
MIDI visibility ($\Theta_{\rm mv}$)	-	35.4	29.8	27.9	27.1
AMBER visibility ($\Theta_{\rm av}$)	-	1.58	3.03	7.11	8.79
Closure Phase ($\Theta_{\rm cp}$)	-	0.15	0.14	1.89	0.25
Total (Θ)	-	37.7	33.4	38.3	37.6

The errors are calculated from the parameter sample standard deviation over the N_{GA} GAs. Where the standard deviation is larger than the parameter value we provide it as a positive upper limit, the lower limit (followed by :) is the lowest value in the model sample.

phases, specifically in the case of the amorphous silicate disc, show asymmetries not observed. The AS-MVW and CS-MVW models do not fit the energy distributions at short wavelengths. The DENIS fluxes in Figure 7.13 for example, indicate significantly less energy is present at wavelengths short-ward of $\sim 1\mu$m than displayed by the AS-MVW and CS-MVW models. This excess can only be explained by a significantly higher reddening than suggested in literature, though they are not out of the range of possibility, and the aperture resolving capabilities must be considered. We cannot conceive of a model class that fit successfully the short wavelength side of our data set.

7.7 Summary and discussion

It is evident that the GADRAD models of IRAS16279 display systematic differences with the interferometric data products of the true source. The differences likely indicate that the chosen model class, a simple 2D stratified disc density and a

multi-temperature point source, does not generalise well enough to characterise a model representative of the observed environment. However, the simple model-class adopted, may be suited to the determination of the general characteristics of the central star temperature and luminosity for example, as well as the disc size. Similar to our discussion of IRAS08005 (Section 6.7) we suggest that an expansion of parameter space to include asymmetric features, would require additional data. However, considering a simple circumstellar gas structure, or other simple 2D disc density structures, may be worth pursuing in future modelling attempts. Also to be considered is a larger surrounding disc extending form ∼650 to ∼3400 AU (e.g., Matsuura et al., 2004), or even a third disc from ∼2700 to ∼5300 (though at these spatial scales they would likely be over resolved by the VLTI).

In the attempt of gaining disc environment constraints, a number of model sub-classes were explored. As IRAS16279 is a dual-dust chemistry object, we explored a number of dust compositions, in particular amorphous carbon, amorphous silicate and crystalline silicate disc compositions. We explore disc composition model sub-classes independently, this was done in the attempt to determine individual parameter limitations for many possibilities. Exploring these sub-classes independently, allows us to study the extremes of the given model class parameter space. The adopted model class is unlikely to be a true representation of the object. However, parameter *upper* limits hopefully include an accurate representation of the *true* parameters.

Regarding disc composition, we find that both silicate species, amorphous and crystalline, as well as the carbon dust, are comparable in terms of overall model fitness. However, we find the non-weighted amorphous and crystalline silicates models are best able to reproduce the MIDI spectrum feature at $\sim 9\mu$m, this feature was attempted to be reproduced with a carbon disc, however following exploration over a range of primary and secondary temperatures and luminosities the MIDI-spectrum-weighted GADRAD implementations, produces flat spectrums. This suggests the feature is a result inherent to a silicate disc, as opposed to a crossover point of two potential blackbodies, as suggested by B13. It is possible that a larger silicate disc is seen by MIDI while a smaller, carbon-rich dust distribution is seen by AMBER.

The MIDI visibilities of IRAS16279 could not be reproduced, with the data product providing consistently the poorest representation for all model types. Though slight improvement in the fits came in the application of the three MIDI-visibility-weighted models, good representation remained elusive. The carbon MVW model produced the best reproduction of the MIDI visibility in terms of the fitness measure, but the characteristic features detected were not reproduced, with the solution simply providing a flat contribution over the N-bandwidth, in essence 'averaging' over the features. The AMBER visibilities, were best produced by the equal weighted carbon and amorphous silicate discs, other models consistently showed disagreement at shorter wavelengths in-particular, the visibility steepness indicated the modelled objects were less extended then the true source at the shorter wavelengths. However, AMBER closure phases showed good agreement in all instances, likely suggesting the higher resolution K-band data products are ill-constraining in regard to our adopted model class. The AS-MVW and CS-MVW models show some short wavelength energy excesses with the literature, overall however, models show poor representation at short wavelengths, we cannot conceive of a model class that would provide good representation at the short

wavelength side of our data set.

These 7 GADRAD models are summarised with relation to their fitness quality to a given data product in Table 7.6. We, rather arbitrarily, assign a check-mark (✓) to the models that display 'good-fitness' values with Θ between 0 and 2, a cross-checkmark (×✓) to the 'moderate-fitness' models with fitness ranging from 2 and 15, and a cross (×) to 'poor-fitness' models with measures above 15. Only the MIDI spectrum and AMBER closure phases are well reproduced by all model sub-classes. It is also evident that the MIDI visibility was the hardest data product to reproduce, with poor-fitness resulting in all model cases. Considered in this manner, the carbon and amorphous silicate equal-weighted models provide the best overall representation. Due to the ability of the amorphous silicate model to reproduce the 10μm feature observed in the MIDI spectrum, we posit that this is the best representation of IRAS16279 for this given model class.

Table 7.6: IRAS 16279-4757 model overview: MS and AS represent the MIDI and AMBER spectrums respectively, AV and AC represent the AMBER visibility and closure phase data products respectively. Check-marks in the SED column are awarded to the models that show little to no energy excess with regards to the literature.

	MS	MV	AV	AC	SED
C-EW	✓	×	✓	✓	✓
C-MSW	✓	×	×✓	✓	✓
C-MVW	✓	×	×✓	✓	✓
AS-EW	✓	×	✓	✓	✓
AS-MVW	✓	×	×✓	✓	×✓
CS-EW	✓	×	×✓	✓	✓
CS-MVW	✓	×	×✓	✓	×✓

Similarly to IRAS08005 we determine appropriate accretion rate mechanisms responsible for energetic outflows observed in IRAS16279. Adopting the mass loss rate of 5×10^{-4} $M_{\odot}$ (e.g., Matsuura et al., 2004), and a dynamical time scale for the outflow of 450 years (i.e., Silva et al., 1993), we estimate an outflow mass of 0.25 $M_{\odot}$. With outflow velocities of 15-20 km s^{-1} (e.g., Silva et al., 1993; Matsuura et al., 2004), we determine a scalar momentum of approximately 1×10^{39} g cm s^{-1}. For comparison we plot in Figure 7.14 the accretion rate derived for IRAS16279 as a function of efficiency parameter Q (see Equation 4.1 in Section 4.5.2), along-

side that derived for IRAS08005 (see Section 6.7). We conclude that similarly to IRAS08005, the likely momentum of the outflow necessitates common-envelope-type accretion, or Roche lobe overflow onto a main sequence star.

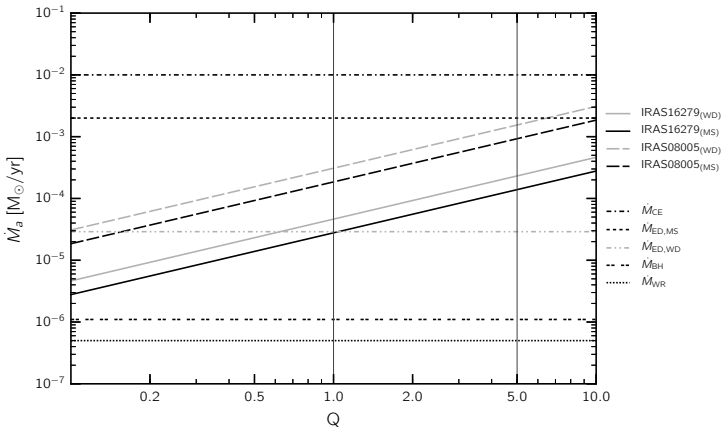

Figure 7.14: Theoretical mass accretion rate onto a putative companion versus efficiency parameter Q for IRAS 16279-4757 and IRAS 08005-2356 following Blackman & Lucchini (2014). The accretion mechanisms (horizontal lines; from top to bottom) for a 1-$M_\odot$, 1-$R_\odot$ main sequence (MS) star and a 0.6-$M_\odot$, 0.014-$R_\odot$ white dwarf (WD) star represent: common envelope accretion ($\dot{M}_{CE}$=10^{-2} $M_\odot yr^{-1}$ with $\dot{M}_{CE,MS}$=$\dot{M}_{CE,WD}$); Eddington accretion for a MS star ($\dot{M}_{ED,MS}$=2×10^{-3} $M_\odot yr^{-1}$); Eddington accretion for a WD star ($\dot{M}_{ED,WD}$=2.9×10^{-5} $M_\odot yr^{-1}$); Bondi-Hoyle accretion ($\dot{M}_{BH}$=1.1×10^{-6} $M_\odot yr^{-1}$ with $\dot{M}_{BH,MS}$=$\dot{M}_{BH,WD}$) and, finally, accretion caused by wind Roche lobe overflow ($\dot{M}_{WR}$=5×10^{-7} $M_\odot yr^{-1}$, where again $\dot{M}_{WR,MS}$=$\dot{M}_{WR,WD}$). The IRAS16279 WD and MS accretion cases are plotted as the grey and black solid lines respectively, IRAS08005 equivalents are represented by the long dashed lines. For a given Q value, viable accretion mechanisms are those found above the object's estimated accretion.

Chapter 8

Conclusions and outlook

"...our result is vitiated, not, of course, by any confusion or irregularity in Nature, but by our ignorance of essential elements in the calculation."

H.D. Thoreau – 1854

A consistent narrative that fully characterises the post-Asymptotic Giant Branch (post-AGB) to planetary nebula (PN) evolutionary transition, has yet to be established. This highly transformative stage of stellar evolution is complex, with magnetic fields, accretion discs, jets and binary interactions, all proposed to act either in isolation or in a coordinated effort to drive the complex outflows seen in these objects (e.g., Balick & Frank, 2002; De Marco, 2009). Circumstellar discs, whether the small accretion discs or larger circumbinary discs are accepted as an important agent in the shaping of asymmetric PNe.

In this thesis we aimed to constrain the larger (AU scale) cool and dusty circumbinary discs. Determination of a disc's physical parameters, can provide insights into their formation history. For example, constraints on a disc's geometry, mass, chemical composition and central star properties can provide the information necessary in the determination of the disc's role in shaping the bipolar outflows, whether directly or indirectly (e.g., Balick & Frank, 2002). Finding discs with different characteristics may, for example, provide better understanding of their evolutionary path.

Resolving these milliarcseconds scale discs remains challenging, however. We achieve the required angular resolution via optical interferometric techniques. In these often complex objects, however, interpretation of interferometry observations relies heavily on numerical modelling approaches such as radiative transfer. Such models are not trivial, and often come at non-inconsequential computational expense, and are further complicated by the numerous parameters that can associated for a given model class. We suggest that searching these often complex parameter spaces requires robust optimisation techniques.

In an attempt to improve upon previous *ad-hoc* radiative transfer procedures, we have developed `GADRAD`, a radiative transfer model search heuristic that efficiently fits disc models to the interferometric data products of post-AGB environments. This process is an ill-posed general inverse type problem. By applying genetic algorithms to radiative transfer model classes, we have demonstrated that `GADRAD` can

efficiently determine parameter sets that describe post-AGB environments.

In contrast to previous genetic algorithm (GA) radiative transfer fitting procedures (as applied in other astrophysical systems, e.g., Hetem & Gregorio-Hetem 2007; Menu et al. 2014 and De Geyter et al. 2013), GADRAD relies on a number ($N_{\rm GA}$) of GAs to independently sample the objective function near its minima, from which we construct parameter distributions. Ultimately these distributions provide insight into appropriate solution sets, in addition to confidence intervals on the individual parameters. This approach allows us to determine regions of parameter space that represent *good-fitting* model solutions for a given model class. This procedure is a significant improvement on previous fitting techniques, which rely on *a priori* constraints, which can often lead to model biases. It is evident that GADRAD provides a systematic, efficient and thorough approach to the determination of the discs within these post-AGB environments.

GADRAD provides seamless interfacing between the developed GA python modules and the FORTRAN radiative transfer code RADMC−3D. We developed GADRAD to be parallelised to run using the OpenMPI library, which affords us the ability of running each RADMC−3D simulation on a separate computational thread. Not common to all GA methods, GADRAD allows parameter dependencies to be accounted for, thus limiting search spaces.

However, model solutions provided by GADRAD do not represent an *exact* solution, but quasi-solutions, i.e., solutions of a certain model class. The determination of the model class within which to explore parameter space is left to the modeller, something that presents its own limitations and biases. For example, the GADRAD solutions of Mz3 and M2-9, were found to provide good representation of the object's data products. The model's simplicity, suggests that the solutions provide good characterisation of the predominant geometry and energy features of the true object. In the more complex objects IRAS08005 and IRAS16279, however, the model class is likely too simple. For example, it was found that the fitting of one interferometric data product came at the expense of a second, which suggests a different model class is likely.

8.1 Post-AGB objects

In this section we provide an overview of the GADRAD model results of the post-AGB objects considered in the this thesis. Mz3, to which previous radiative transfer models had been applied with good success e.g., C07, was selected as a test subject, in which the GADRAD method could be applied, and resulting model fitnesses given context. With promising results, we considered Mz3's spectroscopic twin, M2-9, in which similar radiative transfer models had been applied (e.g., L11). Finally, the two-mixed chemistry objects, IRAS08005 and IRAS16279, were chosen for the good quality AMBER and MIDI data products across a number of baselines, providing appropriate levels of uv-coverage upon which to base 2D radiative transfer models. Both objects have previously determined to be complex morphologically (e.g., B13). We set out to achieve self-consistent, multi-wavelength (K- and N-band) radiative transfer modelling, which had not yet been achieved through previous methods.

8.1.1 Mz3

In agreement with C07, we conclude that an amorphous silicate disc lies at the centre of Mz3, though we predict it to be more massive and compact than previous studies. Based only on the momentum of the lobes, we suggest the bipolar structures observed in Mz3 are likely caused by massive collimated jets, launched either as a result of Roche lobe overflow during the AGB, or during the subsequent common envelope phase. However, the mass in the lobes is too great to have been ejected by jets during the Roche-lobe or the common-envelope phases, as their timescales are too short. We suggest instead that it is more likely that the material was ejected during an event capable of ejecting copious amounts of mass in a short time, such as that of the common-envelope ejection itself (rather than a jet from the companion produced during the common envelope phase). A *polar* common-envelope ejection would require the support of a magnetic field to direct the outflows pole-wards (Nordhaus & Blackman, 2006). Without magnetic fields, common envelope events focus the envelope ejection along the equatorial plane (Passy et al., 2012). We expect the observed silicate disc, if formed prior to the outflow event, to perhaps have played a small role in diverting the outflows. However, the disc could have formed subsequently to the common-envelope ejection event, as fall-back gas composed of the material that failed to be ejected entirely (e.g., Kuruwita et al., 2016). Based on the temperature and luminosity of the central star determined by GADRAD, we, contrary to what to what has been suggested (e.g., Calvet & Peimbert, 1983; Smith, 2003), find Mz3 to be inconsistent with a symbiotic description. We suggest instead that it is a post-AGB star surrounded by the stellar envelope ejected and collimated by the common envelope event.

8.1.2 M2-9

We apply GADRAD to M2-9 similarly to what was done for Mz3. The resulting parameter probability distributions, suggest a more luminous and distant central source to what was previously presented to the literature. Our disc was found to be consistent with recent flux measurements, which are inconsistent with the Lykou et al. (2011) model.

The primary temperature and luminosity estimated by GADRAD (12,700 K and 3960 $L_\odot$) suggest that the central star of M2-9 is a 0.55 $M_\odot$ post-AGB star, which similarly to Mz3, puts it at odds with the white dwarf and giant companion symbiotic description (e.g., Clyne et al., 2015). Following similar arguments to those applied to Mz3, we suggest the high momentum bipolar structures observed can only be caused as a result of accretion on the companion at the time of Roche lobe overflow or during a common envelope phase. Aside from the central source likely being a post-AGB star, the potential outflow momentum provided by Bondi-Hole accretion and wind-Roche lobe overflow in a symbiotic system, are unlikely to meet the momentum requirements seen in M2-9's outflows. As was the case for Mz3, however, only a polar common-envelope ejection could form such massive lobes in short time available (see $t_{\rm acc}$ in Table 8.2). In this case, the observed ∼90 yr period in M2-9's light curve, suggests that the original system was a triple, in which the observed wide companion was in orbit about a close binary, which went through the common envelope event. The common envelope would have either

merged the binary, or there is today a closer companion obscured by the dusty disc.

8.1.3 IRAS 08005-2356

The description obtained of the dual-chemistry post-AGB object IRAS08005, is however less clear-cut than the scenarios determined for both Mz3 and M2-9 previously. An accurate representation of the true model class could not be determined, and instead we rely on a total of 68 GAs across 6 model sub-classes.

We determine, in line with the literature constraints, evidence of both 'cool-star' and 'hot-star' primary models (with T_1 of 7200±1700 K and 13,000±1200 K, respectively), which both suggest a post-AGB star is at the heart of the nebula. We find evidence of a compact silicate disc at the core of IRAS08005, supporting the theory of Waters et al. (1998) in which such discs are proposed to exist as an oxygen storage disc in the dual-chemistry post-AGB objects. We point out however, that the model class adopted for its geometric simplicity is non-physical. Our disc structure surrounds a point source comprising two blackbodies: the star and a cooler gaseous structure (800-1200 K). However, the gaseous structure often extends beyond the inner radius of the dusty disk. This suggests that the boundary between the gaseous structure and the dust disk may not be so clearly defined. Pursuing this type of continuous gas to dust transition disc, may prove favourable in future modelling attempts. Other environments to consider in future work are those where a second, larger, amorphous carbon disc, surrounds the regions considered here (e.g., Oppenheimer et al., 2005).

IRAS08005, similarly to Mz3 and M2-9 displays high outflow momentum, that can only be achieved by jets launched during common envelope accretion, or Roche lobe overflow onto a main sequence star is necessary to account for the high momentums involved. Similarly to the previous two objects, a polar common envelope ejection is suggested because of the large mass found in the collimated lobes.

In considering the collimation *strength* of the silicate disc modelled, we determine that the disc, though with a relatively small inner-radius, is unlikely to play a significant role in diverting the outflow, but suggest instead that it may assist in a small way as a secondary collimating agent, if formed prior to the outflow events. Detection of a ∼6 yr light variability, if interpreted as an orbital period, suggests that the disc is likely circumbinary for binaries with combined masses of up to ∼1 $M_\odot$. However, such a binary could be problematic for a common envelope interpretation. The orbit is too wide for the binary to be post common envelope, but too small to have accommodated an inner binary in the past. The options open are therefore a Roche lobe overflow that ejected the lobes very efficiently and avoided CE all together, or a triple whose central binary went through a common envelope (companion undetected or merged) and where the tertiary's orbit decreased.

8.1.4 IRAS 16279-4757

Similarly to the case of IRAS08005, an accurate representation of the true model class could not be determined for IRAS16279, and we rely on 48 `GADRAD` models

across 7 disc model sub-classes. This dual-dust chemistry object, which displays both traces of carbon- and oxygen-rich dust, was determined to harbour a disc that could be made either of amorphous or crystalline silicates, in addition to carbon dust. Both amorphous and crystalline silicates were found to better reproduce IRAS16279's MIDI spectrum, while carbon dust provided a better representation of the MIDI visibilities. The results are likely reflective of the model-class adopted, which, we propose, does not generalise well enough to represent the object observed. Similarly to IRAS08005, we suggest a continuous gas-to-dust transition disc in future modelling attempts. Such an environment would represent a more physical model, and perhaps be a more representative and generalisable model class. A second, surrounding disc may also be worth considering (or even a third, i.e., Matsuura et al., 2004).

Dust composition was found difficult to determine in the case of IRAS16279. For example, a circumbinary/stellar amorphous carbon disc, consistent with the models of B13 and Matsuura et al. (2004), was found to produce reasonable approximations to the data products across both the K- and N-band. However, both amorphous and crystalline silicate discs, also matched data products reasonably well. It is likely that future, high resolution spectroscopic studies, will be necessary to determine the object's true composition. Again, due to the high momenta of the outflows of IRAS16279, formation scenarios available to the object are limited to Roche lobe overflow onto a main sequence star or common envelope accretion. GADRAD estimations of the primary's central star temperature and luminosity indicate that the central star of IRAS16279 is a post-AGB object.

8.1.5 Findings and object comparison

We have applied GADRAD to four post-AGB objects. In each case we have relied on a 2D-stratified-disc model class to represent the density structures of the discs in the given objects. Though small systematic differences may exist in the case of Mz3 and M2-9, we conclude that the models provide a reasonable representation of the objects. In IRAS08005 and IRAS16279, however, the model class was concluded to lack the scope necessary to determine accurately representative solutions. However, due to the inverse nature of the problem, many alternative disc structures await exploration.

It was determined that all objects have high outflow momenta that necessitate the high accretion rates possible only during Roche lobe overflow or during common envelope. However, in all 4 objects the outflows' masses are likely too large to have been ejected during the short-lived Roche lobe overflow or accretion during the common envelope phases. Hence we propose all of the collimated nebulae in these 4 objects are polar ejections of common envelopes. It is also likely that the discs may play a small role in diverting the outflows, but only if their formation preceded the outflow. Discs are compared in Table 8.1, and their central stars and other characteristics are compared in Table 8.2.

Table 8.1: Dusty discs within the post-AGB objects.

Object	disc dust mass (10^{-6}M$_\odot$)	composition	$r_{\rm in}$ (AU)	h_α	h_β
Mz3	35^{+75}_{-22}	AS	15^{+3}_{-4}	4.1	1.15
M2-9	$4.6^{+5.3}_{-1.9}$	AS	18 ± 5	2.9	1.1
IRAS08005	0.2-18.7	AS	4.8-10	3.1-6.6	0.9-1.3
IRAS16279	0.5-15.5	AS,CS,AC	14-23	1.7-2.9	1.0-1.4

Table 8.2: Object central stars.

Object	$T_\star$ (10^3K)	$L_\star$ (10^3L$_\odot$)	$M_\star$ (M$_\odot$)	type	P$_{\rm orb}$ (yr)	$M_{j,\rm ob}$ (M$_\odot$)	$p_{j,\rm ob}$ (g cm s^{-1})	$t_{\rm acc}$ (yr)
Mz3	35^{+12}_{-15}	12 ± 4	0.60-0.68	post-AGB	*	1.9	3.4×10^{40}	1800
M2-9	13^{+13}_{-7}	$4.0^{+0.9}_{-0.8}$	0.53-0.58	post-AGB	92±4	1.5	9.0×10^{39}	2000
IRAS08005	7.2-13	7.8-9.2	0.59-0.66	post-AGB:	6.1	0.25	2.8×10^{39}	190
IRAS16279	8.7-14.8	2.4-6.6	0.52-0.58	post-AGB:	*	0.42	1.0×10^{39}	450

*no periodicity observed.

The four discs within the four objects studied in this thesis are relatively similar, within the error ranges we have established. It is therefore hard to suggest that they were produced by different formation mechanisms. Based on the high outflow momenta and high mass outflows observed, the 4 post-AGB nebulae likely derive from a common envelope ejection. The similarities seen in the discs may then suggest that the discs we are observing may result from fall back of material that was not fully ejected during the common envelope.

It is also worth putting these discs in the context of the so-called naked post-AGB stars, a class of objects that have identical central stars to the pre-PN, but no surrounding visible nebulae. It has been hypothesised (e.g., B13), though not yet proven, that the discs observed in the naked post-AGB stars may be systematically different from those detected in the post-AGB PPN objects. Based on our findings, we conclude, however, that the discs detected in our small sample of post-AGB objects does not show any systematic differences with those of the naked post-AGBs (e.g., Deroo et al., 2007b). We suggest at this time, that the distinction between the naked pAGBs and PPN objects cannot be made, based on these disc properties.

8.2 Future work

The process of GADRAD shows great promise in characterising the small scale discs around post-AGB objects from interferometric data products. Next generation VLTI instruments, i.e., GRAVITY and MATISSE with the potential to provide more comprehensive coverage of the *uv*-plane, would be well suited to the observation of these elusive objects. In extracting information pertaining to the disc structures, we encourage the use of systematic optimisation techniques, such as the GA, over previous *ad-hoc* approaches. We will be making GADRAD publicly available, with concomitant documentation so that it can be used by future generations of interferometric observations.

Broader coverage of the *uv*-plane will likely improve upon the ability of an optimisation algorithm to characterise these often complex regions. The challenge, however, seems to be the determination of viable model classes on which to base radiative transfer models. Potential routes in determining more accurate model classes may come from image-reconstruction, in which light distributions can be constrained, and when used self-consistently, help guide model implementation in numerical reconstruction techniques. Additional observations that characterise the kinematics of the structures (e.g., such as that provided by the Atacama Large Millimetre/submillimetre Array; ALMA) seen with the VLTI would also be of benefit, as they can similarly be incorporated into the fitting routine.

Even without further observational constraint in IRAS08005 and IRAS16279 however, alternative (but simple) model classes may be considered. For example, we could in future treat the gaseous source harboured between the star and the dusty disc as extended, rather than as a point source. Additionally, we could also include a second, larger surrounding disc. Perhaps the most robust method, would be to adopt a so-called multi-objective optimisation function, in which multiple model classes are considered and systematically optimised (e.g., Deb et al., 2016). Multi-objective genetic algorithm variants may be well suited to such tasks. One factor that must be considered in the adoption of systematic large scale optimisation approaches, however, is the computational time requirements of the radiative transfer code, in addition to algorithm efficiency. For deep model exploration, it is likely that efficiency improvements will need to be made on both fronts. In the case of radiative transfer, the balance between model accuracy and efficiency may need to be tuned further. Also worth considering, in cases where model solutions are determined from a significant number of radiative transfer models, is final model accuracy, and whether a large number of low resolution models is preferred to fewer higher resolution models.

Many routes are also available to improve algorithm efficiency, i.e., reducing the number of radiative transfer models required. Hybrid GAs are one such route, in which the GA is combined with other optimisation techniques such as simulated annealing or particle swarm algorithms (e.g., Thangiah et al., 1994; Kao & Zahara, 2008). Surrogate assisted GAs could also be adopted, in which a small fraction of the candidate's fitnesses are determined from other members of the population (e.g., Jin, 2011), foregoing the need to run a radiative transfer model for each candidate solution of the population.

It is evident that the VLTI instruments, when paired with optimisation approaches to determine solutions to ill-posed inverse problems has a lot more to offer disc characterisation in post-AGB objects. Ultimately however, such approaches, supplemented by multi-wavelength observations, and improved theoretical underpinning are required to understand the transition between the AGB and the post-AGB phases.

Bibliography

Ables J. G., 1974, A&A, 15, 383

Acke B., et al., 2013, A&A, 551, A76

Acker A., Marcout J., Ochsenbein F., Stenholm B., Tylenda R., Schohn C., 1992, The Strasbourg-ESO Catalogue of Galactic Planetary Nebulae. Parts I, II.. European Southern Observatory

Akashi M., Soker N., 2008, MNRAS, 391, 1063

Allen D. A., Swings J. P., 1972, ApJ, 174, 583

Bäck T., 1994, in Proceedings of the First IEEE Conference on Evolutionary Computation. pp 57–62

Bäck T., Schütz M., 1996, in Foundations of intelligent systems. Springer, pp 158–167

Baier A., Kerschbaum F., Lebzelter T., 2010, A&A, 516, A45

Bains I., Richards A. M. S., Gledhill T. M., Yates J. A., 2004, MNRAS, 354, 529

Baker J. E., 1985, in Proceedings of an International Conference on Genetic Algorithms and their applications. pp 101–111

Bakker E. J., Lamers H. J. G. L. M., Waters L. B. F. M., Waelkens C., Trams N. R., Van Winckel H., 1996, A&A, 307, 869

Bakker E. J., van Dishoeck E. F., Waters L. B. F. M., Schoenmaker T., 1997, A&A, 323, 469

Balick B., 1987, AJ, 94, 671

Balick B., Frank A., 2002, ARA&A, 40, 439

Baron F., Young J. S., 2008, in SPIE Astronomical Telescopes and Instrumentation. pp 70133X–70133X

Baron F., Monnier J. D., Kloppenborg B., 2010, in Proc. SPIE. p. 77342I

Blackman E. G., Lucchini S., 2014, MNRAS, 440, L16

Blackman E. G., Frank A., Markiel J. A., Thomas J. H., Van Horn H. M., 2001a, Nature, 409, 485

Blackman E. G., Frank A., Welch C., 2001b, ApJ, 546, 288

Blandford R. D., Payne D. G., 1982, MNRAS, 199, 883

Bloecker T., 1995, A&A, 297, 727

Bond H. E., Livio M., 1990, ApJ, 355, 568

Bond H. E., Liller W., Mannery E. J., 1978, ApJ, 223, 252

Bright S. N., 2013, PhD thesis, Macquarie University

Bright S. N., De Marco O., Chesneau O., Lagadec E., Van Winckel H., Hrivnak B. J., 2012, in IAU Symposium. pp 115–118 (arXiv:1109.4999)

Bryan G. L., Volk K., Kwok S., 1990, ApJ, 365, 301

Bujarrabal V., Alcolea J., Neri R., 1998, ApJ, 504, 915

Bujarrabal V., Castro-Carrizo A., Alcolea J., Sánchez Contreras C., 2001, A&A, 377, 868

Bujarrabal V., Neri R., Alcolea J., Kahane C., 2003, A&A, 409, 573

Bujarrabal V., Castro-Carrizo A., Alcolea J., Neri R., 2005, A&A, 441, 1031

Bujarrabal V., Castro-Carrizo A., Alcolea J., Van Winckel H., Sánchez Contreras C., Santander-García M., Neri R., Lucas R., 2013, A&A, 557, L11
Bujarrabal V., Castro-Carrizo A., Alcolea J., Santander-García M., van Winckel H., Sánchez Contreras C., 2016, A&A, 593, A92
Burleigh M. R., Hogan E., Dobbie P. D., Napiwotzki R., Maxted P. F. L., 2006, MNRAS, 373, L55
Cahn J. H., Kaler J. B., Stanghellini L., 1992, A&AS, 94, 399
Calvet N., Peimbert M., 1983, Rev. Mexicana Astron. Astrofis., 5, 319
Cantó J., Curiel S., Martínez-Gómez E., 2009, Astronomy & Astrophysics, 501, 1259
Cardelli J. A., Clayton G. C., Mathis J. S., 1989, ApJ, 345, 245
Castro-Carrizo A., Bujarrabal V., Neri R., Alcolea J., Contreras C. S., Santander-Garcia M., Nyman L.-A., 2017, Astronomy & Astrophysics
Cerruti-Sola M., Perinotto M., 1989, ApJ, 345, 339
Chandrasekhar S., 1960, Radiative Transfer. Dover, New York
Charbonneau P., 1995, ApJS, 101, 309
Chelli A., Duvert G., Malbet F., Kern P., 2009a, A&A, 498, 321
Chelli A., Utrera O. H., Duvert G., 2009b, A&A, 502, 705
Chen P. S., Szczerba R., Kwok S., Volk K., 2001, A&A, 368, 1006
Chesneau O., Rivinius T., 2005, Publications of the Astronomical Institute of the Czechoslovak Academy of Sciences, 93, 36
Chesneau O., et al., 2007a, A&A, 464, 119
Chesneau O., et al., 2007b, A&A, 473, L29
Chesneau O., et al., 2009, A&A, 493, L17
Chevalier R. A., Luo D., 1994, ApJ, 421, 225
Ciardullo R., Bond H. E., Sipior M. S., Fullton L. K., Zhang C.-Y., Schaefer K. G., 1999, AJ, 118, 488
Clayton G. C., De Marco O., Nordhaus J., Green J., Rauch T., Werner K., Chu Y.-H., 2014, AJ, 147, 142
Clyne N., Akras S., Steffen W., Redman M. P., Gonçalves D. R., Harvey E., 2015, A&A, 582, A60
Cohen M., Kunkel W., Lasker B. M., Osmer P. S., Fitzgerald M. P., 1978, ApJ, 221, 151
Cohen M., Walker R. G., Carter B., Hammersley P., Kidger M., Noguchi K., 1999, AJ, 117, 1864
Corradi R. L. M., Balick B., Santander-García M., 2011, A&A, 529, A43
Davis L., 1991, Handbook of genetic algorithms. Van Nostrand Reinhold
De Geyter G., Baes M., Fritz J., Camps P., 2013, A&A, 550, A74
De Marco O., 2009, PASP, 121, 316
De Marco O., Soker N., 2011, PASP, 123, 402
De Marco O., Sandquist E. L., Mac Low M.-M., Herwig F., Taam R. E., 2003, in Revista Mexicana de Astronomia y Astrofisica Conference Series. pp 34–37
De Marco O., Hillwig T. C., Smith A. J., 2008, AJ, 136, 323
De Marco O., Long J., Jacoby G. H., Hillwig T., Kronberger M., Howell S. B., Reindl N., Margheim S., 2015, MNRAS, 448, 3587
DeJong K., 1975, PhD thesis, University of Michigan
Deaven D. M., Ho K. M., 1995, Phys.˜Rev.˜Lett., 75, 288
Deb K., Sindhya K., Hakanen J., 2016, in , Decision Sciences: Theory and Practice. CRC Press, pp 145–184
Derie F., 2000, in Interferometry in Optical Astronomy. pp 25–30

Deroo P., van Winckel H., Verhoelst T., Min M., Reyniers M., Waters L. B. F. M., 2007a, A&A, 467, 1093
Deroo P., Acke B., Verhoelst T., Dominik C., Tatulli E., van Winckel H., 2007b, A&A, 474, L45
de Ruyter S., van Winckel H., Maas T., Lloyd Evans T., Waters L. B. F. M., Dejonghe H., 2006, A&A, 448, 641
Deutsch A. J., 1956, ApJ, 123, 210
Dorigo M., Maniezzo V., Colorni A., 1996, IEEE Trans. Systems, Man, and Cybernetics, Part B, 26, 29
Dorschner J., Begemann B., Henning T., Jaeger C., Mutschke H., 1995, A&A, 300, 503
Douchin D., et al., 2015, MNRAS, 448, 3132
Dullemond C. P., 2011, RADMC: A 2-D Continuum Radiative Transfer Tool, Astrophysics Source Code Library (ascl:1108.016)
Dullemond C. P., 2012, RADMC-3D: A multi-purpose radiative transfer tool, Astrophysics Source Code Library (ascl:1202.015)
Duquennoy A., Mayor M., 1991, A&A, 248, 485
Dwarkadas V. V., 2004, in Asymmetrical Planetary Nebulae III: Winds, Structure and the Thunderbird. p. 430
Dybowski R., Gant V., Weller P., Chang R., 1996, The Lancet, 347, 1146
Eiben A. E., Raue P.-E., Ruttkay Z., 1994, in International Conference on Parallel Problem Solving from Nature. pp 78–87
Eisenhauer F., et al., 2011, The Messenger, 143, 16
Ercolano B., Barlow M. J., Storey P. J., Liu X.-W., 2003, MNRAS, 340, 1136
Exter K., Bond H. E., Stassun K. G., Smalley B., Maxted P. F. L., Pollacco D. L., 2010, AJ, 140, 1414
Frank A., Balick B., Icke V., Mellema G., 1993, ApJ, 404, L25
García-Arredondo F., Frank A., 2004, ApJ, 600, 992
García-Segura G., Langer N., Różyczka M., Franco J., 1999, ApJ, 517, 767
García-Segura G., López J. A., Franco J., 2005, ApJ, 618, 919
García-Segura G., Villaver E., Langer N., Yoon S.-C., Manchado A., 2014, ApJ, 783, 74
Gilman R. C., 1969, ApJ, 155, L185
Glindemann A., 2011, Principles of Stellar Interferometry. Springer Science & Business Media
Glindemann A., et al., 2001, The Messenger, 104, 2
Goldberg D. E., 1989, Genetic Algorithms in Search, Optimization and Machine Learning. Addison-Wesley, Reading, MA
Goldfeld S. M., Quandt R. E., Trotter H. F., 1966, Econometrica, 34, 541
Golub M., 1996, in Proceedings of the 18th International Conference on Information Technology Interfaces. pp 417–422
Gonçalves D. R., Corradi R. L. M., Mampaso A., 2001, ApJ, 547, 302
Goodrich R. W., 1991, ApJ, 366, 163
Grant V., 1985, The evolutionary process: A critical review of evolutionary theory. Columbia University Press
Grefenstette J. J., 1986, Systems, Man and Cybernetics, IEEE Transactions on, 16, 122
Grellmann R., 2012, PhD thesis, lmu
Gromadzki M., Mikołajewska J., Whitelock P., Marang F., 2009, Acta Astron., 59, 169
Guerrero M. A., Chu Y.-H., Miranda L. F., 2004, AJ, 128, 1694

Gutierrez-Moreno A., Moreno H., Cortes G., 1995, PASP, 107, 462
Hanagandi V., Nikolaou M., 1995, Chemical engineering, pp 221–252
Hancock P. J., 1995, Practical Handbook of Genetic Algorithms, 2, 67
Hanner M., 1988, Technical report, Grain optical properties
Hartmann L., MacGregor K. B., 1980, ApJ, 242, 260
Haupt R. L., Haupt S. E., 2004, Practical genetic algorithms. John Wiley & Sons
Heap S. R., et al., 1978, Nature, 275, 385
Herwig F., 2005, ARA&A, 43, 435
Hetem A., Gregorio-Hetem J., 2007, MNRAS, 382, 1707
Hibbert D. B., 1993, Chemometrics and Intelligent Laboratory Systems, 19, 277
Hillen M., 2013, PhD thesis, KU Lueven
Hillen M., et al., 2013, A&A, 559, A111
Hogenhuis H., Visser M., Derie F., 2003, in Traub W. A., ed., Proc. SPIEVol. 4838, Interferometry for Optical Astronomy II. pp 1148–1154
Holland J. H., 1975, Adaptation in natural and artificial systems: an introductory analysis with applications to biology, control, and artificial intelligence. U Michigan Press
Holzer T. E., MacGregor K. B., 1985, in Mass Loss from Red Giants. pp 229–255
Hora J. L., Latter W. B., 1994, ApJ, 437, 281
Hosseinzadeh M., Roghanian E., 2012, International Journal of Business and Social Science, 3, 1
Hrivnak B. J., 1995, ApJ, 438, 341
Hrivnak B. J., Lu W., Bohlender D., Morris S. C., Woodsworth A. W., Scarfe C. D., 2011, ApJ, 734, 25
Hu J. Y., Slijkhuis S., de Jong T., Jiang B. W., 1993, A&AS, 100, 413
Huarte-Espinosa M., Frank A., Blackman E. G., Ciardi A., Hartigan P., Lebedev S. V., Chittenden J. P., 2012, ApJ, 757, 66
Iaconi R., Reichardt T., Staff J., De Marco O., Passy J.-C., Price D., Wurster J., Herwig F., 2017, MNRAS, 464, 4028
Iben Jr. I., 1967, ApJ, 147, 624
Iben Jr. I., 1991, ApJS, 76, 55
Iben Jr. I., 1995, Phys. Rep., 250, 2
Iben Jr. I., Renzini A., 1983, ARA&A, 21, 271
Icke V., 1988, A&A, 202, 177
Icke V., Preston H. L., Balick B., 1989, AJ, 97, 462
Ignace R., Cassinelli J. P., Bjorkman J. E., 1996, ApJ, 459, 671
Ivanova N., et al., 2013, A&A Rev., 21, 59
Jaeger C., Mutschke H., Begemann B., Dorschner J., Henning T., 1994, A&A, 292, 641
Jaynes E. T., 1957, Physical review, 106, 620
Jin Y., 2011, Swarm and Evolutionary Computation, 1, 61
Jura M., Webb R. A., Kahane C., 2001, ApJ, 550, L71
Kahn F. D., West K. A., 1985, MNRAS, 212, 837
Kao Y.-T., Zahara E., 2008, Applied Soft Computing, 8, 849
Kastner J. H., Balick B., Blackman E. G., Frank A., Soker N., Vrtílek S. D., Li J., 2003, ApJ, 591, L37
Kennedy J., Eberhart R., 1995, in Proceedings of IEEE International Conference on Neural Networks IV. IEEE, pp 1942–1948
Kingsburgh R. L., English J., 1992, MNRAS, 259, 635
Kirkpatrick S., Gelatt C. D., Vecchi M. P., et al., 1983, science, 220, 671
Klochkova V. G., 2014, Astrophysical Bulletin, 69, 279

Klochkova V. G., Chentsov E. L., 2004, Astronomy Reports, 48, 301
Klochkova V. G., Szczerba R., Panchuk V. E., Volk K., 1999, A&A, 345, 905
Kuruwita R. L., Staff J., De Marco O., 2016, MNRAS, 461, 486
Kwok S., 2007, The origin and evolution of planetary nebulae. Cambridge University Press
Kwok S., Purton C. R., Fitzgerald P. M., 1978, ApJ, 219, L125
Kwok S., Hrivnak B. J., Geballe T. R., 1995, ApJ, 454, 394
Labeyrie A., Le Coroller H., Dejonghe J., Martinache F., Borkowski V., Lardiere O., Koechlin L., 2003, in Shao M., ed., Proc. SPIEVol. 4852, Interferometry in Space. pp 236–247
Labeyrie A., Lipson S. G., Nisenson P., 2006, An introduction to optical stellar interferometry. Cambridge University Press
Lagadec E., et al., 2011, MNRAS, 417, 32
Le Bouquin J.-B., Lacour S., Renard S., Thiébaut E., Merand A., Verhoelst T., 2009, A&A, 496, L1
Le Bouquin J.-B., et al., 2011, A&A, 535, A67
Leal-Ferreira M. L., Vlemmings W. H. T., Kemball A., Amiri N., 2013, A&A, 554, A134
Leinert C., et al., 2003, Ap&SS, 286, 73
Levenberg K., 1944, Quarterly of applied mathematics, 2, 164
Levin M., 1995, Practical Handbook of Genetic Algorithms, Applications, 2, 53
Li P.-H., Kwon H.-H., Sun L., Lall U., Kao J.-J., 2010, International Journal of Climatology, 30, 1256
Livio M., 1982, A&A, 105, 37
Livio M., 1999, Phys. Rep., 311, 225
Livio M., Soker N., 2001, ApJ, 552, 685
Livio M., Salzman J., Shaviv G., 1979, MNRAS, 188, 1
Lopez J. A., Meaburn J., 1983, MNRAS, 204, 203
Lutz J. H., 1993, in Weinberger R., Acker A., eds, IAU Symposium Vol. 155, Planetary Nebulae. p. 19
Lykou F., Chesneau O., Zijlstra A. A., Castro-Carrizo A., Lagadec E., Balick B., Smith N., 2011, A&A, 527, A105
Marquardt D. W., 1963, Journal of the society for Industrial and Applied Mathematics, 11, 431
Mastrodemos N., Morris M., 1998, ApJ, 497, 303
Mathis J. S., Rumpl W., Nordsieck K. H., 1977, ApJ, 217, 425
Matsuura M., et al., 2004, ApJ, 604, 791
Matt S., Balick B., Winglee R., Goodson A., 2000, ApJ, 545, 965
Meaburn J., Walsh J. R., 1985, MNRAS, 215, 761
Meimon S. C., Mugnier L. M., Le Besnerais G., 2005, Optics Letters, 30, 1809
Mellema G., Frank A., 1995, MNRAS, 273, 401
Menu J., et al., 2014, A&A, 564, A93
Menzel D. N., 1922, Harvard College Observatory Bulletin, 777, 0
Meyer F., Meyer-Hofmeister E., 1979, A&A, 78, 167
Michelson A. A., Morley E. W., 1887, Sidereal Messenger, vol. 6, pp.306-310, 6, 306
Mie G., 1908, Ann. Phys, 25, 337
Miller Bertolami M. M., 2016, A&A, 588, A25
Millour F., 2014, in EAS Publications Series. pp 17–52 (arXiv:1603.01463)
Millour F., et al., 2008, in Kaufer A., Kerber F., eds, 2007 ESO Instrument Calibration Workshop. p. 461 (arXiv:0705.1636)

Minkowski R., 1947, PASP, 59, 257
Miszalski B., Acker A., Moffat A. F. J., Parker Q. A., Udalski A., 2009a, A&A, 496, 813
Miszalski B., Acker A., Parker Q. A., Moffat A. F. J., 2009b, A&A, 505, 249
Mitchell M., 1998, An introduction to genetic algorithms. MIT press
Monnier J. D., 2003, Reports on Progress in Physics, 66, 789
Monnier J. D., 2007, New A Rev., 51, 604
Montez Jr. R., De Marco O., Kastner J. H., Chu Y.-H., 2010, ApJ, 721, 1820
Montez Jr. R., et al., 2015, ApJ, 800, 8
Morris M., 1981, ApJ, 249, 572
Morris M., 1987, PASP, 99, 1115
Moscato P., et al., 1989, Caltech concurrent computation program, C3P Report, 826, 1989
Murakawa K., Ueta T., Meixner M., 2010, A&A, 510, A30
Nelder J. A., Mead R., 1965, The computer journal, 7, 308
Nenkova M., Ivezić Ž., Elitzur M., 2000, Thermal Emission Spectroscopy and Analysis of Dust, Disks, and Regoliths, 196, 77
Neri R., Kahane C., Lucas R., Bujarrabal V., Loup C., 1998, A&AS, 130, 1
Nordhaus J., Blackman E. G., 2006, MNRAS, 370, 2004
Nordhaus J., Blackman E. G., Frank A., 2007, MNRAS, 376, 599
O'Donnell J. E., 1994, ApJ, 422, 158
Ohnaka K., et al., 2005, A&A, 429, 1057
Olofsson H., 1999, in Le Bertre T., Lebre A., Waelkens C., eds, IAU Symposium Vol. 191, Asymptotic Giant Branch Stars.
Olofsson H., Vlemmings W. H. T., Maercker M., Humphreys E. M. L., Lindqvist M., Nyman L., Ramstedt S., 2015, A&A, 576, L15
Oppenheim A. V., Lim J. S., 1981, IEEE Proceedings, 69, 529
Oppenheimer B. D., Bieging J. H., Schmidt G. D., Gordon K. D., Misselt K. A., Smith P. S., 2005, ApJ, 624, 957
Paczyński B., 1971, Astrophys. Lett., 9, 33
Paczynski B., 1976, in Eggleton P., Mitton S., Whelan J., eds, IAU Symposium Vol. 73, Structure and Evolution of Close Binary Systems. p. 75
Parker Q. A., et al., 2006, MNRAS, 373, 79
Pascoli G., 1987, A&A, 180, 191
Pascoli G., 1997, ApJ, 489, 946
Passy J.-C., et al., 2012, ApJ, 744, 52
Patriarchi P., Perinotto M., 1991, A&AS, 91, 325
Petrov R. G., et al., 2007, A&A, 464, 1
Pottasch S. R., Surendiranath R., 2005, A&A, 444, 861
Raghavan D., et al., 2010, ApJS, 190, 1
Rastrigin L., 1974, Theoretical foundations of engineering cybernetics series, 3
Regős E., Tout C. A., 1995, MNRAS, 273, 146
Reimers D., 1975, Memoires of the Societe Royale des Sciences de Liege, 8, 369
Renzini A., 1981, in Iben Jr. I., Renzini A., eds, Astrophysics and Space Science Library Vol. 88, Physical Processes in Red Giants. pp 431–446
Reyes-Ruiz M., López J. A., 1999, ApJ, 524, 952
Ricker P. M., Taam R. E., 2008, ApJ, 672, L41
Ricker P. M., Taam R. E., 2012, ApJ, 746, 74
Robbe-Dubois S., et al., 2007, A&A, 464, 13
Rosenfield P., et al., 2014, ApJ, 790, 22

Ruiz-Velasco A. E., Wittkowski M., Wachter A., Schröder K.-P., Driebe T., 2011, A&A, 535, A100
Ruiz N., Guerrero M. A., Chu Y.-H., Gruendl R. A., 2011, AJ, 142, 91
Russell H. N., 1914, The Observatory, 37, 165
Sabin L., Wade G. A., Lèbre A., 2015, MNRAS, 446, 1988
Sahai R., 2004, in Meixner M., Kastner J. H., Balick B., Soker N., eds, Astronomical Society of the Pacific Conference Series Vol. 313, Asymmetrical Planetary Nebulae III: Winds, Structure and the Thunderbird. p. 141
Sahai R., Patel N. A., 2015, ApJ, 810, L8
Sahai R., Trauger J. T., 1998, AJ, 116, 1357
Sahai R., Young K., Patel N. A., Sánchez Contreras C., Morris M., 2006, ApJ, 653, 1241
Sahai R., Morris M., Sánchez Contreras C., Claussen M., 2007, AJ, 134, 2200
Sahai R., Morris M. R., Villar G. G., 2011, AJ, 141, 134
Sahai R., Vlemmings W. H. T., Huggins P. J., Nyman L.-Å., Gonidakis I., 2013, ApJ, 777, 92
Sánchez Contreras C., Sahai R., Gil de Paz A., 2002, ApJ, 578, 269
Sandquist E. L., Taam R. E., Chen X., Bodenheimer P., Burkert A., 1998, ApJ, 500, 909
Santander-García M., Corradi R. L. M., Balick B., Mampaso A., 2004, A&A, 426, 185
Santander-García M., Bujarrabal V., Alcolea J., Castro-Carrizo A., Contreras C. S., Quintana-Lacaci G., Corradi R., Neri R., 2016, Astronomy & Astrophysics
Savage B. D., Mathis J. S., 1979, ARA&A, 17, 73
Schechtman-Rook A., Bershady M. A., Wood K., 2012, ApJ, 746, 70
Schmeja S., Kimeswenger S., 2001, A&A, 377, L18
Schöller M., Wilhelm R., Koehler B., 2000, A&AS, 144, 541
Schwarz H. E., Corradi R. L. M., Melnick J., 1992, A&AS, 96, 23
Schwarz H. E., Aspin C., Corradi R. L. M., Reipurth B., 1997, A&A, 319, 267
Schwarzschild M., Härm R., 1965, ApJ, 142, 855
Shakura N. I., Sunyaev R. A., 1973, A&A, 24, 337
Silva A. M., Azcarate I. N., Poppel W. G. L., Likkel L., 1993, A&A, 275, 510
Skarbnik N., Yehoshua Y C. S., 2009, The Importance of phase in image processing. Technion-Israel Institute of Technology, Faculty of Electrical Engineering
Slijkhuis S., de Jong T., Hu J. Y., 1991, A&A, 248, 547
Smith N., 2003, MNRAS, 342, 383
Smith N., Gehrz R. D., 2005, AJ, 129, 969
Soker N., 1995, MNRAS, 274, 147
Soker N., 1996, MNRAS, 283, 1405
Soker N., 1997, ApJS, 112, 487
Soker N., 2002, MNRAS, 330, 481
Soker N., 2006, PASP, 118, 260
Soker N., 2016, MNRAS, 455, 1584
Soker N., Livio M., 1989, ApJ, 339, 268
Soker N., Rappaport S., 2000, ApJ, 538, 241
Staff J. E., De Marco O., Macdonald D., Galaviz P., Passy J.-C., Iaconi R., Low M.-M. M., 2016, MNRAS, 455, 3511
Suárez O., García-Lario P., Manchado A., Manteiga M., Ulla A., Pottasch S. R., 2006, A&A, 458, 173
Swamy K. S. K., Stecher T. P., 1969, PASP, 81, 873

Tallon-Bosc I., et al., 2008, in Society of Photo-Optical Instrumentation Engineers (SPIE) Conference Series.
Tatulli E., et al., 2007, A&A, 464, 29
te Lintel Hekkert P. T. L., Chapman J. M., Zijlstra A. A., 1992, ApJ, 390, L23
Thangiah S. R., Osman I. H., Sun T., 1994, Computer Science Department, Slippery Rock University, Technical Report SRU CpSc-TR-94-27, 69
Thiébaut E., 2008, in Optical and Infrared Interferometry. p. 70131I
Thiébaut É., 2013, in Mary D., Theys C., Aime C., eds, EAS Publications Series Vol. 59, EAS Publications Series. pp 157–187
Timmerman S., Matveev S., Gress M., Davies G., 2015, Journal of Geochemical Exploration, 159, 243
Tocknell J., De Marco O., Wardle M., 2014, MNRAS, 439, 2014
Toon O. B., Ackerman T. P., 1981, Appl. Opt., 20, 3657
Torres-Peimbert S., Arrieta A., 1998, in Dufour R. J., Torres-Peimbert S., eds, Revista Mexicana de Astronomia y Astrofisica, vol. 27 Vol. 7, Revista Mexicana de Astronomia y Astrofisica Conference Series. p. 171
Trammell S. R., Dinerstein H. L., Goodrich R. W., 1994, AJ, 108, 984
Treffers R., Cohen M., 1974, ApJ, 188, 545
Tristram K. R. W., Burtscher L., Jaffe W., Meisenheimer K., Hönig S. F., Kishimoto M., Schartmann M., Weigelt G., 2014, A&A, 563, A82
Ueta T., Meixner M., Bobrowsky M., 2000, ApJ, 528, 861
van Cittert P. H., 1934, Physica, 1, 201
van der Veen W. E. C. J., Habing H. J., Geballe T. R., 1989, A&A, 226, 108
Van de Steene G. C., van Hoof P. A. M., Wood P. R., 2000, A&A, 362, 984
Vassiliadis E., Wood P. R., 1994, ApJS, 92, 125
van Winckel H., 2003, ARA&A, 41, 391
van Winckel H., et al., 2009, A&A, 505, 1221
Volk K., Kwok S., 1988, ApJ, 331, 435
Volk K. M., Kwok S., 1989, ApJ, 342, 345
Waelkens C., Van Winckel H., Waters L. B. F. M., Bakker E. J., 1996, A&A, 314, L17
Warner B., 2003, Cataclysmic Variable Stars. Cambridge University Press
Waters L. B. F. M., Waelkens C., Trams N. R., 1993, in European Southern Observatory Conference and Workshop Proceedings. p. 298
Waters L. B. F. M., et al., 1996, A&A, 315, L361
Waters L. B. F. M., et al., 1998, Nature, 391, 868
Weingartner J. C., Draine B. T., 2001, ApJ, 548, 296
Werner M. W., et al., 2014, ApJ, 780, 156
Whitley D., 1994, Statistics and computing, 4, 65
Whitney B. A., 2011, Monte Carlo radiative transfer. World Scientific Publishing Co, pp 151–176
Willson L. A., 2000, ARA&A, 38, 573
Wittkowski M., et al., 2011, A&A, 532, L7
Woitke P., et al., 2016, A&A, 586, A103
Wolf S., 2003, Computer Physics Communications, 150, 99
Wolf S., Henning T., Stecklum B., 1999, A&A, 349, 839
Wood K., Whitney B., Bjorkman J., Wolff M., 2001, Introduction to Monte Carlo radiation transfer
Woolf N. J., Ney E. P., 1969, ApJ, 155, L181
Yao X., Liu Y., Lin G., 1999, Evolutionary Computation, IEEE Transactions on, 3, 82

Young T., 1802, Philosophical Transactions of the Royal Society of London Series I, 92, 12
Young J., Thiébaut E., 2014, in EAS Publications Series. pp 133–147
Yungelson L. R., Tutukov A. V., Livio M., 1993, ApJ, 418, 794
Zernike F., 1938, Physica, 5, 785
Zhang Y., Liu X.-W., 2002, MNRAS, 337, 499
Zhang Y., Liu X.-W., 2006, in Planetary Nebulae in our Galaxy and Beyond. pp 547–548
Zijlstra A. A., 2006, arXiv preprint astro-ph/0610558
Zijlstra A. A., Gaylard M. J., te Lintel Hekkert P., Menzies J., Nyman L.-A., Schwarz H. E., 1991, A&A, 243, L9
Zijlstra A. A., Chapman J. M., te Lintel Hekkert P., Likkel L., Comeron F., Norris R. P., Molster F. J., Cohen R. J., 2001, MNRAS, 322, 280
Zijlstra A. A., Bedding T. R., Mattei J. A., 2002, MNRAS, 334, 498
Zubko V. G., Mennella V., Colangeli L., Bussoletti E., 1996, MNRAS, 282, 1321
Zuckerman B., Aller L. H., 1986, ApJ, 301, 772
Zweigle J., Neri R., Bachiller R., Bujarrabal V., Grewing M., 1997, A&A, 324, 624